Improving the stoichiometry in lead iodide and perovskite micro-crystals, towards the fabrication of more efficient perovskite solar cells

Tsevas Konstantinos

Department of Chemical and Biological Engineering

University of Sheffield

Thesis submitted for the degree of Doctor of Philosophy

September 2019

Acknowledgements

Initially I would like to thank my supervisors Dr. Alan Dunbar (1st), Prof. David Lidzey (2nd) and Dr. Cornelia Rodenburg (3rd) for their excellent supervision and guidance during the awarded scholarship of the Doctor of Philosophy course. Also, I would exceptionally thank Prof. Ken Durose, the director of the Centre of Doctoral Training of Photovoltaics (CDT-PV) and all colleagues who work on that. The CDT-PV is a multicentre scheme for doctoral training and development consisted by seven Universities (Liverpool, Bath, Sheffield, Loughborough, Southampton, Oxford and Cambridge) and funded by the United Kingdom's Government, the Engineering and Physical Sciences Research Council (EPSRC) and industrial sector. In addition, thanks to Mr. Joel Smith for his assistance with perovskite solar cell devices and information, to Dr. Vikas Kumar for the scanning electron microscopy assistance and information, to Dr. Nik Reeves McLaren from the University of Sheffield for providing the D2 Phaser (Bruker) X-ray diffractometer, to Dr. Deborah B. Hammond operator of the X-ray photoelectron spectroscopy characterization and relevant information. Also, my special thanks to Prof. Hans-Arno Synal, Dr. Christof Vockenhuber and their colleagues from the Laboratory of Ion Beam Physics at ETH Zurich facilities (Switzerland), who conducted measurements with Rutherford backscattering spectrometry and analysed the data of lead iodide samples. Many thanks also to the PhD students of the group: Abdulaziz Alrajeh, Francesco Bastianini, Gabriel Perez, Edwin Pineda and Adam Urwick. Finally, I would like to express my especially appreciation to my family for their multiannual support.

Abstract

The technology of photovoltaics provides a renewable and ecofriendly way of conversion of photons to electricity. Low cost photovoltaics with high efficiency and extended life time are some of the main goals during their fabrication. Perovskite solar cells (PSC) have been promoted to potential candidates in the field of photovoltaics. In this thesis, chapter 1 provides a general background theory about the field of perovskites and their use to fabricate PSC. In chapter 2, experimental details are provided, supporting the work that was made and the relevant theory of characterization techniques used. Chapter 3, mainly focusing on a low-cost, energy efficient and water-free synthesis of lead iodide (PbI_2) a material widely used for the fabrication of perovskites, by planetary ball milling (mechanochemical), controlling both stoichiometry and number of polytypic phases. Chapter 4, focusing on the stability of PSC fabricated with an optimum stoichiometry between different ions present in the photoactive layer. Synthesis of controllably doped or undoped methylammonium lead triiodide ($CH_3NH_3PbI_3$) micro-crystals with various amounts of dopants of either methylammonium bromide (CH_3NH_3Br) or formamidinium iodide ($CH(NH_2)_2I$) or $CH(NH_2)_2I$ and bromine (Br_2), was achieved. Characterization techniques used, included X-ray diffraction (XRD), X-ray photoelectron spectroscopy (XPS), Rutherford backscattering spectrometry (RBS), atomic force microscopy (AFM), scanning electron microscopy (SEM), UV-Vis spectroscopy, controllable chemical synthesis of micro-crystals and testing operational PSC devices. The results presented in chapter 3, indicated that the use of the sub-stoichiometric PbI_2 (when iodine content is below the optimum 1 : 2 ratio of Pb : I atoms) during the fabrication of the photoactive layer in PSC devices, results in unreacted PbI_2. The presence of unreacted PbI_2 reduces the average power conversion efficiency (PCE) of the PSC from ~ 15.5 % to ~ 4.6 %. Whereas, the results presented in chapter 4, indicated that controllable doping of $CH_3NH_3PbI_3$ micro-crystals with different incorporated ions, reveals a minimum of distortion in the resulted perovskite crystal structure. That might lead to an optimum composition in perovskites with enhanced chemical stability as function of the exposed conditions. Un-encapsulated PSC devices fabricated using controllably doped $CH_3NH_3PbI_3$ micro-crystals, showed a reduction in the average PCE from ~14 (±1.5)% to ~13.7 (±0.5)%, after storage in dark and under ambient conditions for 240 hours.

Publications

Vikas Kumar, Jeremy Barbe, Whitney L. Schmidt, Konstantinos Tsevas, Buse Ozkan, Christopher M. Handley, Colin L. Freeman, Derek C. Sinclair, Ian M. Reaney, Wing C. Tsoi, Alan Dunbar and Cornelia Rodenburg, "Stoichiometry-dependent local instability in $MAPbI_3$ perovskite materials and devices", *Journal of Materials Chemistry A, 2018,* ***6****, 23578-23586.*

Conferences

CDT-PV Showcase, Liverpool, 9th November 2017 (oral presentation)

PGR, Sheffield, 6th June 2017 (poster presentation)

PV-SAT 14, London, 18th April 2018 (poster presentation)

PGR, Sheffield, 6th June 2018 (oral presentation)

Awards

Clifton Wray Memorial, 3rd July 2019

Table of contents

Chapter 1

Background theory

1.1 Introduction

Since the dawn of organic-inorganic perovskites as a new class of semiconductors, several researchers have been studying their optoelectronic properties through fabrication of devices, such as photovoltaics, light emitting diodes (LEDs), photodetectors, batteries or even in the field of spintronics. [1–5] Their scientific attractiveness originates from the low cost, the remarkable variability in optoelectronic properties as function of ratio between the mixed organic-halogen and their simplicity of fabrication process. In the first chapter, the broad motivation for research and the necessity of renewable sources of energy is described, emphasizing more in photovoltaic solar technologies. Specifically, a range of information are provided, building up a background on perovskite solar cells, such as, their main device architectures, types of defects, principles of operation and obstacles to their commercialization. Additionally, in this chapter attention is given to the topic of stoichiometry and polytypism in lead iodide and perovskite photoactive layer and its links to durability and stability, being the main motivations for that specific work presented here and puts it in context.

1.2 Motivation

1.2.1 Global warming

Energy demand is expected to increase in all realistic scenarios of the near future world-wide as estimated by the U.S. Energy Information Administration, International Energy Outlook 2017, as shown in figure 1.1, due to the rise of industrial activity, food production, services and increase of the global population. The primary natural energy sources, such as petroleum (and derivatives), coal and natural gas, have remained the main sources of energy for the last 29 years. [6] However, growing concerns that have been triggered by the high emission of greenhouse gases such as carbon dioxide (CO_2), nitrous oxide (N_2O) and methane (CH_4), which inevitably leads to climate change and global warming, as stated by the IPCC (Intergovernmental Panel on Climate Change) and temperature global vs solar activity observations conducted by NASA/JPL-Caltech, as shown in figures 1.2 and 1.3. The challenge that we are facing is not only to terminate the consumption of our planet's current sources of energy originated from fossil fuels, but to rely on technologies for power generation with lower emission of greenhouse gases and elevated degree of abundancy. The development of renewable sources of energy is widely expected to serve both these options. Global energy production based on renewable sources of energy such as wind, tidal, hydropower, geothermal, biomass and solar photovoltaic technologies (excluding nuclear fusion), show a stable steady pace of growth, as shown in figure 1.4 and reported by REN21 global status report (Renewable Energy Policy Network). However, even though primary installed infrastructures related to renewable sources of energy are suffering from prohibitive costs, optimization research in materials used and construction methods result in completive options in comparison with the widely dominated market of fossil fuels sources of energy. In 2018 for example, the levelized cost per kWh of electricity produced (including materials, installation and land) related to large scale photovoltaic installations in Germany, was almost 20 % lower in contrast with the cost per kWh of electricity produced in facilities utilizing coal or natural gas, as provided by Fraunhofer Institute for Solar Energy Systems (ISE) and shown in figure 1.5. In 2017, only ~ 19 % out of the total global energy production originated from renewable sources of energy. Approximately, a share of 20 % out of the total renewable sources of energy, corresponds to photovoltaics, the same year. However,

is believed that a strong candidate for supplying all the global energy required could be provided solely by photovoltaics. Since the amount of incident solar energy that hits the Earth per hour is ~ 4.1 * 10^{20} joules, while the total annual global consumed energy is ~ 4.3 * 10^{20} joules (as provided by the World Energy Council). That could practically be translated, that if photovoltaics with power conversion efficiency of 15 % are evenly installed around the world, requires a total global land area of ~ 2 %, so that the annual global energy (electricity) production be fulfilled.

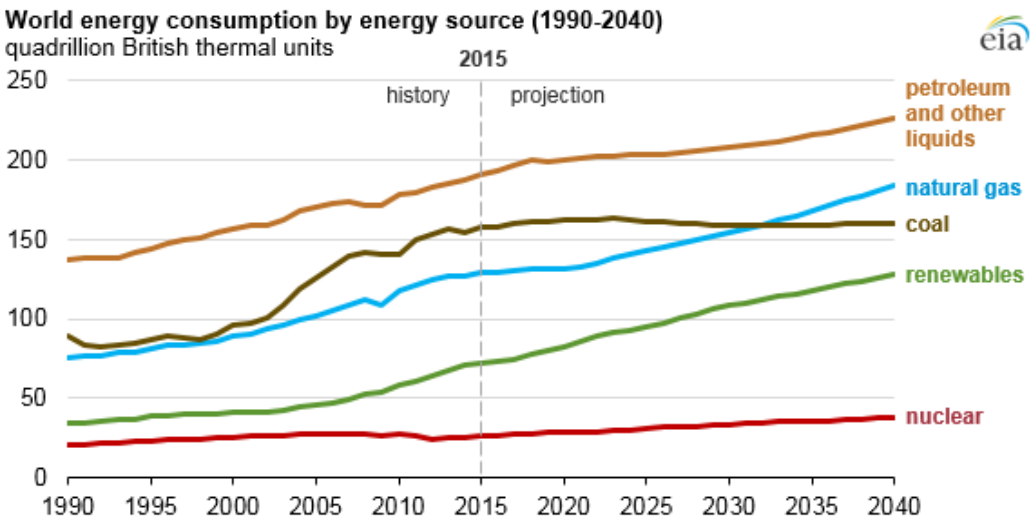

*Figure 1.1: World energy consumption by energy source from 1990 to 2040 (predicted). Source - U.S. Energy Information Administration, International Energy Outlook 2017 (*https://www.eia.gov/*).*

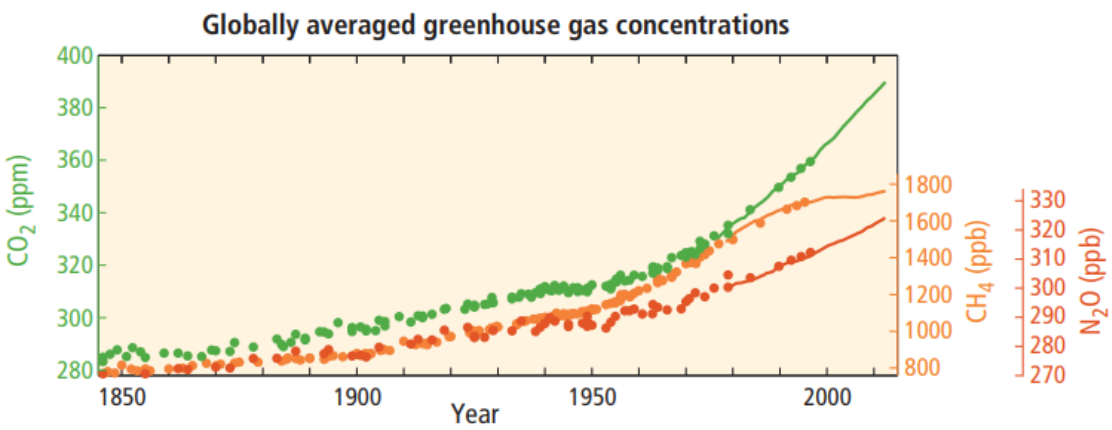

*Figure 1.2: Globally averaged greenhouse gas concentrations from 1850 to 2000. Source - IPCC (Intergovernmental Panel on Climate Change) (*https://www.ipcc.ch/*).*

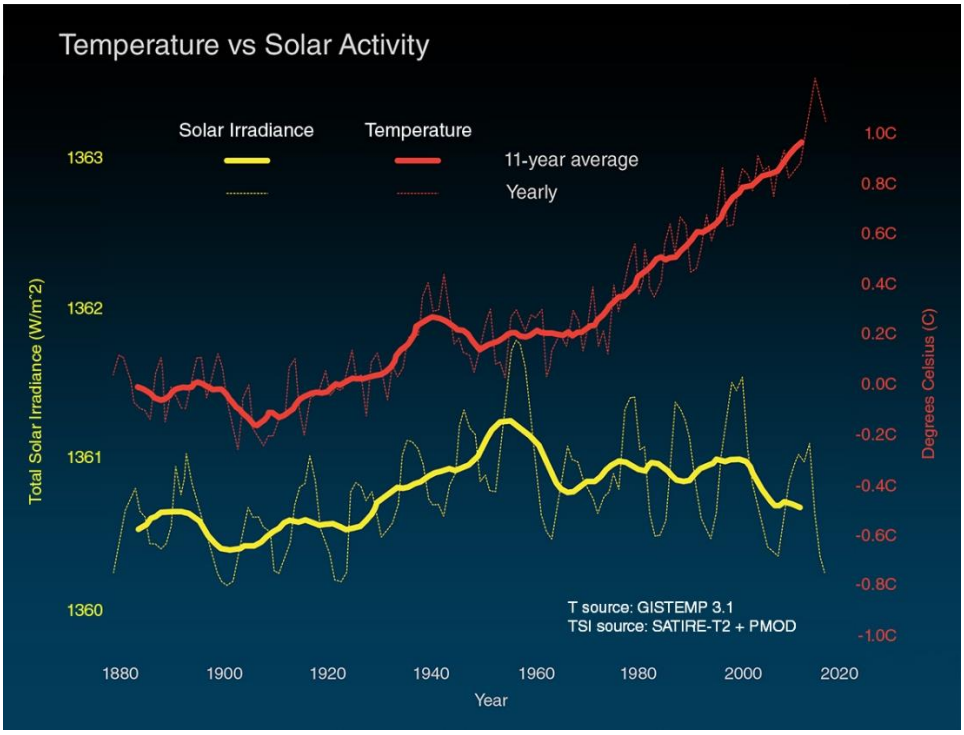

Figure 1.3: Earth temperature vs solar activity from 1880 to 2015. Source - NASA/JPL-Caltech (https://climate.nasa.gov/).

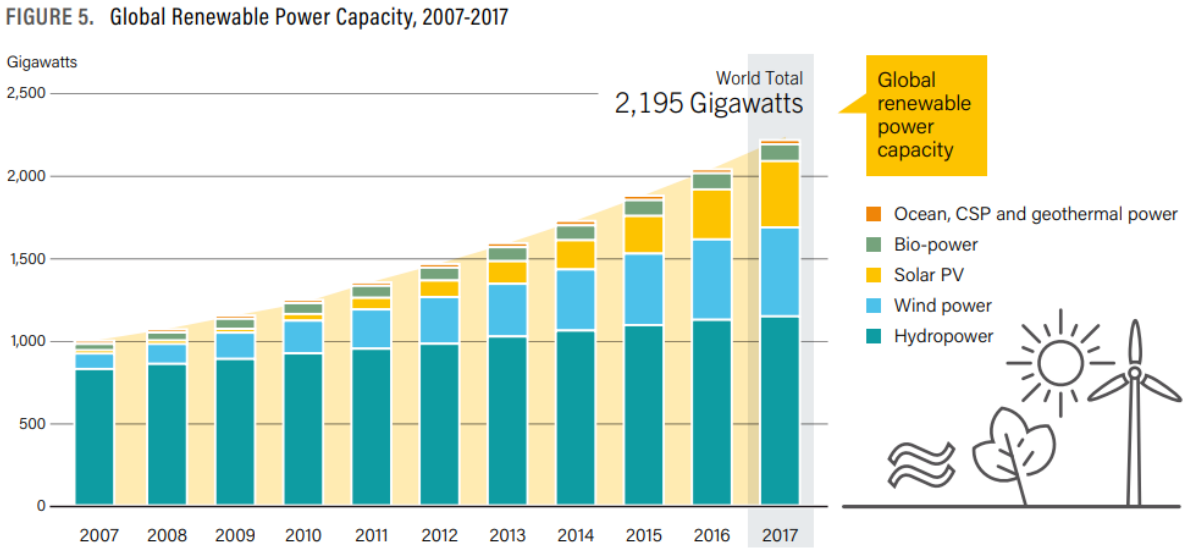

Figure 1.4: Global renewable power capacity from 2007 to 2017. Source - REN21 global status report (Renewable Energy Policy Network) (https://www.ren21.net/).

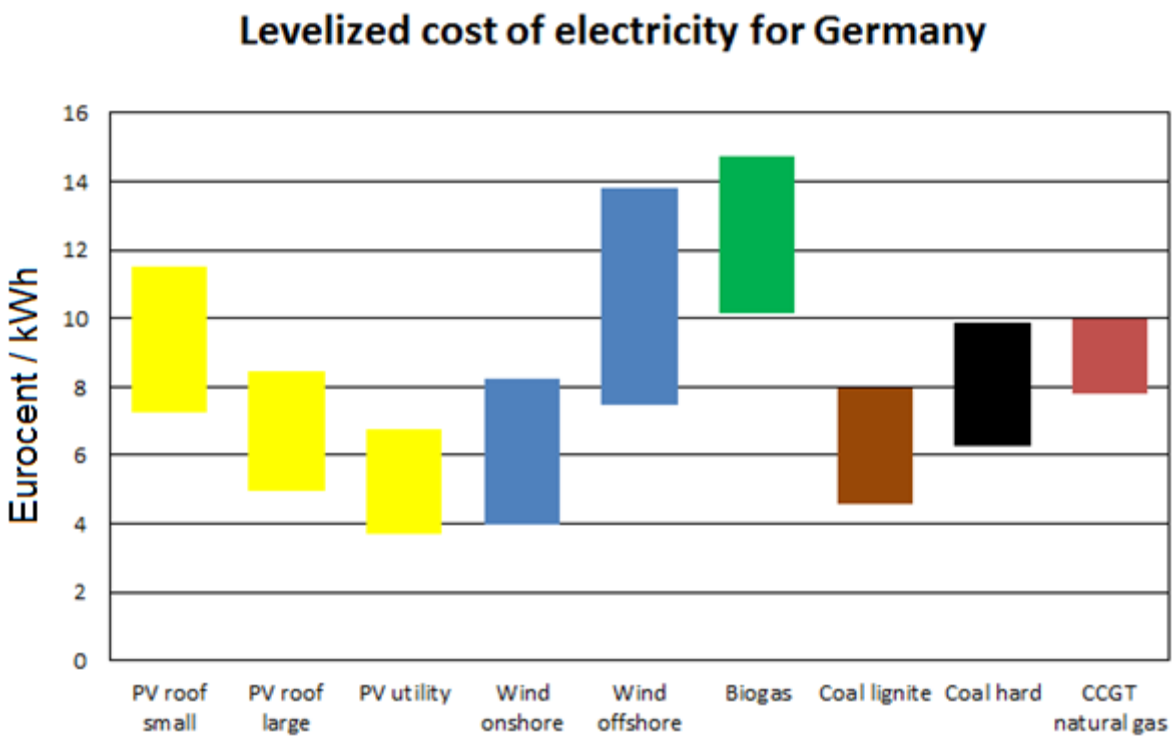

*Figure 1.5: Levelized cost of electricity (Eurocent / kWh) produced by newly built infrastructures, based on renewable and fossil fuels sources of energy. Source: Fraunhofer Institute for Solar Energy Systems (ISE) (*https://www.ise.fraunhofer.de/*).*

1.2.2 Renewable energy sources and photovoltaics

The constantly increasing global energy demand, combined with the rising emission of gases that are responsible for the greenhouse effect (CO_2 / N_2O / CH_4), has caused significant environmental and political concerns during the last two decades. Combined with the climate change, the importance of development towards a more environmentally friendly and viable mixture of global energy production sources, free of or with reduced dependency on fossil fuels, is a vital priority for humanity. So far, remarkable progress has been made at the academic and industrial level, exploring, investing and developing a range of renewable sources of energy, as shown in figures 1.6 and 1.7. The major fraction of investment and research, in comparison with all available renewable sources of energy, has been attributed to solar and wind technologies the last two decades. This is reflected by the abundancy of wind and solar irradiation, responsible of the extensive integration of these technologies in the

total mix of energy generation. However, solar photovoltaics consist an excellent choice as a renewable source of energy, since the low cost of fabrication, combined with the small environmental impact, display significant advantage, in comparison with wind power technologies.

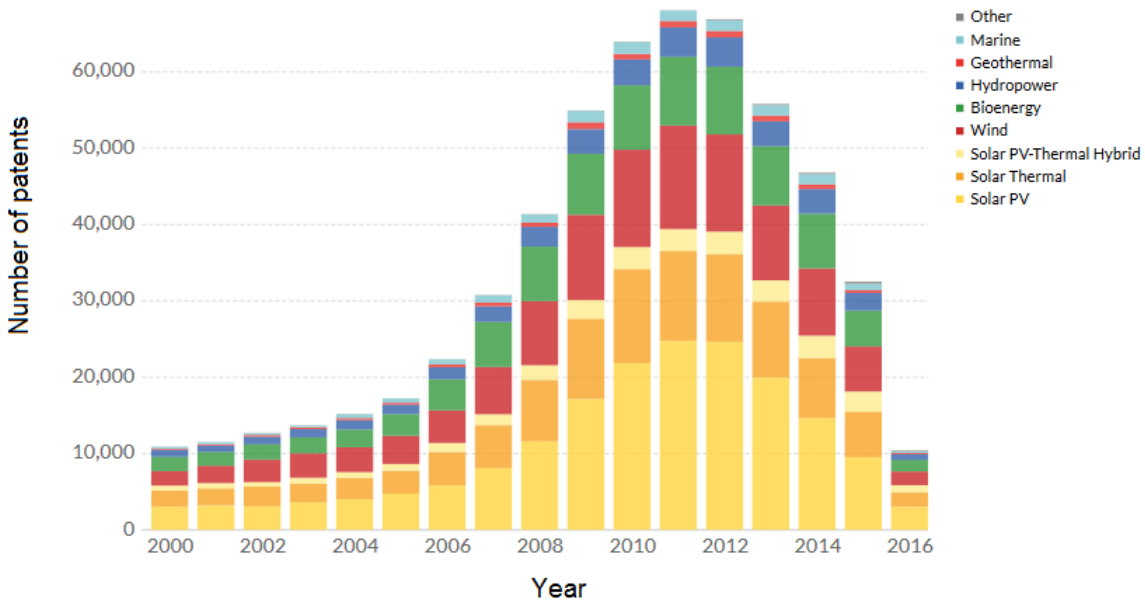

Figure 1.6: Global number of patents per sector in renewable sources of energy from 200 to 2016. Source - International Renewable Energy Agency (IRENA) RE-source Database (EPO PATSTAT Database)(https://ourworldindata.org/renewable-energy*).*

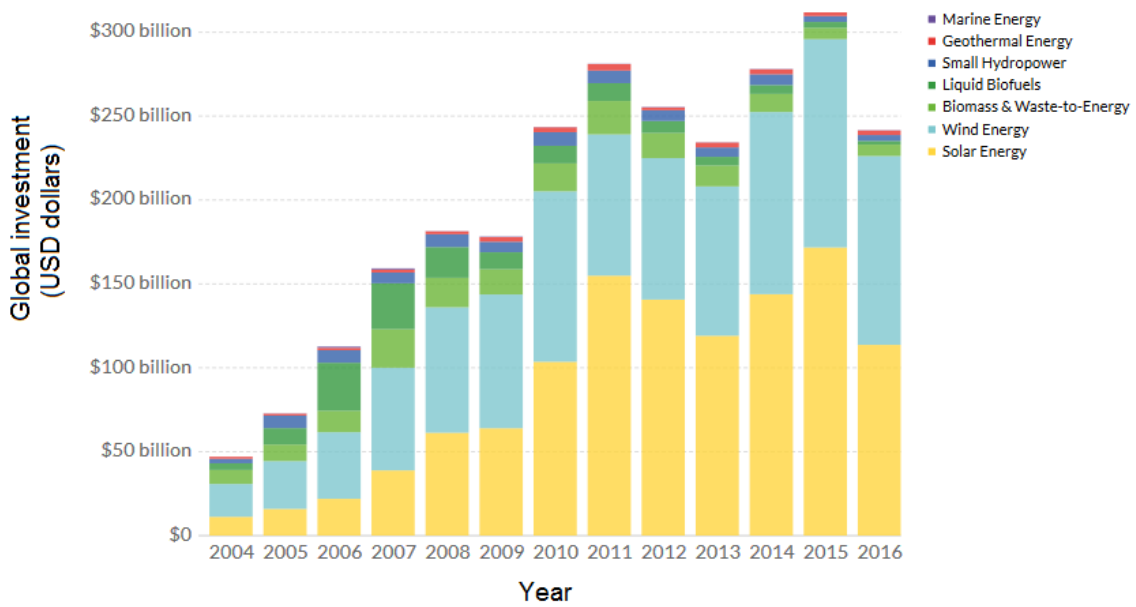

*Figure 1.7: Global investment in renewable sources of energy from 2004 to 2016. Source - International Renewable Energy Agency (IRENA) (*https://ourworldindata.org/energy*).*

Since the fabrication of the first photovoltaic solar cell with power conversion efficiency ~ 6 %, based on doped silicon (Si) semiconductors to construct a p – n (junction), in Bell Laboratories in 1954, significant engineering attention was aroused improving their efficiency and properties. [7] The following 6 decades, through steps of development in materials and engineering, successful fabrication of Si based solar cells with power conversion efficiency ~ 26.6 % was achieved. As such, Si is the leader in the field of photovoltaics, combining low cost of fabrication and moderate power conversion efficiencies. Additionally, exploitation of other configurations and materials as photoactive thin films, such as copper indium gallium selenide (CIGS), copper zinc tin sulfide (CZTS), cadmium telluride (CdTe), organic photovoltaics (OPV), quantum dot solar cells (QDSCs), dye-sensitized solar cells (DSSCs) and doped gallium arsenide (GaAs) in single or multi junctions, exhibited a range of power conversion efficiencies. However, over the last decade remarkable attention has been focused on perovskite solar cells (PSCs), due to the rapid increase in their power conversion efficiency (PCE) values (~ 24 %), as provided by NREL (National Renewable Energy Laboratory) and shown in figure 1.8. Note the much steeper gradient for the increase in PCEs for the perovskite curve.

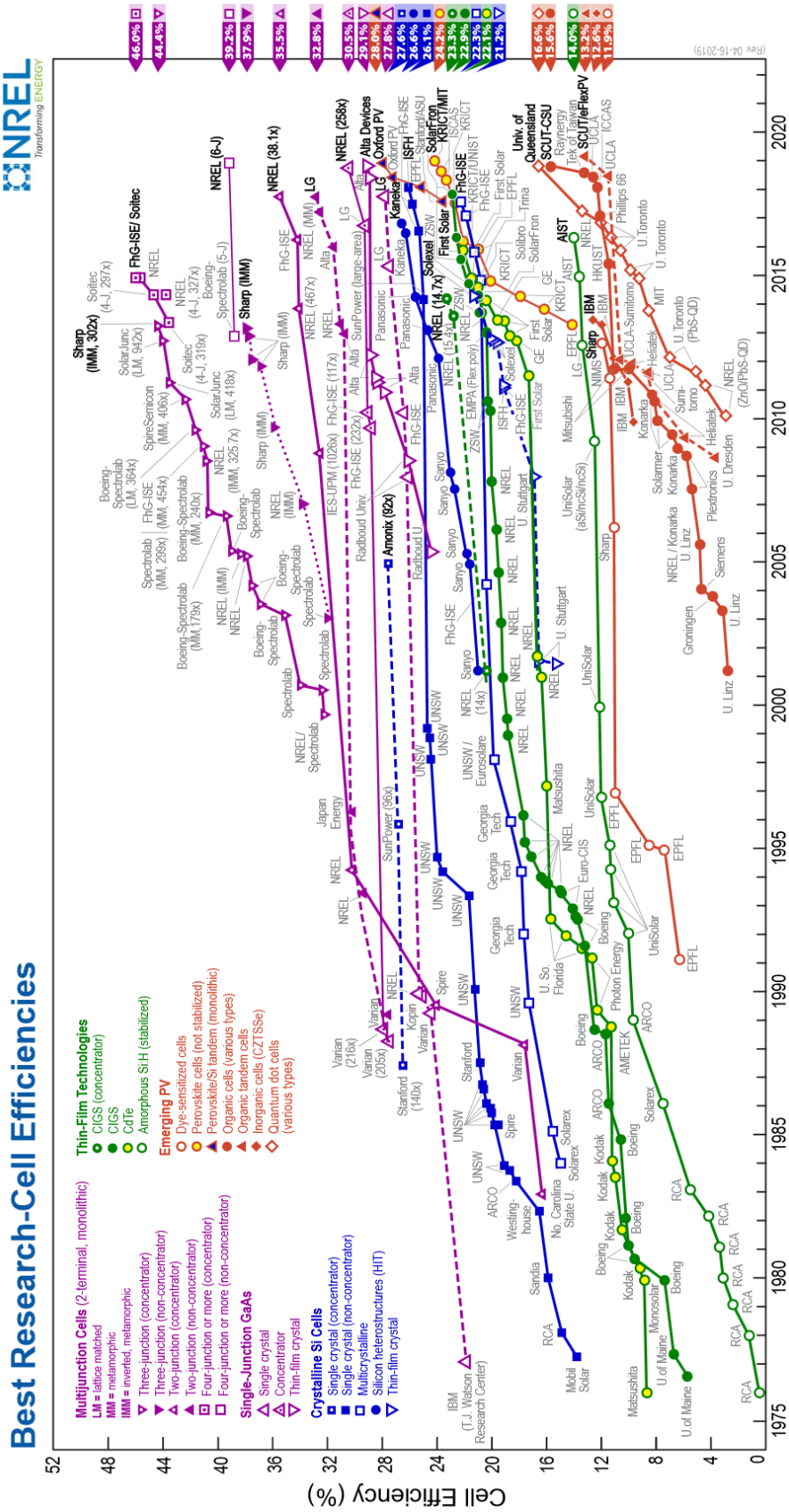

Figure 1.8: Chart of the highest confirmed power conversion efficiencies of solar cells for a range of photovoltaic technologies. Source – NREL (National Renewable Energy Laboratory) (https://www.nrel.gov/pv/cell-efficiency.html).

1.3 Perovskite solar cells

1.3.1 Origin of perovskite semiconductor

Historically, the first perovskite structure described was the calcium titanate ($CaTiO_3$) mineral, that was discovered in the Ural Mountains by Gustasv Rose in 1839 and its name was given in honour of the Russian mineralogist Aleksevich Lev Perovski. In the middle of the 1930s, Victor Goldschmidt first introduced the general chemical formula ABX_3, as the fundamental composition of perovskites and suggested the property of tolerance factor in ABX_3 formula. [8] The family of materials obeying the perovskite formula, includes a large number of metal – oxide and metal – halide compounds. In the field of solar cell research, the most studied metal – halide compounds are well known as halide perovskites, in which A is a cation such as, methylammonium ($CH_3NH_3^+$), formamidinium ($CH(NH_2)_2^+$) or caesium (Cs^+), B being a post-transition metal, such as lead (Pb^{2+}), tin (Sn^{2+}) or bismuth (Bi^{3+}) (bismuth has got more than one oxidation state: - 3, + 1, + 2, + 3 or + 5) [9] and X is a halogen anion such as, bromine (Br^-), chlorine (Cl^-) or iodine (I^-). The ideal crystal structure of halide perovskites at temperatures above 330 K is that with cubic symmetry, composed by a framework of corner shared octahedrons (BX_6^-) in three-dimensional space, as shown in figure 1.9.

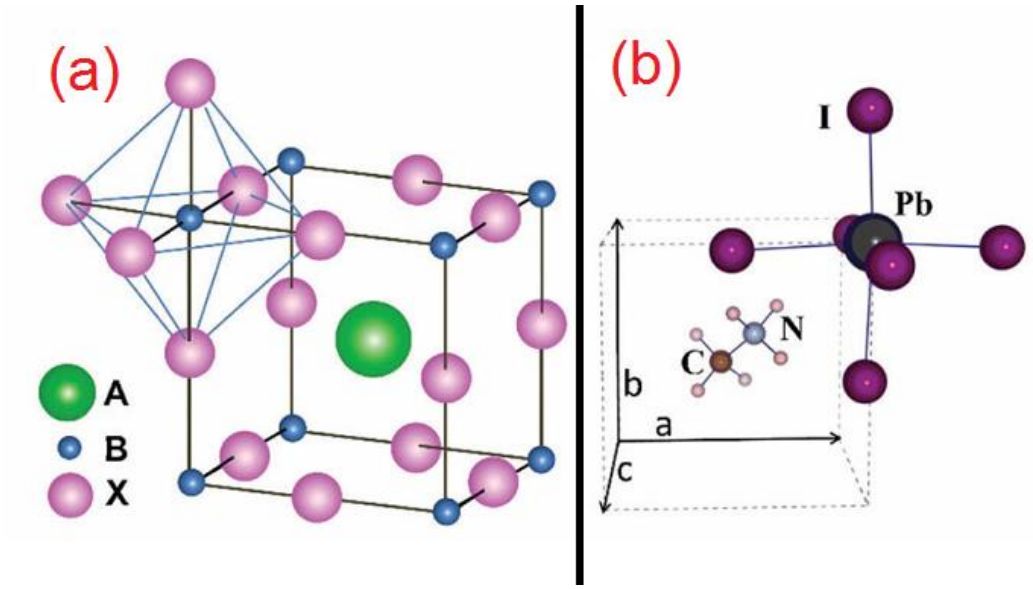

Figure 1.9: (a) Crystal structure of perovskite with chemical formula ABX_3 and (b) unit cell of $CH_3NH_3PbI_3$ perovskite. [10]

In 1958, Moller (a Danish scientist) discovered that $CsPbI_3$ crystallised in the perovskite structure and observed photoconductivity. In 1978, Dieter Weber, a German scientist, replaced the caesium with the methylammonium cation and synthesized the first organic – inorganic (hybrid) perovskite material, using either lead or tin. He also measured the absorbance band edge of these materials being around ~ 800 nm, implying their ability to act as photoactive materials. [11,12] Also, David Mitzi successfully fabricated thin film transistors and light emitting diodes (LEDs), using hybrid perovskite materials, a few years later. [13,14] In 2009, the group of Miyasaka successfully fabricated for the first-time photovoltaics using methylammonium lead triiodide ($CH_3NH_3PbI_3$) hybrid perovskite as a photoactive material with power conversion efficiency 3.8 %, based on the fabrication protocol used on DSSCs. [15] Throughout the following decade, remarkable scientific progress was achieved at the field of hybrid perovskites, with the astonishing PCE of ~ 23.6 % being reached using mixed cation / anion hybrid perovskites.[16]

1.3.2 Tunability and optoelectronic properties of perovskites

$CH_3NH_3PbI_3$ is one of the most studied hybrid perovskites, showing some remarkable optoelectronic properties. With a direct – indirect energy band gap of 1.51 ~ 1.55 eV, low exciton binding energy (~ 16 meV), excitonic effective mass 0.104 * m_e (where m_e is the electron mass), long diffusion lengths for both electrons and holes (0.1 ~ 1 μm) and high charge (electrons / holes) mobilities. [17–22] All these combined parameters, result in efficient diffusion of charge carriers before being recombined, causing $CH_3NH_3PbI_3$ an excellent photoactive layer for fabrication of solar cells. However, due to its inferior stability under moisture and oxygen, more engineering steps were implemented to tackle that problem. [23,24] A mixture of more than one cation / anion at different ratios in hybrid perovskites results in extensive tunability of the energy band gap, with improved stability upon temperature, oxygen and moisture. Both these properties are primarily caused by the structural shift from orthorhombic or tetragonal to more symmetrical ones, such as the cubic crystal structure, due to the different values of the effective ionic radius for the A and X ions used in the general chemical formula ABX_3 of perovskites. [25] A range of different anions / cations have been used, for the fabrication of perovskites, as shown in table 1.1. [26]

A - Cation	r_A (pm)	B - Cation	r_B (pm)	X - Anion	r_X (pm)
Potassium $[K]^+$	138	Germanium $[Ge]^{+2}$	73	Fluorine $[F]^-$	133
Ammonium $[NH4]^+$	146	Zinc $[Zn]^{+2}$	74	Chlorine $[Cl]^-$	181
Rubidium $[Rb]^+$	149	Silver $[Ag]^{+2}$	94	Bromine $[Br]^-$	196
Hydroxylammonium $[NH_3OH]^+$	216	Bismuth $[Bi]^{+3}$	103	Iodine $[I]^-$	220
Caesium $[Cs]^+$	167	Tin $[Sn]^{+2}$	115		
Methylammonium $[CH_3NH_3]^+$	217	Lead $[Pb]^{+2}$	120		
Hydrazinium $[NH_3NH_2]^+$	217				
Azetidinium $[(CH_2)_2NH_2]^+$	250				
Formadinium $[CH(NH_2)_2]^+$	253				
Imidazoline $[C_3N_2H_5]^+$	258				
3-pyrollinium $[NC_4H_8]^+$	272				
Ethylammonium $[CH_3CH_2)NH_3]^+$	274				
Guanidinium $[(NH_2)_3C]^+$	278				
Tetramethylammonium $[(CH_3)_4N]^+$	292				
Thiazolium $[C_3H_4N_5]^+$	320				
Tropylium $[C_7H_7]^+$	333				

*Table 1.1: Effective ionic radius of A – cations, B – cations and X – anio*ns, for perovskites with chemical formula ABX_3. [26]

Pellet et al. have shown that a mixture of FA^+ / MA^+ cations results in a more stable perovskite $FA_xMA_{1-x}PbI_3$ (with $x \leq 0.8$). [27] While Choi et al. have shown that mixture of Cs^+ / MA^+ cations leads to perovskite $Cs_xMA_{1-x}PbI_3$ with enhanced stability, free of the detrimental 2H yellow phase of lead iodide (PbI_2). [28] Also, due to the high toxicity of lead (Pb^{2+}), as a B – cation in the chemical formula ABX_3 of perovskites, its replacement with tin (Sn^{2+}), which is a less toxic metal in comparison with lead, results in PSCs with unfortunately lower values of PCEs ~ 9 %. [29] Also, due to the shift on the oxidation state of Sn^{2+} to Sn^{4+}, after contact with oxygen, this results in PSCs with inferior lifetime. However, perovskites made with a mixture of Pb^{2+} / Sn^{2+}, have shown significant research attention. Since the mixture of Pb^{2+} / Sn^{2+} has shown less toxicity, narrower band gap (~ 1.26 eV) and formatted perovskite with longer stability, might be an ideal candidate for the fabrication of single or tandem PSC devices. [30] On the halide side of perovskites with the ABX_3 chemical formula, substitution of iodine with bromine and / or chlorine, has also been investigated, in combination with either FA^+ or MA^+ cations. A higher amount of incorporated bromine, results in an increase of the energy band gap in the perovskite and less photostability under illumination. [31,32] While chlorine substitution might promote the formation of intermediate phases of perovskite, with different optoelectronic properties. [33] Also, the most stabilized in terms of exposure conditions whilst maintaining highly efficient PSCs (PCEs ≥ 23%), have been fabricated by a mixture of different A – cations and different X- anions. By tuning both A – cation and the X – anion, simultaneously, perovskite formulations such as $FA_xMA_{1-x}PbI_yBr_{1-y}$ or $Cs_x(MA_{0.17}FA_{0.83})_{1-x}Pb(I_{0.83}Br_{0.17})_3$, have shown remarkably stability under illumination with PCE ~18 % and at a range of operating conditions for more than 250 hours. [16,34,35]

1.3.3 Polytypism in lead iodide (PbI_2)

Lead iodide (PbI_2) is one of the most used inorganic materials towards the synthesis of the photoactive layer in PSCs. It is an intrinsic semiconducting material with wide energy band gap E_g = 2.3 - 2.4 eV.[36] Its primary crystalline structure is hexagonally close-packed following the space group of P-3m1, consisting of three alternating layers of lead and iodine atoms (I-Pb-I) within the structural unit, which is a near-

octahedron $[PbI_6]^{4-}$, as graphically illustrated in figure 1.10. The unit cell dimensions are a = b = 0.4557 nm and c = 0.6979 nm, for the 2H polytypic phase only,[37] nonetheless the stacking sequence of the $(I\text{-}Pb\text{-}I)_n$ layers can vary significantly, due to the weak van der Waals interactions between those sequential layers, resulting in the complicated crystallochemical phenomenon of polytypism. In which, different polytypes with variable c axis dimensions, which are not independent from the a and b axes, are formed.[38–40] Classification between different polytypic phases is made by a number followed by a letter (for example 2H, 4H, 6R), the number corresponds to the repetition and the letter to the type of the crystalline structural unit, respectively. More specifically, the letter "H", in the polytype description indicates the hexagonal unit cell, while ("R") to rhombohedral and ("C") to cubic unit cells, based on the Ramsdell symbols.[41] Notable, synthesis of PbI_2 crystallised in cubic structure, has never experimentally or theoretically been recorded.

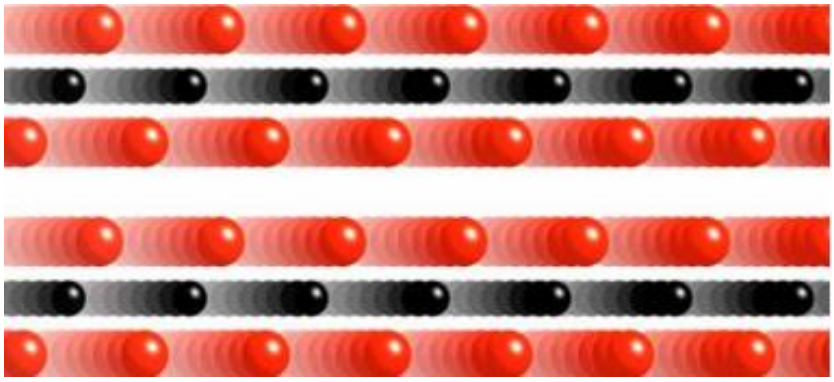

Figure 1.10: Graphical illustration of the alternating layers of lead and iodine atoms (I-Pb-I) within the structural unit of lead iodide (PbI_2). Black solid spheres are lead atoms and red solid spheres are iodine atoms. [38]

Independent of the synthesis process, for example solvothermal, [42] co-solvent,[43] modified-gel,[44] sublimation,[45] epitaxial,[46] or vertical Bridgman-Stockbarger,[47] the formation of multiple polytypic phases present might be responsible for stoichiometric variability and coexistence of several quantum states in PbI_2. While detected reversible and irreversible phase transitions between these polytypic phases,[40,48,49] may affect the optoelectronic properties of the PbI_2 and subsequently formed perovskite, in a way that is analogous to polytypism in silicon carbide.[50] Despite, the identification of more than 40 polytypic phases of the PbI_2 in the last 60 years, using X-ray diffraction, the

exact mechanism of their formation and diversity, remains unknown. A dominant theory was presented by Frank, attributing the formation of polytypes to crystallographic mismatches during the spiral growth of screw dislocations.[51] Based on that theory, initially PbI_2 platelet shaped structures are formed by surface nucleation and then grow layer-by-layer. These platelets might contain twins, syntactic coalescence or stacking faults originated by the coexistence of more than one polytypic phases, due to thermodynamic fluctuations during the growth process, resulting in sub or over stoichiometric PbI_2. Accordingly, Pandey and Krishna suggested a more complicated approach, based on a faulted basic matrix model to provide a theoretical description of polytypism. Notable that model, considers the three following parameters to have predominant role: i) the energy of the fault near the surface of the matrix during the formation of the screw dislocation, ii) the energy of the screw dislocation and iii) the stacking fault energy of the formatted polytype.[52–54]

1.3.4 Goldschmidt tolerance factor and beyond

The Goldschmidt tolerance factor was initially introduced by Victor Moritz Goldschmidt in 1926, as a simple dimensionless indicator of crystallographic stability and distortion in oxide perovskites. [8] The stability determined based on the deviation from a close-pack of hard spheres model, based only on the effective ionic radius of the incorporated ions in the general chemical formula of perovskites (ABX_3), and results only a generic expression of the structural stability in perovskites. In the cubic unit cell the edge is equal with two times the length of B-X bond ($a = 2d_{(B-X)}$), while at the cuboctahedral cage site the width is two times the length of A-X bond ($a\sqrt{2} = 2d_{(A-X)}$), combining these two lengths results the equation 1.1.

$$\frac{d_{(A-X)}}{\sqrt{2} * d_{(B-X)}} = 1 \qquad \text{equation 1.1}$$

Assuming the approximation that the cations and anions in the perovskites with general chemical formula ABX_3 are in contact, the perovskite will crystallize in the ideal cubic structure if the ratio between the ionic radius is equal to unity, as shown in equation 1.2. Where, r_A, r_B and r_X are the radius of A site cation, B site cation and X site

anion, respectively. Values of the tolerance factor can vary from the unity. Theoretical variation of the tolerance factor values are listed in table 1.2.

$$Tolerance\,factor_{\text{(Goldschmidt)}} = \frac{r_A - r_X}{\sqrt{2*}\,(r_B - r_X)} \approx 1 \qquad \text{equation 1.2}$$

Tolerance factor	Structure	Details
Greater than 1	Hexagonal	A cation bigger than B cation or X anion
From 0.9 to 1	Cubic	Identical ionic radius
From 0.7 to 0.9	Tetragonal / Orthorhombic	A cation smaller than B cation or X anion

Table 1.2: Range of Goldschmidt's tolerance factor values and the resulting structure.

However, in the non-oxygen based perovskites the accompanied distortion in the resulting crystal structure is affected by the ionic radius of the incorporated ions, as a function of their centre of mass. Since different organic A-site cations have got more than one degrees of rotational freedom, resulting in an anisotropic molecular Coulomb interaction with respect to the ions present into the perovskite crystal cage, Kieslich et al. have proposed a tolerance factor including an effective radius of the used ions, instead of their ionic radius. [55] The resulting effective ionic radius, includes the size correction in respect to the distance between the farthest atom (excluding hydrogen atoms) from the molecule's centre of mass. This revised expression of the tolerance factor for perovskites, is shown in equation 1.3. Where $h_{X\ \text{effective}}$ is the effective height in the perovskite unit structure.

$$Tolerance\,factor_{\text{(Kieslich)}} = \frac{r_{A_{effective}} + r_{X_{effective}}}{\sqrt{2*}\,(r_B + h_{X_{effective}})} \qquad \text{equation 1.3}$$

However, Bartel et al. proposed a new revised tolerance factor based on a novel sure independence screening and sparsifying operating (SISSO) simulation. This new tolerance factor considers the oxidation state of the A site cation towards the stability and compatibility of perovskite structure, as shown in equation 1.4. In a set of 576 simulated perovskite or non-perovskite compounds with general chemical formula ABX_3, Bartel's tolerance factor predicted successfully 92 % of those tested compounds, in contrast with the only 74 % of correct predictions based on the Goldschmidt's tolerance factor. In which, n_A is the oxidation state of the A site cation, while r_A, r_B and r_X are the effective ionic radius of A site cation, B site cation and X site anion, respectively. [56]

$$Tolerance\,factor_{(\mathrm{Bartel})} = \frac{r_X}{r_B} - n_A\left(n_A - \frac{r_A/r_B}{\ln(r_A/r_B)}\right) \qquad \text{equation 1.4}$$

1.3.5 Octahedral factor

In addition to Goldschmidt's tolerance factor, the octahedral factor (μ) has also been proposed as an extra factor of the perovskites' structural stability, in consideration of the formatted octahedron cages. The octahedral factor is the ratio between the effective ionic radius of the B site cation, in respect to the X site anion. This dimensionless number indicates how many times the radius of the X site anion fits into the radius of the B site cation, as shown in equation 1.5. [57–59]

$$\mu = \frac{r_B}{r_X} \qquad \text{equation 1.5}$$

Also, the values for the octahedral factor lies on the range ~0.4 < μ < ~0.7, as predicted by Rohrer et al. and Li et al. for lead and tin-based hybrid perovskites, respectively. [60] Combined values of Goldschmidt's tolerance and octahedral factors provide

graphically an estimated expression of the relative stability as calculated by Green et al. for lead or tin-based hybrid perovskites, as shown in figure 1.11. [61]

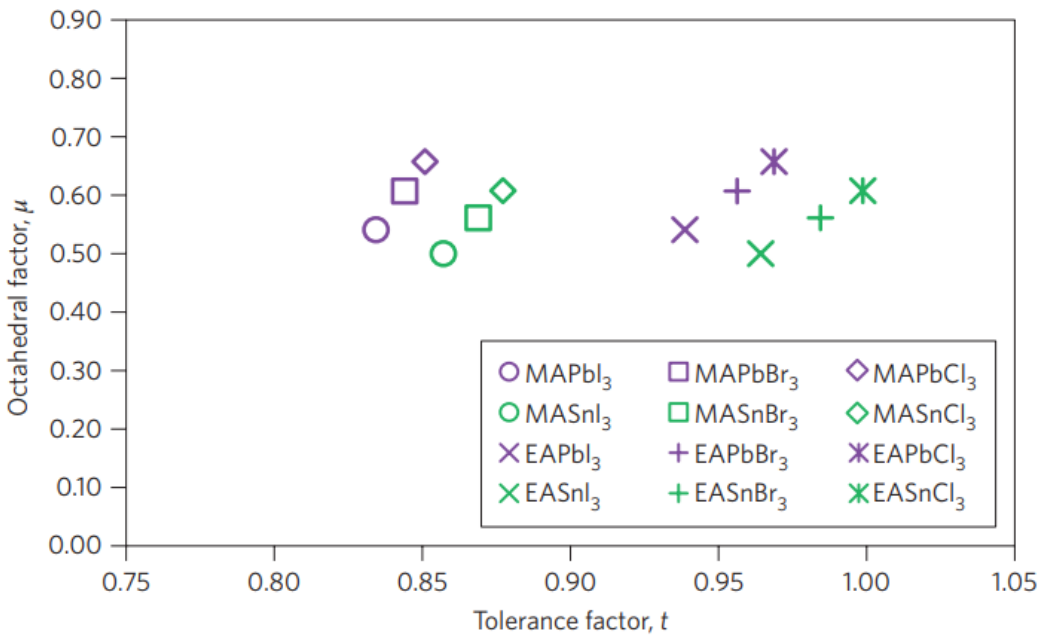

Figure 1.11: The corresponding combined values of Goldschmidt's tolerance and octahedral factors for lead or tin based hybrid perovskites, in respect to different A-site cation used (methylammonium (MA^+) or ethylammonium (EA^+)).[61]

1.3.6 Solar irradiation

An essential parameter for the efficient operation of photovoltaics fabricated with any device configuration or materials employed, is the solar irradiation. The absorbed flux of photons and their conversion into charge carriers are quantified by many factors leading to photovoltaic devices with maximum efficiency. The solar radiation varies throughout the day and global position, causing inhomogeneous distribution of the flux of photons. Standardized solar reference spectrum is required to allow the performance comparison of fabricated photovoltaic devices either in research laboratories or between manufacturers. That complies with the implementation of the international standard solar radiation spectrum ASTM G-173-03 (ISO 9845-1) in 1992. In addition, the standardization of the solar radiation is defined by three spectra, including the terrestrial and space applications. The AM1.5 global spectrum, is referenced for flat plate photovoltaic modules, having an integrated power of 1000 W

/ m^2, proportionally similar to the power used for the simulated spectrum in laboratories. While the AM 1.5 direct (plus circumsolar) spectrum is defined for solar concentrator modules with integrated power of 900 W / m^2. The circumsolar irradiation (or aureole) refers to the sun-light that appears to originate from the region around the sun (a small region which is formed around the sun at angle of ~2.5 degrees in respect to an observer on Earth). [62] Also, for space applications the AM 0 spectrum is used with an integrated power of ~ 1366 W / m^2, since the absorbance of photons is limited by the absence of air mass. All these three standard solar spectra for terrestrial or space applications are graphically plotted, as shown in figure 1.12. [63] The notation AM at each standard solar irradiation spectrum, is referred to the air mass and quantifies the reduction of the solar power as it passes through the atmosphere and photons absorbed by the air, dust or particle molecules. The mathematical expression for the air mass definition, related to the angle of the incident photons hitting the surface of Earth as function of the maximum position of sun (θ = zenith angle in degrees) is given by the equation 1.6.

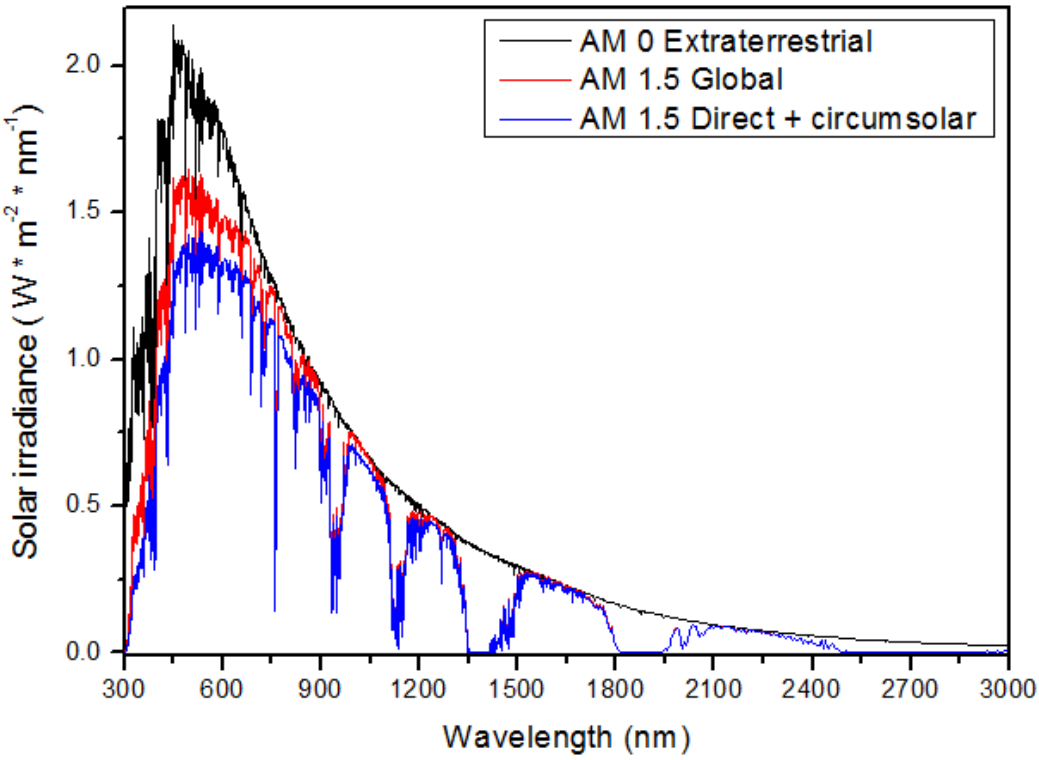

*Figure 1.12: Standard solar spectra for terrestrial or space applications. Source – NREL (National Renewable Energy Laboratory) (*https://www.nrel.gov/grid/solar-resource/spectra.html*).*

$$AM = \frac{1}{\cos(\theta)} \qquad \text{equation 1.6}$$

1.3.7 Perovskite solar cells: device components and architectures

The emergence of perovskite solar cells has undoubtedly motivated both academic and industrial sectors, for research and investment in that specific field of photovoltaics. Since their high-power conversion efficiencies, the materials required and the fabrication techniques that have been employed to manufacture them, reflects a cross mark of low cost and high yield ratio for the next generation of photovoltaic solar cells. The photovoltaic effect in perovskite solar cells, utilizing the perovskite as a photoactive layer for photon harvesting, could be divided into three main operating steps : (1) absorption of photons and conversion into excitons inside the perovskite photoactive thin film, (2) separation of excitons into charge carriers (each exciton is a pair of a negative charged (electron) and a positive charged (hole) carriers) and (3) extraction of those charge carriers. After the exciton dissociation, due to their low binding energy at around ~ 12 meV at room temperature, charge carriers (electrons and holes) are separated and selectively extracted from the perovskite by the electron transporting layer (ETL) and hole transporting layer (HTL), respectively. [64] After drift of charge carriers through the ETL and HTL, their injection and extraction occur into conductive electrodes. Towards the optimization of perovskite solar cells, a range of organic or inorganic ETL and HTL have been used, as shown in figure 1.13. [65] Energy level alignment of those transporting layers within the perovskite's conduction or valence bands, high charge carrier internal mobilities, chemical / photochemical stability and solvent compatibility, are the main factors of their selection. [66] Also, different conductive electrodes have been used to fabricate the resulting PSCs. Generally, good energy alignment between the HTL or ETL with the work function of the conductive electrodes requires the use of transparent conductive oxide (TCO) on glass or polymeric substrates, such as fluorine doped tin oxide (FTO), indium doped tin oxide (ITO) or aluminium doped zinc oxide (AZO). The criteria of TCO selection includes high conductivity and high optical transparency, in respect to the photoactive thin film. While, aluminium, silver or gold are used as metallic conductive electrodes to achieve the completion of the device enabling it to be connected to an electric circuit.

All these individual layers, that are required to compose the PSCs, could be distinguished into two device fabricating architectures, the regular (n – i – p) or the inverted (p – i – n), as shown in figures 1.14 a and 1.14 b. [67–69]

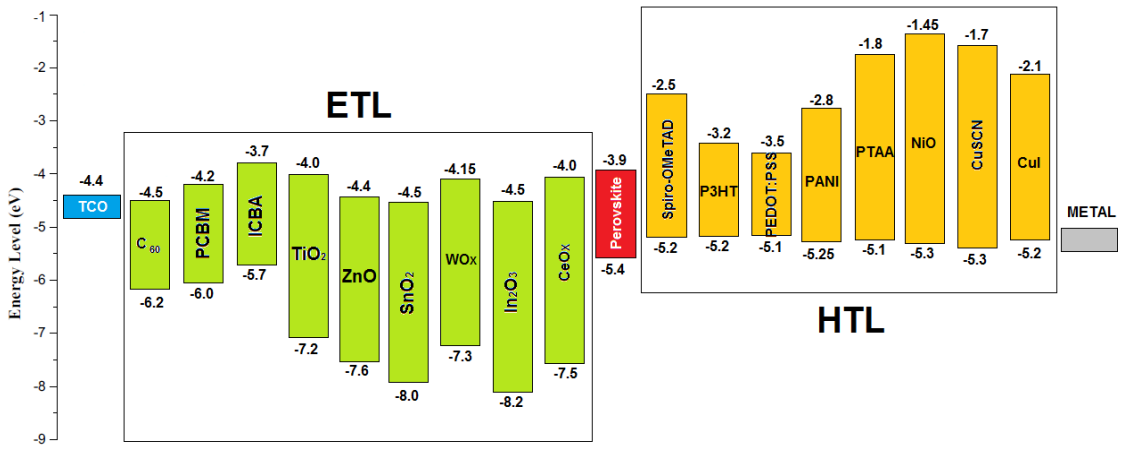

Figure 1.13: Energy levels (valence band or HOMO) and (conduction band or LUMO) of different materials, acting as electron transporting layer (ETL) and hole transporting layer (HTL).

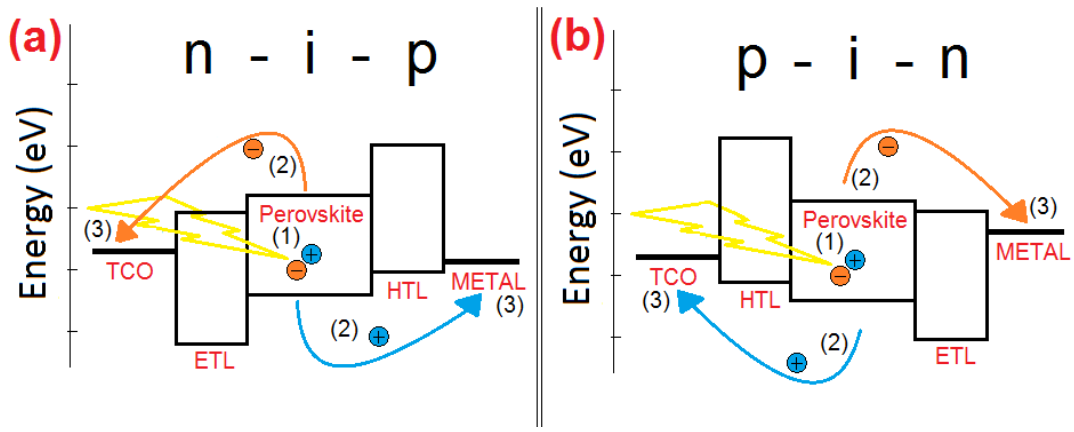

Figure 1.14: Perovskite device architectures and energy band alignment: (a) regular (n – i – p) and (b) inverted (p – i – n).

These two device architectures can be further divided into two configurations. The mesoscopic or the planar device architectures. The mesoscopic device architecture, characterized by the use of a mesoporous scaffold layer made of titanium dioxide (TiO_2) or aluminium oxide (Al_2O_3) acting as an electron conductive layer or nickel oxide

(NiO) acting as a hole conductive layer, with thicknesses from 150 to 300 nm that is filled with perovskite, while the planar device architecture consisted by a sequence of planar layers, as shown in figure 1.15. [70] However, perovskite solar cells, free of either ETL or HTL, have demonstrated remarkably functional devices. Ke et al. fabricated free of ETL perovskite devices with structure glass / TCO / perovskite / HTL / gold and champion efficiency 14.14 %. [71] While Lin et al. fabricated free of HTL perovskite devices with structure glass / TCO / ETL / perovskite / carbon and champion efficiency 14.5 %. [72]

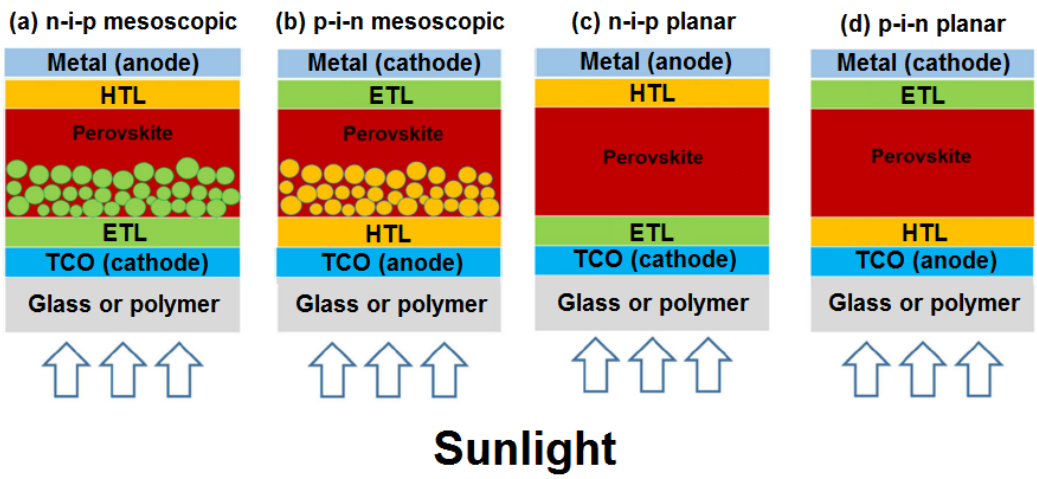

Figure 1.15: Perovskite device architectures: (a) (n – i – p) mesoscopic, (b) (p – i – n) mesoscopic, (c) (n – i – p) planar (regular) and (d) (p – i – n) planar (inverted). [65]

1.3.8 Type of defects and their effect in perovskite solar cells

Even though fabrication of perovskite thin films, as a photoactive layer in solar cells, have demonstrated a high tolerance to defects, recent research is still showing that formation of deep defects in perovskite, hinder the power conversion efficiency approaching the Schockley – Queisser limit (~ 31 %). [73] These defects can be classified into four main groups in semiconductors: point, line, surface and volume defects, respectively. Specifically, in ionic crystallized materials such as the perovskites, vacancies, interstitials, substitutional, Schottky and Frenkel, consist a sub-group of point defects. While, edge or screw dislocations, make up another sub-group of the line defects. Also, at the sub-group of the surface defects, could be

allocated defects related with twins or grains boundaries. Whereas, voids, cracks, inclusions or precipitates, are collectively known as volume defects, as summarized in table 1.3.

Defects in crystals			
Point defects	**Line defects**	**Surface defects**	**Volume defects**
Vacancies	Edge dislocation	Grain boundaries	Voids
Interstitial	Screw dislocation	Twin boundaries	Cracks
Substitutional			Inclusions
Schottky			Precipitates
Frenkel			

Table 1.3: Classification of defects in crystalline semiconductors.

Significant scientific research has been published regarding the point and surface defects in perovskites. Specifically, a Schottky point defect occurs when oppositely charged ions (cation and anion) leave their corresponding lattice sites and create a pair of vacancy defects. Also, since that pair of cation / anion leaves the lattice sites simultaneously, the overall electrical neutrality in the crystal is maintained, however the total density of the material is reduced, affecting the material's molecular weight, as shown in figure 1.16 a. Whereas, Frenkel defects consist of a combination of a vacancy and an interstitial point of defect. When an ion leaves its original lattice site, creates a vacancy, that ion occupies an interstitial lattice site, as shown in figure 1.16 b.

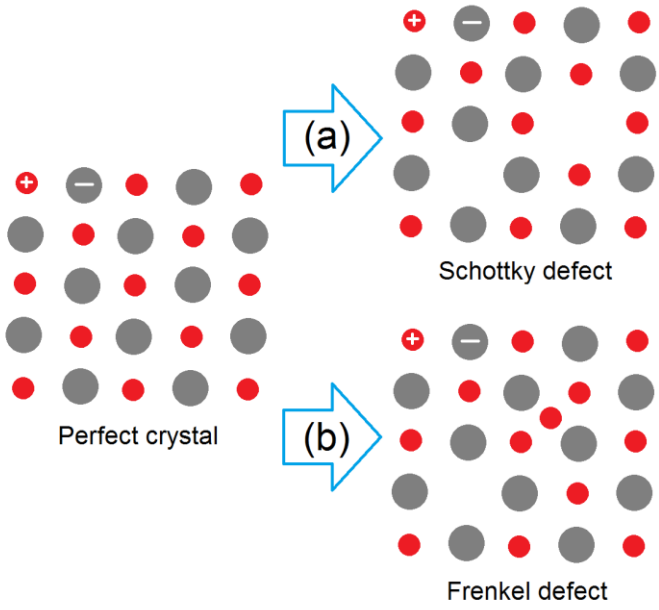

Figure 1.16: Representation of (a) Schottky and (b) Frenkel point defects in ionic crystals.

It is known that Schottky, Frenkel and grain boundary defects influence in a negative way the device performance of perovskite solar cells. The nature and density of those defects, could have impact in the long-term stability and reproducibility of perovskites as light harvesting layers. Schottky and Frenkel defects, are also responsible for the formation of shallow or deep energy levels, acting as traps of charge carriers, below the conduction band or above the valence band. The number of photo-generated charge carriers within the photoactive layer, is reduced by the opposite process, known as recombination. Generally, in semiconductors and consequently in perovskites, there are two types of recombination, radiative and non-radiative. Any photoexcited electron which exists in the conduction band, is in a meta-stable energy state. If it is not extracted, it will eventually transit into the valence band, which is in a lower energy state. Therefore, when the electron stabilizes back into the valence band, recombining with a hole, emitting a photon with the energy difference between the conduction and valence bands or with the energy difference between any shallow / deep state and valence band, as shown in figure 1.17. On the other hand, non-radiative recombination, are categorized into two major types, the Shockley-Read-Hall (SRH) and Auger. [74,75] In SRH recombination of charge carriers, the electron is trapped in a normally forbidden energy state (shallow or deep trap level), which has been introduced by defects or a doping agent, while a hole moves up to the same energy

state before the electron is thermally re-emitted into the conduction band. The rate between these energy transitions of charge carriers depends on the distance of the introduced forbidden energy states, with respect to the energy band edges (valence and conduction bands). Whereas, Auger recombination involves three charge carriers. The recombination of an electron with a hole, however, instead of emitting the energy as photon or heat, exchanges that energy to a third carrier, an electron or a hole which lives in the conduction or valence bands. After multiple collisions with the crystal lattice, that third carrier relaxes back to the edge of the band. The probability of Auger recombination increases in semiconductors, proportionally to the concentration of doping agents and only under non-equilibrium conditions, for example under illumination in solar cells. Additionally, one of the most prevalent mechanisms of charge carrier losses in perovskites, originates through surface and interface recombination between the boundaries of neighbour grains of perovskite and individual incorporated layers (ETL, HTL, conductive electrodes). Trap centres are formed near the surfaces or interfaces of the perovskite photoactive layer or between neighbour grains, due to dangling bonds (or ions diffusion), caused by the discontinuation of the perovskite in respect to the HTL and ETL layers or crystallization process, respectively.

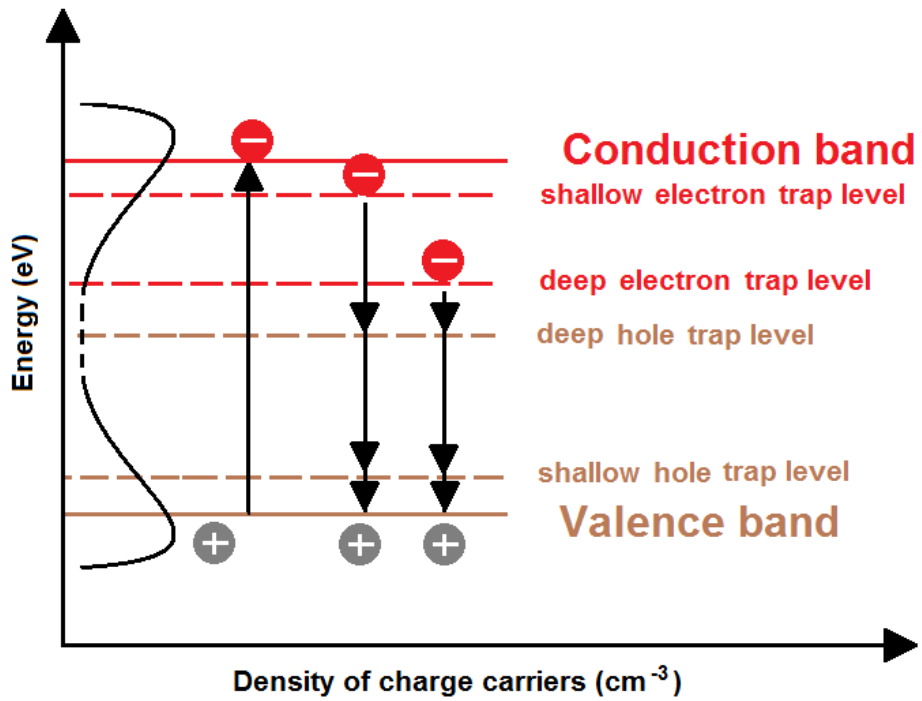

Figure 1.17: Representation of shallow / deep trap levels and density of charge carriers (electrons / holes) (black curve) into the energy band gap of perovskites.

Previous experimental results have shown that the density of defects and their energy allocation into the energy band gap of perovskites is related to the deposition method or conditions. For example, Nazeeruddin et al. have reported that defects related to iodine anions cause the formation of a shallow electron trap level which lies 0.62 eV below the conduction band using one-step deposition technique. In contrast, when a two-step deposition was used, results in the formation of a deeper electron trap level with energy 0.75 eV below the conduction band. [76] Also, Grätzel et al. have already demonstrated suppression of deep trap levels in the perovskite by adding an excess of lead iodide (PbI_2). [77] Whereas, Sargent et al., predicted by computational simulations that growth of perovskite under iodine-rich conditions, promotes the formation of deep electron trap levels. [78] In addition to that, stoichiometric variations between the initially organic / inorganic precursors used or inhomogeneous crystallization mechanism of the perovskite growth, results in the formation of point and surface defects at the grain boundaries of the polycrystalline perovskite thin films. [79–81] Their concentration has already been visualized by Snaith et al. using photoluminescence spectroscopy (PL) measurements. Defect concentrations at the grain boundaries with densities 10^{16} – 10^{17} cm^{-3} was confirmed in polycrystalline perovskite thin films, in comparison to the lower values in perovskite single crystals (10^{9} – 10^{10} cm^{-3}). [82] However, many concerns remain about the charge carrier losses through grain boundaries and the overall perovskite device performance, related to the size of individual perovskite grains and unbalanced accumulation of ions between grains during the crystallization process. [83] Recent, suppression of the surface defects allocated in the grain boundaries of perovskites lead the scientists to adopt chemical passivation, using phenethylammonium iodide (PEAI) as an engineering step, leading to reduced concentration of defects on grain boundaries. [16,84]

1.3.9 Perovskite single crystals

Further investigation of the perovskite intrinsic properties has also been demonstrated by controllable synthesis of perovskite single crystals. This form of high-quality perovskites is accompanied by remarkably low density of defects (< 10^{10} cm^{-3}), long diffusion lengths for the charge carriers (> 1 mm) and chemical stability (> 10.000

hours). These extraordinary long diffusion lengths are derived from the low densities of defects, resulting optimum transportation and extraction of charge carriers within the perovskite material. [85–87] Synthesis of perovskite single crystals with variable organic and halogen moieties has been achieved by different growth processes and summarized in table 1.4. In 1987, Poglitsch et al. fabricated perovskite single crystals via a solution temperature lowering (STL) growth process, in which the solution of gamma butyrolactone (GBL) / dimethylformamide (DMF) / dimethylsulfoxide (DMSO) and mixed ions was heated to 100 ºC followed by cooling down to room temperature. Also, by controlling the cooling rate (0.1 - 0.2 ºC * h^{-1}) Su et al, succeeded to fabricate larger in size perovskite single crystals (> 1 cm) by reselecting and regrowing smaller single crystals (seeds). [88,89] Lian et al. prepared centimetre-size perovskite single crystals without using multiple seeds by the bottom seeded solution growth (BSSG) process. [90] Whereas, Tao et al. reported tin-based mixed halogen centimetre-size perovskite single crystals by employing a top seeded solution growth (TSSG) process. [91,92] However, due to the prolonged in time STL growth process (~ 1 – 2 weeks), Saidaminov et al. designed the inverse temperature crystallization (ITC) process, which results synthesis of perovskite single crystals within ~ 3 – 4 hours. Mixed organic / inorganic precursors are dissolved in GBL and the temperature gradually increased (~ 190 ºC) until single crystals of perovskite are formed during the ITC growth process. [93,94] Also, fast crystallization growth of single crystals was succeeded by Bakr et al. using the antisolvent vapour assisted crystallization (AVC) process, which is a temperature independent method. Dichloromethane (DCM) was added to the mixture of DMF / GBL and organic / inorganic ions, causing a supersaturated solution promoting single crystal formation. [85] Monocrystalline perovskite thin films were successfully grow by the same group, developing the cavitation triggered asymmetrical crystallization (CTAC) process, in which ultrasonic pulses were introduced into the supersaturated in antisolvent vapor solution, accelerating the formation of homogeneous free of grain boundaries perovskite thin films. [95] Additionally, large area (~ 120 cm^2) monocrystalline perovskite thin films with controllable thickness (0.1 – 0.8 mm) were developed by Rao et al. using space limited inverse temperature crystallization (SLITC) process. [96] However, since the high toxicity of DMF and DCM solvents, Acik et al. synthesised perovskite micro-crystals with size < 20 μm at different temperatures and in time duration of 48 hours, using the system of PbI_2 and CH_3NH_3I in a range of non-toxic alcohols. [97]

Method of growth	Single crystal	Size	Duration of growth
Solution temperature lowering (STL)	$CH_3NH_3PbX_3$ (X = Cl, Br, I)	~ 5 mm	3 hours (ref. 87)
	$CH_3NH_3PbX_3$ (X = Br, I)	>10 mm	240 hours (ref. 88)
Bottom seeded solution growth (BSSG)	$CH_3NH_3PbI_3$	>12 mm	360 hours (ref. 89)
Top seeded solution growth (TSSG)	$CH_3NH_3SnI_3$ $CH(NH_2)_2SnI_3$	~ 10 mm	Not provided (ref. 90)
Inverse temperature crystallization (ITC)	$CH_3NH_3PbX_3$ (X = Br, I)	~ 5 mm	~ 3 - 4 hours (ref. 92)
Antisolvent vapor assisted crystallization (AVC)	$CH_3NH_3PbX_3$ (X = Br, I)	>10 mm	Not provided (ref. 84)
Cavitation triggered asymmetrical crystallization (CTAC)	$CH_3NH_3PbBr_3$	2 mm x 2 mm x 0.005 mm	~ 3 - 6 hours (ref. 94)
Space limited inverse temperature crystallization (SLITC)	$CH_3NH_3PbBr_3$	180 mm x 67 mm x 0.4 mm	~ 170 hours (ref. 95)
Alcohol	$CH_3NH_3PbI_3$	< 20 µm	48 hours (ref. 96)

Table 1.4: Perovskite single crystals or monocrystalline thin films growth processes.

Also, due to the superior quality of perovskite single crystals, many groups have used alternative solid-state methods of perovskite synthesis, resulting in controllable stoichiometry. Grätzel et al. and Biswas et al. have synthesized $CH_3NH_3PbI_3$ and $CsPbBr_3$ powders, respectively, by using a mortar as a solvent free mechanochemical way. [98,99] While, Manukyan et al. have synthesized $CH_3NH_3PbI_3$ powder by employing a ball milling process. [100] Notable, synthesis of perovskite oxide powders with high yield and purity by using a planetary ball milling method, has been realized by Lee et al. and Zhang et al. [101,102]

1.3.10 Optoelectronic properties: from p-n junction to perovskites

A pure semiconducting material such as, silicon or germanium, is characterized intrinsic or undoped, when not dopant species of other materials are present. The concentrations between charge carriers (electrons and holes) in intrinsic semiconductors are equal, resulting in a minimum of electrical conductivity. However, to improve the electrical conductivity among many other parameters, different dopant elements are used. The material and amounts of doping elements define the type of doped semiconductor. N-type silicon semiconductors are synthesized by doping the intrinsic one with an electron donor element, such as phosphorous or arsenic. The term n-type points out that the majority of charge carriers are electrons, while holes are the minority carriers. In contrast, p-type silicon semiconductors are synthesized by doping the intrinsic one with an electron acceptor element, such as boron or gallium. Again, the term p-type indicates that the majority of charge carriers are holes, whereas electrons are the minority carriers. Variability between charge carrier concentrations results in variable electrical conductivity in semiconductors and can be represented by the Fermi level (E_F) within the energy band gap (E_g). In n-type semiconductors the Fermi level is closer to the conduction band (CB), while in p-type semiconductors the Fermi level is closer to the valence band (VB), respectively, as shown in figure 1.18.

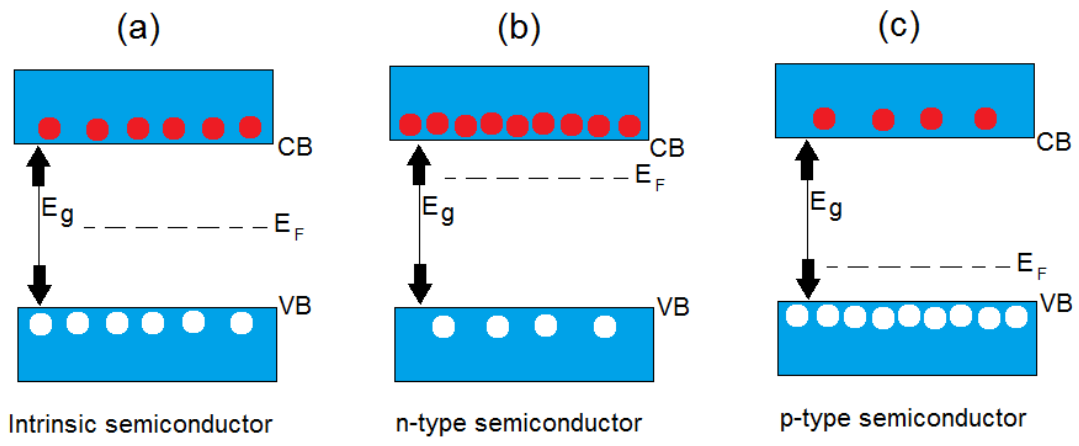

Figure 1.18: Energy levels (valence band (VB), conduction band (CB) and Fermi level (E_F) in (a) intrinsic, (b) n-type and (c) p-type semiconductors. White circles represent positive charge carries (holes), whereas red circles represent negative charge carriers (electrons). [103]

The combined junction between p-type and n-type semiconductors allows electrical current to pass only in one direction into the junction, known as a diode. Also, the resulting p-n heterojunction is the interface between two semiconducting layers of dissimilar crystalline structures and with different energy band gaps (belonging to the III-IV family of doped semiconductors), in comparison with a p-n homojunction, in which the formatted diode based on the different doping of regions inside the same intrinsic semiconducting material. Notably, in p-n heterojunction semiconductors, the formatted energy discontinuity (formation of quantum well) as a function of the individual energy band gap of the incorporated p and n type semiconductors, resulted from the difference between the energy band gaps of p and n types semiconductors and the crystal structure dissimilarity at their interface, as schematically represented in figure 1.19. [104–106] Depending on the concentration of the dopant agents in both p-type and n-type semiconductors in a p-n junction, diffusion of free (in majority) electrons from the n-type side into the p-type side, results the diffusion current. While free in minority electrons from the p-type side drift into the n-type side at the same time, results the drift current. This gradient of free charge carriers flow, creates an electric field as function of the distance (E(x)) near the p-n junction interface, since both positively charged (donor) dopant ions in the n-type side and negatively charged (acceptor) dopant ions in the p-type side are immobile. Leading to the n-type side to become positively charged, while the p-type side to become negatively charged.

These combined regions, form a depletion region for mobile charge carriers through the electric field. The Fermi level in a p-n junction under thermal equilibrium remains at equal stable energy level, leading to the formation of a contact potential qV_o. The total density of current flow for both n-type side and p-type side due to drift of charge carriers into the electric field and the diffusion of charge carriers by the concentration gradient is equal to zero, as shown in figure 1.20. [107]

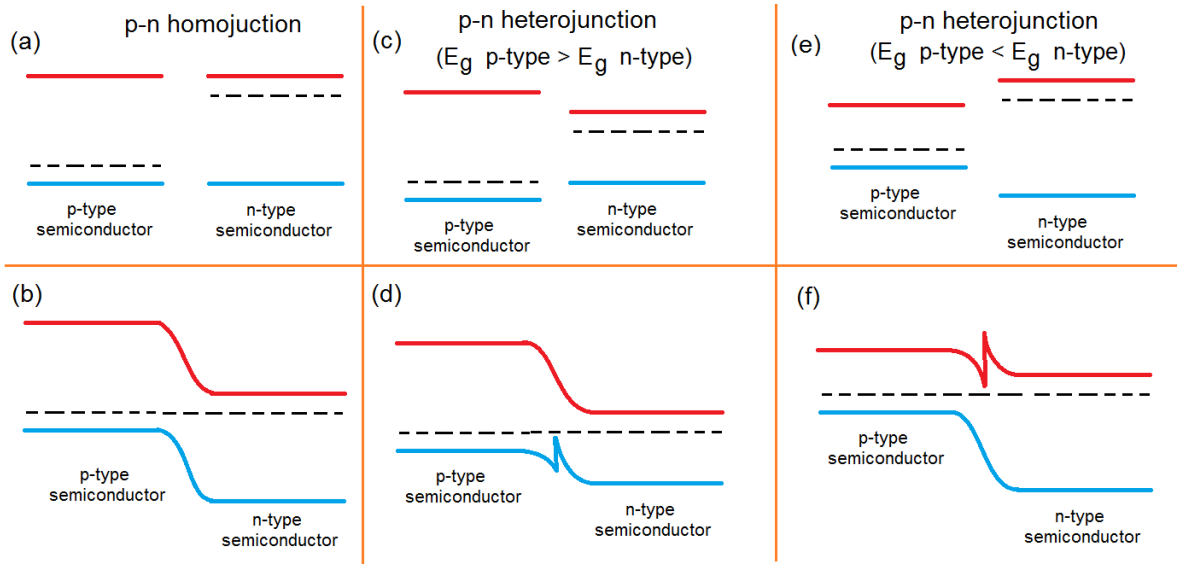

Figure 1.19: Basic schematic representation of p-n homo and hetero junctions. (a), (c) and (e) in thermal equilibrium, whereas (b), (d) and (f) in contact, respectively. Blue lines represent valence bands, while red lines represent conduction bands, dashed lines represent Fermi energy levels. [103]

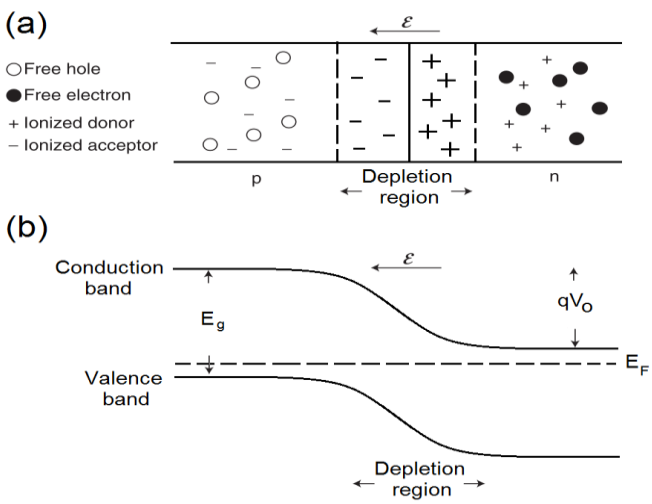

Figure 1.20: (a) Depletion region formation and (b) energy diagram and band bending over the depletion region for a p-n homojunction. [104]

The potential in the depletion region can be calculated by assuming that an instant transition between the depleted of charge carriers and non-depleted in the p and n regions. The charge densities in the depletion region for the p and n sides are $\rho_p = -e*N_A$ and $\rho_n = +e*N_D$, where N_A and N_D are the concentrations of acceptors and donors, respectively. Since, the total charge is neutral at the depletion region as expressed by the equation $N_A*d_p = N_D*d_n$, where d_p and d_n are the depths of the depletion region for both the p and n type sides, the potential can be calculated by solving the Poisson's equation (equation 1.7), in which ρ is the charge density distribution, ϵ is the dielectric constant of the semiconductor and regarding the conditions that the gradient of the potential at the boundaries ($x = -d_p$ and $x = d_n$) is equal to zero.

$$\frac{d^2U(x)}{dx^2} = -\frac{\rho}{\epsilon\epsilon_o} \qquad \text{(equation 1.7)}$$

The total difference of the potential across the depletion region based on the equation 1.7 is:

$$\Delta U = \frac{e}{2\epsilon\epsilon_o}\left(N_D d_n^2 + N_A d_p^2\right) \qquad \text{(equation 1.8)}$$

Also, based on the charge neutrality conditions into the depletion region, the calculated widths for both the p and n type sides are:

$$d_p = \sqrt{\left(\frac{\Delta U 2\epsilon\epsilon_o}{eN_A}\frac{N_D}{N_{A+N_D}}\right)} \quad , \quad d_n = \sqrt{\left(\frac{\Delta U 2\epsilon\epsilon_o}{eN_D}\frac{N_A}{N_{A+N_D}}\right)} \qquad \text{(equation 1.9)}$$

In addition, regarding the Boltzmann approximation for the densities of carriers (majority and minority) into the p and n type sides, these can be written:

$$n_p = N_{eff}^C e^{\frac{\left(E_F - E_g - e\Delta U\right)}{k_B T}} \quad , \quad p_p = N_{eff}^V e^{\frac{-(E_F - e\Delta U)}{k_B T}} \qquad \text{(equation 2.0)}$$

$$n_n = N_{eff}^C e^{\frac{\left(E_F - E_g\right)}{k_B T}} \quad , \quad p_n = N_{eff}^V e^{\frac{(-E_F)}{k_B T}} \qquad \text{(equation 2.1)}$$

In those equations, n_n and p_n are the electron and hole densities in the n-type side, while n_p and p_p are the electron and hole densities in the p-type side. Also N_{eff}^{C} and N_{eff}^{V} are the effective density of states in the conduction and valence bands, respectively. Without any applied external voltage across the p-n homojunction, the drift and diffusion currents are proportionally equal in both p-type and n-type sides and can be written:

$$\left|I_{diffusion}\right| = \left|I_{drift}\right| = \left|I_0\right| = Ce^{\frac{\left(E_F - E_g - e\Delta U\right)}{k_B T}} \quad \text{(equation 2.2)}$$

Where I_0 called reverse saturation current with values ~100 nA, while C is a constant regarding the elementary charge (q) and area between p-n junction interface, k_B is the Boltzmann constant and T is the temperature. If an external positive voltage is applied across the p-n homojunction (n-type side negatively charged and p-type side positively charged), the electron drift current remains unchanged, while the diffusion current is modified because the chemical potential on the n-type side is shifted by + eV and the total current in that forward bias condition is:

$$I = \left|I_{diffusion}\right| - \left|I_{drift}\right| = Ce^{\frac{\left(E_F + eV - E_g - e\Delta U\right)}{k_B T}} - Ce^{\frac{\left(E_F - E_g - e\Delta U\right)}{k_B T}} = I_0\left(e^{\frac{eV}{k_B T}} - 1\right) \quad \text{(equation 2.3)}$$

Whereas, if an external negative voltage is applied across the p-n homojunction (n-type side positively charged and p-type side negatively charged), the electron drift current remains unchanged, while the diffusion current is modified because the chemical potential on the n-type side is shifted by - eV and the total current in that reversed bias condition is:

$$I = \left|I_{diffusion}\right| - \left|I_{drift}\right| = Ce^{\frac{\left(E_F - eV - E_g - e\Delta U\right)}{k_B T}} - Ce^{\frac{\left(E_F - E_g - e\Delta U\right)}{k_B T}} = I_0\left(e^{\frac{-eV}{k_B T}} - 1\right) \quad \text{(equation 2.4)}$$

The relative motion (diffusion or drift) of majority and minority charge carriers between the interfaces in a p-n homojunction, when either thermal equilibrium or forward or reverse bias is applied illustrated in figure 1.21.

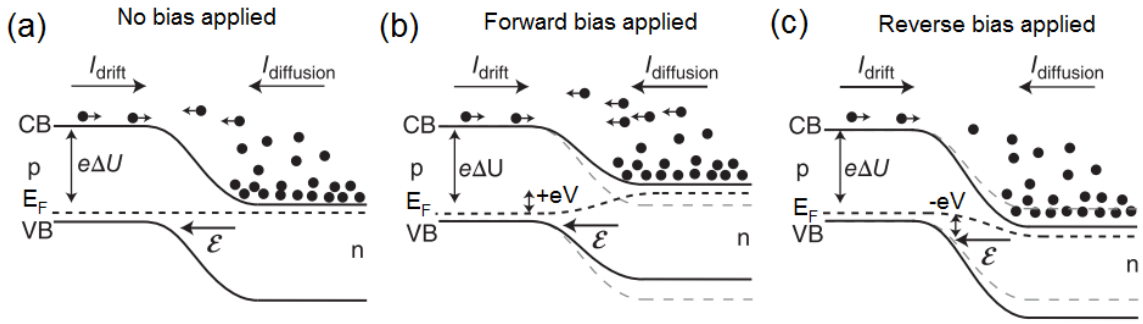

Figure 1.21: p-n homojunction operating as a diode (electrons diffusion and drifting are considered, not the holes) under different bias applied. (a) without any bias, (b) forward bias and (c) reverse bias. [104]

During the electrical characterization of a p-n junction, the relation between the total current and voltage either under illumination or at dark conditions, is expressed by the equation 2.5, in which n is the ideal factor with values at the range 1 < n < 2. Deviation of the ideal factor from the unity indicates formation of a non-ideal diode, resulting increased concentration of recombination centers either in the photoactive layer or between transporting layers and selective contacts. [108,109]

$$I_{total} = I_0\left(e^{\frac{eV}{nk_BT}} - 1\right) - I_{photocurrent} \qquad \text{(equation 2.5)}$$

The characteristic current – voltage curve (I-V) of a diode is vertically lowered proportionally to the photocurrent produced at the 4th quadrant under illumination, enabling the extraction of power from solar cells, as shown in figure 1.22. Under short circuit condition, the total current is equal to the photocurrent, while under open circuit condition the total current is zero and the voltage is:

$$V_{oc} = \frac{nk_BT}{e}\ln\left(\frac{I_{photocurrent}}{I_o} + 1\right) \qquad \text{(equation 2.6)}$$

The open circuit voltage is increased proportionally to the flux of incident photons, however its highest value is limited by the p-n junction properties and operating temperatures. Also, the maximum current and voltage corresponding to the maximum power point (MPP), is related with the squareness of the I-V curve in the 4th quadrant and expressed by the fill factor (FF), as shown in figure 1.23 a. Highest values of FF

indicate better operating performance of solar cells and is affected by the series resistance (R_{series}), which is related with losses in the photoactive layer, conductivity, interfaces and energy alignment with respect to the incorporated layers and the shunt resistance (R_{shunt}), which is related with the losses introduced by shunt paths or pinholes present in the photoactive thin film, as shown in figure 1.23 b. An ideal solar cell should have lower values of R_{series} and higher R_{shunt}, as well. The percentage of power conversion efficiency (PCE), is calculated based on equation 2.7, in respect to the power of incident photons (1000 W / m^2 = 1 sun).

$$PCE\,\% = \frac{P_{output}}{P_{input}} = I_{MPP} * V_{MPP} = \frac{FF * V_{oc} * I_{sc}}{1000\,\frac{W}{m^2}} \qquad \text{(equation 2.7)}$$

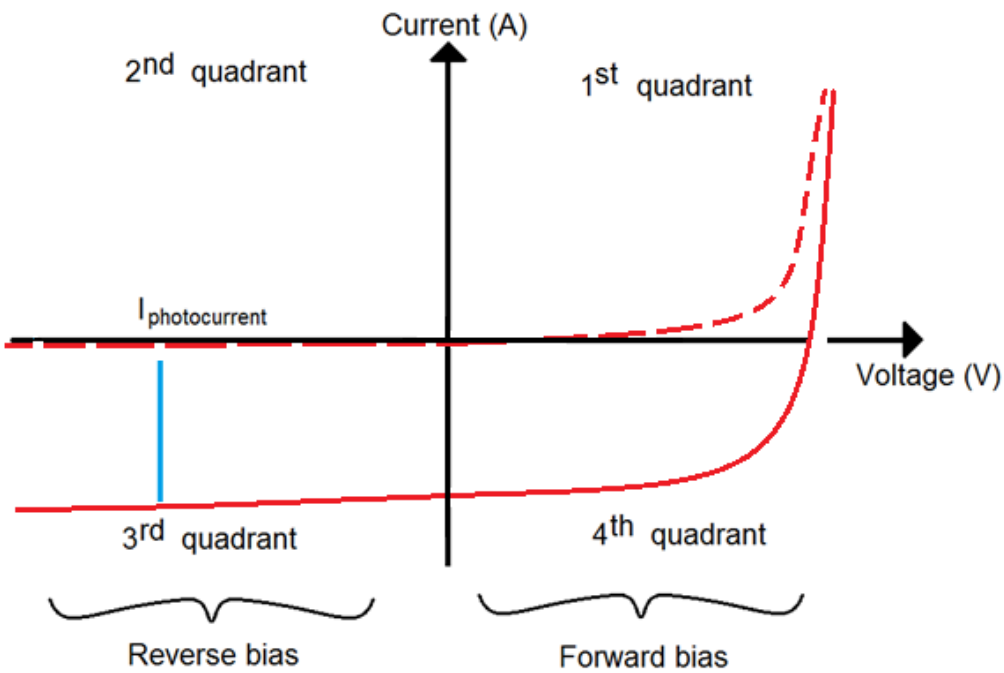

Figure 1.22: Characteristic current – voltage curve of a p-n homojunction at dark condition (dashed curve) or under illumination (solid curve).

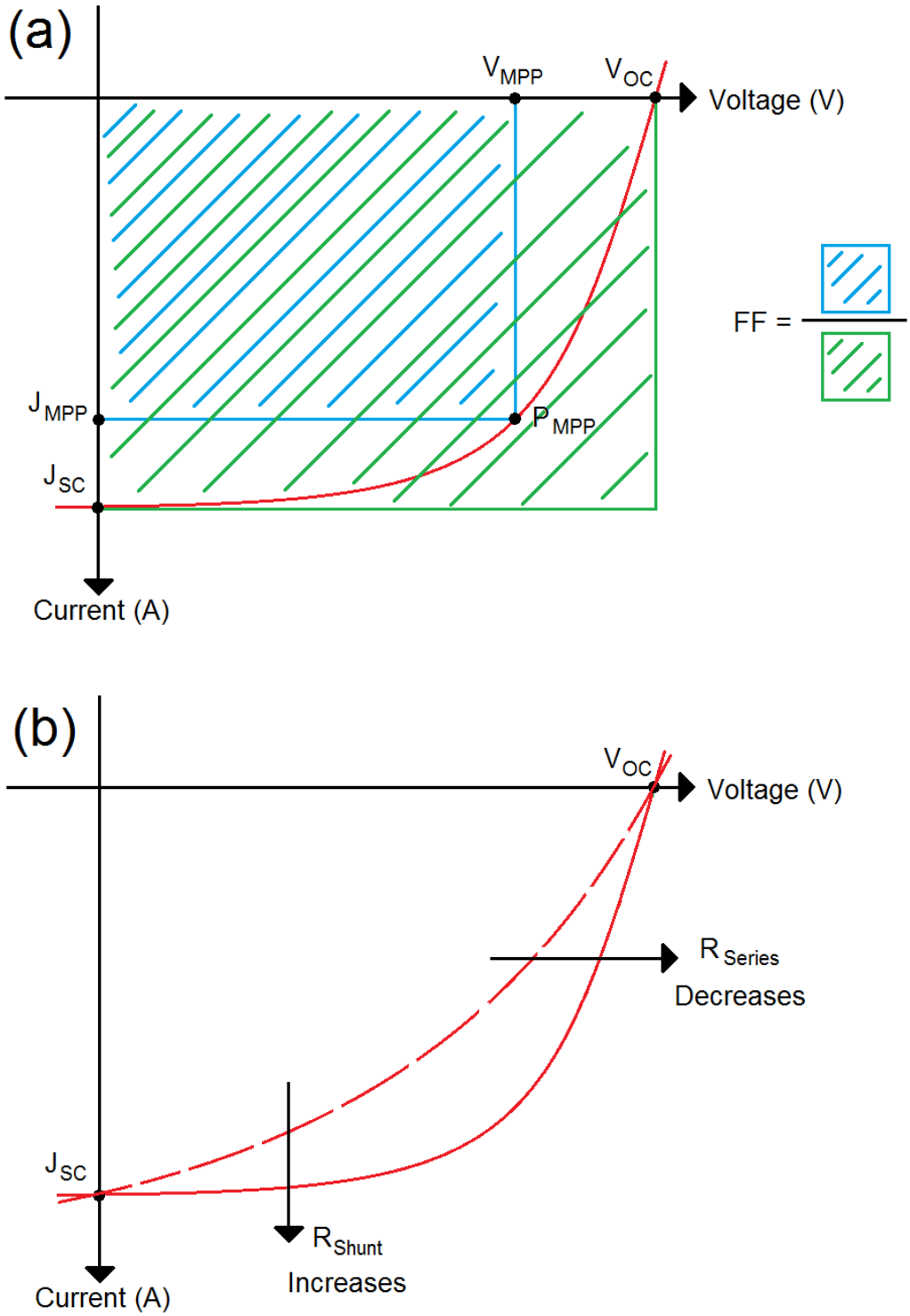

Figure 1.23: (a) Illustration of the maximum power point (MPP), fill factor (FF), short circuit current (I_{SC}) and open circuit voltage (V_{OC}), (b) the effect of series resistance (R_{series}) and shunt resistance (R_{shunt}), in a characteristic current – voltage curve of a p-n homojunction.

However, significant current and voltage losses in solar cells related to five different mechanisms, resulting reduced values of PCE, in respect to the maximum Shockley-Queiseer limit, which is about 31 % for PSCs (using a single photoactive layer). Mismatch between the absorption of photons with energy equal to the perovskite photoactive layer E_g and the wide energy of photons of the solar spectrum, results in the non-absorption of photons with energy below the E_g. Also, strong interactions between the photo-excited charge carriers and lattice phonos introduce thermalization losses, reducing the open circuit voltage. While losses related to Kirchoff's law, are responsible for emission losses, since photoactive layers behave as absorbers and emitters simultaneously. In addition to that, during the absorption and emission of photons from the photoactive layer in an anisotropic way (multiple angles), results an increase in entropy due to the expansion of photon modes, known as Boltzmann losses. Finally, temperature difference between the ambient and solar cell during its operation cause thermodynamic Carnot losses. All these combined losses originated by these five difference mechanisms, are mainly considered to reduce by almost ~ 69 % the maximum conversion of photons to charge carriers, as function of the perovskite photoactive layer E_g and in respect to the power of incident flux of photons (1000 W/m^2 = 1 sun), as summarized in table 1.5 and graphically illustrated in figure 1.24. [110,111]

Mechanism of PCE reduction	**Percentage (%)**
Below E_g	25.5
Thermalization	30.5
Emission	1
Carnot	2.5
Boltzmann	9.5
Shockley-Queiseer limit	31

Table 1.5: Percentage of losses based on the five different mechanisms and Shockley-Queiseer limit in PSCs (numerical values are referred based on simulated models). [111]

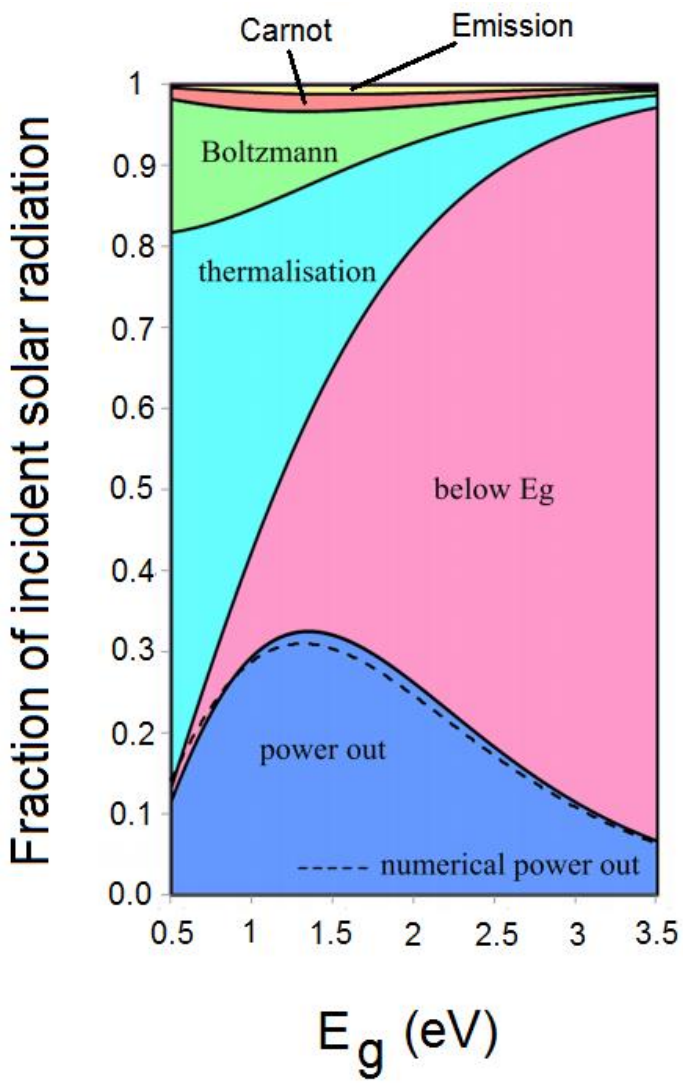

Figure 1.24: Graphically illustration of intrinsic loss mechanisms in single photoactive layer with variable E_g as function of the incident photons radiation, leading to reduced PCE. [111]

Also, the equivalent electrical circuit of a typical solar cell fabricated based on the silicon p-n homojunction, excluding any external resistors of additional metallic contacts, consisted by one diode, the shunt resistance and the series resistance, as depicted in figure 1.25 a. Whereas, the equivalent electrical circuit of a typical solar cell fabricated based on the perovskite either p-i-n or n-i-p heterojunction, excluding any external resistors of additional metallic or TCO contacts, consisted of two diodes, the shunt resistance and the series resistance, as suggested by Liao et al. and shown in figure 1.25 b. [112]

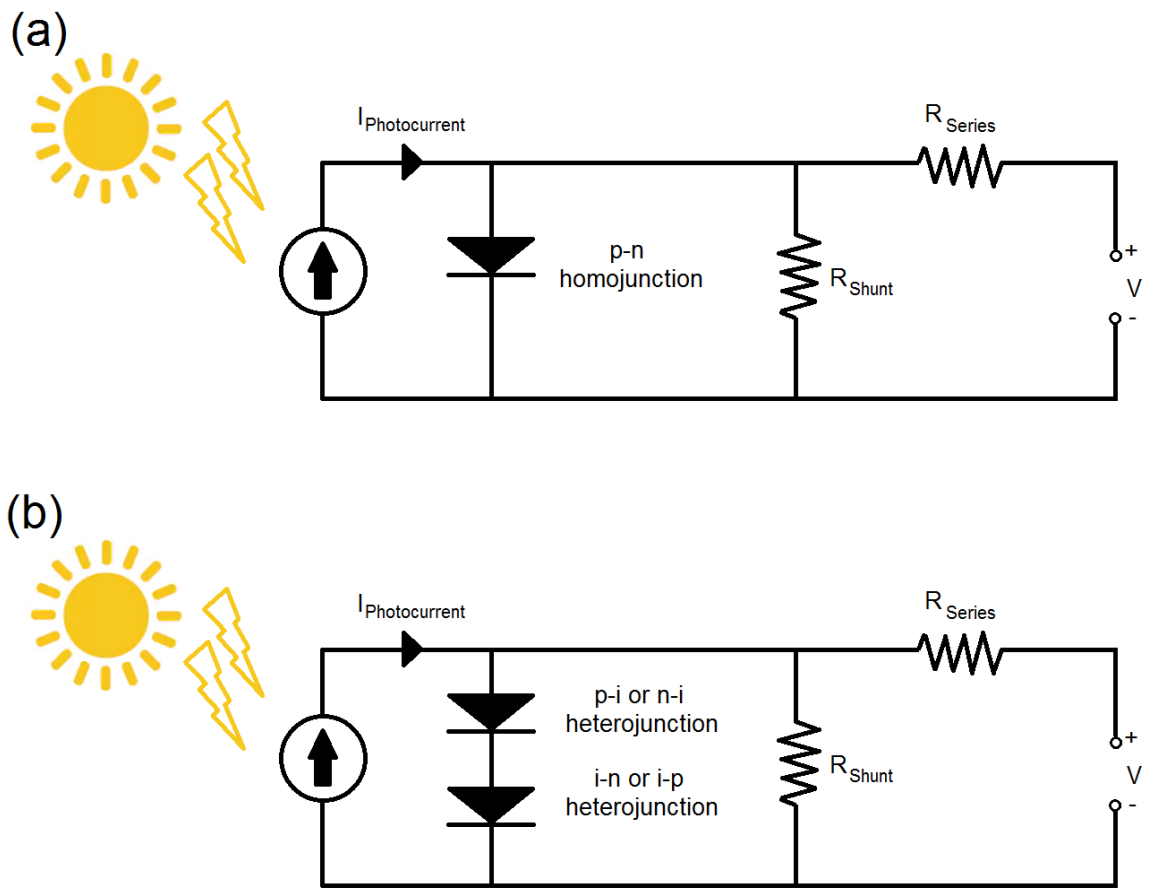

Figure 1.25: Illustration of the equivalent electrical circuits for solar cells based on (a) silicon single p-n homojunction and (b) perovskite either p-i-n or n-i-p heterojunction.

1.3.11 Current-voltage hysteresis

One of the main problems during the electrical characterization of PSCs, is the hysteresis phenomenon, with an observable offset between the characteristic current – voltage curves in respect to the forward and reverse scan directions (forward: from I_{SC} to V_{OC}, reverse: from V_{OC} to I_{SC}) and significantly affected by the scan speed. This hysteretic behaviour has been explained by several mechanisms and depends on ionic motion, localized current fluctuations due to depolarization of ionic accumulation at the interfaces between the HTL / perovskite and perovskite / ETL and at grain boundaries. [113–115] This hysteresis trend is also described by two models. The first model considers the formation of an electric field through the device which is different from the work functions between the two contacts (TCO and metal). This electric field affects the motion of charge carriers in respect to the transporting layers and modified

by the magnitude and speed of the external applied voltage during the electrical characterization. The mobile free ions can drift along the electric field inside the photoactive material, forming two space charge layers that shield or screen the main net electric field between the perovskite / ETL and perovskite / HTL. The formation of those space charge layers influence the charge carrier's collection as shown by step-dwell probe and step-dwell-step probe measurements conducted by Calado et al. and Belisle et al., respectively. [116,117] The second model regards the influence of interfacial chemical reactions between the perovskite / ETL and perovskite / HTL layers. Low or high frequency capacitance measurements in PSCs under illumination, have revealed different degree of interaction between the perovskite with compact titanium dioxide (c-TiO_2), phenyl-C61-butyric acid methyl ester ($PC_{61}BM$), nickel oxide (NiO) or 2,2',7,7'-tetrakis [N,N-di(4-methoxyphenyl)amino]-9,9'-spirobifluorene (spiro-MeOTAD). The formation of weak Ti – I – Pb bonds, accompanied by reversible accumulation of iodine ions causing enhanced hysteresis, in comparison with $PC_{61}BM$ as an ETL layer used. [118]

1.4 Aims for the thesis

Organic-inorganic halide perovskite semiconductors have attracted considerable academic and industrial attention in the last decade, since they have shown comparable or superior optoelectronic properties in comparison with other relevant semiconducting materials (such as silicon, CIGS, CZTS, CdTe, GaAs). Also, their low-cost fabrication applicability into solar cells, light emitting diodes (LED), photodetectors and even batteries have driven research efforts for their further exploitation and materials' quality optimization. However, halide perovskite commercialization perspective is hindered by lead (Pb) toxicity, chemical instability, large scale reproducibility and materials purity.

In this thesis, the first aim was to understand the importance of stoichiometry and polytypism in PbI_2 used, toward the synthesis of the simplest hybrid perovskite $CH_3NH_3PbI_3$ as a photoactive material in PSC devices. To study these two properties (stoichiometry and polytypism) of PbI_2, two different routed of synthesis were selected. Planetary ball milling (water-free) and the solvothermal (present of water) processes

were selected to investigate whether is possible to control the stoichiometry and polytypic phases present in PbI_2. The presence of polytypic phases and the stoichiometry of the synthesized PbI_2 were confirmed by X-ray photoelectron spectroscopy (XPS), X-ray diffraction (XRD) and Rutherford backscattering spectroscopy (RBS), as discussed in chapter 3.

The second aim was to correlate the PCE of PSC devices with the stoichiometry and polytypic phases present in the PbI_2 used. To study that a stoichiometrically optimum PbI_2 synthesized by planetary ball milling was compared with commercially available PbI_2. Also, as experimentally shown, the PCE of PSC devices was affected by the stoichiometry and not the number of polytypes present in PbI_2. That was directly related with the atomic ratio between the lead and iodide, as confirmed by controllably synthesis of $CH_3NH_3PbI_3$ micro-crystals. Whereas, when sub-stoichiometric PbI_2 used for the formation of $CH_3NH_3PbI_3$, resulted in unreacted PbI_2, as evidenced by ultra-violent visible spectroscopy (UV-Vis), which affects the average PCE of PSC devices by a factor of ~ 3.3 times. Unreacted PbI_2 might be correlated to further chemical instability in $CH_3NH_3PbI_3$, as discussed in chapter 3.

The third aim was to understand the chemical instability and correlate the phenomenon of hysteresis between the characteristic current density-voltage curves at forward and reverse scans in PSC devices, as function of mixed organic cations and halogen anions introduced into the $CH_3NH_3PbI_3$ crystal structure. That succeeded by synthesizing controllably doped $CH_3NH_3PbI_3$ micro-crystals and tracing the optimum amount of dopants used by XRD. Also, stability tests were performed in PSC devices for 240 hours, fabricated using doped $CH_3NH_3PbI_3$ micro-crystals, as presented in chapter 4.

1.5 References

1 Z. Shi and A. H. Jayatissa, *Materials.*, 2018, **11 (5)**, 729.

2 N. Kumawat, X.-K. Liu, D. Kabra and F. Gao, *Nanoscale*, 2019, **11**, 2109–2120.

3 J. Miao and F. Zhang, *J. Mater. Chem. C*, 2019, **7**, 1741–1791.

4 N. Vicente and G. Garcia-belmonte, *J. Phys. Chem. Lett.*, 2017, **8 (7)**, 1371–1374.

5 P. Odenthal, W. Talmadge, N. Gundlach, R. Wang, C. Zhang, D. Sun, Z. Yu, Z. V.

Vardeny and Y. S. Li, *Nat. Phys.*, 2017, **13**, 894–899.

6 V. Smil, *Energy Transitions Global and National Perspectives*, Praeger, ISBN: 144085324X, 2 edition., 2016.

7 D. M. Chapin, C. S. Fuller and G. L. Pearson, *J. Appl. Phys.*, 1954, **25**, 676–677.

8 V. V. M. Goldschmidt, *Naturwissenschaften*, 1926, **14 (21)**, 477–485.

9 K. H. Whitmire, *Bismuth : Inorganic Chemistry*, Encyclopedia of Inorganic and Bioinorganic Chemistry, John Wiley & Sons, 2013.

10 N. Park, *Mater. Today*, 2015, **18 (2)**, 65–72.

11 D. Weber, *Naturforsch*, 1978, **33b**, 1443–1445.

12 D. Weber, *Naturforsch*, 1978, **33b**, 862–865.

13 D. B. Mitzi, C. D. Dimitrakopoulos and L. L. Kosbar, *Chem. Mater.*, 2001, **13 (10)**, 3728–3740.

14 D. B. Mitzi, K. Chondroudis and C. R. Kagan, *IBM J. Res. Dev.*, 2001, **45 (1)**, 29–45.

15 A. Kojima, K. Teshima, Y. Shirai and T. Miyasaka, *J. Am. Chem. Soc.*, 2009, **131 (17)**, 6050–6051.

16 Q. Jiang, Y. Zhao, X. Zhang, X. Yang, Y. Chen, Z. Chu, Q. Ye, X. Li, Z. Yin and J. You, *Nat. Photonics*, 2019, **40 (4)**, s41566.

17 A. Miyata, A. Mitioglu, P. Plochocka, O. Portugall, J. T. Wang, S. D. Stranks, H. J. Snaith and R. J. Nicholas, *Nat. Phys.*, 2015, **11**, 582–587.

18 G. Xing, N. Mathews, S. Sun, S. Sien Lim, Y. Ming Lam, M. Gratzel, S. Mhaisalkar and T. Sum, *Science.*, 2013, **342**, 344–347.

19 S. D. Stranks, S. D. Stranks, G. E. Eperon, G. Grancini, C. Menelaou, M. J. P. Alcocer, T. Leijtens, L. M. Herz, A. Petrozza and H. J. Snaith, *Science.*, 2013, **342**, 341–344.

20 Y. Zhao, A. M. Nardes and K. Zhu, *J. Phys. Chem. Lett.*, 2014, **5 (3)**, 490–494.

21 C. C. Stoumpos, C. D. Malliakas and M. G. Kanatzidis, *Inorg. Chem.*, 2013, **52 (15)**, 9019–9038.

22 E. M. Hutter, M. C. Gélvez-rueda, A. Osherov, V. Bulović, F. C. Grozema, S. D. Stranks and T. J. Savenije, *Nat. Mater.*, 2017, **16**, 115–120.

23 R. Brenes, C. Eames, V. Bulović, M. S. Islam and S. D. Stranks, *Adv. Mater.*, 2018, **30**, 1706208.

24 Q. Wang, B. Chen, Y. Liu, Y. Deng, Y. Bai, Q. Dong and J. Huang, *Energy Environ. Sci.*, 2017, **10**, 516–522.

25 B. Philippe, M. Saliba, J. P. Correa-Baena, U. B. Cappel, S. H. Turren-Cruz, M. Grätzel, A. Hagfeldt and H. Rensmo, *Chem. Mater.*, 2017, **29**, 3589–3596.

26 F. Sani, S. Shafie, H. Lim and A. O. Musa, *Materials.*, 2018, **11 (6)**, 1008.

27 N. Pellet, P. Gao, G. Gregori, T. Yang, M. K. Nazeeruddin, J. Maier and M. Grätzel, *Angew. Chemie - Int. Ed.*, 2014, **53**, 3151–3157.

28 H. Choi, J. Jeong, H. Kim, S. Kim, B. Walker, G. Kim and J. Young, *Nano Energy*, 2014, **7**, 80–85.

29 S. Shao, J. Liu, G. Portale, H. Fang, G. R. Blake, G. H. Brink, L. J. A. Koster and M. A. Loi, *Adv. Energy Mater.*, 2018, **8**, 1702019.

30 Y. Wang, W. Fu, H. Chen, J. Yan, J. Chen and W. Yang, *J. Mater. Chem. A*, 2018, **6**, 13090–13095.

31 E. T. Hoke, D. J. Slotcavage, E. R. Dohner, A. R. Bowring, H. I. Karunadasa and M. D. Mcgehee, *Chem. Sci.*, 2015, **6**, 613.

32 G. E. Eperon, S. D. Stranks, C. Menelaou, M. B. Johnston, L. M. Herz and H. J. Snaith, *Energy Environ. Sci.*, 2014, **7**, 982–988.

33 C. Mu, J. Pan, S. Feng, Q. Li and D. Xu, *Adv. Energy Mater.*, 2016, **7 (6)**, 1601297.

34 K. Domanski, J. Correa-Baena, N. Mine, M. K. Nazeeruddin, A. Abate, M. Saliba, W. Tress, A. Hagfeldt and M. Grätzel, *ACS Nano*, 2016, **10**, 6306–6314.

35 M. Saliba, T. Matsui, J. Seo, K. Domanski, J. Correa-Baena, M. Nazeeruddin, S. Zakeeruddin, W. Tress, A. Abate, A. Hagfeldt and M. Grätzel, *Energy Environ. Sci.*, 2016, **9**, 1989.

36 A. Ferreira Da Silva, N. Veissid, C. Y. An, I. Pepe, N. Barros De Oliveira and A. V. Batista Da Silva, *Appl. Phys. Lett.*, 1996, **69**, 1930–1932.

37 K. S. Shah, F. Olschner, L. P. Moy, P. Bennett, M. Misra, J. Zhang, M. R. Squillante and J. C. Lund, *Nucl. Instruments Methods Phys. Res. A*, 1996, **380**, 266–270.

38 P. A. Beckmann, *Cryst. Res. Technol.*, 2010, **45**, 455–460.

39 G. C. Trigunayat, *Solid State Ionics*, 1991, **48**, 3–70.

40 B. Palosz, W. Steurer and H. Schulz, *J. Phys. Condens. Matter*, 1990, **2**, 5285–5295.

41 L. Ramsdell, *Am. Mineral.*, 1947, **32**, 64–82.

42 J. F. Condeles, R. C. Z. Lofrano, J. M. Rosolen and M. Mulato, *Brazilian J. Phys.*, 2006, **36**, 320–323.

43 Q. Wei, B. Shen, Y. Chen, B. Xu, Y. Xia, J. Yin and Z. Liu, *Mater. Lett.*, 2017, **193**, 101–104.

44 A. R. Patel and A. V. Rao, *J. Cryst. Growth*, 1980, **49**, 589–590.

45 R. A. Street, S. E. Ready, F. Lemmi, K. S. Shah, P. Bennett and Y. Dmitriyev, *J. Appl. Phys.*, 1999, **86**, 2660–2667.

46 Z. Zheng, A. Liu, S. Wang, Y. Wang, Z. Li, W. M. Lau and L. Zhang, *J. Mater. Chem.*, 2005, **15**, 4555–4559.

47 X. H. Zhu, Z. R. Wei, Y. R. Jin and A. P. Xiang, *Cryst. Res. Technol.*, 2007, **42**, 456–459.

48 M. A. Hassan, M. M. Jafar, M. Matuchova and B. N. Bulos, *J. Appl. Sci.*, 2010, 10, 3367–3373.

49 E. Salje, B. Palosz and B. Wruck, *J. Phys. C Solid State Phys.*, 1987, **20**, 4077–4096.

50 A. L. Falk, B. B. Buckley, G. Calusine, W. F. Koehl, V. V. Dobrovitski, A. Politi, C. A. Zorman, P. X. L. Feng and D. D. Awschalom, *Nat. Commun.*, 2013, **4**, 1–7.

51 F. C. Frank, *Hilosophical Mag. J. Sci.*, 1951, **7**, 1014–1021.

52 D. Pandey and P. Krishna, *Prog. Cryst. Growth Charact.*, 1983, **7**, 213–258.

53 R. S. Mitchell, *Zeitschrift für Krist.*, 1959, **111**, 372–384.

54 M. T. Sebastian and P. Krishna, *Prog. Cryst. Growth Charact.*, 1987, **14**, 103–183.

55 E. Article, G. Kieslich, S. Sun and A. K. Cheetham, *Chem. Sci.*, 2014, **5**, 4712–4715.

56 C. J. Bartel, C. Sutton, B. R. Goldsmith, R. Ouyang, C. B. Musgrave, L. M. Ghiringhelli and M. Scheffler, *Sci. Adv.*, 2019, **5 (2)**, eaav0693.

57 W. Travis, E. Glover, H. Bronstein, D. Scanlon and R. Palgrave, *Chem. Sci.*, 2016, **7**, 4548–4556.

58 D. Ji, S. Feng, L. Wang, S. Wang, M. Na, H. Zhang, C. Zhang and X. Li, *Vacuum*, 2019, **164**, 186–193.

59 C. Li, X. Lu, W. Ding, L. Feng, Y. Gao and Z. Guo, *Acta Crystallogr. Sect. B Struct. Sci.*, 2008, **64 (6)**, 702–707.

60 G. S. Rohrer, *J. Mater. Educ.*, 1998, **20**, 135.

61 M. a. Green, A. Ho-Baillie and H. J. Snaith, *Nat. Photonics*, 2014, **8 (7)**, 506–514.

62 M. Emilio, J. R. Kuhn, R. I. Bush and I. F. Scholl, *Astrophys. J.*, 2012, **135**, 2–9.

63 International Organization for Standardization, *INTERNATIONAL STANDARD*, 1992, vol. 10–15.

64 A. Jha, H. Duan, V. Tiwari, P. K. Nayak and H. J. Snaith, *ACS Photonics*, 2018, 852–860.

65 I. Hussain, H. P. Tran, J. Jaksik, J. Moore, N. Islam and M. J. Uddin, *Energy Mater.*, 2018, **1 (3)**, 133–154.

66 Z. H. Bakr, Q. Wali, A. Fakharuddin, L. Schmidt-mende, M. Brown and R. Jose, *Nano Energy*, 2017, **34**, 271–305.

67 M. I. Asghar, J. Zhang, H. Wang and P. D. Lund, *Renew. Sustain. Energy Rev.*, 2017, **77**, 131–146.

68 J. Chen and N. Park, *J. Phys. Chem. C*, 2018, **122 (25)**, 14039–14063.

69 D. Yang, R. Yang, S. Priya and S. Liu, *Angew. Chemie Int. Ed.*, 2019, **26 (58)**, 4466–4483.

70 Z. Song, S. C. Watthage, A. B. Phillips and M. J. Heben, *J. Photonics Energy*, 2016, **6 (2)**, 022001.

71 W. Ke, G. Fang, J. Wan, H. Tao, Q. Liu, L. Xiong, P. Qin, J. Wang, H. Lei, G. Yang, M. Qin, X. Zhao and Y. Yan, *Nat. Commun.*, 2015, **6 (1)**, 6700.

72 S. Lin, B. Yang, X. Qiu, J. Yan, J. Shi, Y. Yuan, W. Tan, X. Liu, H. Huang, Y. Gao and C. Zhou, *Org. Electron.*, 2018, **53**, 235–241.

73 L. Pazos-Outon, T. P. Xiao and E. Yablonovitch, *J. Phys. Chem. Lett.*, 2018, **9**, 1703–1711.

74 W. Shockley and W. T. Read, *Phys. Rev.*, 1952, **87 (5)**, 835–842.

75 R. N. Hall, *Phys. Rev.*, 1952, **87**, 387.

76 S. Heo, G. Seo, Y. Lee, D. Lee, M. Seol, J. Lee, J. Park, D. Yun, Y. Kim, J. Shin, T. Ahn and M. Nazeeruddin, *Energy Environ. Sci.*, 2017, **10 (5)**, 1128–1133.

77 D. Bi, W. Tress, M. I. Dar, P. Gao, J. Luo, C. Renevier, K. Schenk, A. Abate, F. Giordano, J.-P. Correa Baena, J.-D. Decoppet, S. M. Zakeeruddin, M. K. Nazeeruddin, M. Gra tzel and A. Hagfeldt, *Sci. Adv.*, 2016, **2 (1)**, e1501170–e1501170.

78 A. Buin, P. Pietsch, O. Voznyy, R. Comin, A. H. Ip, E. H. Sargent and B. Xu, *Nano Lett.*, 2014, **14 (11)**, 6281–6286.

79 H. Yu, F. Wang, F. Xie, W. Li, J. Chen and N. Zhao, *Adv. Funct. Mater.*, 2014, **24**, 7102–7108.

80 C. Ran, J. Xu, W. Gao, C. Huang and S. Dou, *Chem. Soc. Rev.*, 2018, **47 (12)**, 4581–4610.

81 G. Xing, N. Mathews, S. S. Lim, N. Yantara, X. Liu, D. Sabba, M. Grätzel, S. Mhaisalkar and T. C. Sum, *Nat. Mater.*, 2014, **13**, 476–480.

82 W. Dane, S. M. Vorpahl, S. D. Stranks, H. Nagaoka, G. E. Eperon, M. E. Ziffer, J. Henry and D. S. Ginger, *Science,* 2015, **348 (6235)**, 683–686.

83 J.-P. Correa-Baena, W. Tress, K. Domanski, E. H. Anaraki, S. H. Turren-Cruz, B. Roose, P. P. Boix, M. Gratzel, A. Abate and A. Hagfeldt, *Energy Environ. Sci.*, 2017, **10 (5)**, 1207–1212.

84 D. S. Lee, J. S. Yun, J. Kim, A. M. Soufiani, S. Chen, Y. Cho, X. Deng, J. Seidel, S. Lim, S. Huang and A. W. Y. Ho-Baillie, *ACS Energy Lett.*, 2018, **3**, 647–654.

85 D. Shi, V. Adinolfi, R. Comin, M. Yuan, E. Alarousu, A. Buin, Y. Chen, S. Hoogland, A. Rothenberger, K. Katsiev, Y. Losovyj, X. Zhang, P. A. Dowben, O. F. Mohammed, E. H. Sargent and O. M. Bakr, *Science.*, 2015, **347 (6221)**, 519–522.

86 Q. Dong, Y. Fang, Y. Shao, J. Qiu, L. Cao and J. Huang, *Science.*, 2015, **347 (6225)**, 967–970.

87 W. Li, H. Rao, B. Chen, X. Wang and D. Kuang, *J. Mater. Chem. A*, 2017, **5**, 19431–19438.

88 A. Poglitsch and D. Weber, *J. Chem. Phys.*, 1987, **(87) 11**, 6373–6378.

89 J. Su, D. P. Chen and C. T. Lin, *J. Cryst. Growth*, 2015, **422**, 75–79.

90 Z. Lian, Q. Yan, Q. Lv, Y. Wang, L. Liu, L. Zhang, S. Pan, Q. Li, L. Wang and J. Sun, *Sci. Rep.*, 2015, **5 (1)**, 1–10.

91 Y. Dang, Y. Zhou, X. Liu, D. Ju, S. Xia and H. Xia, *Angew. Chemie Int. Ed.*, 2016, **55 (10)**, 3447–3450.

92 Y. Dang, C. Zhong, G. Zhang, D. Ju, L. Wang, S. Xia, H. Xia and X. Tao, *Chem. Mater.*, 2016, **28 (19)**, 6968–6974.

93 M. I. Saidaminov, A. L. Abdelhady, B. Murali, E. Alarousu, V. M. Burlakov, W. Peng, I. Dursun, L. Wang, Y. He, G. Maculan, A. Goriely, T. Wu, O. F. Mohammed and O. M. Bakr, *Nat. Commun.*, 2015, **6 (1)**, 7586.

94 J. M. Kadro, K. Nonomura, D. Gachet, M. Grätzel and A. Hagfeldt, *Sci. Rep.*, 2015, **5**

(1), 11654.

95 W. Peng, L. Wang, B. Murali, K. Ho, A. Bera, N. Cho, C. Kang, V. M. Burlakov, J. Pan, L. Sinatra, C. Ma, W. Xu, D. Shi, E. Alarousu, A. Goriely, J. He, O. F. Mohammed, T. Wu and O. M. Bakr, *Adv. Mater.*, 2016, **28 (17)**, 3383–3390.

96 H. Rao, W. Li, B. Chen, D. Kuang and C. Su, *Adv. Mater.*, 2017, **29 (16)**, 1602639.

97 M. Acik, T. M. Alam, F. Guo, Y. Ren, B. Lee, R. A. Rosenberg, J. F. Mitchell, I. K. Park, G. Lee and S. B. Darling, *Adv. Energy Mater.*, 2018, **8**, 1701726.

98 D. Prochowicz, P. Yadav, M. Saliba, M. Saski, S. M. Zakeeruddin, J. Lewiński and M. Grätzel, *ACS Appl. Mater. Interfaces*, 2017, **9**, 28418–28425.

99 P. Pal, S. Saha, A. Banik, A. Sarkar and K. Biswas, *Chem. - A Eur. J.*, 2018, **24**, 1811–1815.

100 K. V. Manukyan, A. V. Yeghishyan, D. O. Moskovskikh, J. Kapaldo, A. Mintairov and A. S. Mukasyan, *J. Mater. Sci.*, 2016, **51**, 9123–9130.

101 G. J. Lee, E. K. Park, S. A. Yang, J. J. Park, S. D. Bu and M. K. Lee, *Sci. Rep.*, 2017, **7**, 1–11.

102 L. Zhang, Z. Xu, L. Cao and X. Yao, *Mater. Lett.*, 2007, **61**, 1130–1133.

103 M. Dresselhaus, G. Cronin and A. Gomes Souza Filho, *Solid State Properties*, Springer-Verlag Berlin Heidelberg, ISBN: 978-3-662-55922-2, 2018.

104 P. Hofmann, *Solid State Physics*, Callister, WILEY-VCH, ISBN:978-3-527-41282-2, 2015.

105 M. Green, F. D. King and J. Shewchun, *Solid. State. Electron.*, 1974, **17 (6)**, 551–561.

106 N. Peyghambarian, S. W. Koch and A. Mysyrowicz, *Introduction to Semiconductor Optics (Prentice Hall Series in Solid State Physical Electronics)*, Pearson College Div, ISBN:0136389902, 1993.

107 S. Fonash, *Solar Cell Device Physics*, Academic Press, ISBN:9780080912271, 2010.

108 M. Cai, N. Ishida, M. Cai, N. Ishida, X. Li, X. Yang, T. Noda and Y. Wu, *Joule*, 2018, **2**, 1–11.

109 W. Tress, M. Yavari, K. Domanski, P. Yadav, B. Niesen, P. Correa, A. Hagfeldt and M. Grätzel, *Energy Environ. Sci.*, 2018, **11**, 151–165.

110 W. E. I. Sha, X. Ren, L. Chen, W. C. H. Choy, W. E. I. Sha, X. Ren, L. Chen and W. C. H. Choy, *Appl. Phys. Lett.*, 2015, **106 (22)**, 221104.

111 L. C. Hirst and N. J. Ekins-daukes, *Prog. Photovoltaics Res. Appl.*, 2011, **19 (3)**, 286–293.

112 P. Liao, X. Zhao, G. Li, Y. Shen and M. Wang, *Nano-Micro Lett.*, 2018, **10 (5)**, 1–8.

113 Y. Yuan, T. Li, Q. Wang, J. Xing, A. Gruverman and J. Huang, *Sci. Adv.*, 2017, **3 (3)**, e1602164.

114 R. S. Sanchez, V. Gonzalez-pedro, J. Lee, N. Park, Y. S. Kang, I. Mora-sero and J. Bisquert, *J. Phys. Chem. Lett.*, 2014, **5 (13)**, 2357–2363.

115 J. Wei, Y. Zhao, H. Li, G. Li, J. Pan, D. Xu, Q. Zhao and D. Yu, *J. Phys. Chem. Lett.*, 2014, **5 (21)**, 3937–3945.

116 P. Calado, A. M. Telford, D. Bryant, X. Li, J. Nelson, B. C. O. Regan and P. R. F. Barnes, *Nat. Commun.*, 2016, **7**, 13831.

117 R. Belisle, W. Nguyen, A. Bowring, P. Calado, X. Li, S. J. C. Irvine, M. D. Mcgehee, R. F. Barnes and B. C. O'Regan, *Energy Environ. Sci.*, 2016, **10 (1)**, 192–204.

118 H. Kim, I. Jang, N. Ahn, M. Choi, A. Guerrero, J. Bisquert and N. Park, *J. Phys. Chem. Lett.*, 2015, **6 (22)**, 4633–4639.

Chapter 2

Experimental methods

2.1 Introduction

This chapter describes in detail all the experimental methods used for the synthesis of PbI_2, relevant materials used for fabrication of perovskite micro-crystals, perovskite thin films and perovskite solar cells. Specifically, attention is given to the topic of PbI_2 synthesis by two different processes (solvothermal and mechanochemical) and fabrication of doped / undoped perovskite micro-crystals. Controllable and reproducible synthesis of perovskites is an important step towards the commercialization of perovskite-based solar cell devices. Also, the mechanochemical synthesis of PbI_2 might be applied in lead free precursors (such as tin iodide (SnI_2) or bismuth iodide (BiI_3)) leading to formation of perovskites with less toxicity. Chemicals and reagents, were purchased and used without any further purification, unless is specified. Also, in this chapter information and relevant theory is provided about the characterization techniques used. Characterization of all synthesized materials was conducted at less than 24 hours after their preparation.

2.2 Synthesis of chemicals

2.2.1 Synthesis of organohalide compounds

Generally, organic – inorganic perovskite compounds obeying to the general chemical formula ABX_3, are synthesized by the equimolar reaction between organic halide such as methylammonium iodide (CH_3NH_3I) and inorganic halide such as lead iodide (PbI_2) compounds, as shown in chemical reaction 2.1. However, synthesis of perovskite could result from the reaction between non - equimolar amounts of precursors, such as CH_3NH_3I and lead chloride ($PbCl_2$), as shown in chemical reaction 2.2, as summarized in table 2.1. [1] That indicates the complexity of perovskites' synthesis, as a function of their reactant precursors and halogen type. However, this thesis focuses only on the equimolar reactions of reactant compounds (as shown in chemical reaction 2.1) toward the formation of perovskites. Two different amino halogen compounds, CH_3NH_3I and the methylammonium bromide (CH_3NH_3Br) were synthesized by reacting methylamine (CH_3NH_2) with hydroiodic acid (HI) or hydrobromic acid (HBr), respectively, as shown in chemical reactions 2.3 and 2.4. Also, one amidine halogen compound, formamidinium iodide ($CH(NH_2)_2I$) was also synthesized by reacting formamidine acetate ($HN{=}CHNH_2CH_3COOH$) with hydroiodic acid, as shown in chemical reaction 2.5 and summarized in table 2.2.

$$\mathrm{CH_3NH_3I} + \mathrm{PbI_2} \rightarrow \mathrm{CH_3NH_3PbI_3} \qquad \text{chemical reaction 2.1}$$

$$3\,\mathrm{CH_3NH_3I} + \mathrm{PbCI_2} \rightarrow \mathrm{CH_3NH_3PbI_{3-x}Cl_x} + \mathrm{PbI_{2-y}Cl_y} \qquad \text{chemical reaction 2.2}$$

Table 2.1: Chemical reactions between organic and inorganic halide compounds towards the formation of perovskite, (2.1) equimolar and (2.2) non – equimolar.

$$\mathrm{CH_3NH_2} + \mathrm{HI} \rightarrow \mathrm{CH_3NH_3I} \qquad \text{chemical reaction 2.3}$$

$$\mathrm{CH_3NH_2} + \mathrm{HBr} \rightarrow \mathrm{CH_3NH_3Br} \qquad \text{chemical reaction 2.4}$$

$$\mathrm{HN = CHNH_2 \cdot CH_3COOH} + \mathrm{HI} \rightarrow \mathrm{CH(NH_2)_2I} + \mathrm{CH_3COOH} \qquad \text{chemical reaction 2.5}$$

Table 2.2: Chemical reactions between amines or amidine and halide acids, (2.3) methylamine with hydroiodic acid, (2.4) methylamine with hydrobromic acid and (2.5) formamidine acetate with hydroiodic acid.

Methylammonium iodide (CH_3NH_3I) was synthesised in a similar way to Kamat *et al.* [2] by adding 38 mL of hydroiodic acid dropwise (57% w / w in water, Alfa Aesar) into 30 mL of methylamine solution (40% w / w in water, Sigma Aldrich) in a 250 mL round bottom flask at 0 ºC (ice bath) and constantly stirring (400 rpm) for 2 hours. After mixing both liquids, the round bottom flask was transferred into an oil bath at a temperature of 90 ºC, to evaporate the water for 6 - 7 hours. The resulting yellow/white precipitate was further purified by recrystallisation two times using pure anhydrous ethanol. The white / transparent crystallised flakes were collected by vacuum filtration using a Whatman filter paper grade 5 with a pore size of 2.5 µm and dried in a vacuum oven at 50 ºC for 24 hours, before storage in a vial under dark conditions. The same CH_3NH_3I, was used for both the synthesis of the undoped or doped $CH_3NH_3PbI_3$ micro-crystals and perovskite solutions, as well.

Methylammonium bromide (CH_3NH_3Br) was similarly synthesised in a way that presented by Noh *et al.* [3] by adding 43 mL of hydrobromic acid dropwise (48% w / w in water, Sigma Aldrich) into 30 mL of methylamine solution (40% w / w in water, Sigma Aldrich) in a 250 mL round bottom flask at 0 °C (ice bath) and constantly stirring (400 rpm) for 2 hours. After mixing both liquids, the round bottom flask was transferred into an oil bath at a temperature of 90 ºC, to evaporate the water for 6 - 7 hours. The resulting yellow/white precipitate was further purified by recrystallisation process two times, using pure anhydrous ethanol. The white / transparent crystallised flakes were collected by vacuum filtration using a Whatman filter paper grade 5 with a pore size of 2.5 µm and dried in a vacuum oven at 50 ºC for 24 hours, before storage in a vial under dark conditions. The CH_3NH_3Br, was used for controllable doping during the synthesis of doped $CH_3NH_3PbI_3$ micro-crystals.

Formamidinium iodide ($CH(NH_2)_2I$) was synthesised in a similar way to Eperon *et al.* [4] by dissolving 8 g of formamidinium acetate powder (99%, Alfa Aesar) in a 1.2 times molar excess of 12.2 mL hydroiodic acid (57% w / w in water, Alfa Aesar) in a 250 mL round bottom flask at 0 ºC (ice bath) and constantly stirring (400 rpm) for 2 hours. After mixing both reactants, the round bottom flask was transferred into an oil bath at a temperature of 90 ºC, to evaporate the water for 4 - 5 hours. The resulting yellow/white precipitate was further purified by recrystallisation one time using pure anhydrous

ethanol. The white / transparent crystallised flakes were collected by vacuum filtration using a Whatman filter paper grade 5 with a pore size of 2.5 μm and dried in a vacuum oven at 50 ºC for 24 hours, before storage in a vial under dark conditions. The $CH(NH_2)_2I$, was used as controllable doping agent during the synthesis of doped $CH_3NH_3PbI_3$ micro-crystals.

2.2.2 Synthesis of solvothermal PbI_2

Solvothermal synthesis of PbI_2 powder was achieved by dissolving 1 g of lead (II) nitrate ($Pb(NO_3)_2$) (≥ 99 %, Sigma Aldrich) and 1.01 g of potassium iodide (KI) (≥ 99 %, Honeyell Fluka) in a 1 L volume round bottom flask filled with 1 L of boiled (100 ºC) ultra-pure deionised water (Sigma Aldrich) with resistivity 18.2 MΩ. The round bottom flask was covered with blanket made of fiberglass and left to cool down slowly to room temperature for 24 hours. An excess of potassium iodide moles (~ 2 %) were used to complete the reaction of the $Pb(NO_3)_2$, as shown in the chemical reaction 2.6. The golden coloured crystalline flakes of PbI_2 (as shown in figure 2.1), were collected after vacuum filtration using Whatman filter paper grade 5 with a pore size of 2.5 μm and dried in a vacuum oven at 50 ºC for 24 hours, before storage in a vial under dark conditions.

$$\mathrm{Pb(NO_3)_2 + 2KI \rightarrow PbI_2 + 2KNO_3} \qquad \text{chemical reaction 2.6}$$

Figure 2.1: Image of solvothermal synthesised PbI_2 powder, scale bar represents 2 cm.

2.2.3 Synthesis of mechanochemical PbI_2

Mechanochemical synthesis of PbI_2 powder was achieved using a planetary ball milling machine (PM 100 Retsch) at variable revolutions per minute and time duration, as shown in table 2.3. Initially, 30 g of $Pb(NO_3)_2$ (≥ 99 %, Sigma Aldrich), 30.07 g of KI (≥ 99 %, Honeyell Fluka) and 160 stainless steel spheres of diameter 6 mm, were mixed together in a ball milling jar of capacity 500 mL. The yellow coloured PbI_2 powder (as shown in figure 2.2) was then separated from the stainless-steel spheres and washed 5 times with deionised water (70 - 80 mL each time) during vacuum filtration using Whatman filter paper grade 5 with a pore of size 2.5 μm to remove any potassium nitrate by-product. Finally, the PbI_2 was dried in a vacuum oven at 50 ºC for 24 hours, before storage in a vial under dark conditions. The yield of the PbI_2 produced was defined by the relative number of moles of product (PbI_2) to the moles of reactant ($Pb(NO_3)_2$), considering as ideal molecular weight for the PbI_2, to be 461.01 g / mol), resulting:

$$\left(\frac{40.32\ g}{461.01\ g*mol^{-1}}\right) / \left(\frac{30\ g}{331.21\ g*mol^{-1}}\right) * 100\ \% \approx 96.5\ \%$$

Lead iodide sample	Mechanochemical conditions of synthesis
MC1	200 rpm 2 hours
MC2	400 rpm 1 hour
MC3	400 rpm 4 hours

Table 2.3: Mechanochemical PbI_2 powders (MC 1 to 3) synthesized using planetary ball milling process under different conditions (revolutions per minute and time duration).

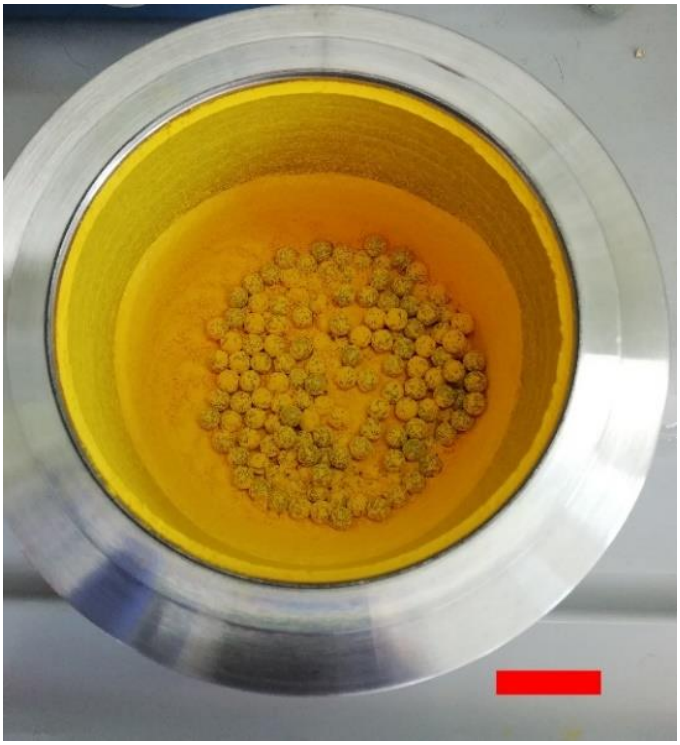

Figure 2.2: Image of mechanochemically synthesised PbI_2 powder and stainless-steel spheres inside the crucible used for the planetary ball milling process, scale bar represents 2 cm.

2.2.4 Synthesis of undoped or doped $CH_3NH_3PbI_3$ micro-crystals

Synthesis of undoped or doped $CH_3NH_3PbI_3$ micro-crystals was achieved based on a method similar to the reaction between alcohol / PbI_2 / CH_3NH_3I, introduced by Acik et al. [5]

The undoped $CH_3NH_3PbI_3$ micro-crystals were synthesised by reacting 0.7 g of mechanochemical MC2 or commercial (99.999 %, Sigma Aldrich) PbI_2 powder with either an equimolar amount of CH_3NH_3I (0.2414 g) or an equimolar amount plus 30% excess by weight of CH_3NH_3I (0.2414 g + 0.0724 g = 0.3138 g), in 15 mL of 1-pentanol at variable temperatures (20 ºC, 50 ºC, 70 ºC and 90 ºC) and constant stirring (400 rpm) for 24 hours. In this process, 1-pentanol which is a polar protic non-toxic alcohol, was used to selectively dissolve only the CH_3NH_3I, but neither the PbI_2 powder nor the final product of the undoped $CH_3NH_3PbI_3$ micro-crystals. The synthesised black powder (as shown in figure 2.3) was collected by vacuum filtration using Whatman filter paper grade 5 with a pore size of 2.5 µm and washed with 5 mL of chlorobenzene

(99.9 %, Alfa Aesar) during the filtration step, followed by drying in a vacuum oven for 30 min at room temperature, before storage in a vial under dark conditions.

Doped $CH_3NH_3PbI_3$ micro-crystals were synthesised by reacting 0.7 g of mechanochemical MC2 PbI_2 powder with an equimolar amount plus 10% excess by weight of CH_3NH_3I (0.2414 g + 0.0241 g = 0.2655 g) and various amounts (as function of PbI_2 moles) of CH_3NH_3Br, $CH(NH_2)_2I$ or Br_2, respectively. All the mixed precursors were stirred constantly (400 rpm) in 15 mL of 1-pentanol at constant temperature of 90 ºC for 24 hours. The resulting black powder was collected by vacuum filtration using Whatman filter paper grade 5 with a pore size of 2.5 µm and washed with 5 mL of chlorobenzene (99.9 %, Alfa Aesar) during the filtration step, followed by drying in a vacuum oven for 30 min at room temperature, before storage in a vial under dark conditions.

Figure 2.3: Black powder of undoped or doped $CH_3NH_3PbI_3$ micro-crystals after 24 hours of synthesis in oil bath, scale bar represents 30 mm.

2.3 Preparation of perovskite solutions

2.3.1 Dry dimethyl sulfoxide (DMSO)

Dry dimethyl sulfoxide (DMSO) (≥ 99.5 %, Sigma Aldrich) was prepared by mixing 150 mL of DMSO and 20 g of magnesium sulfate ($MgSO_4$) (Fisher Chemical) in a 250 mL round bottom flask. The round bottom flask was capped and left in a fume hood at room temperature for at least two weeks before extracting dry DMSO as a transparent colourless solution. The less expensive drying process of DMSO with $MgSO_4$ was selected in comparison with other processes involving distillation under vacuum or use of molecular sieves.

2.3.2 Perovskite solution preparation for solar cell devices

Two groups of perovskite solutions for the fabrication of solar cell devices were prepared. For the first group, 0.4 g of mechanochemical MC 2 or commercial PbI_2 powders, directly mixed with an equimolar amount of CH_3NH_3I (0.1379 g) and dissolved in 0.620 mL of dry DMSO, with a final concentration of 2.8 M. Whereas, for the second group, 0.4 g of the undoped $CH_3NH_3PbI_3$ micro-crystals synthesised using mechanochemical MC 2 or commercial PbI_2 powders, dissolved in 0.571 mL of dry DMSO with a final concentration of 1.13 M. All perovskite solutions were kept (capped in the glass vial) on a hot plate at a temperature of 100 ºC for 10 min to ensure complete dissolution of the reactants in dry DMSO. Yellowish solutions were filtered through a PTFE filter with a pore size of 0.45 µm into a new clean glass vial and kept under constant stirring (~ 300 rpm) and temperature (65 - 70 ºC) in a custom-made aluminium block before deposition, as shown in figure 2.4. The block helped to reduce condensation of the dry DMSO on the inside walls of the vial and preventing premature perovskite crystallisation. In all the experiments with undoped or doped $CH_3NH_3PbI_3$ micro-crystals, the solutions were prepared directly after the synthesis of micro-crystals. Also, the volume of dry DMSO added into the undoped or doped $CH_3NH_3PbI_3$ micro-crystals results in the pre-defined concentration of solutions 1.13 M, calculated based on the assumption of perfectly crystallised micro-crystals with corresponding molecular weights, as defined by the sum of the atomic mass units of each element

and summarised in table 2.4. Whereas, in all the experiments with either commercial or mechanochemical PbI_2 powders, the solution concentrations were calculated based on the false assumption of stoichiometrically perfect PbI_2 (Pb : I = 1 : 2, atoms ratio), with molecular weight 461.01 g * mol^{-1}.

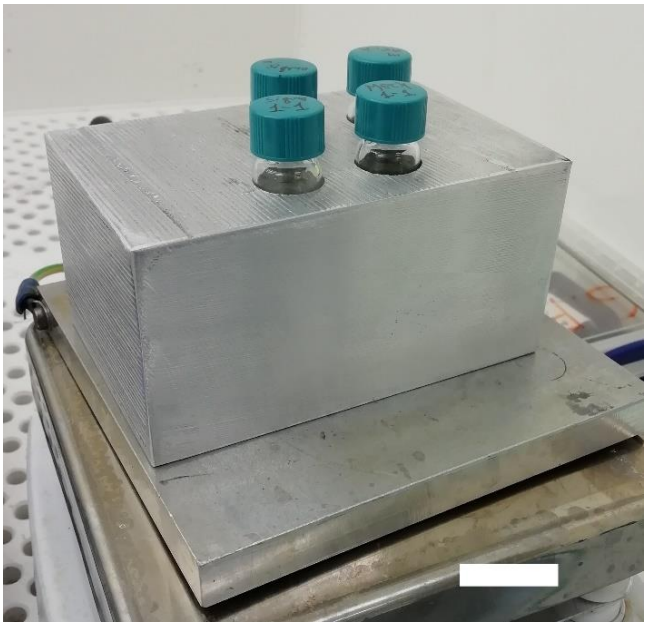

Figure 2.4: Image of the custom-made aluminium block used to keep the perovskite solutions warm, under constant stirring (~ 300 rpm) at a temperature of 65 ~ 70 ºC before deposition. Scale bar represents 20 mm.

Type of micro – crystals	Estimated chemical formula	Estimated molecular weight (g * mol^{-1})
A	$CH_3NH_3PbI_{2.6}Br_{0.4}$	601.18
B	$(CH_3NH_3)_{0.86}(CH(NH_2)_2)_{0.14}PbI_3$	621.80
C	$(CH_3NH_3)_{0.86}(CH(NH_2)_2)_{0.14}PbI_{2.8}Br_{0.2}$	612.40
D	$CH_3NH_3PbI_3$	619.98

Table 2.4: Type of doped or undoped $CH_3NH_3PbI_3$ micro-crystals synthesised using the almost stoichiometric mechanochemical MC2 PbI_2 in reaction with equimolar plus an excess 10 % by weight of CH_3NH_3I and (A) 40 % moles of CH_3NH_3Br, (B) 14 % moles of $CH(NH_2)_2I$, (C) 14 % moles of $CH(NH_2)_2I$ and 10 % moles of Br_2 and (D) no other dopant. Also, estimated chemical formula and molecular weight, is provided for each type.

2.4 Preparation of perovskite devices

2.4.1 Perovskite solar cells fabrication

Perovskite solar cell devices were fabricated by employing the n-i-p planar (regular) architecture, as graphically illustrated in figure 2.5. Glass substrates pre-patterned with six ITO (indium tin oxide) pixels (20 Ω / square, Ossila) were first cleaned by sonicating for 10 min in a solution made of 1 mL detergent (Hellmanex (III)) and 250 mL boiled deionised water (100 ºC). Any residual detergent was subsequently washed off by rinsing the substrates three times with 100 mL (each time) of deionised water. The Glass / ITO substrates, were further sonicated two more times for 10 min (each time) in 250 mL acetone and then 250 mL isopropanol. The cleaned substrates were then treated with oxygen plasma using a Zepto surface plasma cleaner (model 8) at power of 100 watts and oxygen flow rate adjusted at 200 mbar for 10 min to remove organic contaminants. The clean glass / ITO substrates were then transferred into a cleanroom (class 1000) with constant temperature 20 ºC and humidity 30 %, for deposition of the electron transporting layer and perovskite thin film. Commercially available colloidal dispersion of tin (IV) oxide (SnO_2) in deionised water (15 %, Alfa Aesar) was re-diluted in deionised water, in 1:4 volume ratio and then filtered with a PVDF filter with a pore size of 0.2 µm. Then 50 µL of re-diluted SnO_2 solution was spin coated at 3000 rpm for 30 s, followed by removal of the SnO_2 from part of the substrate using a dry cotton bud, re-exposing the ~ 4 - 5 mm ITO electrode. The coated substrates were then annealed at 150 ºC for 30 min and cooled down to 20 ºC, without any further treatment.[6] 50 µL of the perovskite solutions made of either undoped or doped $CH_3NH_3PbI_3$ micro-crystals in DMSO with concentration 1.13 M or solutions of mechanochemical MC 2 or commercial PbI_2 reacted with equimolar amount of CH_3NH_3I in DMSO with concentration 2.8 M, were statically dispersed onto the glass / ITO / SnO_2 samples followed by spin coating. The spinning speed was 2500 rpm for all the solutions with concentration 1.13 M, while 3100 rpm spinning speed was used for the solutions with concentration 2.8 M. In all cases, the spinning time regardless of the speed was 10 s. Also, the concentration of solutions was adjusted in respect to the spinning speed towards the formation of $CH_3NH_3PbI_3$ thin films with reduced accumulation of material at the edges of substrate, as shown in figure 2.6. Immediately after the spin coating process, each substrate was placed in a custom-made vacuum

chamber for 120 s and pressure ~ 0.02 mbar, as shown in figures 2.7 a and 2.7 b. Then each substrate was annealed on a hot plate at 100 ºC for 30 s for crystallisation of perovskite. All glass / ITO / SnO_2 / $CH_3NH_3PbI_3$ samples were then transferred inside a nitrogen filled glove box for the synthesis and deposition of doped hole transporting layer of 2,2',7,7'-Tetrakis [*N,N*-di (4-methoxyphenyl) amino]-9,9'-spirobifluorene (spiro-OMeTAD) (≥ 99.5%, Ossila). Then 86.6 mg of spiro-OMeTAD powder was dissolved in 1 mL of chlorobenzene. The solution was then doped with lithium bis(trifluoromethanesulfonyl)imide (Li-TFSI) (≥ 99%, Sigma Aldrich), 4-*tert*-butylpyridine (TBP) (96.6%, Sigma Aldrich) and FK209 (FK 209 Co(II) PF6), (Greatcell). The quantity of dopants used in 1 mL of the spiro-OMeTAD / chlorobenzene solution was as follows, 20 µL of Li-TFSI (500 mg*mL^{-1} in acetonitrile), 34 µL of TBP and 11 µL of FK209 (300 mg*mL^{-1} in acetonitrile). The solution was filtered with a PTFE filter with a pore size of 0.2 µm and then 50 µL was spin coated on each sample dynamically at 4000 rpm for 30 s. For perovskite solar cell devices, fabricated by doped $CH_3NH_3PbI_3$ micro-crystals synthesised using only the mechanochemical MC 2 PbI_2 powder, the HTL layer (spiro-OMeTAD) was free of FK209 dopant agent. All the devices were left overnight in dry air to allow the Li^+ cations to oxidise, since Li_2O converts the spiro-OMeTAD into an enhanced p-type semiconductor. [7] Finally, gold electrodes with thickness ~ 80 nm, were deposited through a template mask using an Edwards thermal evaporator at pressure < 8 * 10^{-7} mbar, with a deposition rate 0.1 Å s^{-1} for the first 2 nm and then 1 Å s^{-1} for the remaining thickness.[8] All un-encapsulated PSCs devices, as shown in figure 2.8, were immediately characterised electrically.

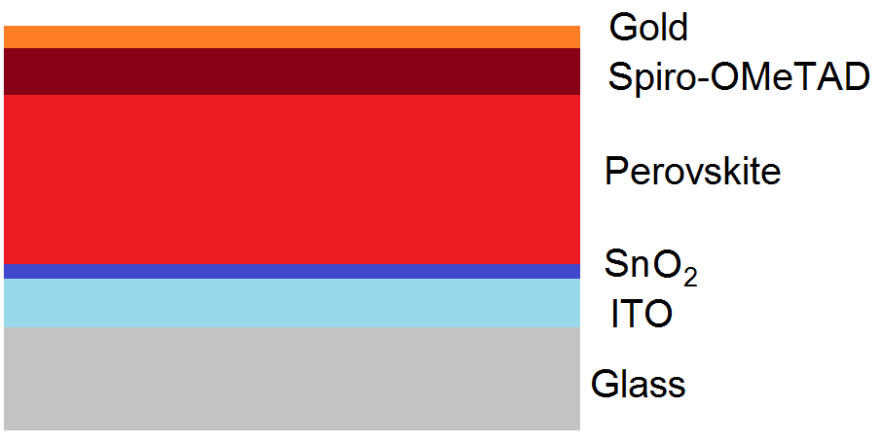

Figure 2.5: Graphically illustration of ITO / SnO2 / Perovskite / Spiro – OMeTAD / Gold layers in perovskite solar devices with n-i-p planar (regular) architecture.

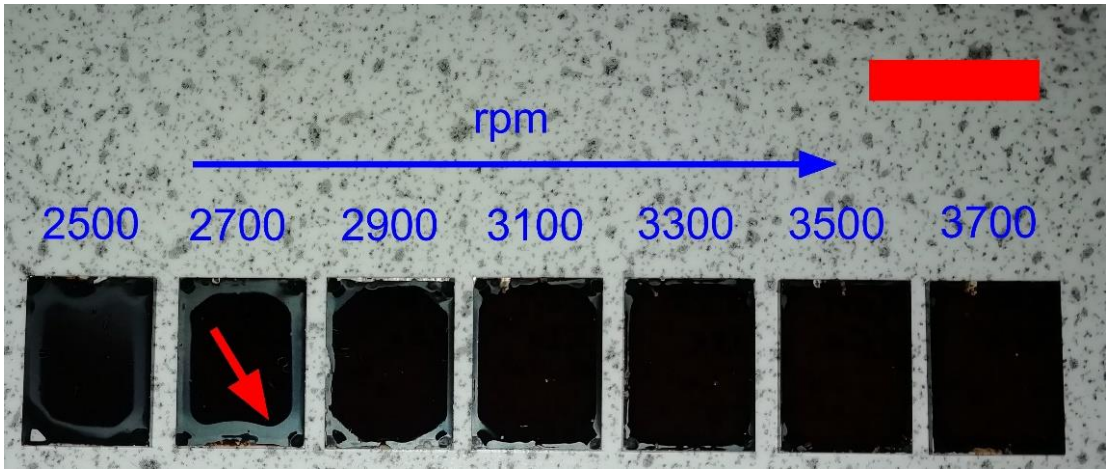

Figure 2.6: Reduced accumulation of $CH_3NH_3PbI_3$ at substrate edges in respect to the spinning speed, scale bar represents 15mm.

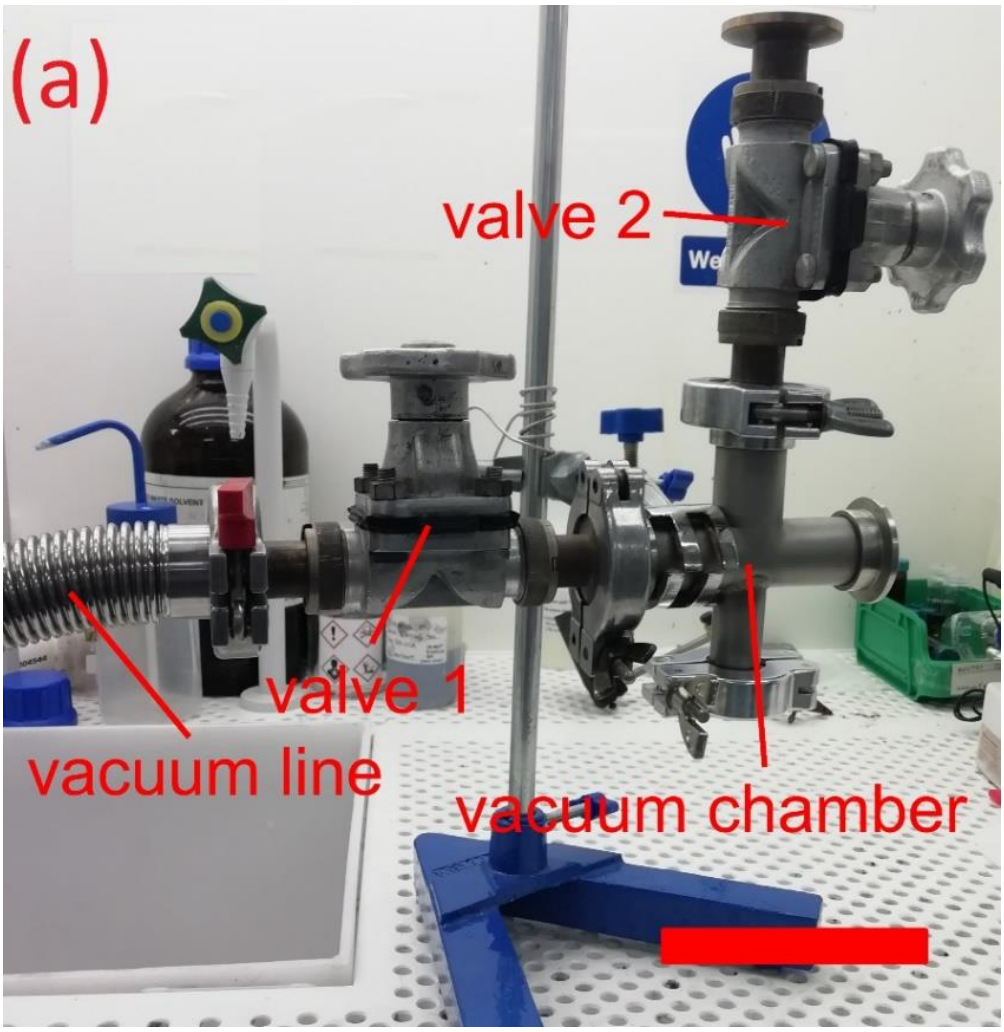

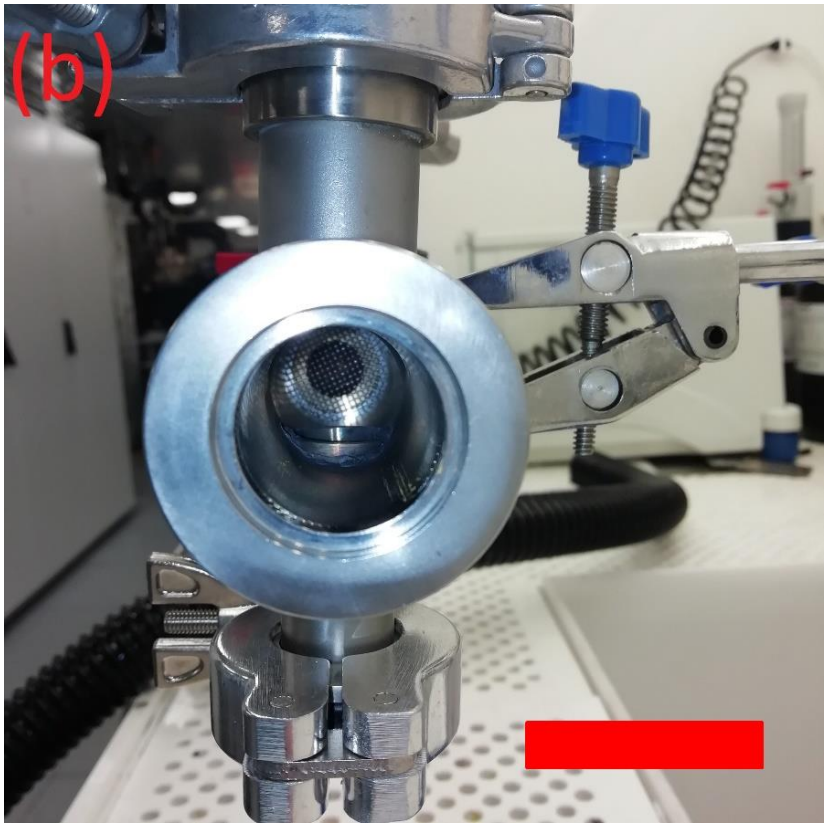

Figure 2.7: The custom-made vacuum chamber consisting of a vacuum line connected to a rotary vane dual stage mechanical vacuum pump (Edwards), valve 1 regulating the pressure and valve 2 resetting the pressure to one bar in the vacuum chamber, respectively (a), scale bar represents 10 cm. Inside view of the vacuum chamber (b), scale bar represents 2 cm.

Figure 2.8: Image of complete un-encapsulated PSCs device with 6-pixel (individual) solar cells, scale bar represents 10 mm.

2.5 Characterization techniques

2.5.1 X-ray diffraction

X-ray diffraction (XRD) is a technique that is used to determine the atomic or molecular crystal structure of materials. The incoming electromagnetic beam of x-ray radiation is primarily scattered by the outer electrons of atoms in the sample producing secondary spherical waves by the elastic scattering effect. Since the atoms in the materials are arranged in planes within a crystal lattice, these spherical waves deconstructively interfere and cancel each other in the majority of directions, but in a few specific directions the spherical waves constructively interfere and are detectable, as shown in figures 2.9 a and 2.9 b. The arrangement of atoms in unit cells in materials define the degree of crystallinity, higher crystallinity results more repeated unit structures, whereas materials with low crystallinity (more amorphous) are characterized by low localized repeatability of the unit structure. In perfect crystals with high order crystallinity, atoms are placed in planes parallel to each other separated by a distance d_{hkl} (identified by the hkl Miller indices which determines their direction and distance in 3 - dimensional space). The resulting constructive interference of spherical waves with the same phase takes place, if the path difference between the rays from consecutive planes, which is $2*d_{hkl}*\sin\theta$, is equal to an integer number of the x-ray wavelengths (λ) and obeys to the Bragg's law, as shown in equation 2.7:

$$n * \lambda = 2d_{hkl} * \sin\theta \qquad \text{equation 2.7}$$

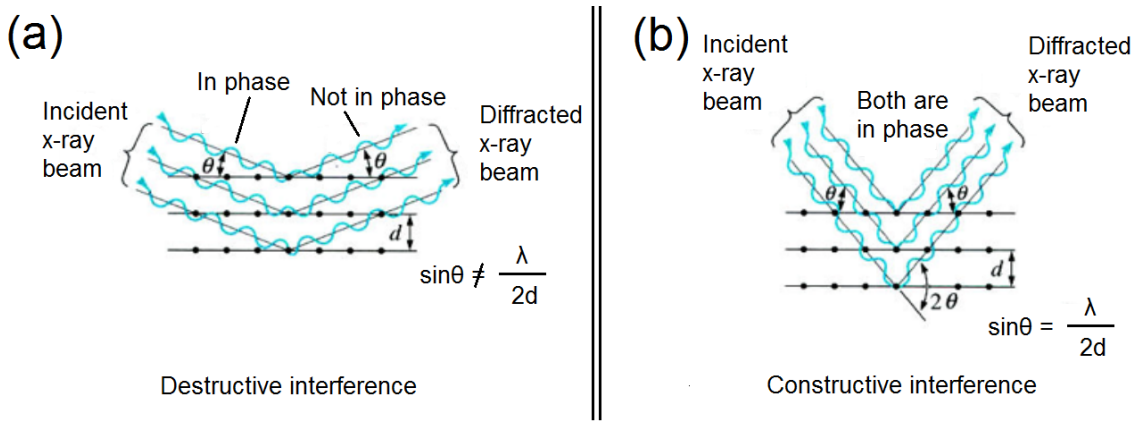

Figure 2.9: Schematic illustration of the XRD characterization in materials. When incident and diffracted x-ray beams are not in phase results (a) destructive interference, whereas if incident and diffracted x-ray beams are in phase results (b) constructive interference.

The measured signal of diffracted x-ray intensity as a function of the scattered angle (2θ) provides information about the atom spacing between planes in the crystal structure and is affected by many factors. The relative intensity of the diffracted peaks is primarily ruled by the structural factor F_{hkl}, in which f_n is the atomic scattering factor and u_n / v_n / w_n the unit cell's dimensions, as defined by the equation 2.8: [9,10]

$$F_{hkl} = \sum_{n=1}^{N} f_n \exp(2\pi i\left(h u_n + k v_n + l w_n\right)) \qquad \text{equation 2.8}$$

However, there are other factors influencing the x-ray diffracted intensity. In certain lattice structures, the spacing and arrangement of planes produces diffractions from groups of planes that are exactly 180º out of phase, resulting in the phenomenon of extinction. Also, when a number of similar planes cut through a unit cell in a particular plane in a repeatable way, then it is called multiplicity. One more factor that affects the diffraction intensity is known as the Lorentz factor, which occurs when a lattice point on the reciprocal lattice intersects the diffractometer that moves on the trajectory of a circle (x-ray detector). Additionally, phenomena of fluorescence and polarization, related with polyphase samples and monochromatic incident x-ray beam, introduces further factors of signal influence. Crystallite size also contributes to the nature of the diffraction peaks, for example in materials with small particle size the number of lattice planes may be insufficient for an effective destructive interference with respect to the scattering angles close to Bragg's angles, which results in deviation and broadening of the characteristic diffracted peaks. Finally, uniform and non-uniform strains (tensile or compressive forces) in the material can alter the crystal structure slightly and generate macrostrain effects, resulting in shifts, asymmetry and broadening of the diffracted peaks, as shown in figure 2.10. [11] For our experiments a D2 Phazer (Bruker) diffractometer was used, with a monochromatic source of x-rays generated by a copper anode (Cu-k(alpha) lines) with wavelength λ = 1.54184 Å, as schematically illustrated in figure 2.11. The samples were mounted in the holder, while the angle between the sample and the incident beam is θ, the detector maintained at an angle of 2θ, in respect to the incident beam of X-ray. Both divergence and receiving slits are kept at fixed positions during the measurement. The x-ray scattering intensity for PbI_2 powders and undoped / doped $CH_3NH_3PbI_3$ micro-crystals were measured as function of the 2θ angle, with a step size 2θ = 0.020273 º over the 2θ range from 9 º to 52 º

and an acquisition time of 0.4 s per step. Also, the x-ray scattering intensity for doped $CH_3NH_3PbI_3$ micro-crystals as function of the 2θ angle, was measured with step size 2θ = 0.020273 º degrees over the 2θ ranges from 11 º to 16 º, 27 º to 30 º and 30 º to 33 º increasing the acquisition time to 0.9 s per step for higher resolution. All measurements of powders, were made using a zero - background holder made of monocrystalline silicon. All XRD data were plotted using Origin Pro v 8.1 software.

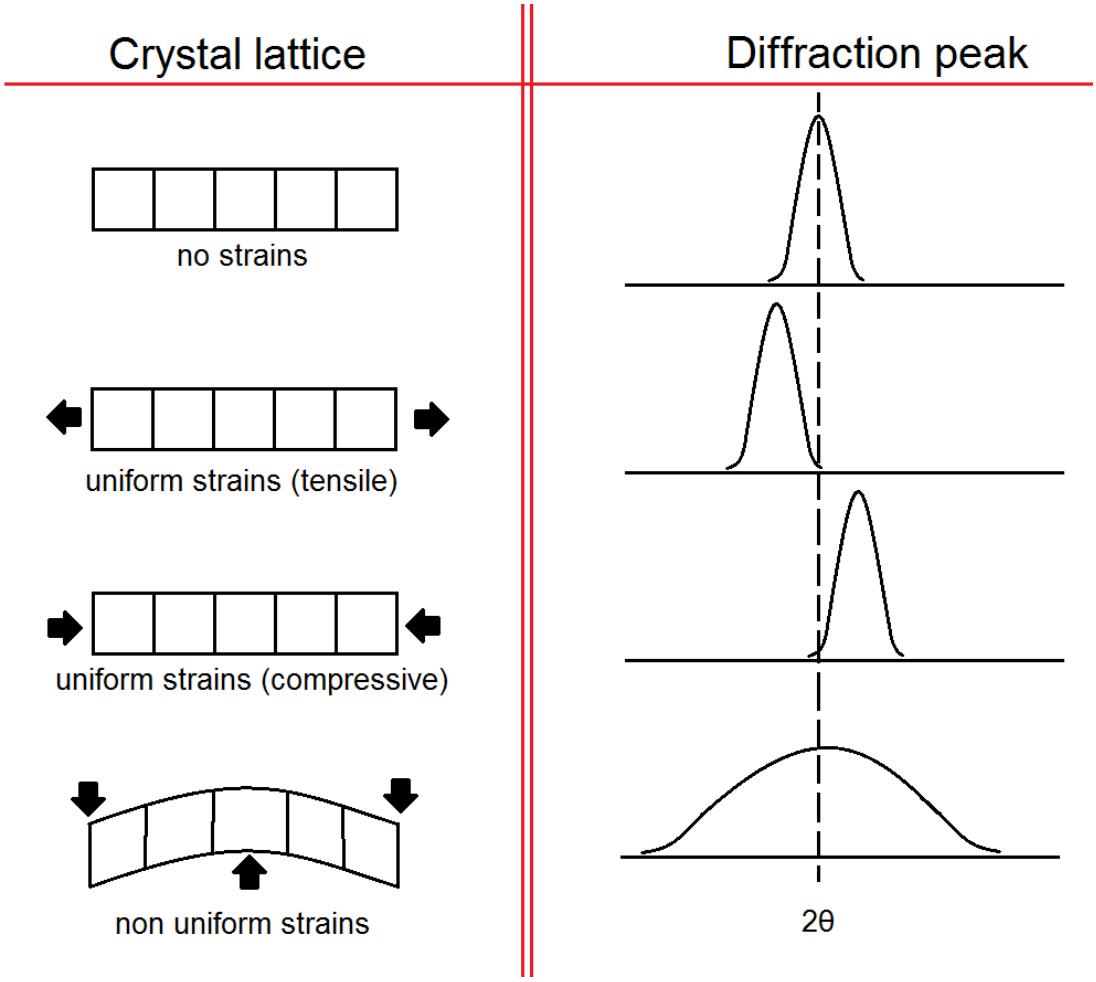

Figure 2.10: Schematic illustration of the applied strains in crystal structure and associated diffracted peak variability.

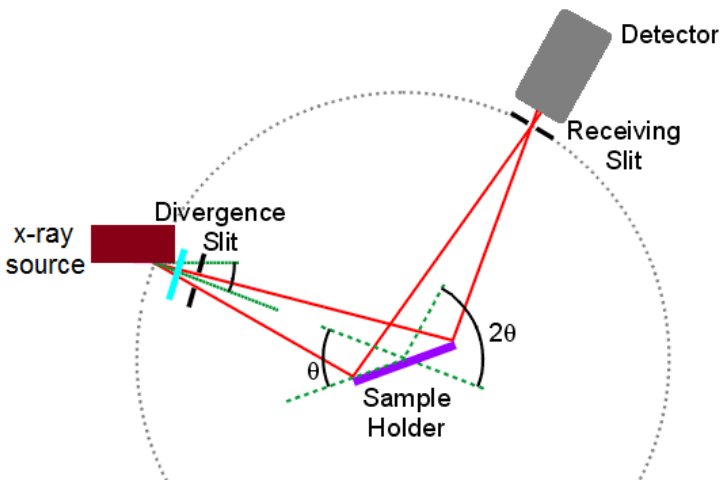

Figure 2.11: Schematic illustration of x-ray diffractometer apparatus. [11]

2.5.2 Scanning electron microscopy

Scanning electron microscopy (SEM) is a characterization technique of samples made of various materials, that includes imaging and elemental analysis of specimens. In a typical SEM, a beam of electrons is accelerated by an applied voltage from a few 100V to ~ 25 kV and then passed through a series of electromagnetic lenses (condenser and objective lenses) before interacting with the sample. Incident electrons interact with the surface of the specimen, resulting in excitation of electrons from the sample. The sample and apparatus are kept under vacuum, in order to eliminate electron interactions with air or chemical molecules. Electrons scattered from the sample, after elastic and inelastic scattering events with the electrons of atoms in specimen are detected while the beam position scans the surface of the sample. The detected signal of electron intensity, is reconstructed by software, forming images with magnification within the range of ~ 10 to 10^6 times, as shown in figure 2.12. The resolution of collected SEM images is affected by many parameters. These include the thickness and electron transparency of the specimen and the accelerating voltage, which causes variability of the electron penetration into the specimen. This provides different mechanisms of interaction between the incident electrons and the atoms/electrons of the specimen, resulting in a range of emitted electrons and radiation categorized as Auger electrons (AE), Secondary electrons (SE), Backscattered electrons (BSE), x-rays (EDX) and Cathodoluminescence (CLE), which all have different escape depths

from the specimen. This can be illustrated by the intercalation volume and expressed as the spatial distribution of electron trajectories inside the specimen, as shown in figure 2.13. [12] The detection of those emitted electrons and radiation, is achieved by a range of detection sensors used in SEM. For example, SE provide topographical information of the samples' surface and are emitted from the first ~100 nm in the sample with energies < 50 eV, based mainly on ionization phenomenon. Those SE can be effectively detected using a through lens detector (TLD) in a high-resolution immersion mode. During the immersion mode, emitted SE pass up through the electron column and can be selectively deflected by an array of electromagnetic coils before being detected by the SE detector mounted above the objective lens in a lateral position with respect to the electron column, as shown in figure 2.14. [13] Some important features of using TLD imaging in SEM, is the low energy required for the accelerated electrons of the beam (< 2 keV) in combination with the minimum working distance (~ 2 - 4 mm) between the lower edge of electron column and specimen. Both these features provide sufficient detection of the low concentration of SE emitted from the specimen in a less destructive way, and resulting in maximum of contrast between features of different elemental composition or optoelectronic properties (such as the work function). [14]

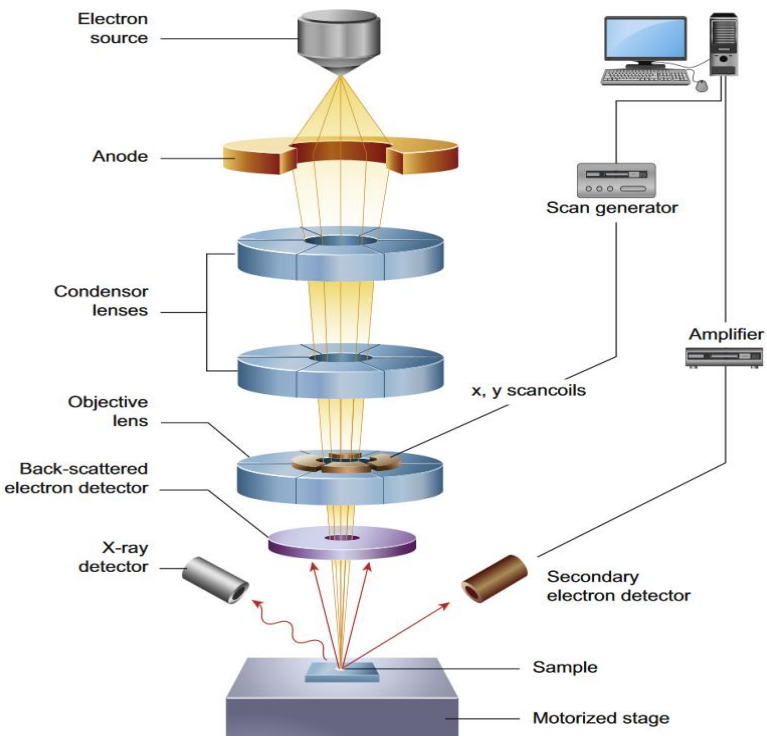

Figure 2.12: Schematic diagram of the main components of a scanning electron microscope (SEM). Electron source, anode, condenser/objective lenses consist the electron column. [12]

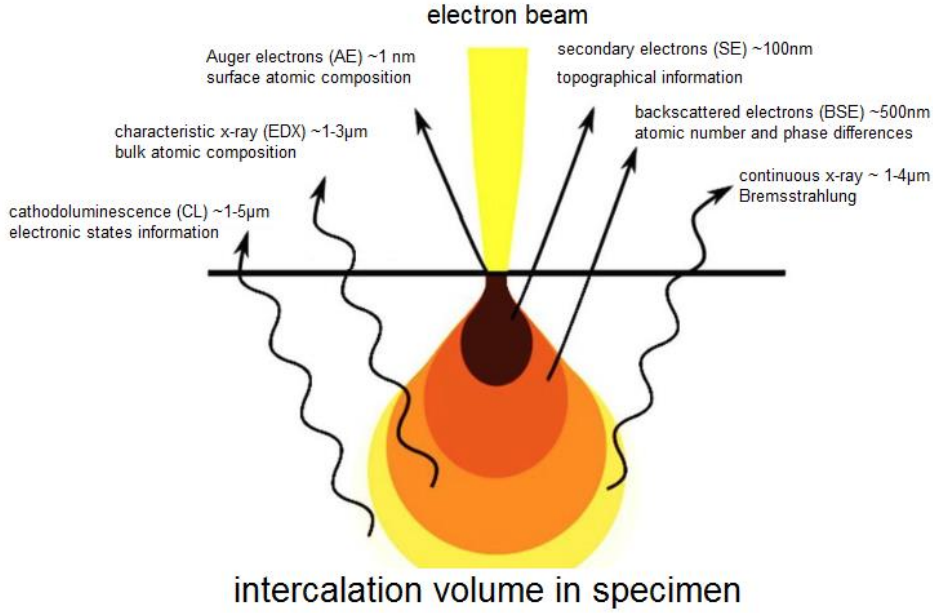

Figure 2.13: Schematic illustration of intercalation volume in SEM and types of emitted electrons. [13]

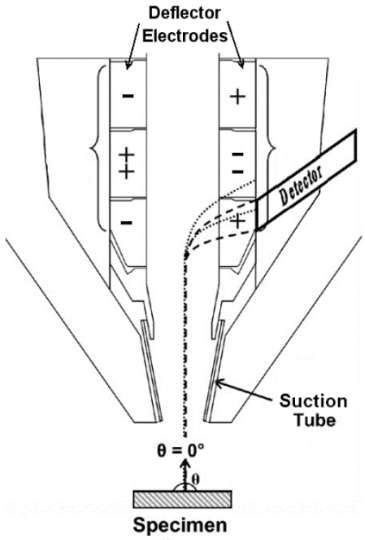

Figure 2.14: Schematic representation of a through lens detector (TLD) inside the electron column of a scanning electron microscope. [13]

Also, SEM is capable for elemental analysis known as energy dispersive x-ray spectroscopy (EDS), which is performed by measuring the energy and intensity distribution of the emitted x-rays generated by the specimen under a focused high accelerated beam of electrons with energy > 10 keV. The incident electrons from the beam, excite an electron from an inner shell creating an electron hole (vacancy). An electron from an outer shell with higher energy occupies that hole in the inner shell

and the difference between the shell energies is emitted as an x-ray. These emitted x-r-ay energies are characteristic of the shell transitions of electrons in each type of atoms, allowing the correct detection of elements in specimens. However, EDS only provides a relative estimation of elemental composition, since multiple transitions of electrons between shells and emission of BSE and CLE introduce interfering effects for the detection of those characteristic x-rays. [13]

For the experiments reported in this thesis, most of the SEM images and EDS (elemental analysis of points or in full images) from PbI_2 powders or perovskite micro – crystals in chapter 3 and 4, were obtained using a JSM-6010LA (JEOL) at accelerating voltages 12 kV and 15 kV and working distance 10 mm, respectively.

Whereas, the single or sequential acquisition of TLD-SEM images were obtained using a FEI Helios NanoLab G3 UC SEM at accelerating voltage 2 kV using a TLD biased from 0 to 30 V with step size 0.2 V at working distance of 4.2 mm and with beam current of 13 pA. Also, a FEI Nova NanoSEM 450 was used at an accelerating voltage 1 kV using a TLD biased from 0 to 30 V with step size 0.2 V at working distance of 2 mm and with beam current of 15 pA. All SE images (single or sequential acquisition) in chapter 3, were obtained either by preparing pellets of PbI_2 with diameter ~ 13 mm under an applied press of 9 tons of mass or by preparing thin films of perovskite on cleaned glass. SE spectra were obtained after alignment of sequential TLD-SEM images and calculated using ImageJ v1.5e software, while all data were plotted using Origin Pro v 8.1 software.

2.5.3 Photocurrent density-voltage

Un-encapsulated perovskite solar cells with device structure glass / ITO / SnO_2 / $CH_3NH_3PbI_3$ / spiro-OMeTAD / Au were placed into the push fit test board with the glass side facing upward (Ossila Ltd). A shadow mask with six square apertures and an area of ~ 0.025 cm^2 per square was placed on top of the glass, the aperture pre-defining the area of the solar cells exposed to irradiation, as shown in figure 2.15. Solar cells were exposed to irradiation that corresponds to AM 1.5 G of the solar spectrum, simulated using a Newport 92251A-1000 solar simulator. Before electrical characterization of solar cell devices, the photon density was calibrated using a NREL

certified silicon reference cell at 100 mW * cm^{-2} at 25 °C. Each cell was biased from -0.2 V to +1.2 V and then back to -0.2 V at a scan step of 0.1 V * s^{-1} measuring the current density employing a Keithley 237 as a source measure unit. The recorded data were plotted using Origin Pro v 8.1 software.

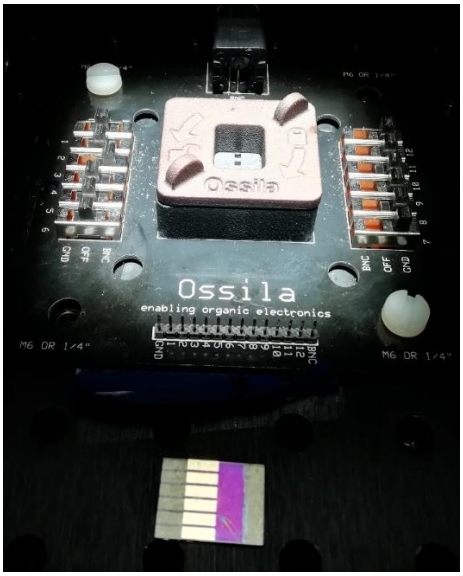

Figure 2.15: Image of push fit test board from Ossila Ltd (on the top), perovskite solar cell device (at the bottom).

2.5.4 X-ray photoelectron spectroscopy

X-ray photoelectron spectroscopy (XPS) is considered one of the most accurate characterization techniques for elemental or chemical composition in materials. The operating principle of XPS is based on the light-matter interaction, known as the photoelectric effect which was discovered by H. Hertz in 1887. By irradiating the specimen with monochromatic low energy photons ~ 1 – 2 keV (x-rays), photoelectrons are emitted originating from either by the atomic core shells or from the valence band. The kinetic energy of the emitted photoelectrons is determined by equation 2.9, in which KE is the measured kinetic energy of the excited electrons, hv the incident energy of x-rays, BE the binding energy of the core shell electron in respect to the Fermi level and Φ_S is the spectrometer work function, as shown in figure 2.16.

$$\mathrm{KE} = \mathrm{hv} - \mathrm{BE} - \Phi_S \qquad \text{equation 2.9}$$

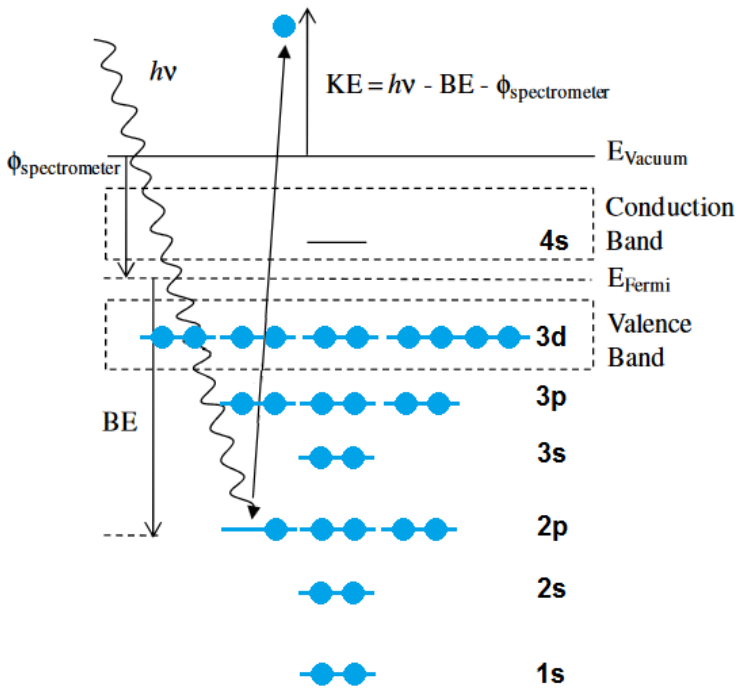

Figure 2.16: Illustration of photoemitted electron from 2p atomic orbital by x-ray photon. [15]

Φ_S is the energy required to promote the electron from the highest occupied electronic level to the unbound state with zero kinetic energy (vacuum level). Also, during XPS characterization of specimens, the photo-ionized atom returns to a more stable energy state, either by filling the hole of the photoelectron emitted with an electron from a higher core shell level accompanied by emission of characteristic to the transition x-ray, or by emitting an Auger electron. An Auger electron is ejected, when the core hole is filled with an electron from a higher core shell without the emission of characteristic to the transition x-ray. In a typical XPS spectra, binding energy versus electron intensity is plotted, independent of the incident x-ray energy used during the measurement. The resulting peak positions correspond to specific elements as a function of the binding energy and their intensity reflects the atomic concentration. The intensity of each peak is given approximately by the Beer – Lambert law (as shown in equation 2.10) and expresses the probability of the photoemitted electron to reach the surface of specimen and be detected.

$$I_d = I_0 \, e^{\left(\frac{-d}{\lambda * \cos \Theta}\right)} \qquad \text{equation 2.10}$$

Where I_d is the photoemitted electron density in respect to escape depth d from specimen, I_0 is the incident intensity of electrons, λ is the electron inelastic mean free path (IMFP) and θ is the angle of the photoemitted electron with respect to the specimen surface. The IMFP statistically is the average distance that a photoemitted electron can travel inside the material before any inelastic scattering event occurs and depends on the specimen density and the KE of the electron. In XPS, high energy resolution of the characteristic peak of elements is required. The resulting spectra collected contain a series of peaks that are defined by the full width at half maximum (FWHM), which is a convolution of the x-ray characteristic line width, the width of the photoemitted electron lines, surface charging and the analyser / detector resolution. Typically, in XPS the x-ray sources used are based on either monochromator (aluminium) or dual (aluminium and magnesium) anode-targets. Anode-targets are made of aluminium, which have a $k(alpha)_{1,2}$ transition with energy of 1486.6 eV and FWHM of 0.85 eV, while magnesium targets have a $k(alpha)_{1,2}$ transition with energy of 1253.6 eV and FWHM of 0.7 eV. The different FWHM in terms of energies of both anodes provide different energy resolution in the resulting XPS spectra, since the x-ray monochromator allows reduction of the unwanted x-ray satellites and Auger electrons. Photoemitted electrons are passing through the concentric hemispherical energy analyser before being retarded by biased apertures and their kinetic energy being measured by the detector, as graphically illustrated in figure 2.17.

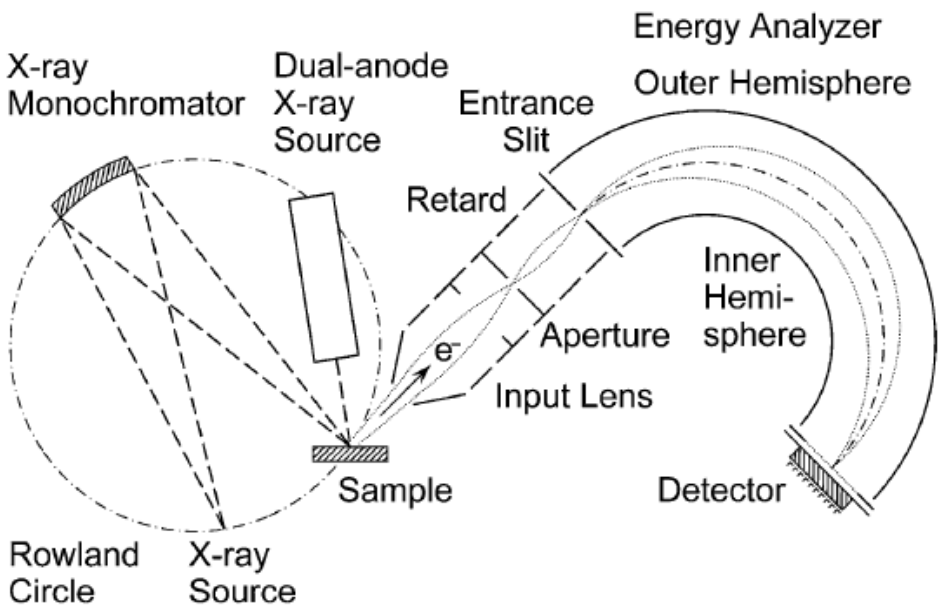

Figure 2.17: A graphical illustration of an XPS spectrometer equipped with monochromator or dual anode x-ray source, retardation aperture, concentric hemispherical energy analyzer and detector. [16]

XPS instruments require regular calibration to secure accurate measurement of the binding energy of elements. Calibration is achieved by measuring specific samples which are made of gold. The recorded XPS spectra are divided into two groups: the main low energy resolution survey spectra and the high energy resolution spectra for the accurate quantitative analysis of the elements of interest. Additionally, quantitative analysis of elements in XPS spectra requires the introduction of the Schofield relative sensitivity factors (RSF) and characteristic transmission functions for the analyser as provided by the National Physical Laboratory (NPL) for normalization of the photoemitted electron intensities of all the elements present in specimen. [15,16] For the experiments reported here, mechanochemical or solvothermal or commercial PbI_2 powder was mounted for analysis by pushing the powder into indium foil. The indium foil was then placed directly onto the sample holder using double sided conducting carbon tape. The analysis was carried out using a Kratos Supra instrument with a monochromatic aluminium source of x-rays with energy of 1486.69 eV. Low energy resolution survey scans were collected between binding energies from 1200 to 0 eV, at 1 eV intervals with an acquisition time of 10 min (per point) from two analysis points per sample. While high energy resolution scans were also collected for the I 3d, O 1s, C 1s and Pb 4f core levels, at 0.1 eV intervals with an acquisition time of 5 min, for each point. The data collected were calibrated in intensity using a transmission function characteristic of the instrument to make the values instrument independent. All data were then quantified using the CasaXPS software. Binding energy calibration of all the low energy resolution survey scans or high energy resolution scans was conducted with respect to the Pb $4f_{7/2}$ core level at 138.0 eV. No escape depth correction was applied at each low energy resolution survey or high energy resolution scans, before starting any further quantification analysis.[17] For the compositional analysis of the core level spectra of I $3d_{5/2}$, O 1s, C 1s and Pb $4f_{7/2}$, the Scofield relative sensitivity factors of 16, 2.52, 1 and 13.7 were used, respectively. The binding energy regions used for analysis, were kept constant with respect to each element at each low energy resolution survey or high energy resolution scans. Also, for each binding energy region, a Shirley type background function was used. The resulting data were plotted using Origin Pro v 8.1 software.

2.5.5 Rutherford backscattering spectroscopy

Rutherford backscattering spectroscopy (RBS) is considered one of the most accurate characterization techniques for elemental analysis in depth or near the surface of materials. Initially, in 1911 Ernest Rutherford first experimentally determined the existence of atomic nuclei by measuring the backscattered alpha particles from gold foil. Since then, tremendous development has been made in apparatus and data analysis related to RBS. In principle, the specimen (target) is installed and bombarded at specific angles (5 º – 15 º) with respect to the beam of highly accelerated particles of helium ions ($^{4}He^{+}$) within the energy range from 0.5 to 3 MeV. The energy loss of the backscattered particles caused by the interaction with the nuclei within the target, which depends on the atomic number Z of each element in the target, is recorded by a solid-state detector at scattering angles (θ) from 150º to 170º, resulting in the quantitative determination of elemental composition in materials, as graphically illustrated in figure 2.18. Some of the advantages of RBS technique are the absence of the need for a reference sample, in depth resolution of elemental composition of the order of 0.2 – 20 µm and the high detection resolution of heavy elements. Whereas, a significant disadvantage of RBS is the low detection resolution of light elements (in comparison with the heavier elements). Since the only mechanism of energy loss during the RBS measurement is the momentum transfer from incident particles to the target's nuclei, the energy ratio of incident particles before and after interaction with specimen is known as the kinematic factor (K) and given by the equation 2.11. In which, M_1 is the mass of incident particles, M_2 the mass of nuclei in the specimen and θ the scattering angle.

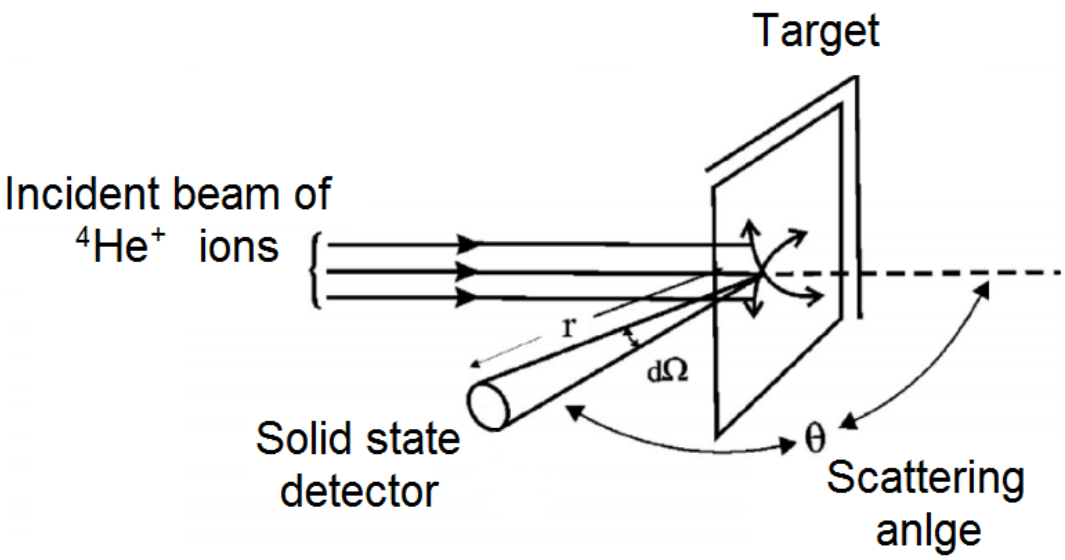

Figure 2.18: Graphically illustration of Rutherford backscattering spectroscopy characterization technique. [18]

$$\mathrm{K}(\theta, M_1, M_2) = \frac{E_1}{E_0} = \left(\frac{\left(M_2^2 - M_1^2 \sin^2\theta\right)^{1/2} + M_1 \cos\theta}{M_1 + M_2} \right)^2 \qquad \text{equation 2.11}$$

As the mass of atoms in the target increases, the energy of the backscattered particles progressively approaches the energy of the incident particles. Also, during analysis of specimens with RBS as a characterization technique, some important parameters must be considered. The first important parameter is related to the energy limit of the incident particles that interact with the specimen. If highly accelerated incident particles interact with the nuclei of atoms surpassing the Coulomb barrier, the resulting nuclear reactions with the target can create radioactive isotopes. An empirical formula that provides the maximum energy of the incident particles as given by the equation 2.12, is regarded for elimination of those undesirable nuclear reactions. Where E_0 is the kinetic energy of the incident particles in MeV, Z_1 / M_1 and Z_2 / M_2 are the atomic numbers and nuclei masses of incident particles and of the atoms in specimen (average values of the Z_2 / M_2 are considered for multi-elemental specimens), respectively.

$$E_0 < \frac{Z_1 Z_2}{M_1^{1/3} + M_2^{1/3}} \qquad \text{equation 2.12}$$

The second parameter that must be considered, the cross section, is related to reduced probability of scattering events in the detector direction. Generally, scattered particles with trajectories out of detector position, are following directions at an angle of either forward (Φ < - 90 º) or backward (Φ < + 90 º), as shown in figure 2.19. By definition the cross section of scattered incident particles has got multiple impacts during the RBS characterization of specimens. Mainly affecting the number of backscattered particles from the target's nuclei, the position of the solid-state detector for maximum backscattered particles detection and the kinetic energy of the incident particles. [18,19] For our experiments a 1.7 MV Tandetron RBS linear type tandem ion-beam accelerator was used, which is located in the Laboratory of Ion Beam Physics at the ETH Zurich facilities in Switzerland. Commercial and synthesized PbI_2 pellets, with diameter ~ 13 mm and thickness ~ 1.5 mm, were prepared under an applied press of 9 tons of mass and measured using accelerated ions of $^4He^+$ at 2 MeV, while a PIN diode detector was placed at angle 168 º with respect to the ions of incident beam. The resulting data were plotted using the RUMP simulation software.

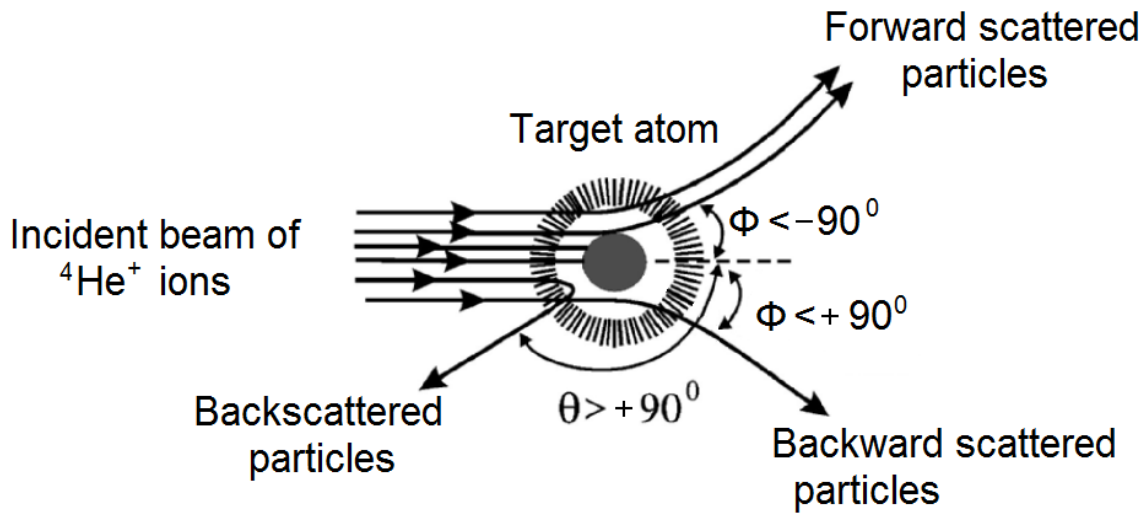

Figure 2.19: Schematic diagram of trajectories with corresponding angles for forward (Φ < - 90 º) and backward (Φ < + 90º) scattered particles. [18]

2.5.6 Atomic force microscopy

Atomic force microscopy (AFM) is a non-destructive characterization technique for high resolution topographical imaging of various materials (solid – organic – liquid - biological samples etc.). In principle, AFM surface imaging is based on the weak interactions between a tip and the surface of specimen, as invented by Gerd Binning et al. in 1986. Typically, an AFM consisted of a laser diode for spot positioning, a cone-shaped small tip (probe) made of silicon or silicon nitride positioned on the free end of a cantilever, a piezoelectric module for positioning and height movements of the cantilever allowing scanning of the tip over the specimen in three directions (X – Y – Z) and a four-quadrant positioning photodiode, as shown in figure 2.20.

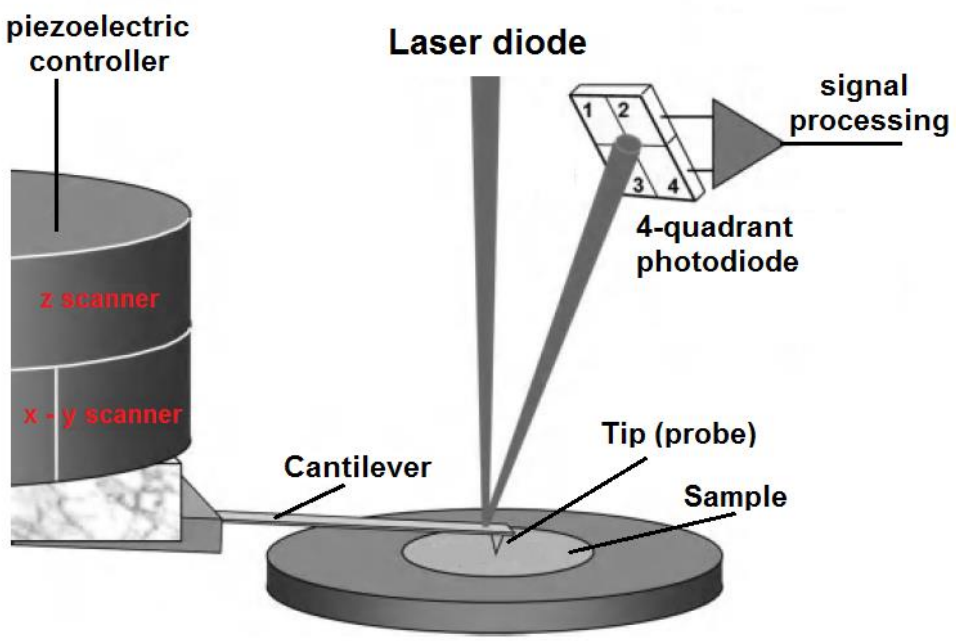

Figure 2.20: Schematic diagram of atomic force microscope (AFM) components. [20]

When the probe approaches and scans the surface of specimen in X – Y directions, repulsive and attractive interactions based on Coulomb and Van der Waals forces respectively, causes vertical bending of the cantilever with respect to the surface of specimen, as shown in figure 2.21. Different modes of materials characterization in AFM (contact / tapping / no contact) utilise different regions within this plot of probe sample interactions.

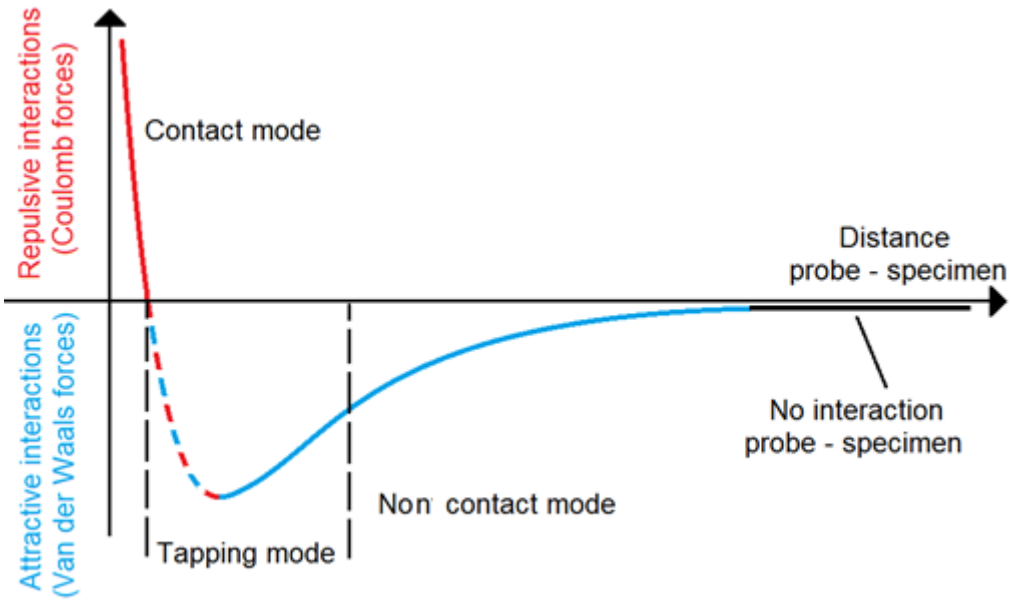

Figure 2.21: Schematic illustration of the relationship between forces (attractive and repulsive attractions) and probe distance.

These vertical diversions of the cantilever result a weak displacement in the laser beam spot being detectable by the four-quadrant positioning photodiode. The signal (voltage) fluctuation generated by the photodiode during the scanning process of the specimen is processed and reconstructed as a topographical image by specific software. The geometry and materials used for the construction of the cantilever and probe, combined with the scanning velocity, affect the resolution of acquired topographical images. The characteristic spring constant that relates to the material and geometry of cantilever. The candilever obeys to the Hooke's law, as given in equation 2.13. Where F is the resulting force, k the cantilever constant and y the vertical diversion of cantilever. [20]

$$F = -k * y \qquad \text{equation 2.13}$$

For our experiments, roughness and thickness measurements of perovskite thin films were performed using a Dimension icon with ScanAsyst AFM (Bruker) with a cantilever consisting of a silicon probe on a silicon nitride cantilever (Bruker) with characteristic properties (f = 70 kHz, k = 0.4 N * m^{-1}). AFM data analysis was conducted by using Nanoscope Analysis v 1.3 software.

2.5.7 Visible-infrared (Vis-IR) spectroscopy

Visible-infrared (Vis-IR) spectroscopy is a non-destructive characterization technique, based on light - matter interactions. Generally, there are different mechanisms of light absorption in semiconductors, such as inter-band, dopant, excitonic, by charge carriers and crystal lattice. However, the intra-band light absorption is considered as the fundamental mechanism, resulting in the determination of the optical band gap in semiconductors. The minimum energy of a photon (quantum) that is sufficient to excite an electron from the highest level of the valence energy state (valence band) to the lowest level of the conduction energy state (conduction band), is equal to the band gap (E_g) in semiconductors. Also, semiconductors with indirect E_g require increased number of absorbed photons, due to the need for the presence of a crystal lattice oscillation (phonon) during the absorption of a photon, in comparison with a semiconductor with direct E_g. The minimum absorbed energy required by the semiconductor is related to the wavelength by the Planck equation, as shown in equation 2.14. In which, h is Planck's constant, c the speed of light in vacuum and λ is the wavelength of photons that correspond to the absorption edge of semiconductor.

$$\mathrm{E_g} = \frac{\mathrm{h*c}}{\lambda} \qquad \text{equation 2.14}$$

Also, the distribution of allowed electron transitions in semiconductors with either direct or indirect band gap, are described by the absorption coefficient (a), as shown in equations 2.15 and 2.16, respectively. In which, $E_{photons}$ is the energy of incident photons and A and B are constants not related to the light absorption.

$$\mathrm{a_{direct}} = \mathrm{A}\frac{\left(E_{photons} - \mathrm{E_g}\right)^{1/2}}{E_{photons}} \qquad \text{equation 2.15}$$

$$\mathrm{a_{indirect}} = \mathrm{B}\frac{\left(E_{photons} - \mathrm{E_g}\right)^{2}}{E_{photons}} \qquad \text{equation 2.16}$$

The dependence between absorption coefficient and wavelengths can be used to accurately determination of the E_g from a graphical fitting process using a Tauc plot. In addition, the absorption coefficient (a) in semiconductors with either direct or indirect

band gap is determined by the Urbach energy (E_U), which is related to the degree of structural disorder (defects), as given in equation 2.17. In which a_0 is a constant.

$$a_{(\text{direct or indirect})} = a_0 * \exp\left(\frac{h*c - E_g}{E_U}\right) \qquad \text{equation 2.17}$$

For our experiments, absorption spectra of perovskite thin films deposited on clean glass, were obtained using a spectrometer (USB2000 + UV – VIS – ES) equipped with a deuterium halogen light source (UV – VIS - NIR_DT – MINI – 2 - GS), both from Ocean optics. Data were collected using the Ocean Optics SpectraSuite software and the recorded data were plotted using Origin Pro v 8.1 software. [21]

2.6 References

1 L. Fan, Y. Ding, J. Luo, B. Shi, X. Yao, C. Wei, D. Zhang, G. Wang, Y. Sheng, Y. Chen and A. Hagfeldt, *J. Mater. Chem. A Mater. energy Sustain.*, 2017, **5**, 7423–7432.

2 K. G. Stamplecoskie, S. Manser and P. V Kamat, *Energy Environ. Sci.*, 2015, **8**, 208–215.

3 J. H. Noh, S. H. Im, J. H. Heo, T. N. Mandal and S. Il Seok, *Nano Lett.*, 2013, **13 (4)**, 1764–1769.

4 G. E. Eperon, S. D. Stranks, C. Menelaou, M. B. Johnston, L. M. Herz and H. J. Snaith, *Energy Environ. Sci.*, 2014, **7**, 982–988.

5 M. Acik, T. M. Alam, F. Guo, Y. Ren, B. Lee, R. A. Rosenberg, J. F. Mitchell, I. K. Park, G. Lee and S. B. Darling, *Adv. Energy Mater.*, 2018, **8**, 1701726.

6 Q. Jiang, L. Zhang, H. Wang, X. Yang, J. Meng, H. Liu, Z. Yin, J. Wu, X. Zhang and J. You, *Nat. Energy*, 2016, **2**, 16177.

7 R. Scho, M. H. Karlsson, S. K. Eriksson, H. Siegbahn, E. M. J. Johansson and H. Rensmo, *J. Phys. Chem. C*, 2012, **116 (50)**, 26300–26305.

8 M. Saliba, J. P. Correa-Baena, C. M. Wolff, M. Stolterfoht, N. Phung, S. Albrecht, D. Neher and A. Abate, *Chem. Mater.*, 2018, **30**, 4193–4201.

9 J. M. Cowley, *Electron Diffraction Techniques Vol 1*, Oxford Science, ISBN 9780198555582, 1992.

10 T. Egami and S. Billinge, *Underneath the Bragg Peaks, Vol. 16*, Pergamon, ISBN 9780080971414, 2012.

11 M. Birkholz, *Thin Film Analysis by X-Ray Scattering*, Wiley-VCH, ISBN 3-527-31052-5, 2006.

12 B. J. Inkson, *Scanning electron microscopy (SEM) and transmission electron microscopy (TEM) for materials characterization*, Woodhead Publishing, ISBN: 9780081000571, 2016.

13 J. I. Goldstein, D. E. Newbury, J. R. Michael, N. W. M. Ritchie, J. H. J. Scott and D. C. Joy, *Scanning Electron Microscopy and X-Ray Microanalysis*, Springer-Verlag New York, ISBN: 978-1-4939-6676-9, Fourth Edi., 2018.

14 Y. Zhou, D. S. Fox, P. Maguire, R. O. Connell, R. Masters, C. Rodenburg, H. Wu, M. Dapor, Y. Chen and H. Zhang, *Sci. Rep.*, 2016, **6 (1)**, 21045.

15 P. van der Heide, *X-ray Photoelectron Spectroscopy An introduction to Principles and Practices*, Wiley, ISBN: 978-1118062531, 1st Editio., 2011.

16 D. Schild, *X-ray Photoelectron Spectroscopy*, Springer, ISBN:978-3-540-69925-5, 2008.

17 C. J. Powell and A. Jablonski, *Surf. Interface Anal.*, 2002, **33**, 211–229.

18 H. R. Verma, *Atomic and Nuclear Analytical Methods*, Springer-Verlag Berlin Heidelberg, ISBN: 978-3-540-30279-7, 1st Editio., 2007.

19 L. Palmetshofer, *Surface and Thin Film Analysis: A Compendium of Principles, Instrumentation, and Applications*, Wiley, ISBN: 9783527636921, 2nd Editio., 2011.

20 G. Haugstad, *Atomic force microscopy*, Wiley, ISBN: 978-1-118-36066-8, 2012.

21 M. Dresselhaus, G. Cronin and A. Gomes Souza Filho, *Solid State Properties*, Springer-Verlag Berlin Heidelberg, ISBN: 978-3-662-55922-2, 2018.

Chapter 3

Implications of stoichiometry and polytypism in PbI_2 used to fabricate perovskite ($CH_3NH_3PbI_3$)

3.1 Introduction

The improvement in photovoltaic performance of perovskite solar cells (PSCs) as the next potential candidate of a low-cost conversion technology of solar power to electricity has been tremendous. Devices based on one of the most studied hybrid organic / inorganic perovskites, known as methylammonium lead triiodide ($CH_3NH_3PbI_3$), have seen their power conversion efficiencies (PCE) rocket from 3.8 % to 21.2 % in a decade.[1,2] Mixtures of organic and inorganic cations, predominantly methylammonium, formamidinium and caesium (MA^+ / FA^+ / Cs^+) with various halogen anions, such as chloride, bromide and iodide (Cl^- / Br^- / I^-) have been incorporated to improve the stability in PSCs. However, long term stability and durability in PSCs have remained barriers to their commercialisation. These effects might be related to deficiency of the iodide in the crystal structure of perovskite as presented by Jacobsson *et al.*, Graetzel *et al.* and an optimum tolerance factor closer to unity that corresponds to the cubic crystal structure as presented by Saliba *et al.*.[3–7] This degradation occurs regardless of the device architecture configuration utilised (p-i-n or n-i-p).[8] In this chapter is described in detail the importance of stoichiometry and polytypism present in PbI_2 used for fabrication of PSCs based on $CH_3NH_3PbI_3$, two properties that might be related to the mechanism of degradation and poor stability in PSCs. Determination of the polytypes present and the stoichiometry of PbI_2 powders synthesised by solvothermal and mechanochemical routes have been compared to commercially available PbI_2 powders. This was accomplished using X-ray diffraction (XRD), X-ray photoelectron spectroscopy (XPS), Rutherford backscattering

spectroscopy (RBS) and controlled synthesis of $CH_3NH_3PbI_3$ micro-crystals. Also, we show that the use of commercial sub-stoichiometric PbI_2 for the formation of $CH_3NH_3PbI_3$ might results in unreacted PbI_2 as determined by Vis-IR spectroscopy and the presence of the impurity is reflected in terms of PCE in the fabricated PSCs. The presence of unreacted PbI_2 (~ 10 %) causes an average PCE reduction of the PSCs from ~ 15.5 % to ~ 4.6 %.

3.2 Results and discussion

3.2.1 EDS analysis of PbI_2 powders

PbI_2 powders synthesized by solvothermal (ST) and mechanochemical (MC) routes were characterized by scanning electron microscopy (SEM) and integrated energy dispersive spectroscopy (EDS). ST synthesis of PbI_2 resulted in the formation of needle shaped crystals on top of hexagonal PbI_2 platelets, as shown in figure 3.1 a. The incorporation of oxygen was detected in these needles as indicated by EDS analysis from 3 points, is possibly attributed to autoionization of water molecules caused by strong Coulomb interactions between the ions (Pb^{2+} and I^-) and water molecules. This results in the formation of a mixture of lead oxyiodide and lead iodide hydroxide compounds, with the general chemical formulae $Pb(I_{1-x}O_x)_2$ and $Pb(I_{1-y}(OH)_y)_2$, respectively.[9–11] Whilst an absence of oxygen was detected from a single point on top of the PbI_2 platelet, as shown in table 3.1. In order to avoid the incorporation of oxygen from water, MC synthesis of PbI_2 was selected. This free of water process may reduce the concentration of the needle shaped crystals formed. MC synthesis of PbI_2 powder exhibited characteristic fragmentation and deformation of the PbI_2 platelets with an average size smaller than 4 µm, as shown in figure 3.1 b. While, no oxygen was detected in the MC PbI_2 platelets, as indicated by EDS analysis and shown in table 3.1. Also, for the commercially available powders from Sigma Aldrich (SA) and Tokyo Chemical Industries (TCI), the PbI_2 platelets had an average size smaller than 25 µm and 20µm, as shown in figures 3.1 c and 3.1 d, respectively.

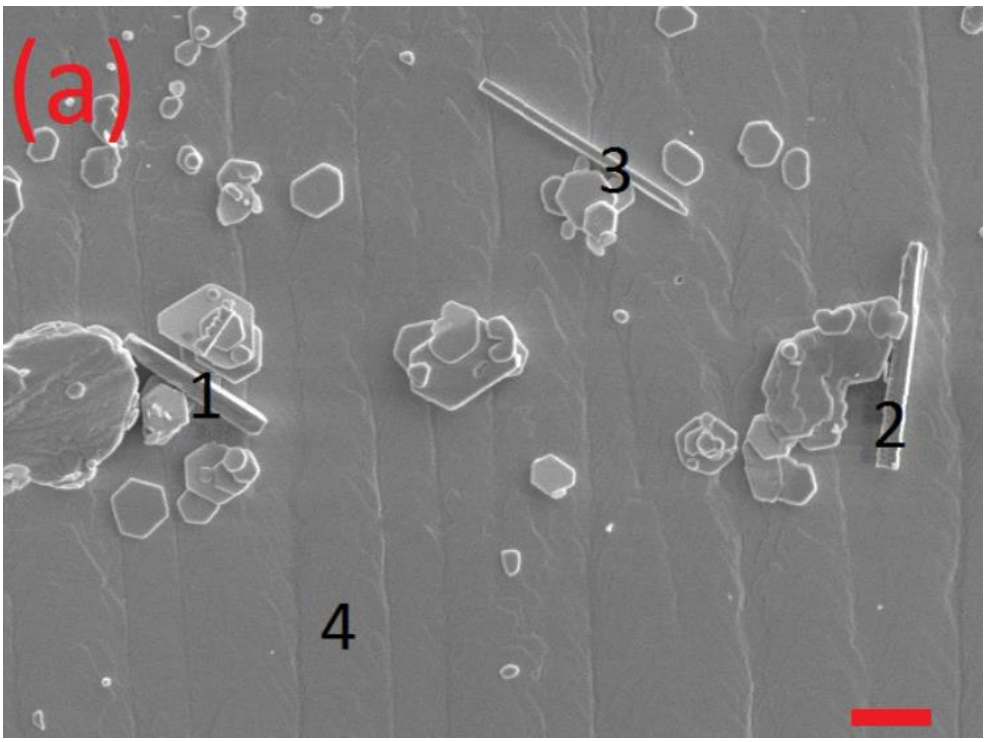
(a)
3
1
2
4

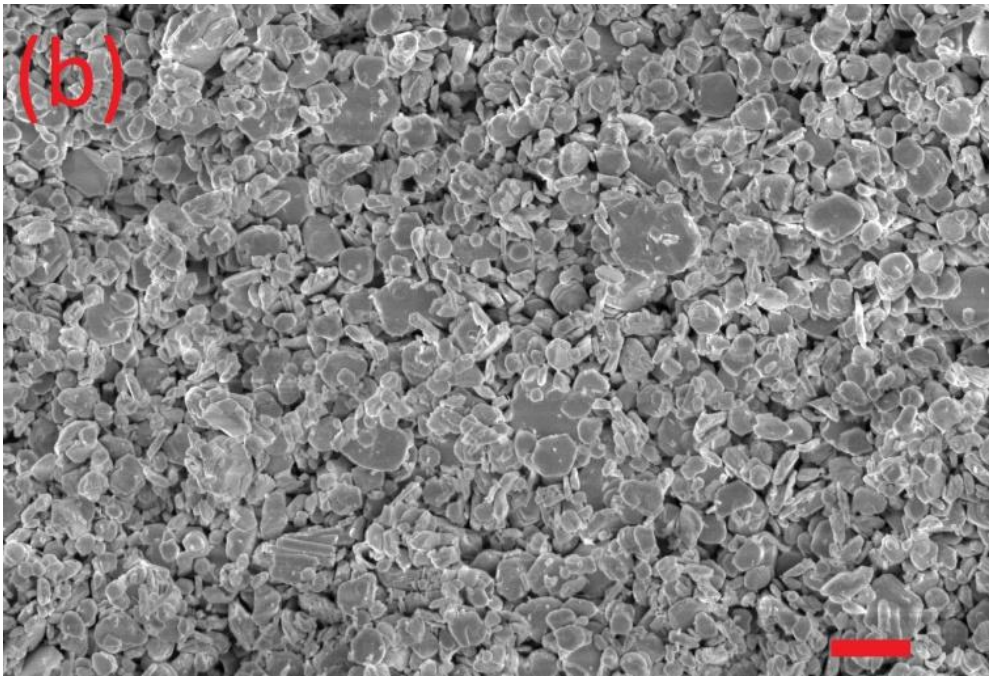
(b)

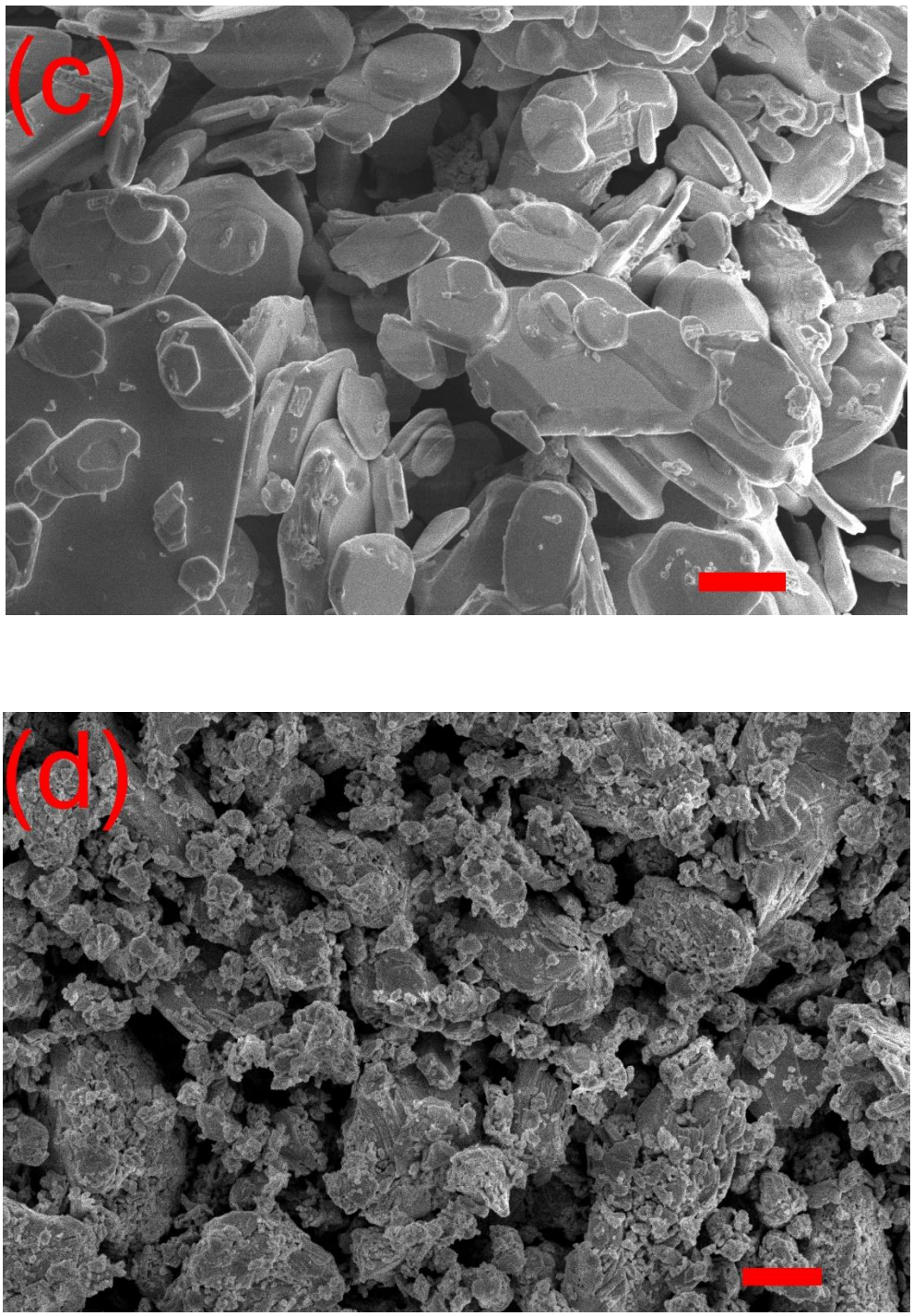

Figure 3.1: Scanning electron microscopy (SEM) images of lead iodide powders as synthesised by (a) solvothermal (ST) and (b) mechanochemical (MC) routes, or commercially available from (c) Sigma Aldrich (SA) and (d) Tokyo Chemical Industries (TCI), scale bars represent 10μm.

	Solvothermal (ST)				Mechanochemical (MC)	
Points	1	2	3	4	All image	
Carbon	12.37%	15.68%	11.15%	12.61%	15.80%	12.26%
Oxygen	8.93%	7.42%	14.52%	None detected	None detected	None detected
Iodide	38.68%	41.32%	36.00%	56.87%	56.26%	58.26%
Lead	40.02%	35.58%	38.07%	30.52%	27.94%	29.48%

Table 3.1: Scanning electron microscopy-energy dispersive spectroscopy (SEM-EDS) atomic percentage composition of lead iodide, synthesised by solvothermal (ST) or mechanochemical (MC) methods.

3.2.2 X-ray diffraction analysis of PbI_2 powders

Different PbI_2 powders, one synthesised by the ST method and several by the MC method at various speeds of rotation and duration times during the planetary ball milling process (MC1: 200 rpm / 2 hours, MC2: 400 rpm / 1 hour and MC3: 400 rpm / 4 hours) were characterised by XRD and compared with two commercially available PbI_2 powders of high purity, one from Sigma Aldrich with purity 99.999% (SA) and the second one from Tokyo Chemical Industries with purity 99.99% (TCI). Significant differences in the XRD patterns were observed between the commercial SA, TCI, ST and mechanochemical MC1 / MC2 / MC3 PbI_2 powders, as shown in figure 3.2. Also, for better clarity, the detected XRD peaks were categorized into two groups of peaks based on the diffracted 2θ angle and the Miller indices of the corresponding crystallographic planes. Peaks with Miller indices of planes (001), (002) and (003), form the primary group (indicated by the red colour in figure 3.2), while the (100), (101), (102), (110), (111), (103) and (201), form the secondary group (indicated by the green colour in figure 3.2) and summarized in table 3.2. Based on the International Centre for Diffraction Database, the primary XRD peaks correspond to the 2H polytypic phase of the PbI_2 with code (01-071-6147), while the secondary XRD peaks, correspond mainly to a mixture of 4H (04-017-4470), 14H (04-007-2277) and 20H (04-007-2278) polytypic phases, with characteristic c axis unit cell dimensions 1.3962 nm, 4.8853 nm and 6.979 nm, respectively. However, the possibility of undetected minor fractions of PbI_2 crystallised in a rhombohedral structure cannot be excluded.

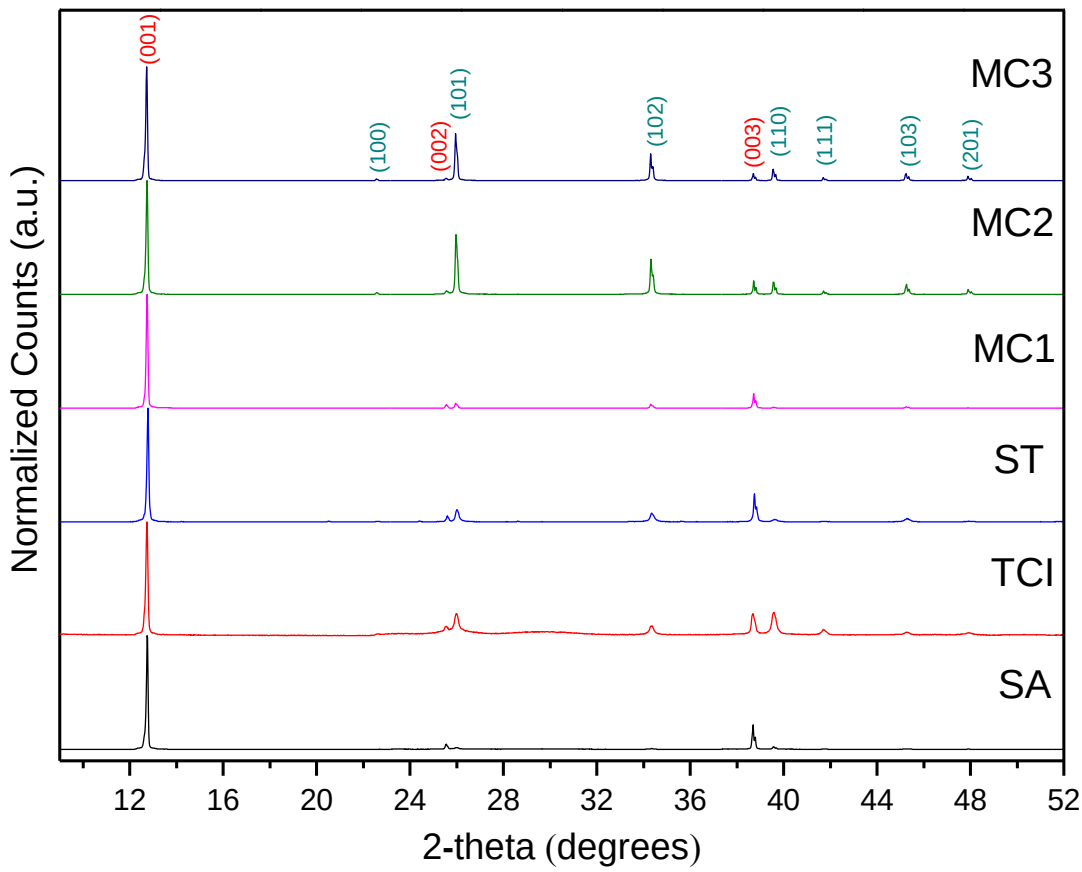

Figure 3.2: XRD patterns of commercial Sigma Aldrich (SA), Tokyo Chemical Industry (TCI), solvothermal (ST) and mechanochemical at different conditions (MC1 to 3) PbI_2 powders. Normalization of XRD patterns, was in respect to (001) peak in all spectra. Peaks with the red in colour Miller indices indicating the crystallographic planes (001), (002) and (003) correspond to 2H polytypic phase, whereas Peaks with the green in colour Miller indices indicating the crystallographic planes (100), (101), (102), (110), (111), (103) and (201) correspond to mixture of 2H – 4H – 14H and 20H polytypic phases.

Peak group	Miller indices	2-theta (degrees)
Primary	(001)	12.74
Secondary	(100)	22.60
Primary	(002)	25.56
Secondary	(101)	25.98
Secondary	(102)	34.32
Primary	(003)	38.70
Secondary	(110)	39.58
Secondary	(111)	41.70
Secondary	(103)	45.27
Secondary	(201)	47.92

Table 3.2: Peak group, Miller indices and XRD diffracted angle (2-theta) of the lead iodide.

Based on the collected XRD spectra, the mechanochemical MC1 PbI_2 powder, did not display strong diffraction at the corresponding secondary XRD peak positions, indicating that MC1 has mainly crystallised in a single polytypic phase similar to that of SA sample. Whereas, mechanochemical MC2 and MC3 PbI_2 powders, display enhanced diffraction intensity at the corresponding secondary XRD peak positions, mostly caused by the higher speed of rotation and not the time duration during the planetary ball milling process. Also, the presence of those three additional polytypic phases in the mechanochemical MC2 and MC3 PbI_2 powders, makes them more comparable with the polytypic phases present in the TCI PbI_2 sample. It is presumed that, the formation of different polytypic phases during the growth of the PbI_2 platelets using the planetary ball milling process, is correlated to the amount of kinetic energy transferred to the reactant powders trapped between the colliding stainless - steel spheres during inelastic collisions.

3.2.3 XPS analysis and stoichiometry in PbI_2

XPS characterization was conducted for determination of the oxygen content and lead to iodide ratio of the commercial SA, TCI, ST and mechanochemical MC1 / MC2 / MC3 PbI_2 powders. The calculated ratios between the lead and iodide based on the average values from two different points of analysis on specimens indicated significant variation in the stoichiometry of the PbI_2 powders and the amount of oxygen, as summarised in table 3.3. In the SA material, the lead to iodide ratio was less than the stoichiometric 1 : 2. Whereas, for the TCI, ST, MC1 and MC3 PbI_2 samples the lead to iodide ratio was above the stoichiometric 1 : 2. Only the MC2 PbI_2 sample was shown to have an almost stoichiometric ratio between the lead and iodide atoms. This variation has been attributed to the different parameters of synthesis used, primarily the speed of rotation and secondarily the time duration, during the complicated planetary ball milling process.[12] Also, the higher percentage of oxygen amount detected in the ST sample, in comparison with all the MC synthesised PbI_2 powders, possibly attributed to the formation of the lead oxyiodide and lead iodide hydroxide compounds, as a result of the presence of water in the solvothermal method. The oxygen content was also tentatively manipulated in the mechanochemical MC3 sample. In contrast to the MC1 and MC2 PbI_2 samples, which were synthesised with the presence of air. For the MC3, the air was displaced inside the ball milling jar with argon gas of purity 99 %, which

resulted in an oxygen reduction by ~ 36 (± 10) %, in comparison with the rest of the mechanochemical samples synthesised without the introduction of argon gas. It is assumed further oxygen reduction in the mechanochemically synthesised PbI_2 powders, might be achievable by drying the reactants in a vacuum oven at temperature of 50 ºC for 24 hours and simultaneously by displacing the air with ultra-pure argon gas (> 99.99 %) inside the ball milling jar.

Lead iodide sample	Synthesis conditions/ sample information	Ratio of Pb:I	Amount of oxygen (%)
MC1	Mechanochemical (200 rpm 2 hours)	1:2.1 (± 0.1)	5.2 (± 0.8)
MC2	Mechanochemical (400 rpm 1 hour)	1:2.00 (± 0.1)	4 (± 0.2)
MC3	Mechanochemical (400 rpm 4 hours)	1:2.1 (± 0.1)	2.9 (± 0.1)
ST	Solvothermal (in water)	1:2.1 (± 0.1)	7.2 (± 0.2)
TCI	Tokyo Chemical Industries 99.99%	1:2.3 (± 0.1)	4.5 (± 0.1)
SA	Sigma Aldrich 99.999%	1:1.7 (± 0.1)	4.9 (± 0.1)

Table 3.3: The stoichiometric ratios between lead and iodide and amount of oxygen in commercial (SA and TCI), solvothermal (ST) and mechanochemically synthesized under three different conditions (MC1, MC2 and MC3) PbI_2 powders. All values correspond to the average numbers from two different points of analysis determined by high resolution XPS scans (a survey scan followed by high resolution scans was used for all samples).

Also, it should be clarified that the lead to iodide ratio and amount of oxygen were determined based on the average values that correspond to the intensity of photoexcited electrons from the Pb 4f 7/2, I 3d 5/2 and O 1s core levels, were accompanied by localised deviation from point to point, due to the inhomogeneous crystal structure of the more than one polytypic phases present in PbI_2 powders. This crystal structure inhomogeneity affects the relative intensity of the emission peaks as a consequence of the signal attenuation from the scattered electrons that varies as function of the kinetic energy of the emitted electrons. Additionally, it was found from

the XPS spectra acquisition sequence used (survey scan followed by high resolution scans or single high-resolution scan) can introduce variations between the lead to iodide ratio. A possible mechanism of that variation might be correlated to sublimation of iodide atoms from the PbI_2 powder as function of the interactions with the energy given by x-rays, resulting in an enhanced signal that corresponds to metallic lead. This effect was evaluated by comparing a survey scan followed by a high-resolution scan and a single high-resolution scan without any survey scan collected from two identical TCI PbI_2 powders, as shown in figures 3.3 a and 3.3 b, respectively. The lead to iodide ratio in the TCI PbI_2 sample was 1 : 2.3 (± 0.1), when a survey scan followed by high-resolution scan were conducted as signal acquisition modes. Whereas, the lead to iodide ratio was 1 : 2.4 (± 0.1) when a single high-resolution scan was conducted as a signal acquisition mode. Therefore, exact determination of the lead to iodide ratio in PbI_2 powders using XPS characterisation was laboured and the extracted data are considered only for a general trend between the lead to iodide ratios.

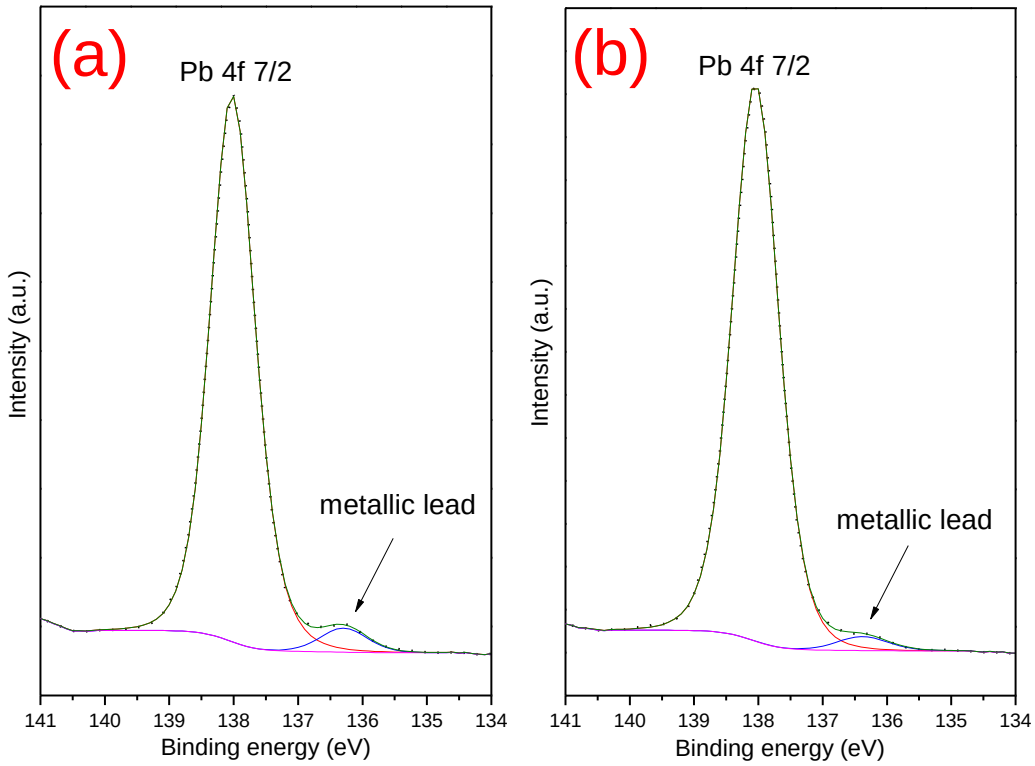

Figure 3.3: XPS high - resolution spectra of Pb 4f 7/2 core level and metallic lead for the TCI lead iodide from different scanning modes. (a) survey scan followed by high-resolution scan and (b) single high-resolution scan.

However, further research is required to better understand the impact of using over-stoichiometric PbI_2 material (such as TCI, MC1 or MC3) for the fabrication of PSC

devices. Over-stoichiometric PbI_2 material enriched with iodide, might result in a gradient of accumulated iodide into the perovskite grains or at the grain boundaries. [13] That localised agglomeration of iodide may affect the optoelectronic properties of perovskite, causing a reduction in the PSC performance which can vary with respect to the operating conditions, such as the presence of oxygen, inert gas or moisture. [14,15] Also, excess iodide originated by the incorporation of an additional either >10% moles of PbI_2 or >5% moles of CH_3NH_3I into the PSC devices with $CH_3NH_3PbI_3$ as photoactive material, reduces the PCE as indicated by Carmona *et al.* and Zhang *et al.*.[7,16] Furthermore, diffusion of excess iodide might interact with the additional layers, such as hole and electron transporting layers or metallic contacts and contribute to their accelerated degradation through secondary chemical reactions. [17–19]

3.2.4 Determining the stoichiometry in PbI_2 by RBS

Rutherford backscattering spectroscopy (RBS) characterization was also conducted for determination of the lead to iodide ratio of the commercial SA, TCI, ST and mechanochemical MC1 / MC2 / MC3 PbI_2 powders. The calculated ratios between the lead and iodide atoms based on a single point of analysis on each specimen, are summarised in table 3.4. All values contain 4 % systematic error, due to the uncertainty in stopping power of accelerated ions of $^4He^+$ with energy 2 MeV during the RBS characterization. Also, RBS spectra of all PbI_2 samples, are shown in figure 3.4. The lead to iodide ratio in the SA PbI_2 sample was 1 : 1.9 (± 0.008), whereas the same ratio in all other samples was either identical (such as in the ST) or contain an excess of iodide. Also, calculated ratios between the lead and iodide atoms in all PbI_2 samples based XPS and RBS characterization were quantitatively summarized in column graph, as shown in figure 3.5. Is noticeable that the number of iodide atoms in SA PbI_2 is below the optimum 1:2 ratio in both characterization techniques. Whereas, the number of iodide per lead atoms is closer to the optimum ratio (1:2) in MC2 PbI_2 and both the characterization techniques indicated very similar numerical values of iodide atoms in comparison with every other PbI_2 sample (SA / TCI / ST / MC1 / MC3). That possible related with the different interaction of photons (in XPS) and ions (in RBS) with the lead and iodide atoms and their penetration depth in PbI_2 samples which might related with a formatted gradient of iodide atoms between the surface and bulk (inner volume) directly correlated with the polytypic nature of PbI_2.

Lead iodide sample	Synthesis conditions/ sample information	Ratio of Pb:I
MC1	Mechanochemical (200 rpm 2 hours)	1:2.029 (± 0.007)
MC2	Mechanochemical (400 rpm 1 hour)	1:2.002 (± 0.008)
MC3	Mechanochemical (400 rpm 4 hours)	1:2.050 (± 0.007)
ST	Solvothermal (in water)	1:2.000 (± 0.007)
TCI	Tokyo Chemical Industries 99.99%	1:2.009 (± 0.007)
SA	Sigma Aldrich 99.999%	1:1.900 (± 0.008)

Table 3.4: The stoichiometric ratios between lead and iodide in commercial (SA and TCI), solvothermal (ST) and mechanochemically synthesized under three different conditions (MC1, MC2 and MC3) PbI_2 powders. All values correspond to a single point of analysis determined by Rutherford backscattering spectroscopy.

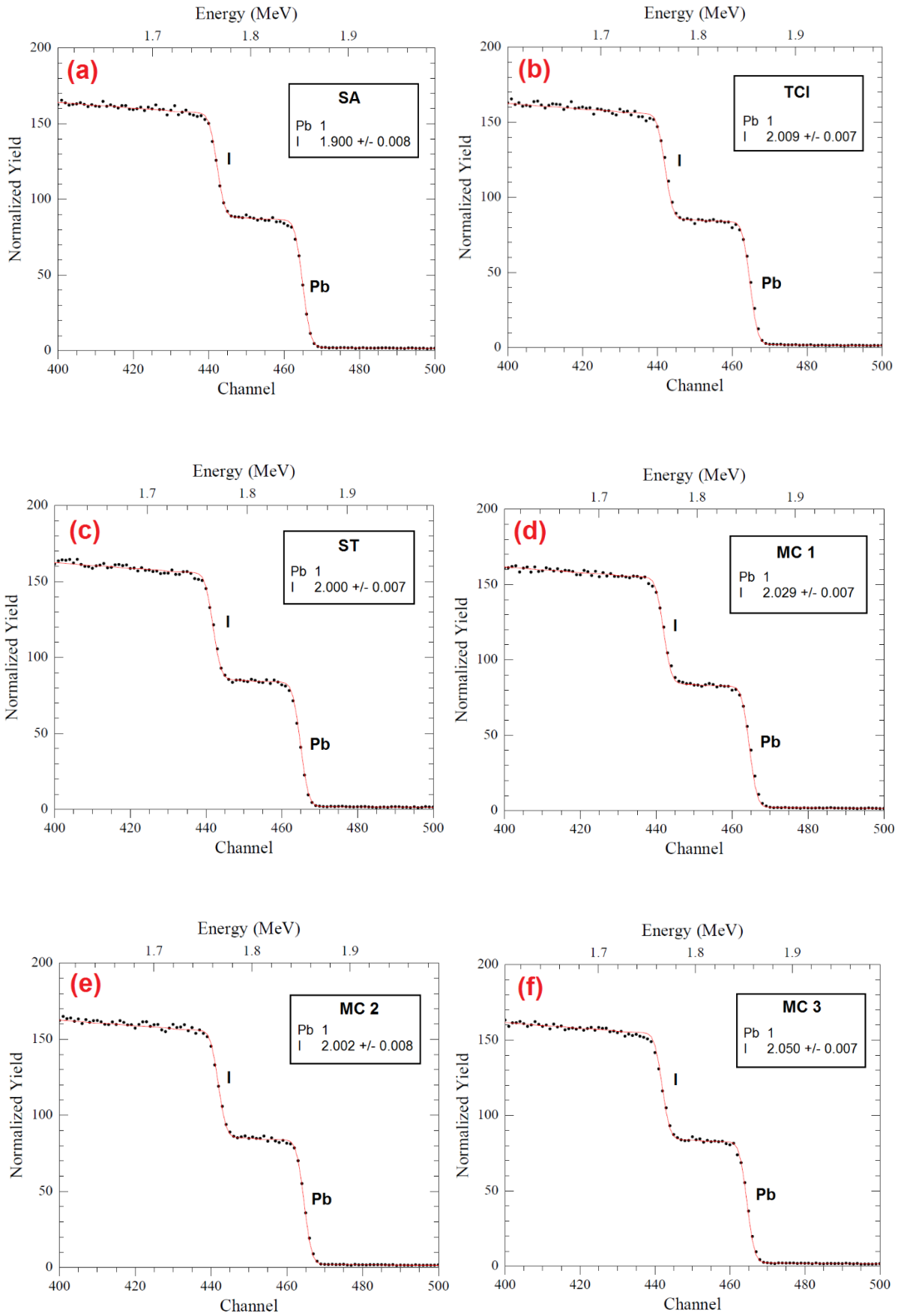

Figure 3.4: Rutherford backscattering spectra (RBS) from PbI_2 pellets made of commercial SA (a), TCI (b), solvothermal ST (c), mechanochemically MC1 (d), MC2 (e) and MC3 (f) synthesized under three different conditions.

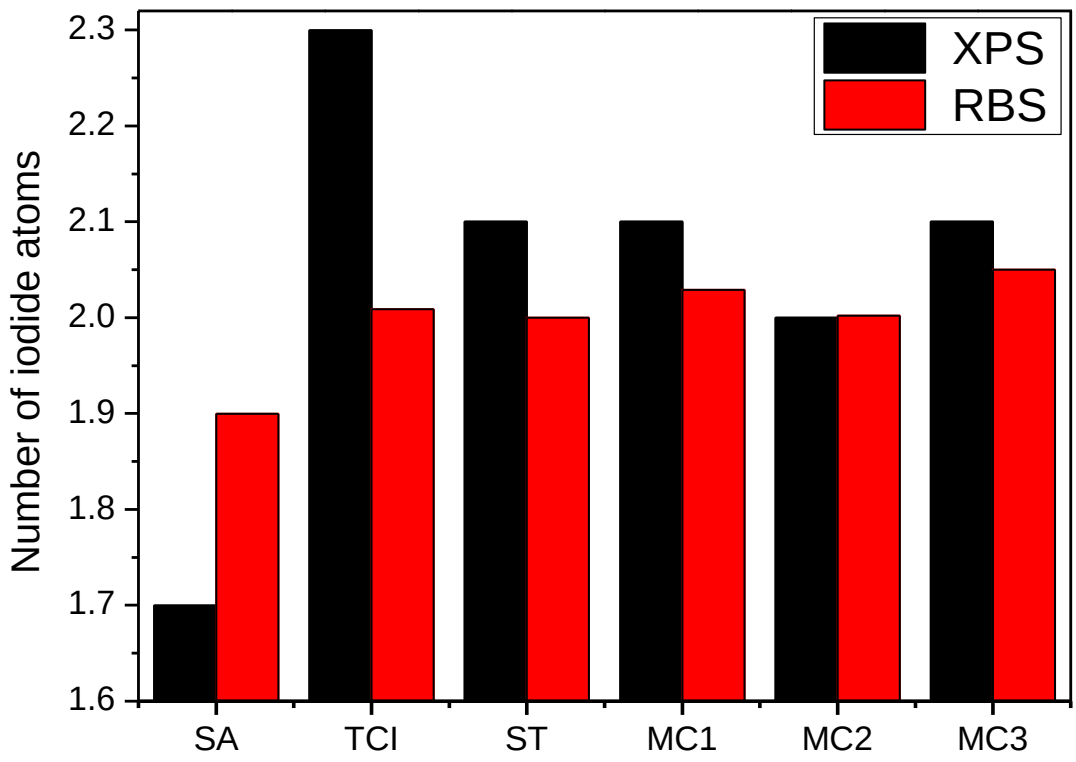

Figure 3.5: Number of iodide atoms per lead atom in PbI_2 as characterized by XPS (in black colour) and RBS (in red colour) of commercial SA, TCI, solvothermal ST, mechanochemically MC1, MC2 and MC3.

3.2.5 Determining the stoichiometry in PbI_2 by XRD

A series of samples of $CH_3NH_3PbI_3$ micro-crystals were synthesised and characterised by XRD to further evaluate the stoichiometric ratio between lead and iodide in the sub-stoichiometric SA and the almost stoichiometric MC2 samples as determined by XPS analysis and previously discussed. The method of 1-pentanol / PbI_2 / CH_3NH_3I was used to synthesise $CH_3NH_3PbI_3$ micro-crystals with different controlled excesses by weight of CH_3NH_3I. [20] This approach to stoichiometry determination in the PbI_2, is based on the critical amount of iodide ions introduced through the excess of CH_3NH_3I needed to result in complete elimination of the unreacted PbI_2 during the synthesis of $CH_3NH_3PbI_3$ micro-crystals. The XRD spectra of the corresponding synthesised $CH_3NH_3PbI_3$ micro-crystals after the reaction of the sub-stoichiometric SA with an excess by weight of CH_3NH_3I (10 %, 15 %, 20 % and 25 %) for 24 hours at constant temperature of 90 ºC, are shown in figures 3.6 a and 3.6 b. When 20 % excess by

weight of CH_3NH_3I was used in reaction with the sub-stoichiometric SA PbI_2 powder, results in a weak XRD peak at diffracted angle 2θ = 12.74° (indicated with an asterisk) that corresponds to a small fraction of unreacted PbI_2, as shown in figure 3.6 b. Consequently, the preferred excess by weight of CH_3NH_3I amount used in reaction with the sub-stoichiometric SA for absolute elimination of the unreacted PbI_2 during the synthesis of the $CH_3NH_3PbI_3$ micro-crystals, should be slightly greater than 20 %. Also, the excess added iodide ions introduced in the reaction by the 20 % excess amount by weight of CH_3NH_3, is comparable with the 10 % excess of PbI_2 found in literature, resulting to optimum PCEs for PSC devices.[7] However, correcting the iodide content into the sub-stoichiometric SA by adding 10 % excess of PbI_2 during the fabrication of perovskite solar cells is accompanied by introduction of excess lead ions, resulting in accumulation of those lead ions into the perovskite grains or at the grain boundaries.

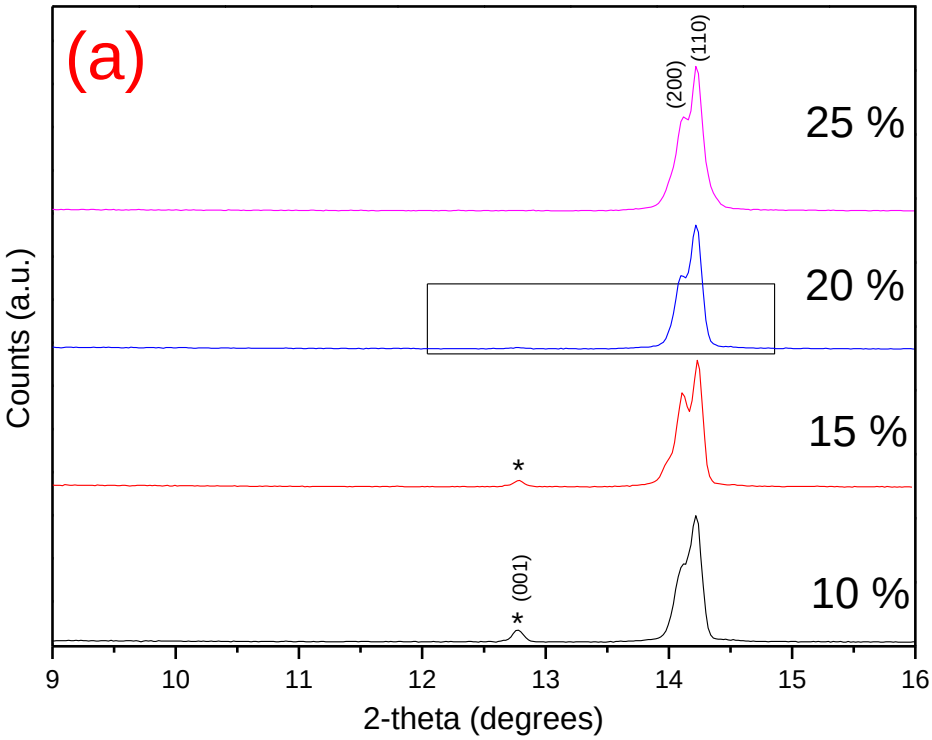

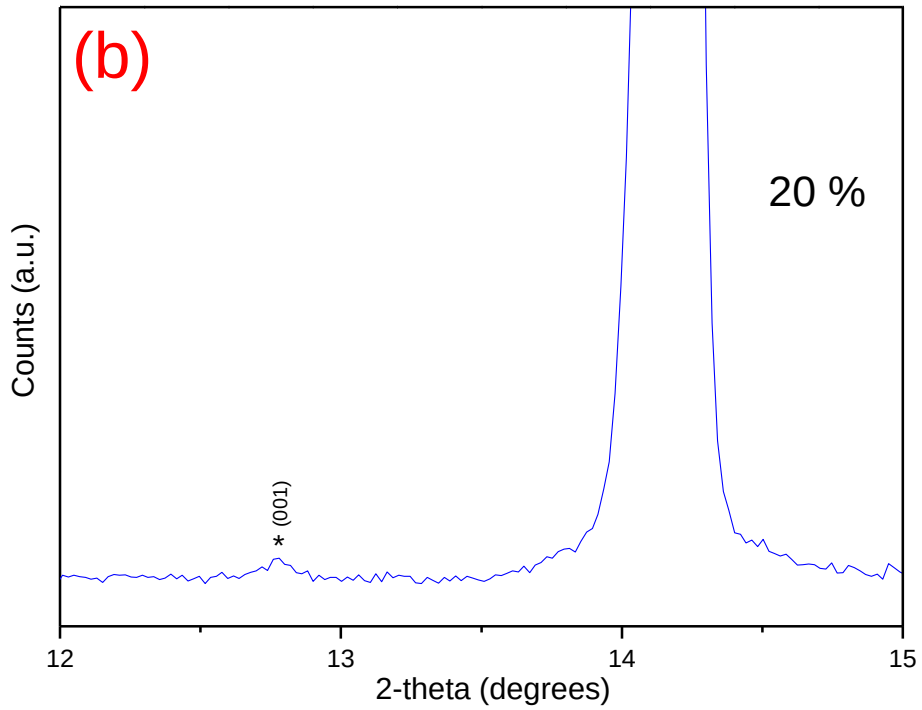

Figure 3.6: XRD patterns of $CH_3NH_3PbI_3$ micro-crystals synthesized using commercial sub-stoichiometric SA PbI_2 in reaction (a) with different amount of excess by weight of CH_3NH_3I (10 %, 15 %, 20 % and 25 %) and (b) with 20 % excess by weight of CH_3NH_3I at higher magnification. Asterisk marks indicate the XRD peak correspond to the unreacted PbI_2 with Miller indices (001). XRD peaks with Miller indices (200) and (110) correspond to the perovskite with tetragonal crystal structure.

Whereas, the XRD spectra of the corresponding synthesised $CH_3NH_3PbI_3$ micro-crystals after the reaction of the almost stoichiometrically corrected in iodide MC2 with an excess by weight of CH_3NH_3I (2 %, 4 % and 6 %) for 24 hours at constant temperature of 90 ºC, are shown in figure 3.7 a and 3.7 b. When 4 % excess by weight of CH_3NH_3I amount was used in reaction with the almost stoichiometric MC2 PbI_2 powder, this resulted in an even weaker XRD peak at diffracted angle 2θ = 12.74º that corresponds to unreacted PbI_2 and annotated with asterisk, as shown in figure 3.7 b. The stoichiometric ratios between the lead and iodide for the SA and MC2 PbI_2 powders, were calculated based on the need of 20 % more by weight amount of CH_3NH_3I reacting with the sub-stoichiometric SA or a 4 % excess by weight amount of CH_3NH_3I reacting with the almost stoichiometric MC2, for an approximate elimination of the XRD signal that corresponds to unreacted PbI_2 present in the $CH_3NH_3PbI_3$ micro-crystals. Subsequently, the lead to iodide ratio for the sub-stoichiometric SA and the almost stoichiometric MC2 were determined, based on the following analysis.

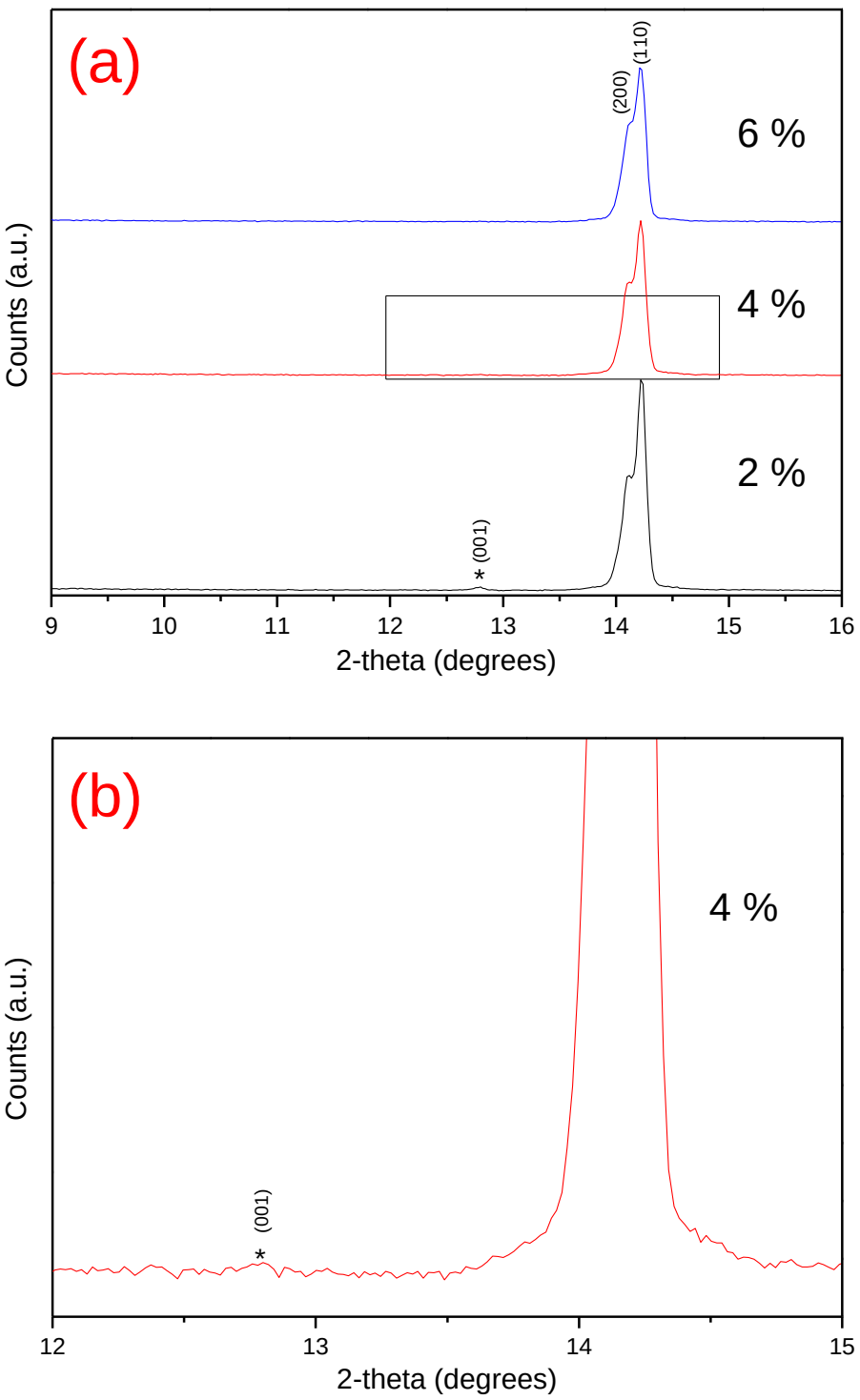

Figure 3.7: XRD patterns of $CH_3NH_3PbI_3$ micro-crystals synthesized using almost stoichiometric MC2 PbI_2 in reaction (a) with different amount of excess CH_3NH_3I by weight (2 %, 4 % and 6 %) and (b) with 4 % of excess CH_3NH_3I by weight at higher magnification. Asterisk marks indicate the XRD peak correspond to the unreacted PbI_2 with Miller indices (001). XRD peaks with Miller indices (200) and (110) correspond to the perovskite with tetragonal crystal structure.

0.5 g of the sub-stoichiometric SA PbI_2 powder and an equimolar amount plus 20 % excess by weight of CH_3NH_3I (0.1724 g + 0.0345 g), were mixed in 15 mL of 1-pentanol and stirred for 24 hours at constant temperature of 90 ºC. The mass of the sub-stoichiometric SA PbI_2 powder might vary, however proportionally 20 % excess by weight of CH_3NH_3I, must be added. The excess added mass of CH_3NH_3I which is 0.0345 g contains 0.0069 g of $CH_3NH_3^+$, corresponding to the summation of the atomic mass units of the elements present in $CH_3NH_3^+$, which for carbon is 12.0107 a.m.u., hydrogen 1.0079 a.m.u. and nitrogen 14.0067 a.m.u. While the remaining 0.0276 g correspond to the mass of I^- (iodide) with atomic mass unit of 126.9045 a.m.u. Based on the previous parameters, in order for the 0.5 g of the sub-stoichiometric SA PbI_2 powder be stoichiometrically correct, it should contain an extra mass of iodide that corresponds to 0.0276 g. The corrected in iodide sub-stoichiometric SA PbI_2, with mass 0.5276 g (0.5 g + 0.0276 g), now is used for determination of its actual stoichiometry. Considering first the number of PbI_2 molecules were calculated after dividing the new corrected weight of PbI_2 (0.5276 g) with the molecular weight of PbI_2 (461.01 g * mol^{-1}) and multiplying by the Avogadro constant (6.022 * 10^{23} molecules * mol^{-1}), resulting in 6.8918 * 10^{20} being the number of PbI_2 molecules. However, in each of these PbI_2 molecules there are 3 atoms (1 lead atom and 2 iodide atoms), resulting in 20.6754 * 10^{20} of atoms in total. Proportionally the number of iodide present in PbI_2, corresponds to 66.66 % of the total number of atoms (13.7836 * 10^{20}), while the remaining 33.33% are lead atoms (6.8918 * 10^{20} atoms). Also, the number of iodide atoms originating from the excess CH_3NH_3I was calculated by dividing the mass of excess iodide added (0.0276 g) with the molecular weight of elemental iodide (126.9045 g * mol^{-1}) and multiplying by the Avogadro constant (6.022 * 10^{23} atoms * mol^{-1}), resulting in 1.3097 * 10^{20} being the number of iodide atoms that are missing from the sub-stoichiometric SA PbI_2 powder. Consequently, the total number of iodide atoms actually present in the initially neat sub-stoichiometric SA PbI_2 was (12.4739 * 10^{20}), based on the correction of iodide content in PbI_2 occurring after adding 20 % excess by weight of CH_3NH_3I minus the iodide atoms added (13.7836 * 10^{20} - 1.3097 * 10^{20} = 12.4739 * 10^{20}). Therefore, the final ratio between the lead to iodide atoms in the sub-stoichiometric SA PbI_2 is 1: (12.4739 * 10^{20} / 6.8918 * 10^{20}) or 1 : 1.81. However, since a weak diffracted peak that corresponds to unreacted PbI_2 was detected during the synthesis of $CH_3NH_3PbI_3$ micro-crystals, as shown in figure 3.6 b, implies that the excess amount of CH_3NH_3I used should be slightly larger, perhaps

~21 – 22 % by weight for complete elimination of the unreacted PbI_2. For comparison, the calculated lead to iodide ratio for the sub-stoichiometric SA is 1 : 1.79, when 22 % excess by weight of CH_3NH_3I was used. The same retrospective methodology was followed when the almost stoichiometric MC2 PbI_2 powder used in reaction with 4 % excess by weight of CH_3NH_3I, during the synthesis of $CH_3NH_3PbI_3$ micro-crystals, results in a ratio between the lead to iodide atoms to be 1 : 1.96.

To understand the presence and formation of unreacted PbI_2 into the $CH_3NH_3PbI_3$ when sub-stoichiometric PbI_2 is used, the following theory was developed:

Since the general chemical formula of perovskite is ABX_3, that requires the presence of 3 halogen atoms. Specifically, in $CH_3NH_3PbI_3$ two iodide atoms originated from the PbI_2 while one iodide atom originated from CH_3NH_3I. That requires both reactants (PbI_2 and CH_3NH_3I) being stoichiometrically perfect. However, when sub-stoichiometric PbI_2 is used, its correct chemical formula must be written as PbI_x with $x < 2$. The percentage of unreacted PbI_2 into the $CH_3NH_3PbI_3$ when sub-stoichiometric PbI_x is used could be calculated from mathematical equation 3.1:

$$\left(\left(1 - (x \div 2)\right) * 2\right) * 100\ \% \qquad \text{mathematical equation 3.1}$$

In which, x is the number of iodide ions into the initially sub-stoichiometric PbI_x used, $\left(1 - (x \div 2)\right) * 100\ \%$ is the percentage of iodide missing from the initially sub-stoichiometric PbI_x used and 2 is the number of iodide ions that needed for the formation of unreacted PbI_2. Also, we accept the condition that unreacted PbI_2 is again stoichiometrically perfect and not sub-stoichiometric, otherwise if the unreacted PbI_2 is sub-stoichiometric then its amount into the $CH_3NH_3PbI_3$ is even higher. To examine that approach a few examples are provided in table 3.5. Based on the previous analysis, initially more iodide is missing from the sub-stoichiometric PbI_x used towards the synthesis of $CH_3NH_3PbI_3$ higher the amount of unreacted PbI_2. Also, similar trend is calculated for the remaining $CH_3NH_3^+$ ions that do not participate at the chemical reaction.

Chemical reaction	$PbI_{1.65}$ + CH_3NH_3I	$PbI_{1.92}$ + CH_3NH_3I
Total number of ions	1 Pb^+ 1 $CH_3NH_3^+$ 2.65 I^-	1 Pb^+ 1 $CH_3NH_3^+$ 2.92 I^-
Total number of ions forming the $CH_3NH_3PbI_3$	0.65 Pb^+ 0.65 $CH_3NH_3^+$ 1.95 I^- or (0.65 $CH_3NH_3PbI_3$)	0.92 Pb^+ 0.92 $CH_3NH_3^+$ 2.76 I^- or (0.92 $CH_3NH_3PbI_3$)
Total number of ions for unreacted PbI_2	0.35 Pb^+ 0.7 I^- or (0.35 PbI_2)	0.08 Pb^+ 0.16 I^- or (0.08 PbI_2)
Total number of $CH_3NH_3^+$ ions	0.35 $CH_3NH_3^+$	0.08 $CH_3NH_3^+$

Table 3.5: Examples of chemical reactions between sub-stoichiometric PbI_x and CH_3NH_3I towards the formation of $CH_3NH_3PbI_3$ and resulted unreacted PbI_2 and $CH_3NH_3^+$ ions.

3.2.6 Through lens detector-SEM spectra of PbI_2

In order to qualify the influence of variability in the stoichiometry and polytypism between the sub-stoichiometric SA PbI_2 crystallised in a single polytypic phase and the almost stoichiometric MC2 PbI_2 crystallised in more than one polytypic phases, spectra of secondary electrons (SE) were collected from PbI_2 pellets using a through lens detector in scanning electron microscope (TLD-SEM). The differentiated intensity

of the SE as function of their deflected energy, indicated significant energy difference in the work function (Φ) between the sub-stoichiometric SA and the almost stoichiometric MC2 PbI_2, as shown in figure 3.8. That may be attributed to the presence of more than one polytypic phase present in the almost stoichiometric MC2 PbI_2. This results in displacement of the Fermi energy closer to the conduction band, since the differentiated intensity of the SE is more enhanced for the almost stoichiometric MC2 PbI_2.

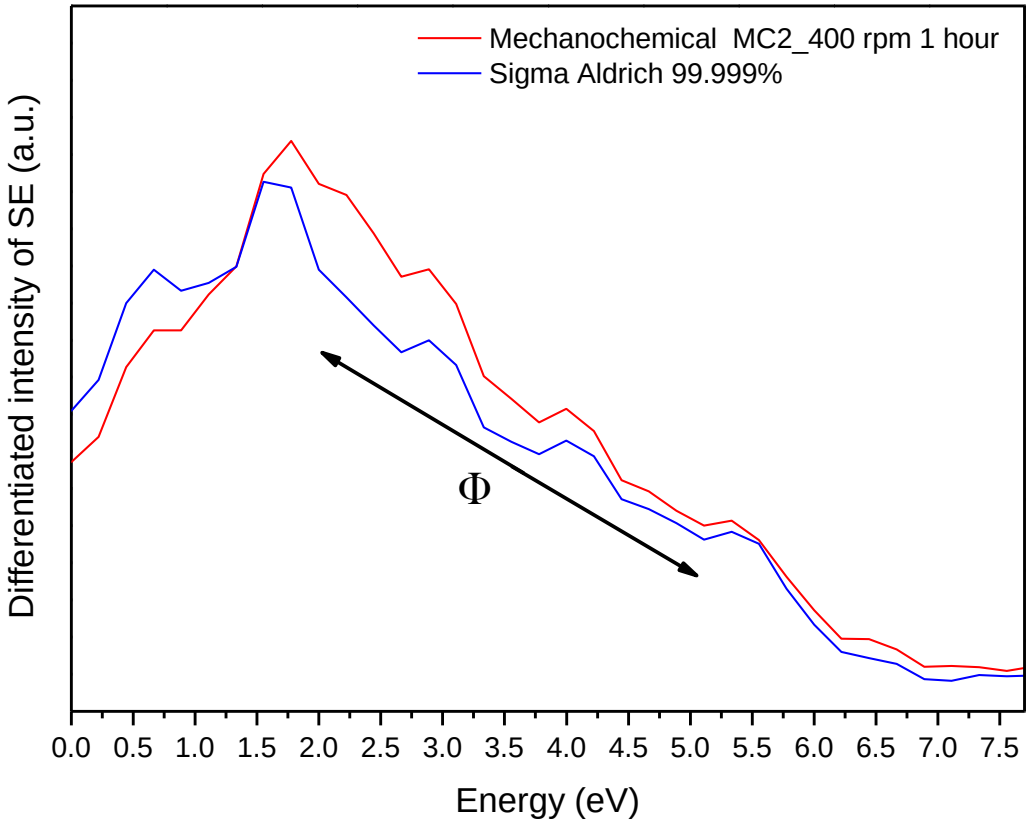

Figure 3.8: Differentiated intensity spectra of the SE as function of their deflected energy from pellets made of the sub-stoichiometric SA or the almost stoichiometric MC2 PbI_2. Φ represents the work function.

3.2.7 Implications of stoichiometry and polytypism of PbI_2 used to fabricate perovskite

The importance of stoichiometry and polytypism has been studied by comparing the sub-stoichiometric SA crystallised in a single polytypic phase and the almost stoichiometric MC2 crystallised in more than one polytypic phase PbI_2 powders used to fabricate $CH_3NH_3PbI_3$. The method of synthesis 1-pentanol / PbI_2 / CH_3NH_3I, similar

to Acik *et al.*,[20] was used in the preparation of $CH_3NH_3PbI_3$ micro-crystals, followed by XRD characterisation. The $CH_3NH_3PbI_3$ micro-crystals were prepared at range of temperatures (20 ºC, 50 ºC, 70 ºC and 90 ºC) and over a constant time of 24 hours. With regards to the PbI_2 used and the amount of CH_3NH_3I, samples were categorised into two groups. In the first group, mechanochemical almost stoichiometric MC2 PbI_2 powder reacted with a) an equimolar amount of CH_3NH_3I or b) an excess of CH_3NH_3I (30% more CH_3NH_3I by weight) followed by XRD characterisation, as shown in figures 3.9 a and 3.9 b, respectively. Whereas, in the second group, sub-stoichiometric SA PbI_2 powder reacted with c) an equimolar amount of CH_3NH_3I or d) an excess of CH_3NH_3I (30% more CH_3NH_3I by weight), followed by XRD characterisation, as shown in figures 3.9 c and 3.9 d, respectively.

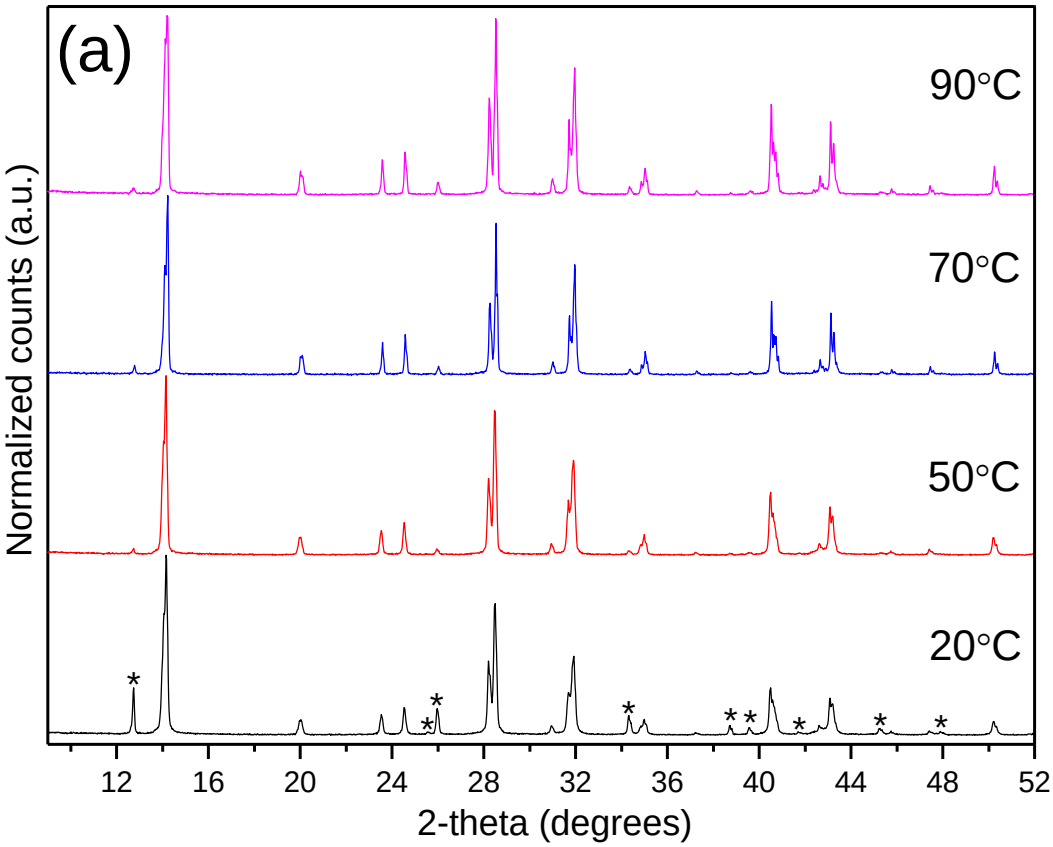

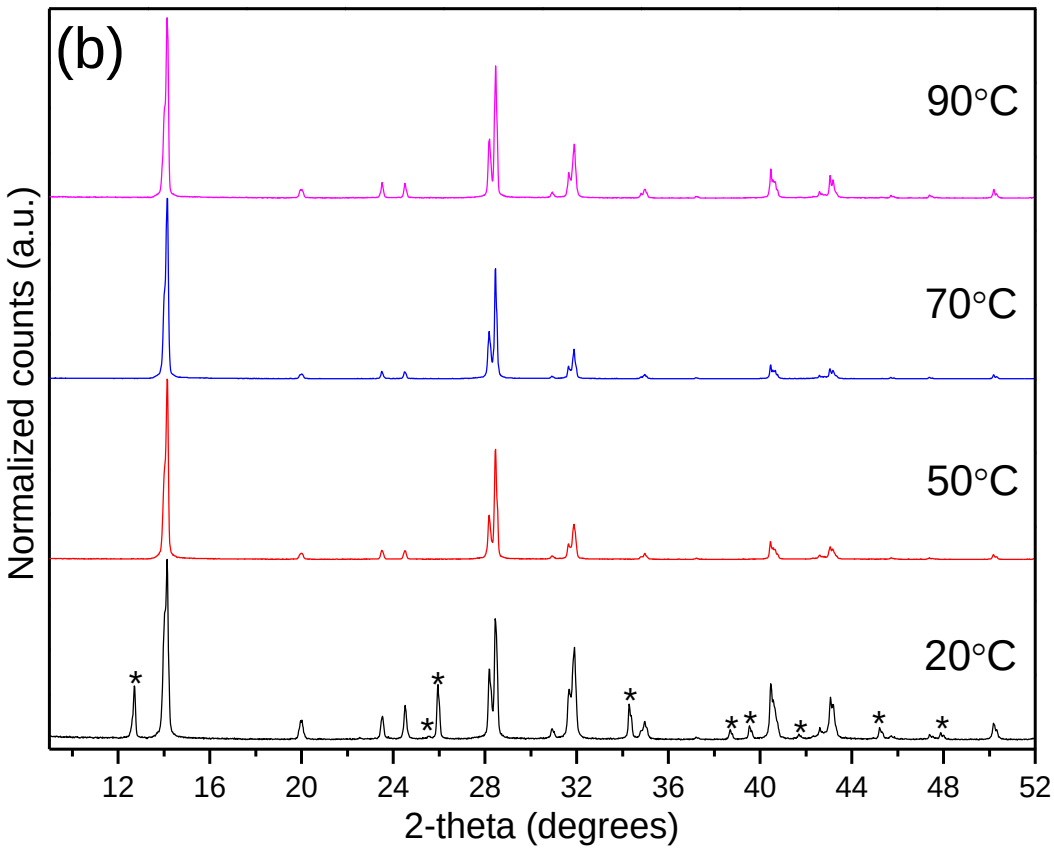
(b)
90°C
70°C
50°C
20°C
Normalized counts (a.u.)
12
16
20
24
28
32
36
40
44
48
52
2-theta (degrees)

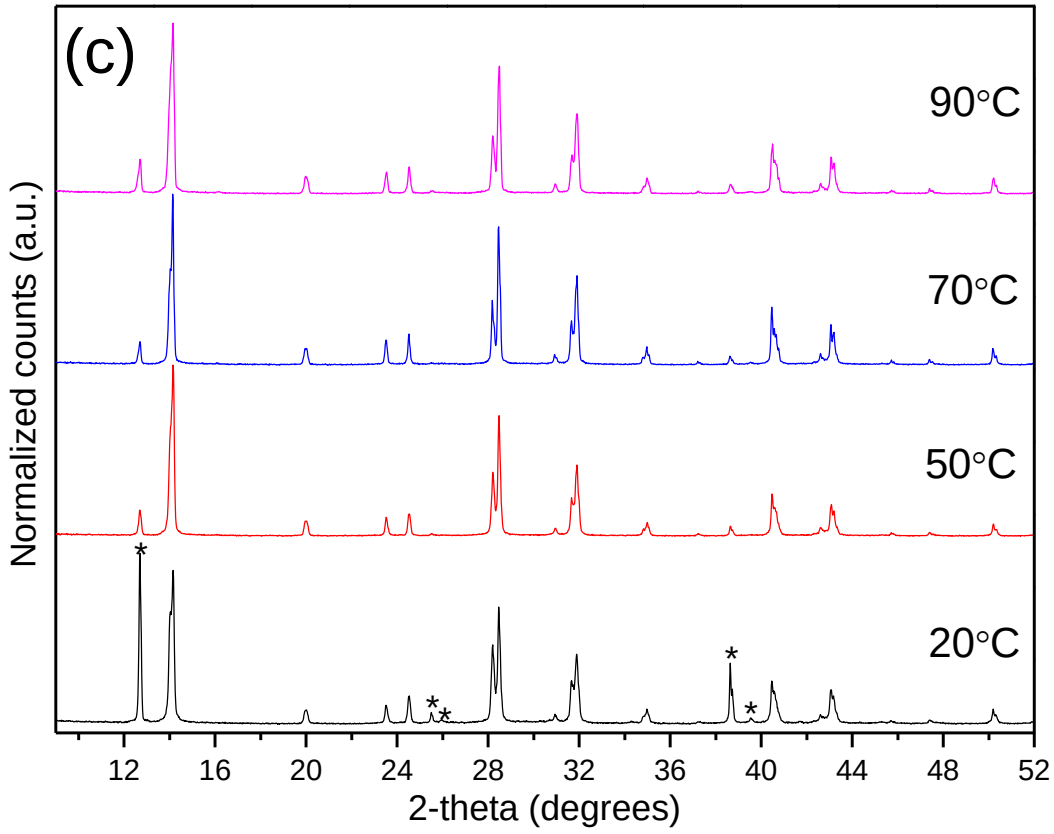
(c)
90°C
70°C
50°C
20°C
Normalized counts (a.u.)
12
16
20
24
28
32
36
40
44
48
52
2-theta (degrees)

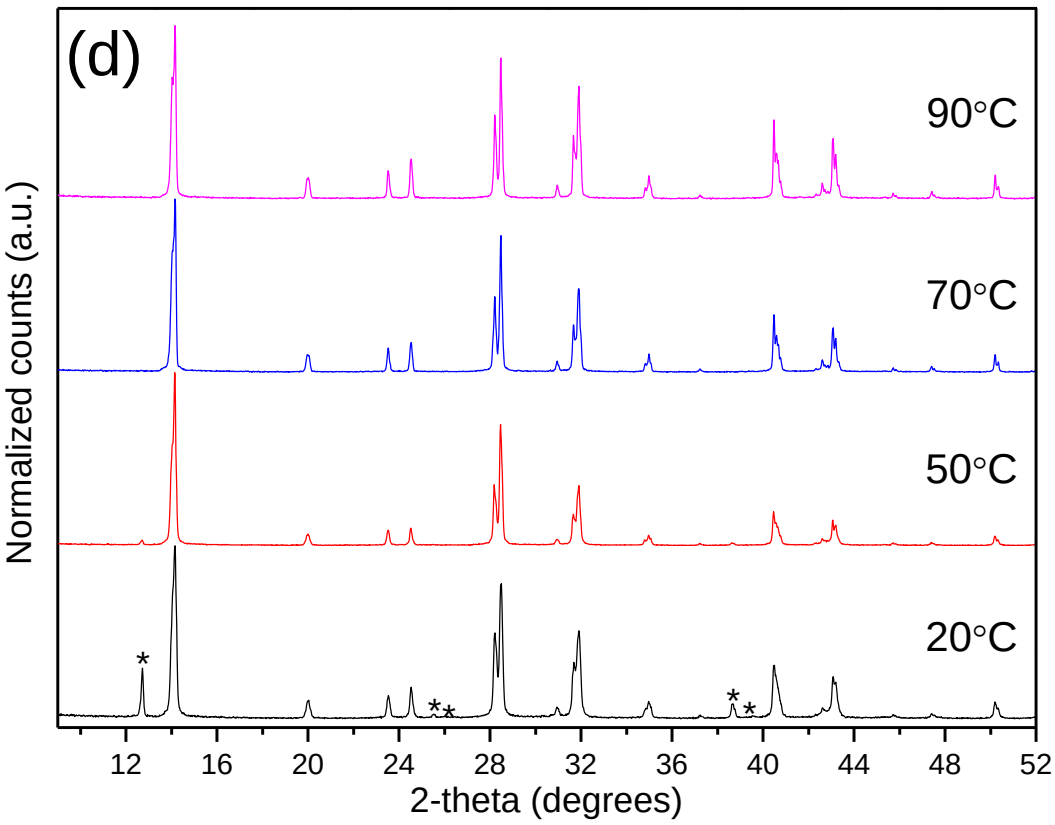

Figure 3.9: XRD patterns of the $CH_3NH_3PbI_3$ micro-crystals synthesised at different temperatures and using different PbI_2 samples (asterisks correspond to the XRD peaks of the lead iodide). (a) mechanochemical MC2 and equimolar CH_3NH_3I, (b) mechanochemical MC2 and equimolar CH_3NH_3I plus 30% by weight of CH_3NH_3I, (c) commercial SA and equimolar CH_3NH_3I, (d) commercial SA and equimolar CH_3NH_3I plus 30% by weight of CH_3NH_3I. Normalization of XRD patterns, was in respect to (110) peak that corresponds to $CH_3NH_3PbI_3$ with tetragonal crystal structure in all patterns, except from that of (c) commercial SA and equimolar CH_3NH_3I at 20 ºC, which is in respect to the peak of the lead iodide (001).

When equimolar amounts of reactants were used in the synthesis of the $CH_3NH_3PbI_3$ micro-crystals, an XRD peak at the diffraction angle 2θ = 12.74º that corresponds to unreacted PbI_2 (annotated with an asterisk) was detected. Also, that diffraction peak was less strong when the almost stoichiometric MC2 instead of the sub-stoichiometric SA PbI_2 powders were used. The percentage of the unreacted PbI_2 present in the powder of the $CH_3NH_3PbI_3$ micro-crystals after each reaction at each temperature was calculated based on the relative integrated area under the primary XRD peak at the diffraction angle 2θ = 12.74º of PbI_2 with Miller indices (001), with respect to the integrated area under the pair of XRD peaks at diffraction angles 2θ = 14.1º and 2θ = 14.2º that correspond to the $CH_3NH_3PbI_3$ with tetragonal crystal structure and planes

with Miller indices (200) and (110), as summarized in table 3.6. It was noted that, the 52.5 % of unreacted PbI_2 powder yellow in colour, was easily observed during the filtration process of $CH_3NH_3PbI_3$ micro-crystal powder synthesised using equimolar amounts of the sub-stoichiometric SA PbI_2 and CH_3NH_3I under constant temperature of 20 ºC, as shown in figure 3.10.

	Percentage (%) of unreacted PbI_2	
Temperature (ºC)	MC2 / CH_3NH_3I equimolar	SA / CH_3NH_3I equimolar
20	14.5	52.5
50	3.1	10.9
70	4.5	11.4
90	3.9	15.7

Table 3.6: Percentage of the unreacted PbI_2 present in $CH_3NH_3PbI_3$ micro-crystals, as function of the temperature and source of PbI_2.

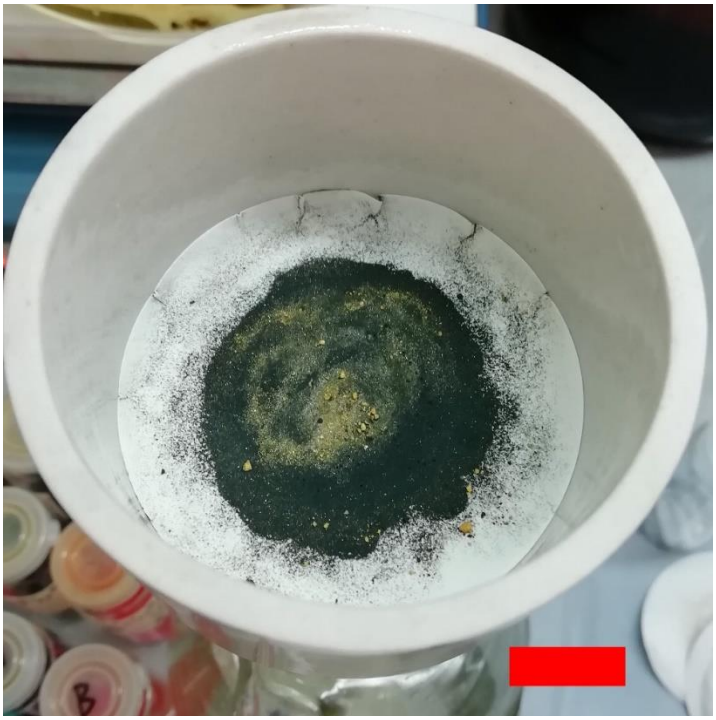

Figure 3.10: Unreacted PbI_2 powder (yellow colour) in the synthesised powder of the $CH_3NH_3PbI_3$ micro-crystals synthesised using equimolar amounts of the sub-stoichiometric SA PbI_2 and CH_3NH_3I under a constant temperature of 20 ºC for 24 hours, scale bar represents 10 mm.

The varying percentage of unreacted PbI_2 present into the $CH_3NH_3PbI_3$ micro-crystals powders synthesised using equimolar amounts of either the sub-stoichiometric SA or almost stoichiometric MC2 PbI_2 with CH_3NH_3I, indicates the stoichiometric deviation from the optimum ratio between the lead and iodide atoms present in the PbI_2. We assume, when equimolar amounts of either the sub-stoichiometric or the almost stoichiometric MC2 PbI_2 and CH_3NH_3I react together, the concentration of iodide anions (I^-) originating from the CH_3NH_3I were not adequate to fulfil the formation of the $CH_3NH_3PbI_3$ and resulted in some unreacted PbI_2. This is consistent with the reported incorporation of hydroiodic acid (HI) sometimes used as an additive, during the formation of $CH_3NH_3PbI_3$ for improved device performance, resulting in a correction of the iodide content in the PbI_2.[21] In contrast, when a 30% excess by weight of CH_3NH_3I was added during the synthesis of the $CH_3NH_3PbI_3$ micro-crystals at temperatures above 50 ºC, zero amount of unreacted PbI_2 was detected by XRD, regardless of the PbI_2 source used (either almost stoichiometric MC2 or sub-stoichiometric SA). Additionally, only minor differences were observed in the XRD spectra of the $CH_3NH_3PbI_3$ micro-crystals synthesised above 50 ºC, related to the number of different polytypic phases present in either the almost stoichiometric MC2 or sub-stoichiometric SA PbI_2, as shown in figures 3.9 b and 3.9 d, respectively. In figures 3.9 b and 3.9 d, nine XRD peaks correspond to unreacted PbI_2 crystallised in different polytypic phases, as indicated with asterisks. These were detected after the synthesis of $CH_3NH_3PbI_3$ micro-crystals at a temperature of 20 ºC using the almost stoichiometric MC2 PbI_2. Whereas, only five XRD peaks corresponding to unreacted PbI_2 crystallised in a single polytypic phase, as indicated with asterisks, were detected after the synthesis of $CH_3NH_3PbI_3$ micro-crystals at 20 ºC using the sub-stoichiometric SA PbI_2. Consequently, the number of different polytypic phases present in the PbI_2, does not affect the formation of perovskite. However, in contrast the stoichiometric ratio between the lead to iodide in the PbI_2 used does affect the formation of perovskite.

3.2.8 Morphology of perovskite thin films

Morphological characterisation of the $CH_3NH_3PbI_3$ thin films fabricated either by $CH_3NH_3PbI_3$ micro-crystals or equimolar amounts of PbI_2 with CH_3NH_3I, indicates the formation of two-dimensional $CH_3NH_3PbI_3$ layered structures independent of the stoichiometric variability in the PbI_2 used. These layered structures have also been

noted in literature [22–24] and were confirmed by atomic force microscopy (AFM) and through lens detector scanning electron microscopy (TLD-SEM) images, as shown in figures 3.11 and 3.12, respectively. Random orientation of those layered structures, accompanied by the presence of unreacted PbI_2, may provide an explanation for the spatial variability of the J_{SC} within individual $CH_3NH_3PbI_3$ grains reported in the literature.[25] Furthermore, spatial interconnections between the individual grains containing two dimensional layered structures were observed, when the $CH_3NH_3PbI_3$ thin films were fabricated from either $CH_3NH_3PbI_3$ micro-crystals regardless of the PbI_2 used (sub-stoichiometric SA or almost stoichiometric MC2) or by reacting equimolar amounts of the almost stoichiometric MC2 PbI_2 with CH_3NH_3I. In contrast, when the $CH_3NH_3PbI_3$ thin films fabricated by reacting equimolar amounts of the sub-stoichiometric SA PbI_2 with CH_3NH_3I, reduced spatial interconnection between individual grains containing the two-dimensional layered structures was noticed. The grains in figures 3.11 d and 3.12 d have more distinct boundaries than the grains in all the other corresponding images. The measured roughness of all fabricated $CH_3NH_3PbI_3$ thin films using the vacuum assisted method was less than 16 nm, as measured by AFM. Also, an increased concentration of formed voids on top of the $CH_3NH_3PbI_3$ thin films fabricated by the $CH_3NH_3PbI_3$ micro-crystals regardless of the PbI_2 used (sub-stoichiometric SA or almost stoichiometric MC2) as observed in TLD-SEM images 3.12 a and 3.12 b, might originate from the low concentration (1.13 M) of the dissolved $CH_3NH_3PbI_3$ micro-crystals in dry DMSO. Also, through all the TLD-SEM images in figure 3.12, grain size distribution calculations were summarized as shown in figure 3.13. Specifically, the majority of grains in $CH_3NH_3PbI_3$ thin films had an average size of 110 ± 10 nm when $CH_3NH_3PbI_3$ micro-crystals employed and fabricated using the almost stoichiometric MC2 PbI_2. Whereas the majority of grains had an average size of 90 ± 10 nm when $CH_3NH_3PbI_3$ micro-crystals used which made using the sub-stoichiometric SA PbI_2. However, equimolar amounts of the almost stoichiometric MC2 PbI_2 / CH_3NH_3I results in thin films with maximum average grain size 175 ± 25 nm. Simultaneously, thin films of perovskite made of equimolar amounts of sub-stoichiometric SA PbI_2 / CH_3NH_3I shown an average grain size of 130 ± 10 nm. Obviously, a different growth mechanism in perovskite thin films is applied between the use of $CH_3NH_3PbI_3$ micro-crystals and equimolar amounts of reactants, which requires further investigation.

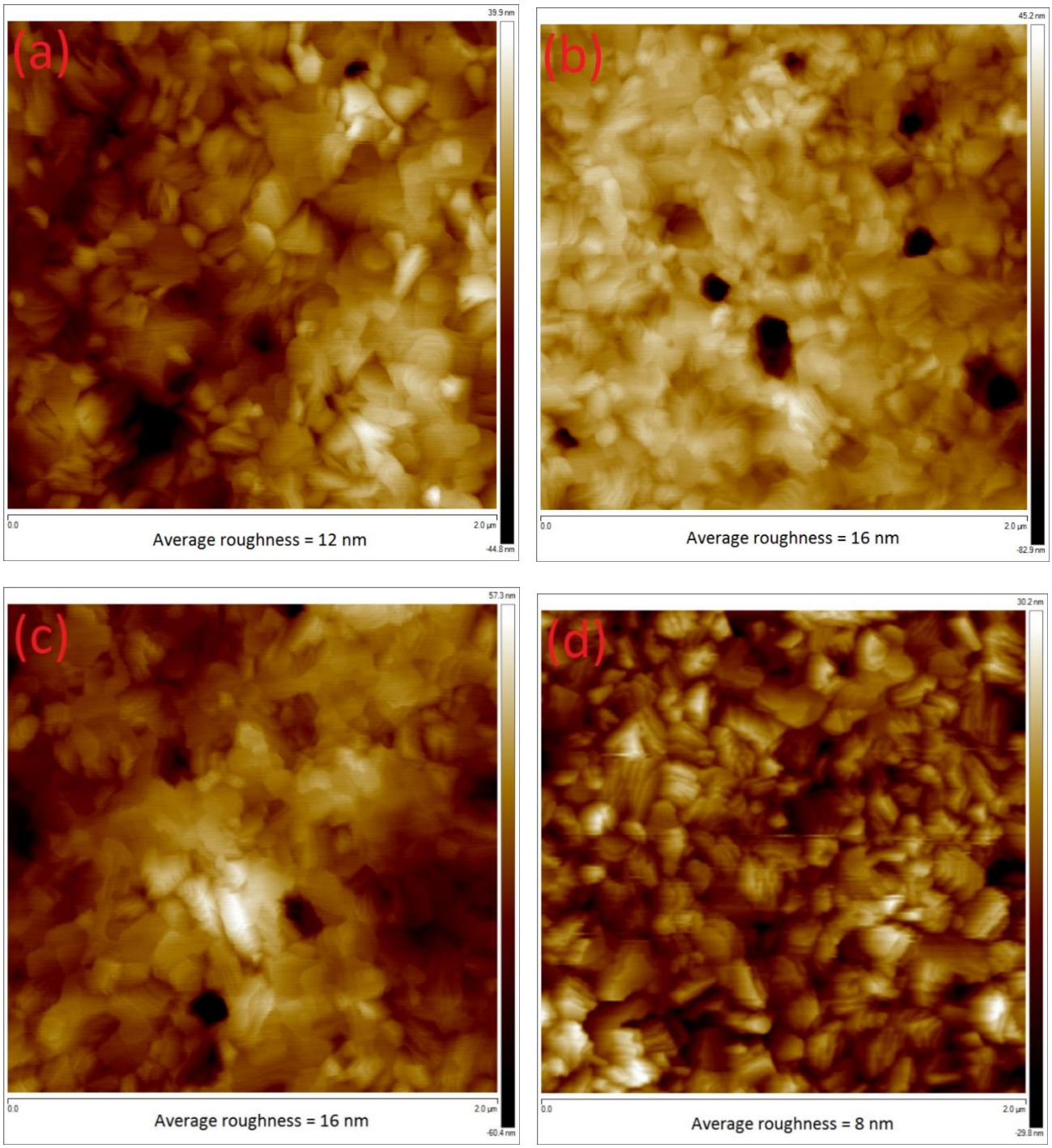

Figure 3.11: AFM images of $CH_3NH_3PbI_3$ thin films fabricated using, (a) $CH_3NH_3PbI_3$ micro-crystals made using almost stoichiometric MC2 PbI_2, (b) $CH_3NH_3PbI_3$ micro-crystals made using sub-stoichiometric SA PbI_2, (c) equimolar amounts of almost stoichiometric MC2 PbI_2 / CH_3NH_3I, (d) equimolar amounts of sub-stoichiometric SA PbI_2 / CH_3NH_3I. The average values of roughness, are listed below at each image.

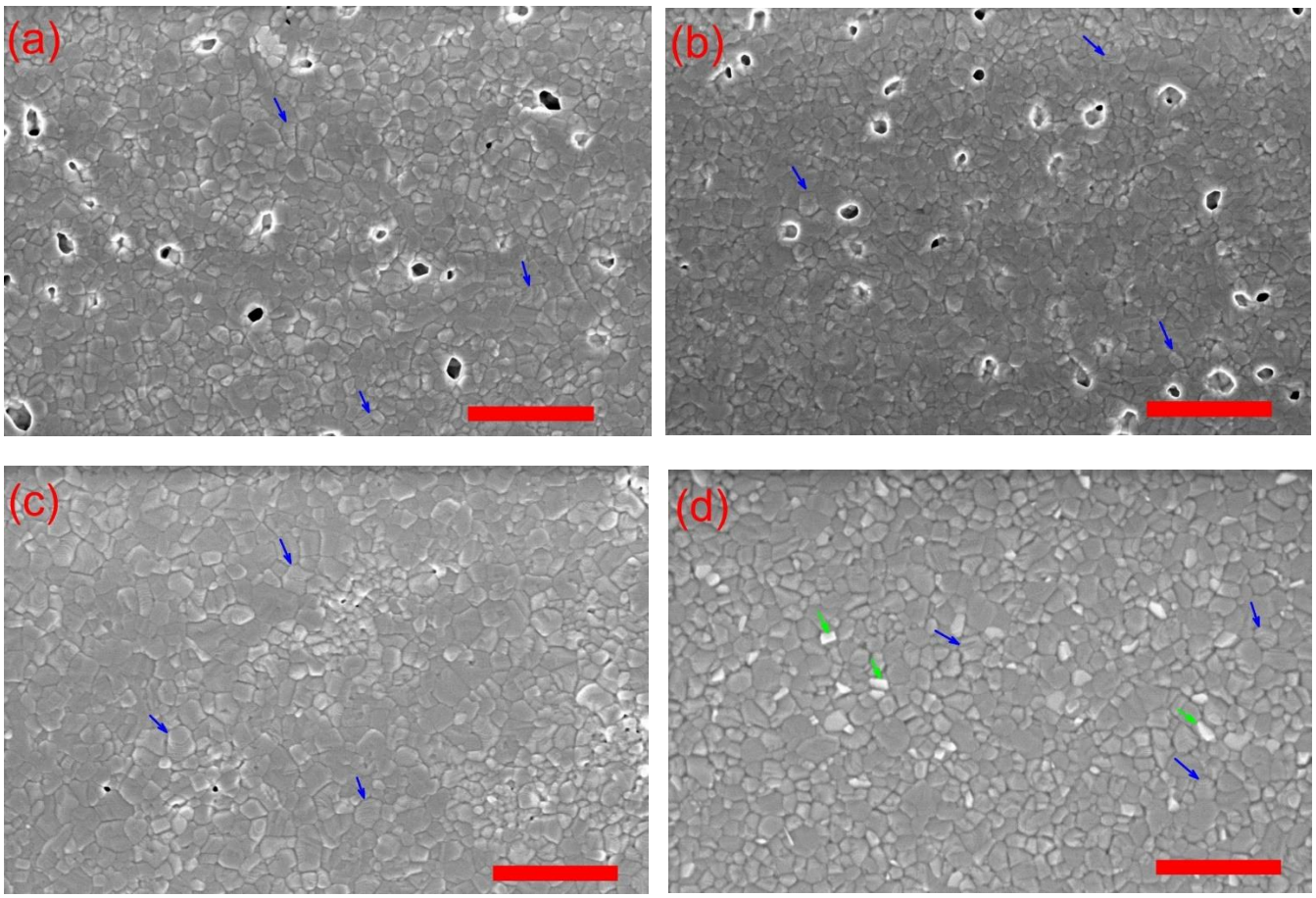

Figure 3.12: Low voltage through lens detector scanning electron microscope (TLD - SEM) images of $CH_3NH_3PbI_3$ thin films fabricated using, (a) $CH_3NH_3PbI_3$ micro-crystals made using almost stoichiometric MC2 PbI_2, (b) $CH_3NH_3PbI_3$ micro-crystals made using sub-stoichiometric SA PbI_2, (c) equimolar amounts of almost stoichiometric MC2 PbI_2 / CH_3NH_3I and (d) equimolar amounts of sub-stoichiometric SA PbI_2 / CH_3NH_3I. Two dimensional layered structures of $CH_3NH_3PbI_3$ into grains, are indicated with blue arrows in all images, while unreacted PbI_2 is indicated with green arrows. Scale bars represent 1 μm.

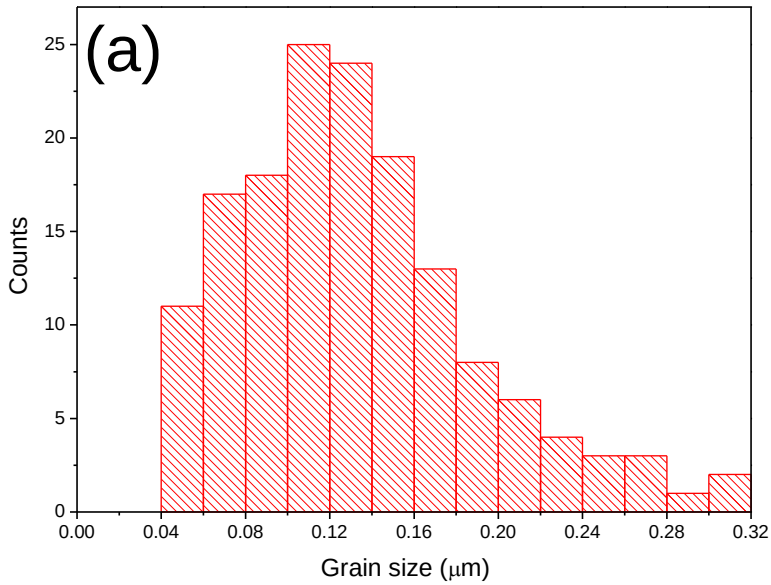

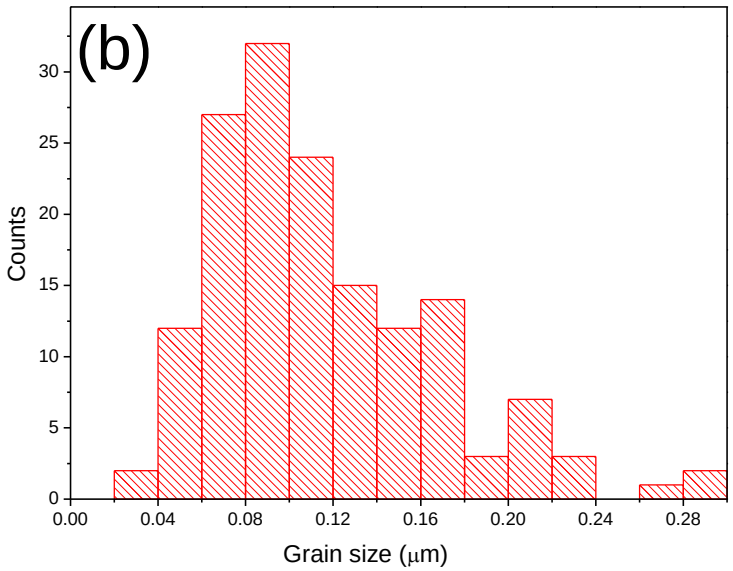
(b)
Counts
Grain size (μm)
0
5
10
15
20
25
30
0.00
0.04
0.08
0.12
0.16
0.20
0.24
0.28

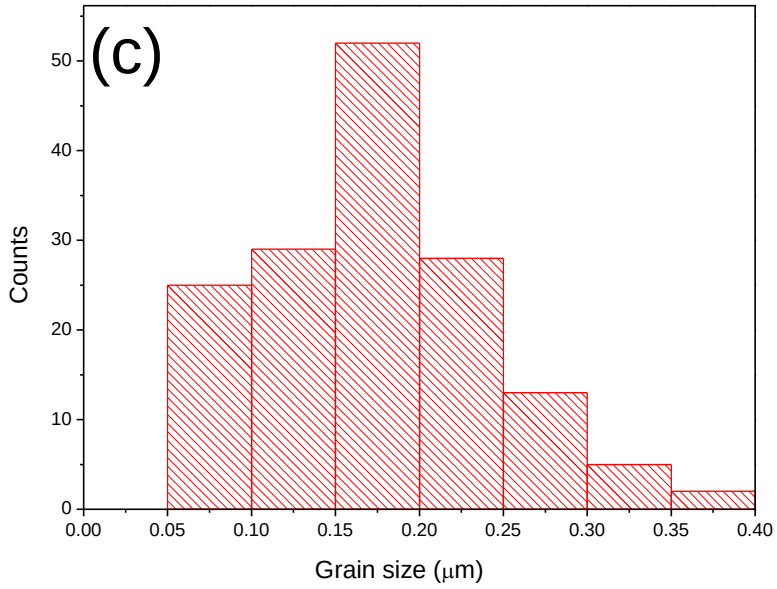
(c)
Counts
Grain size (μm)
0
10
20
30
40
50
0.00
0.05
0.10
0.15
0.20
0.25
0.30
0.35
0.40

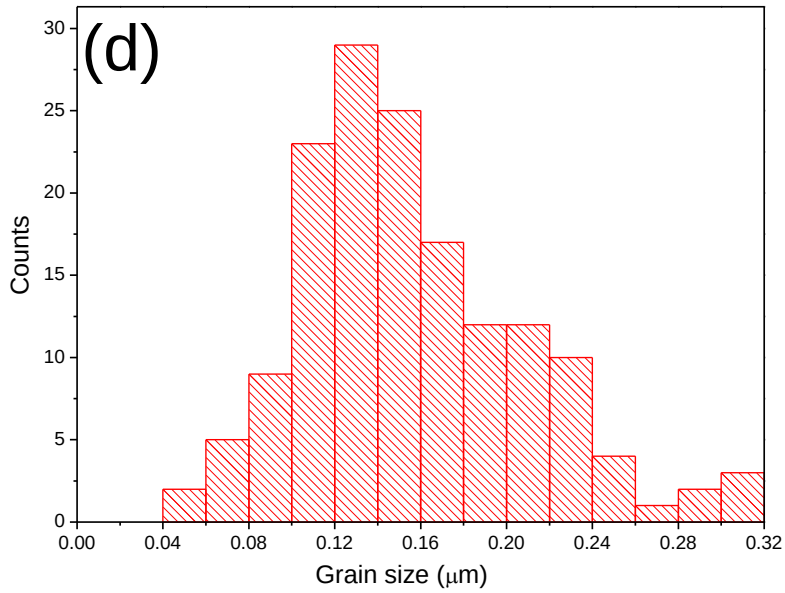

Figure 3.13: Grain size distribution of $CH_3NH_3PbI_3$ thin films (based on TLD - SEM images) fabricated using, (a) $CH_3NH_3PbI_3$ micro-crystals made using almost stoichiometric MC2 PbI_2, (b) $CH_3NH_3PbI_3$ micro-crystals made using sub-stoichiometric SA PbI_2, (c) equimolar amounts of almost stoichiometric MC2 PbI_2 / CH_3NH_3I and (d) equimolar amounts of sub-stoichiometric SA PbI_2 / CH_3NH_3I.

3.2.9 Vis-IR spectra of perovskite thin films as function of the PbI_2 used

The presence of unreacted PbI_2 either between or within the grains of the $CH_3NH_3PbI_3$ thin films fabricated using equimolar amounts of the sub-stoichiometric SA PbI_2 in reaction with CH_3NH_3I, was confirmed by the strong absorption observed around ~ 530 nm, as shown in the visible-infrared (Vis-IR) spectra in figure 3.14. The optical band gap values (E_{obg}) of the unreacted PbI_2 present (E_{obg}= 2.34 eV (± 0.02 eV) was calculated based on five measurements, while the optical band gap related to the $CH_3NH_3PbI_3$ (E_{obg}= 1.48 eV) for the thin films fabricated using equimolar amounts of the sub-stoichiometric SA PbI_2 in reaction with CH_3NH_3I. The relevant Tauc plots, are shown in figures 3.15 and 3.16. The hypothesis that unreacted PbI_2 might be present within the perovskite grains, is supported by the values of the optical band gaps that correspond to the neat PbI_2 (E_{obg}= 2.36 eV) and the $CH_3NH_3PbI_3$ (E_{obg}= 1.51 eV),[26] as shown in figures 3.15 and 3.16, respectively. It is assumed, that in the $CH_3NH_3PbI_3$ thin films fabricated using equimolar amounts of the sub-stoichiometric SA PbI_2 in reaction with CH_3NH_3I, the amount of iodide present in the sub-stoichiometric SA PbI_2,

is insufficient to form a continuous composition of the $CH_3NH_3PbI_3$. This results in the formation of zones that are sufficiently iodide enriched (~ at least three iodide ions) and other zones that are depleted of iodide (less than three iodide ions). [27] Unreacted PbI_2 is formed in the depleted zones, while $CH_3NH_3PbI_3$ is formed in the enriched zones within the perovskite grains, respectively.

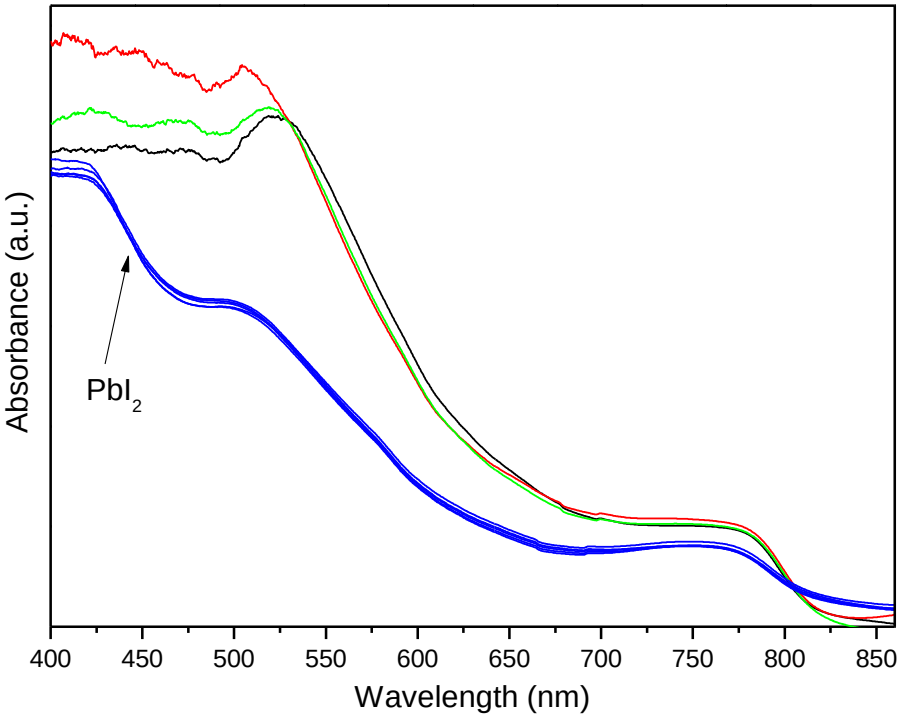

Figure 3.14: Visible-infrared (Vis-IR) absorption spectra of perovskite thin films synthesised from, $CH_3NH_3PbI_3$ micro-crystals (using almost stoichiometric MC2 PbI_2) (black curve), $CH_3NH_3PbI_3$ micro-crystals (using sub-stoichiometric SA PbI_2) (red curve), equimolar amounts of almost stoichiometric MC2 PbI_2 / CH_3NH_3I (green curve) and equimolar amounts of sub-stoichiometric SA PbI_2 / CH_3NH_3I (blue curves from five different measurements). Strong absorption at ~ 530 nm corresponds to unreacted PbI_2 as indicated with black arrow.

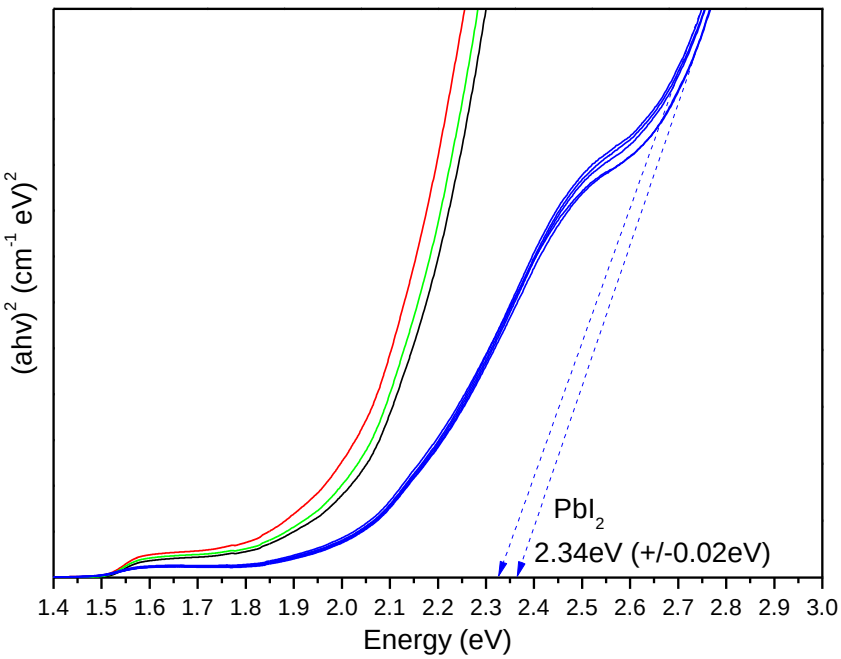

Figure 3.15: Tauc plots of perovskite thin films synthesised from, $CH_3NH_3PbI_3$ micro-crystals (using almost stoichiometric MC2 PbI_2) (black curve), $CH_3NH_3PbI_3$ micro-crystals (using sub-stoichiometric SA PbI_2) (red curve), equimolar amounts of almost stoichiometric MC2 PbI_2 / CH_3NH_3I (green curve) and equimolar amounts of sub-stoichiometric SA PbI_2 / CH_3NH_3I (blue curves from five different measurements).

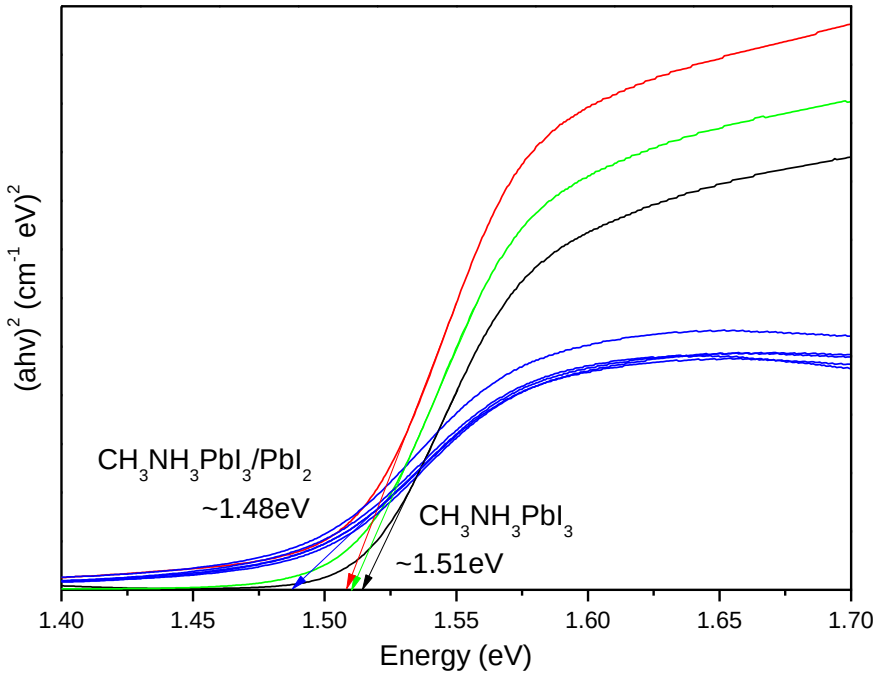

Figure 3.16: Tauc plots of perovskite thin films synthesised from, $CH_3NH_3PbI_3$ micro-crystals (using almost stoichiometric MC2 PbI_2) (black curve), $CH_3NH_3PbI_3$ micro-crystals (using sub-stoichiometric SA PbI_2) (red curve), equimolar amounts of almost stoichiometric MC2 PbI_2 / CH_3NH_3I (green curve) and equimolar amounts of sub-stoichiometric SA PbI_2 / CH_3NH_3I (blue curves from five different measurements). The $CH_3NH_3PbI_3$ optical band gaps (~ 1.51 eV) are indicated with black / red / green arrows. $CH_3NH_3PbI_3$ / PbI_2 optical band gap (~ 1.48 eV) is indicated with blue arrow.

3.2.10 The importance of the stoichiometry in PbI_2 used to produce perovskite solar cells

Perovskite solar cell (PSC) devices with regular (n – i – p) architecture were fabricated with the stacking sequence: glass / ITO / SnO_2 / $CH_3NH_3PbI_3$ / Spiro-MeOTAD / Au, in order to determine the importance of the variable stoichiometry and polytypism present in the PbI_2 used. Deposition of all the $CH_3NH_3PbI_3$ photoactive layers was accomplished using the same vacuum assisted method, as described in experimental methods (chapter 2) and shown in figures 3.17 a and 3.17 b. [28] The vacuum applied accelerates the extraction of dry DMSO solvent in a single step without any antisolvent rinsing process. One set of PSCs devices were fabricated by dissolving either the sub-stoichiometric SA or the almost stoichiometric MC2 PbI_2 powders, with equimolar amounts of CH_3NH_3I in dry DMSO, results in photoactive thin films with thicknesses ~ 350 nm (± 10 nm), as determined by atomic force microscopy (AFM). A second set of PSC devices was fabricated by re-dissolving the corresponding $CH_3NH_3PbI_3$ micro-crystals in dry DMSO (synthesised as described below), results in photoactive thin films with thicknesses ~ 300 nm (± 10 nm), as determined by atomic force microscopy (AFM).

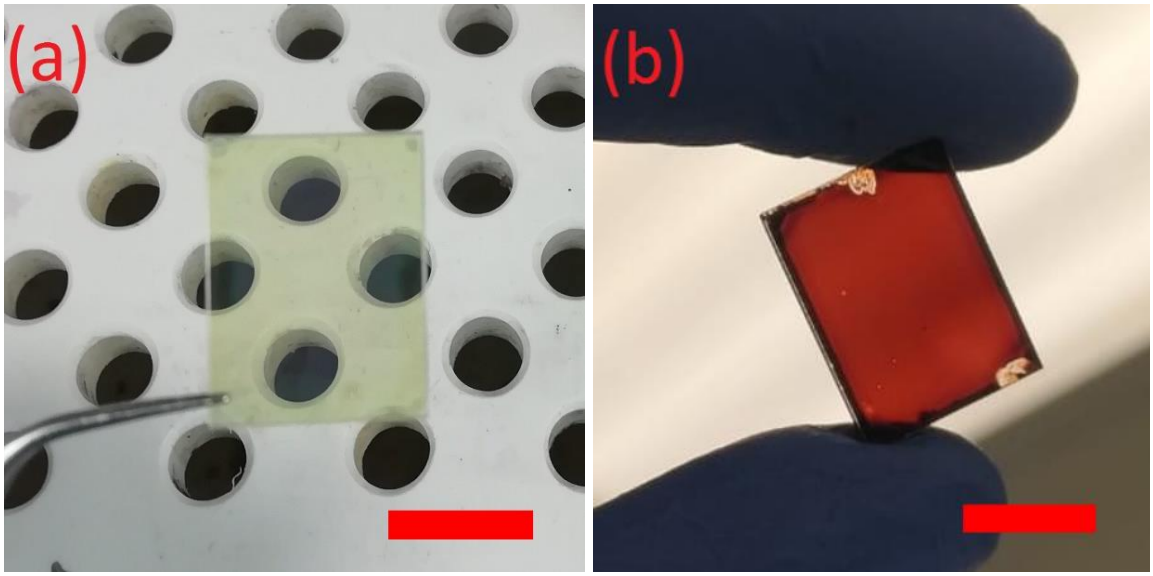

Figure 3.17: Images of glass / ITO / SnO_2 / perovskite after (a) extracting the dry DMSO under vacuum for 120 s before annealing and (b) after annealing at 100 °C for 30 s, scale bars represent 10 mm. (Corresponding marks near the edges of sample in figure (b) are made by tweezers).

$CH_3NH_3PbI_3$ micro-crystals were synthesised at a temperature of 90 ºC using either the sub-stoichiometric SA or the almost stoichiometric MC2 PbI_2 powders in reaction with a 30 % excess by weight of CH_3NH_3I. Minor differences were observed in the morphology of the $CH_3NH_3PbI_3$ micro-crystals as observed by scanning electron microscopy (SEM) images, as shown in figures 3.18 a and 3.18 b.

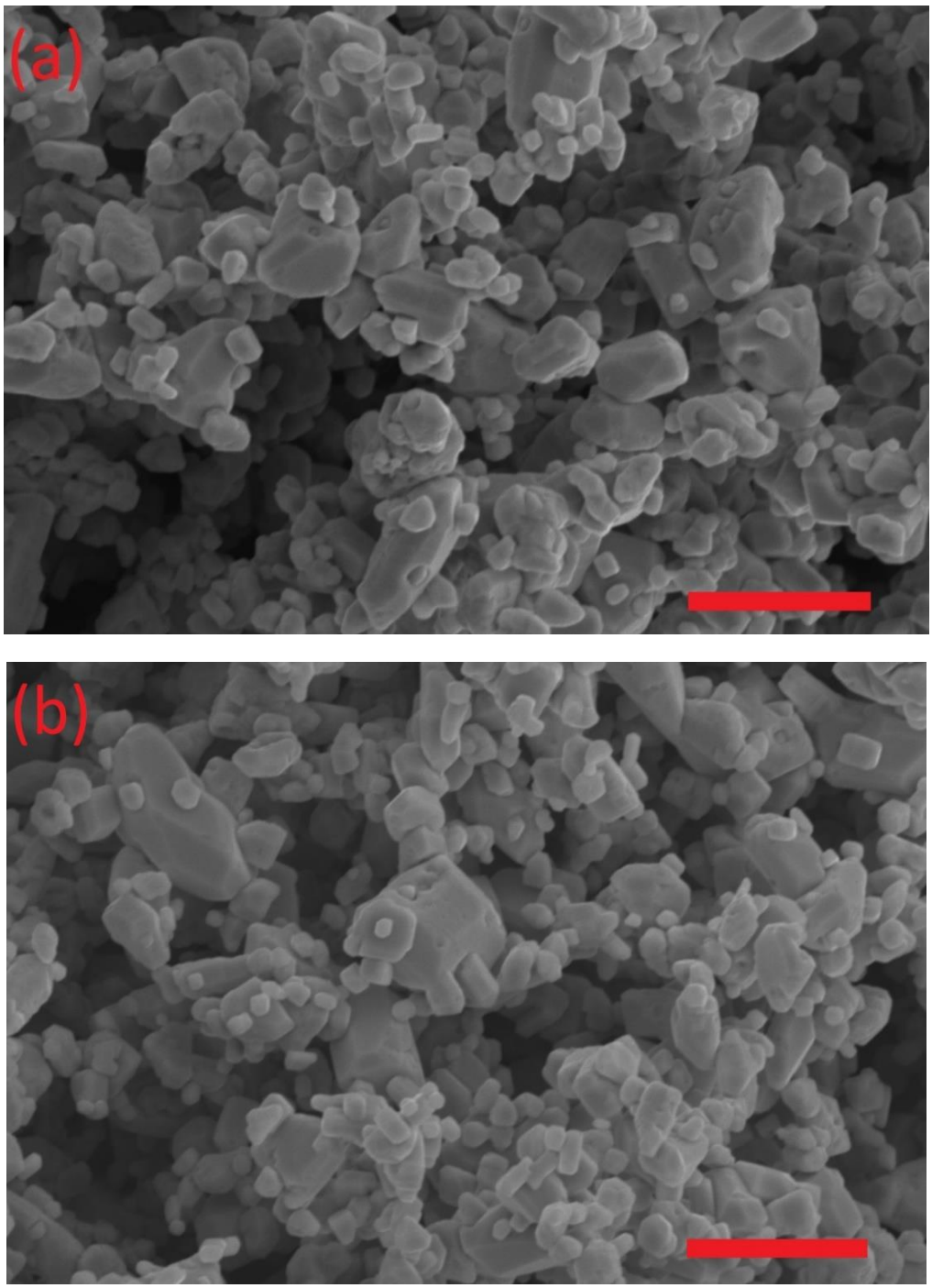

Figure 3.18: Scanning electron microscopy (SEM) images of $CH_3NH_3PbI_3$ micro-crystals synthesised at temperature 90 ˚C, using (a) the almost stoichiometric mechanochemical MC 2 or (b) the sub-stoichiometric SA PbI_2 powders in reaction with a 30% more by weight of CH_3NH_3I, scale bars represent 10µm.

The average and champion photovoltaic parameters (Fill Factor (FF), short circuit current (J_{SC}), open circuit voltage (V_{OC}) and power conversion efficiency (PCE)), of the PSCs were measured during a reverse scan ($V_{OC} \rightarrow 0$) with a scan step of 100 mV, are listed in table 3.7 and illustrated graphically in figure 3.19. Also, the characteristic current density – voltage curves in forward ($0 \rightarrow V_{OC}$) and reverse ($V_{OC} \rightarrow 0$) scans of PSC devices with structure glass / ITO / SnO_2 / $CH_3NH_3PbI_3$ / Spiro-MeOTAD / Au, as a function of the photoactive layer fabricated using either $CH_3NH_3PbI_3$ micro-crystals or equimolar amounts of different PbI_2 with CH_3NH_3I, are shown in figure 3.20. In all the following plots, black curves correspond to the average of all current density – voltage curves recorded and the coloured stripes represent the deviation between each initially recorded current density – voltage curve from the black curve. green coloured stripes that represent the measurements of fresh PSCs,

		FF (%)	J_{SC} (mA/cm^2)	V_{OC} (Volts)	PCE (%)
Dissolution of $CH_3NH_3PbI_3$ micro-crystals in DMSO	$CH_3NH_3PbI_3$ micro-crystals (synthesised using MC2 PbI_2)	**68.19** (73.66)	**20.98** (21.61)	**1.03** (1.04)	**14.69** (16.55)
	$CH_3NH_3PbI_3$ micro-crystals (synthesised using SA PbI_2)	**72.08** (75.82)	**20.87** (21.65)	**1.06** (1.06)	**16.02** (17.40)
Dissolution of equimolar PbI_2 / CH_3NH_3I in DMSO	MC2 PbI_2 / CH_3NH_3I (equimolar)	**71.75** (75.29)	**21.09** (21.60)	**1.04** (1.05)	**15.77** (17.07)
	SA PbI_2 / CH_3NH_3I (equimolar)	**34.18** (41.01)	**13.06** (14.96)	**1.02** (1.02)	**4.58** (6.26)

Table 3.7: The Fill Factor (FF), short circuit current (J_{SC}), open circuit voltage (V_{OC}) and power conversion efficiency (PCE)) of PSCs devices with structure glass / ITO / SnO_2 / $CH_3NH_3PbI_3$ / Spiro - OMeTAD / Au, as a function of the PbI_2 powder and the synthesised $CH_3NH_3PbI_3$ micro-crystals used. The PSCs parameters correspond to the average values from 20 devices in bold and champion devices in parenthesis.

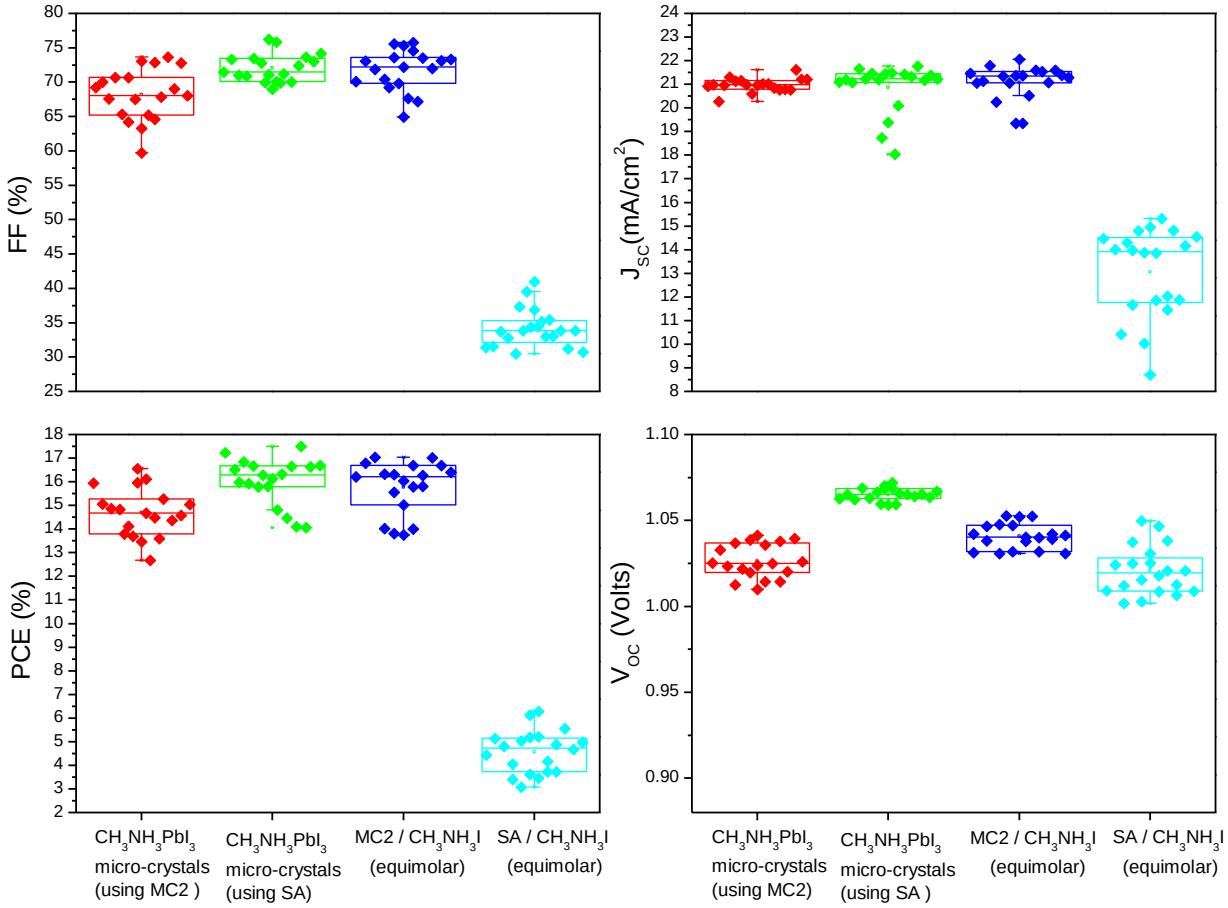

Figure 3.19: The Fill Factor (FF), short circuit current (J_{SC}), power conversion efficiency (PCE) and open circuit voltage (V_{OC}) of PSCs devices with structure glass / ITO / SnO_2 / $CH_3NH_3PbI_3$ / Spiro-OMeTAD / Au, as a function of the PbI_2 powder and the synthesised $CH_3NH_3PbI_3$ micro-crystals used.

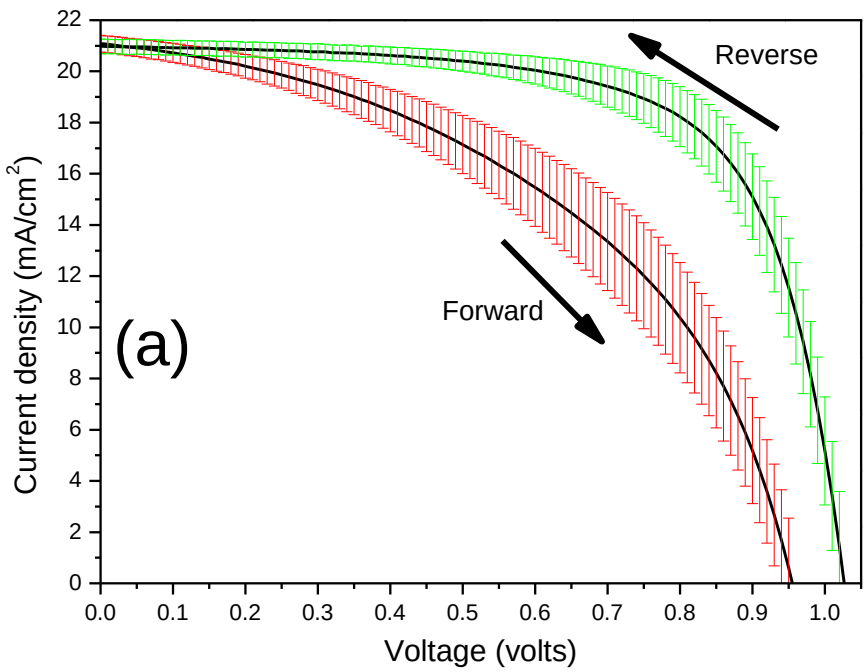

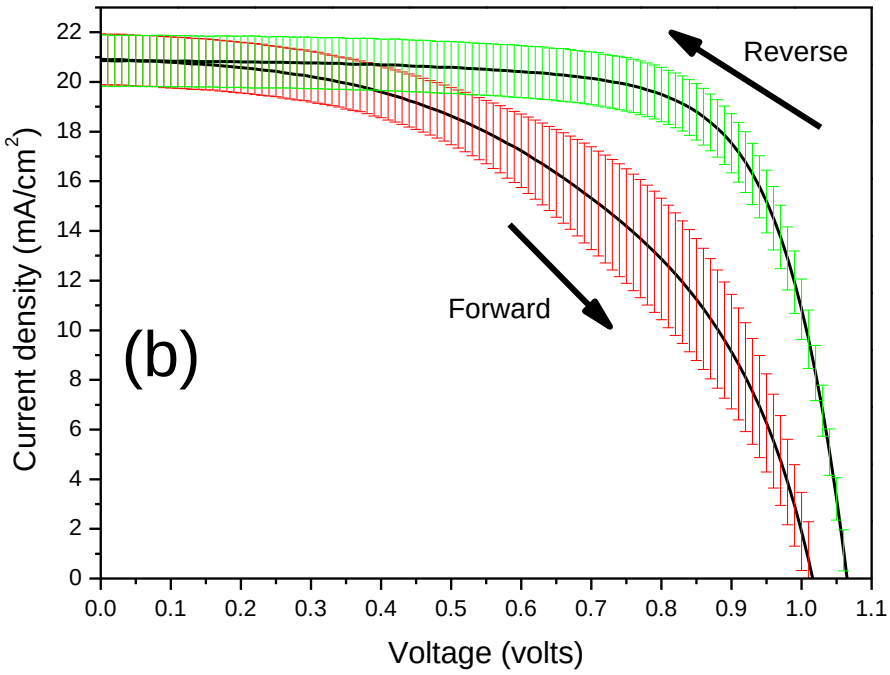
(b)
Reverse
Forward
Current density (mA/cm^2)
Voltage (volts)
0
2
4
6
8
10
12
14
16
18
20
22
0.0
0.1
0.2
0.3
0.4
0.5
0.6
0.7
0.8
0.9
1.0
1.1

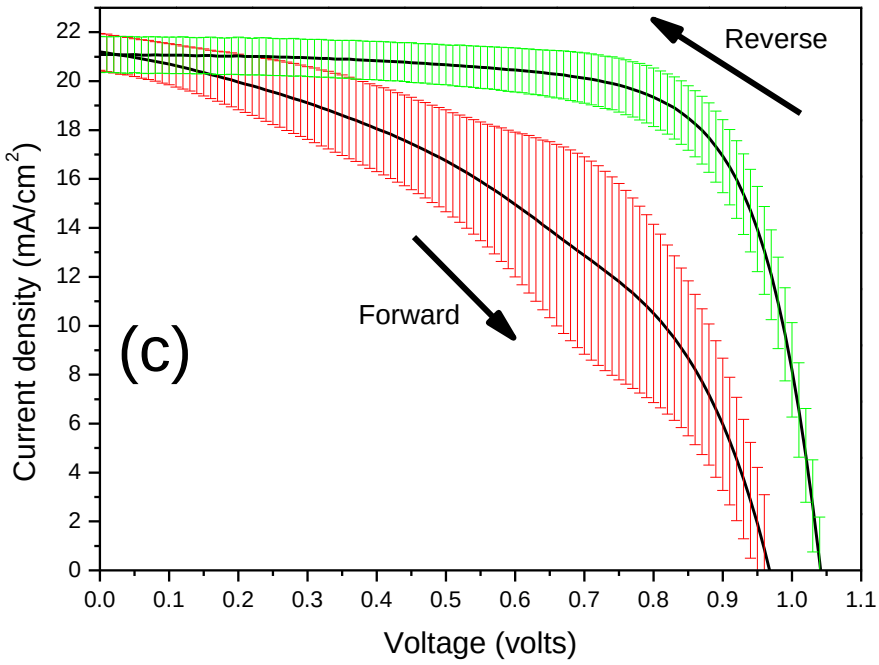
(c)
Reverse
Forward
Current density (mA/cm^2)
Voltage (volts)
0
2
4
6
8
10
12
14
16
18
20
22
0.0
0.1
0.2
0.3
0.4
0.5
0.6
0.7
0.8
0.9
1.0
1.1

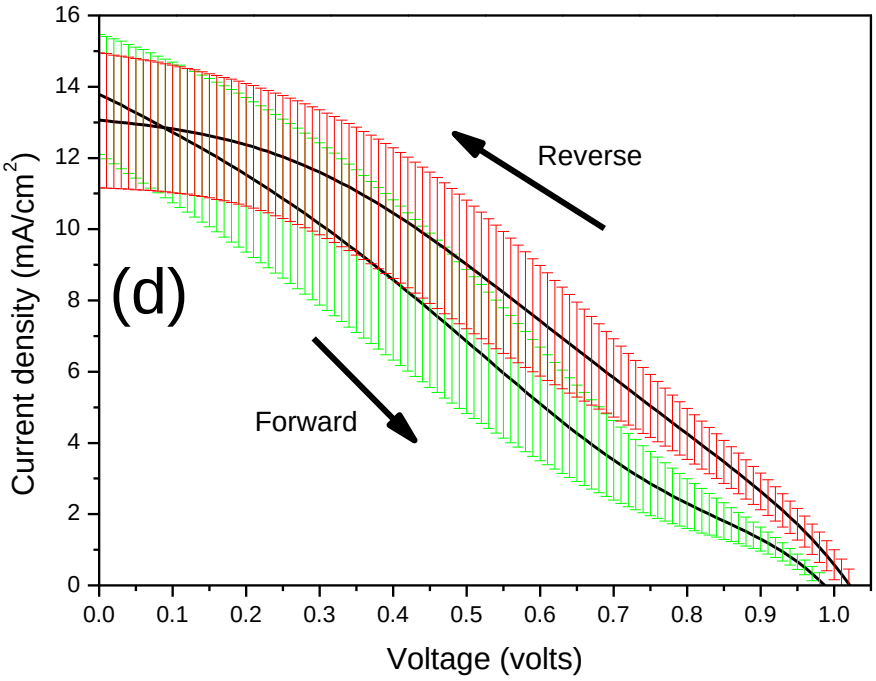

Figure 3.20: Characteristic current density – voltage curves in forward (0 → V_{OC}) and reverse (V_{OC} → 0) scans of PSC devices with structure glass / ITO / SnO_2 / $CH_3NH_3PbI_3$ / Spiro - OMeTAD / Au, as function of the photoactive layer fabricated using either $CH_3NH_3PbI_3$ micro-crystals or equimolar amounts of different PbI_2 with CH_3NH_3I. (a) $CH_3NH_3PbI_3$ micro-crystals made using almost stoichiometric MC2 PbI_2, (b) $CH_3NH_3PbI_3$ micro-crystals made using sub-stoichiometric SA PbI_2, (c) equimolar amounts of almost stoichiometric MC2 PbI_2 / CH_3NH_3I and (d) equimolar amounts of sub-stoichiometric SA PbI_2 / CH_3NH_3I. Black curves correspond to the average of current density – voltage curves and coloured stripes to their deviation from the average black curve. Green and red coloured stripes, indicate current density – voltage data collected in forward (0 → V_{OC}) and reverse (V_{OC} → 0) scans, respectively.

The photovoltaic parameters (FF, V_{OC}, J_{SC} and PCE) of PSC devices were significantly enhanced, when the photoactive layer was fabricated by using either the re-dissolved $CH_3NH_3PbI_3$ micro-crystals or equimolar amounts of almost stoichiometric MC2 PbI_2 with CH_3NH_3I. Using the re-dissolved micro-crystals, will have the effect of correcting the iodide content in the used PbI_2 (both the sub-stoichiometric SA or almost stoichiometric MC2), because the micro-crystals were synthesised in a 30 % excess by weight of CH_3NH_3I. The almost stoichiometric MC2 PbI_2 had a closer to the identical lead to iodide ratio. In contrast, when the photoactive layer was fabricated by using equimolar amounts of the sub-stoichiometric SA PbI_2 in reaction with CH_3NH_3I, the photovoltaic parameters (FF, J_{SC} and PCE) of PSC devices were remarkably inferior.

That is reflected by the non-identical (1:2) atomic ratio between the lead to iodide in SA PbI_2 used and the presence of unreacted PbI_2, as analysed in the previous section (3.2.5 Determining the stoichiometry in PbI_2 by XRD). However, the values of V_{OC} did not follow the similar inferior trend, indicating absence of shunt paths. The presence of unreacted PbI_2 either between or presumably within the grains of the $CH_3NH_3PbI_3$,[29–31] is responsible for charge carriers recombination which reduces the photocurrent and hinders device performance, when the $CH_3NH_3PbI_3$ thin film is fabricated using equimolar amounts of the sub-stoichiometric SA PbI_2 in reaction with CH_3NH_3I. Additionally, a debatable issue has been emerged around the role of the excess PbI_2 used and the presence of unreacted PbI_2 during the formation of perovskite as previously presented by Adachi *et al., Dai et al.*, Seok *et al.* and Jacobsson *et al.*.[3,32–34] We believe that if sub-stoichiometric PbI_2 is used for the synthesis of perovskites as a first step, the content of halogen should be carefully corrected obeying to the general chemical formula for perovskites (ABX_3) in a repeatable way and as a further in parallel second step the excess of PbI_2 added to be correlated with optoelectronic properties of the final perovskite. Theoretically, the presence of added ions in a stoichiometrically perfect perovskite originated from the excess of PbI_2 used, will improve the optoelectronic properties of PSC devices due to improved charge carriers transportation between the grain boundaries, inner volume of grains and the interfaces ETL/perovskite – perovskite/HTL. However, the amount of excess PbI_2 used might have an upper limit, which above that acts as a hindering barrier for the stability of perovskite, as noted by Adachi *et al*.[32]

3.3 Conclusion

In conclusion, the synthesis of PbI_2 by employing planetary ball milling is a low-cost, water-free and energy efficient (~ 31.3 watts per hour per gram) process to produce moderate quantities (≥ 40 grams per run and yield ~ 96 ± 0.5 %). This mechanochemical method, is able to regulate both the stoichiometry and polytypism of the resulting PbI_2, by varying the mechanochemical parameters of synthesis (revolutions per minute and time duration), as determined by XRD, XPS and RBS analysis. Stoichiometric ratio between the lead to iodide atoms of mechanochemical and commercial PbI_2 powders was also evaluated by controllable synthesis of

$CH_3NH_3PbI_3$ micro-crystals. Planetary ball milling synthesis might result in reduction of lead oxyiodide and lead iodide hydroxide compounds, in comparison with the solvothermal process, as determined by EDS-SEM and XPS analysis. This is due to the absence of water molecules in the planetary ball milling process. Also, further reduction of oxygen ~ 36 (± 10) %) in mechanochemical PbI_2, is achievable by displacing the ambient air inside the ball milling jar with argon gas. PSC devices fabricated with $CH_3NH_3PbI_3$ thin films as photoactive layers manufactured using sub - stoichiometric PbI_2, showed reduction in their average performance from ~ 15.5 % to ~ 4.6 % due to the presence of unreacted PbI_2, unless additional iodide was introduced via an excess of CH_3NH_3I, during the fabrication of $CH_3NH_3PbI_3$ micro-crystals. Also, $CH_3NH_3PbI_3$ thin films were manufactured using only DMSO which is a non-toxic solvent. In combination with a single step vacuum assisted method, promotion of two-dimensional layered structures were formed, regardless of the stoichiometry and polytypic phase present in the PbI_2 used. We believe, that using materials with corrected stoichiometry, alongside a simple and repeatable deposition process for the fabrication of PSC devices, might hold the key to consistently achieving high efficiency and more stable PSC.

3.4 References

1 A. Kojima, K. Teshima, Y. Shirai and T. Miyasaka, *J. Am. Chem. Soc.*, 2009, **131 (17)**, 6050–6051.

2 S. S. Shin, E. J. Yeom, W. S. Yang, S. Hur, M. G. Kim, J. Im, J. Seo, J. H. Noh and S. Il Seok, *Science,* 2017, **356**, 167–171.

3 T. J. Jacobsson, J. P. Correa-Baena, E. H. Anaraki, B. Philippe, S. D. Stranks, M. E. F. Bouduban, W. Tress, K. Schenk, J. Teuscher, J. E. Moser, H. Rensmo and A. Hagfeldt, *J. Am. Chem. Soc.*, 2016, **138**, 10331–10343.

4 R. Wang, M. Mujahid, Y. Duan, Z. Wang, J. Xue and Y. Yang, *Adv. Funct. Mater.*, 2019, **1808843**, 1–25.

5 F. Huang, M. Li, P. Siffalovic, G. Cao and J. Tian, *Energy Environ. Sci.*, 2019, **12**, 518–549.

6 M. Saliba, T. Matsui, J. Seo, K. Domanski, J. Correa-Baena, M. Nazeeruddin, S. Zakeeruddin, W. Tress, A. Abate, A. Hagfeldt and M. Grätzel, *Energy Environ. Sci.*, 2016, **9**, 1989.

7 C. Rolda-Carmona, P. Gratia, I. Zimmermann, G. Grancini, P. Gao, M. Graetzel and M. K. Nazeeruddin, *Energy Environ. Sci.*, 2015, **8**, 3550–3556.

8 Z. Song, S. C. Watthage, A. B. Phillips and M. J. Heben, *J. Photonics Energy*, 2016, **6 (2)**, 022001.

9 M. A. Bredig, C. E. Bamberger and D. M. Richardson, *J. Inorg. Nucl. Chem.*, 1978, **40**, 1497–1500.

10 F. J. Berry, C. H. W. Jones and M. Dombsky, *J. Solid State Chem.*, 1983, **46**, 41–45.

11 F. Tavakoli, M. Salavati-Niasari and F. Mohandes, *Ultrason. Sonochem.*, 2013, **21**, 234–241.

12 P. Y. Butyagin and A. N. Streletskii, *Phys. Solid State*, 2005, **47**, 856–862.

13 S. Wang, Y. Jiang, E. J. Juarez-Perez, L. K. Ono and Y. Qi, *Nat. Energy*, 2016, **2**, 16195.

14 R. Brenes, C. Eames, V. Bulović, M. S. Islam and S. D. Stranks, *Adv. Mater.*, 2018, **30**, 1706208.

15 Q. Wang, B. Chen, Y. Liu, Y. Deng, Y. Bai, Q. Dong and J. Huang, *Energy Environ. Sci.*, 2017, **10**, 516–522.

16 Y. Zhang, H. Lv, C. Cui, L. Xu, P. Wang, H. Wang, X. Yu, J. Xie, J. Huang, Z. Tang and D. Yang, *Nanotechnology*, 2017, **28**, 205401.

17 S. Kim, S. Bae, S. Lee, K. Cho, K. D. Lee, S. Park, G. Kwon, S. Ahn, H. Lee, Y. Kang, S. Lee and D. Kim, *Sci. Rep.*, 2017, **7**, 1200.

18 C. Besleaga, L. E. Abramiuc, V. Stancu, A. G. Tomulescu, M. Sima, L. Trinca, N. Plugaru, L. Pintilie, G. A. Nemnes, M. Iliescu, H. Gud, A. Manolescu and I. Pintilie, *J. Phys. Chem. Lett.*, 2016, **7**, 5168–5175.

19 M. Wong-Stringer, O. S. Game, J. A. Smith, T. J. Routledge, B. A. Alqurashy, B. G. Freestone, A. J. Parnell, N. Vaenas, V. Kumar, M. O. A. Alawad, A. Iraqi, C. Rodenburg and D. G. Lidzey, *Adv. Energy Mater. Energy*, 2018, **8**, 1801234.

20 M. Acik, T. M. Alam, F. Guo, Y. Ren, B. Lee, R. A. Rosenberg, J. F. Mitchell, I. K. Park, G. Lee and S. B. Darling, *Adv. Energy Mater.*, 2018, **8**, 1701726.

21 J. H. Heo, D. H. Song, H. J. Han, S. Y. Kim, J. H. Kim, D. Kim, H. W. Shin, T. K. Ahn, C. Wolf, T. Lee and S. H. Im, *Adv. Mater.*, 2015, **27**, 3424–3430.

22 M. U. Rothmann, W. Li, Y. Zhu, U. Bach, L. Spiccia, J. Etheridge and Y.-B. Cheng, *Nat. Commun.*, 2017, **8**, 14547.

23 Y. Liu, L. Collins, R. Proksch, S. Kim, B. R. Watson, B. Doughty, T. R. Calhoun, M. Ahmadi, A. V. Levlev, S. Jesse, S. T. Retterer, A. Belianinov, K. Xiao, J. Huang, B. G. Sumpter, S. V. Kalinin, B. Hu and O. S. Ovchinnikova, *Nat. Mater.*, 2018, **17**, 1013–1019.

24 C. Lan, Z. Zhou, R. Wei and J. C. Ho, *Mater. Today Energy*, 2019, **11**, 61–82.

25 Y. Kutes, Y. Zhou, J. L. Bosse, J. Steffes, N. P. Padture and B. D. Huey, *Nano Lett.*, 2016, **16**, 3434–3441.

26 V. A. Clemente da Silva Filho, J. M. Ermakov and F. C. Marques, *Sci. Rep.*, 2018, **8**, 1–8.

27 A. Buin, R. Comin, J. Xu, A. H. Ip and E. H. Sargent, *Chem. Mater.*, 2015, **27**, 4405–4412.

28 C. Wu, Q. Zhang, Y. Liu, W. Luo, X. Guo, Z. Huang, H. Ting, W. Sun, X. Zhong, S. Wei, S. Wang, Z. Chen and L. Xiao, *Adv. Sci.*, 2017, **1700759**, 2–9.

29 A. Ummadisingu and M. Grätzel, *Sci. Adv.*, 2018, **4**, e1701402.

30 B. Philippe, M. Saliba, J. P. Correa-Baena, U. B. Cappel, S. H. Turren-Cruz, M. Grätzel, A. Hagfeldt and H. Rensmo, *Chem. Mater.*, 2017, **29**, 3589–3596.

31 T. Du, C. H. Burgess, J. Kim, J. Zhang, R. Durrant and M. A. Mclachlan, *Sustain. Energy Fuels*, 2017, **1**, 119–126.

32 G. Tumen-ulzii, C. Qin, D. Klotz, M. R. Leyden, P. Wang, M. Auffray, T. Fujihara, T. Matsushima, J. Lee, S. Lee, Y. Yang and C. Adachi, *Adv. Mater.*, 2020, **1905035**, 1–7.

33 F. Liu, Q. Dong, M. K. Wong, A. B. Djurišic, A. Ng, Z. Ren, Q. Shen, C. Surya, W. K. Chan, J. Wang, A. Man and C. Ng, *Adv. Energy Mater.*, 2016, **6**, **1502206**, 1–9.

34 B. Park, N. Kedem, M. Kulbak, D. Y. Lee, W. S. Yang, N. J. Jeon, J. Seo, G. Kim, K. J. Kim, T. J. Shin, G. Hodes, D. Cahen and S. Il Seok, *Nat. Commun.*, 2018, **(9) 3301**, 1–8.

Chapter 4

Implications of dopant agents in perovskite ($CH_3NH_3PbI_3$)

4.1 Introduction

As presented in chapter 3, only the stoichiometric ratio between the lead and iodide atoms and not the number of polytypic phases present in the PbI_2 powder (either commercial or mechanochemical), has significant implications at the quality of the $CH_3NH_3PbI_3$ formed. The optoelectronic properties in perovskites (such as the energy band gap, improved charge carrier transport), are strongly influenced by the different cations and halogens used. [1] The concept of controllable doping might lead to reproducible synthesis of perovskites with optimum and repeatable optoelectronic properties, since the coexistence of different mixtures of A and X ions with variable effective ionic radius, require a specific ratio between them resulting in a minimum of distortion in the crystal structure of perovskites formatted. In this chapter further steps, which include controllable doping either of the A or X or A and X sites the implications in the crystal structure of $CH_3NH_3PbI_3$ with general chemical formula ABX_3 are considered. Also, will be described in detail the importance of controllable substitution of methylammonium with formamidinium cations and iodide with bromide anions. The optimum ratio between the different substituted ions in the $CH_3NH_3PbI_3$ crystal structure, was determined by the tetragonal to cubic crystal structure transition in synthesised micro-crystals, in respect to the amount of substituted ions, as observed by X-ray diffraction (XRD) spectra. Morphological characterisation of the doped perovskite micro - crystals as fabricated and when cast into thin films, was accomplished by scanning electron microscopy (SEM) and atomic force microscopy (AFM). The results were compared, alongside the undoped $CH_3NH_3PbI_3$ micro-crystals and thin films. Fluctuations in the optical band gap values, were also observed

in respect to the selective substitution of different ions in the $CH_3NH_3PbI_3$ crystal structure, as determined by visible-infrared (Vis-IR) spectroscopy. Additionally, the power conversion efficiency (PCE) of the perovskite solar cells (PSCs) devices subsequently fabricated using the synthesised perovskites with controlled doping levels within the photoactive layers, were evaluated over 240 hours.

4.2 Results and discussion

4.2.1 X-ray diffraction analysis of doped $CH_3NH_3PbI_3$ micro-crystals

Doped $CH_3NH_3PbI_3$ micro-crystals were synthesised by the method of 1-pentanol / PbI_2 / CH_3NH_3I,[2] in reaction with various amounts of dopants, either CH_3NH_3Br or $CH(NH_2)_2I$ or $CH(NH_2)_2I$ and Br_2, at a temperature of 90 ºC and for a fixed duration of 24 hours. The amount dopants were calculated based on the number of PbI_2 moles used. All versions of the micro-crystals were fabricated by using the almost stoichiometric MC2 PbI_2 mixed with an equimolar amount plus 10 % excess by weight of CH_3NH_3I in reaction with the dopants, followed by XRD characterisation. An excess 10 % by weight of CH_3NH_3I was used in all chemical reactions during the manufacture of doped $CH_3NH_3PbI_3$ micro-crystals, since the mechanochemically synthesised MC2 PbI_2 is deficient in iodide by a 4 % (see chapter 3). The first group of doped $CH_3NH_3PbI_3$ micro-crystals were fabricated with various amounts of CH_3NH_3Br. This resulted in an optimum percentage of ~ 40 % additional CH_3NH_3Br moles, as defined by the transition from tetragonal to cubic crystal structure. The transition was indicated in the high resolution XRD patterns when the 1st, 2nd and 3rd high intensity sets of peaks with diffraction angles 2θ in the ranges 11 º to 16 º, 27 º to 30 º and 30 º to 33 º , respectively, as shown in figures 4.1 a, 4.1 b, 4.1 c and 4.1 d. Change from the sets of multiple peaks to single peak, is indicative of the tetragonal to cubic structure transition. Similar crystallographic structural transitions, have also been observed in mixed cation halide perovskite single crystals, as noted in literature. [3–5] For the 1st set of peaks, the reduction of the diffracted peak that corresponds to plane with Miller indices (200) at angle 2θ ≈ 14.06 º, was observed as function of the CH_3NH_3Br added This is not immediately evident in figure 4.1 a, but is noticeable when shown at higher resolution in figure 4.1 b. Meanwhile for the 2nd and 3rd sets of peaks, similar reductions were noted for the diffracted peaks that correspond to planes with Miller indices (004)

and (222) at angles 2θ ≈ 28.26 º and 2θ ≈ 31.72 º, as shown in figures 4.1 c and 4.1 d, respectively. [6,7]

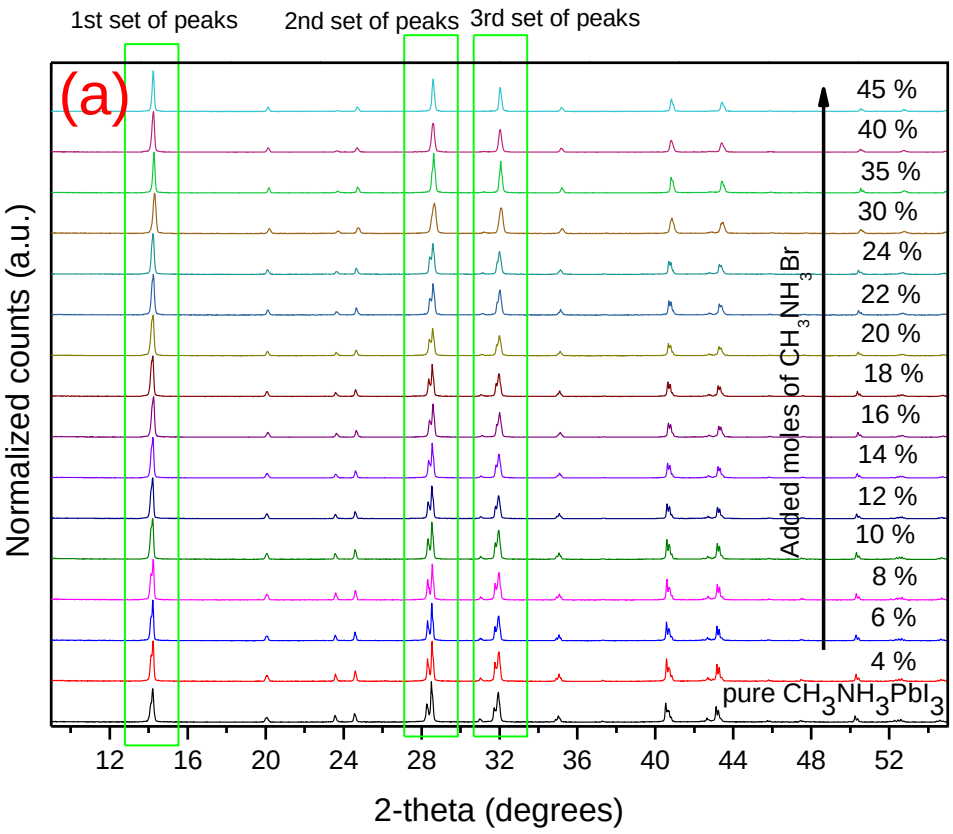

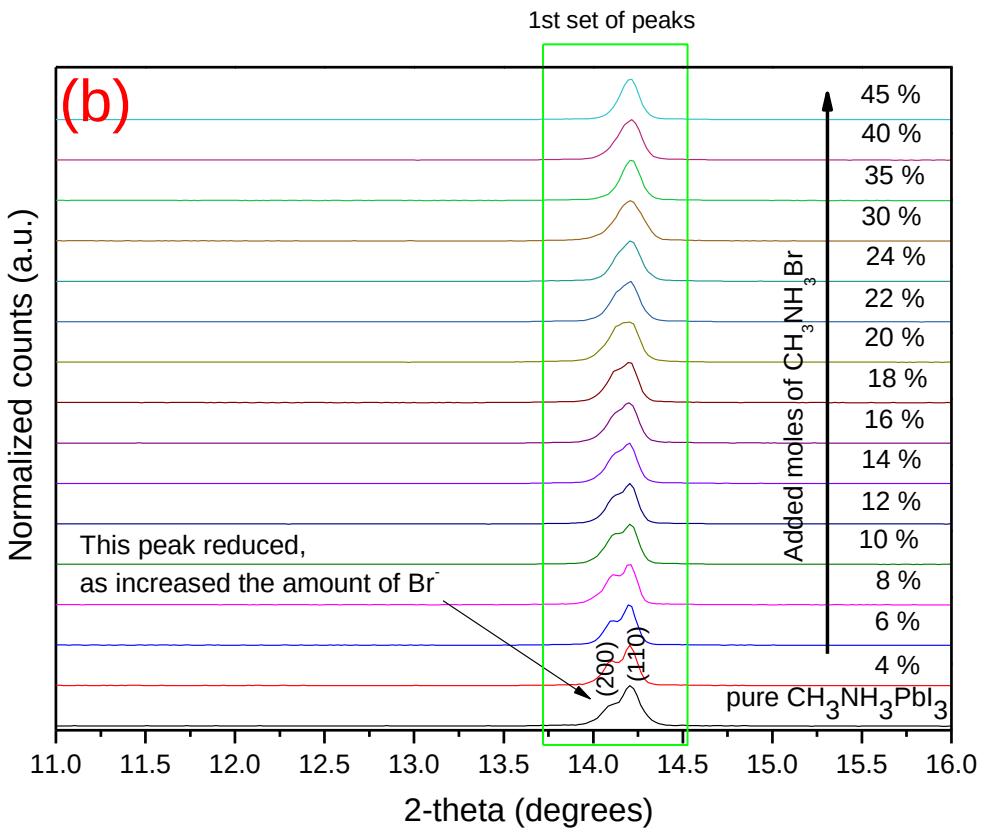
1st set of peaks
(b)
Normalized counts (a.u.)
2-theta (degrees)
11.0
11.5
12.0
12.5
13.0
13.5
14.0
14.5
15.0
15.5
16.0
45 %
40 %
35 %
30 %
24 %
22 %
20 %
18 %
16 %
14 %
12 %
10 %
8 %
6 %
4 %
pure CH3NH3PbI3
Added moles of CH3NH3Br
This peak reduced,
as increased the amount of Br-
(200)
(110)

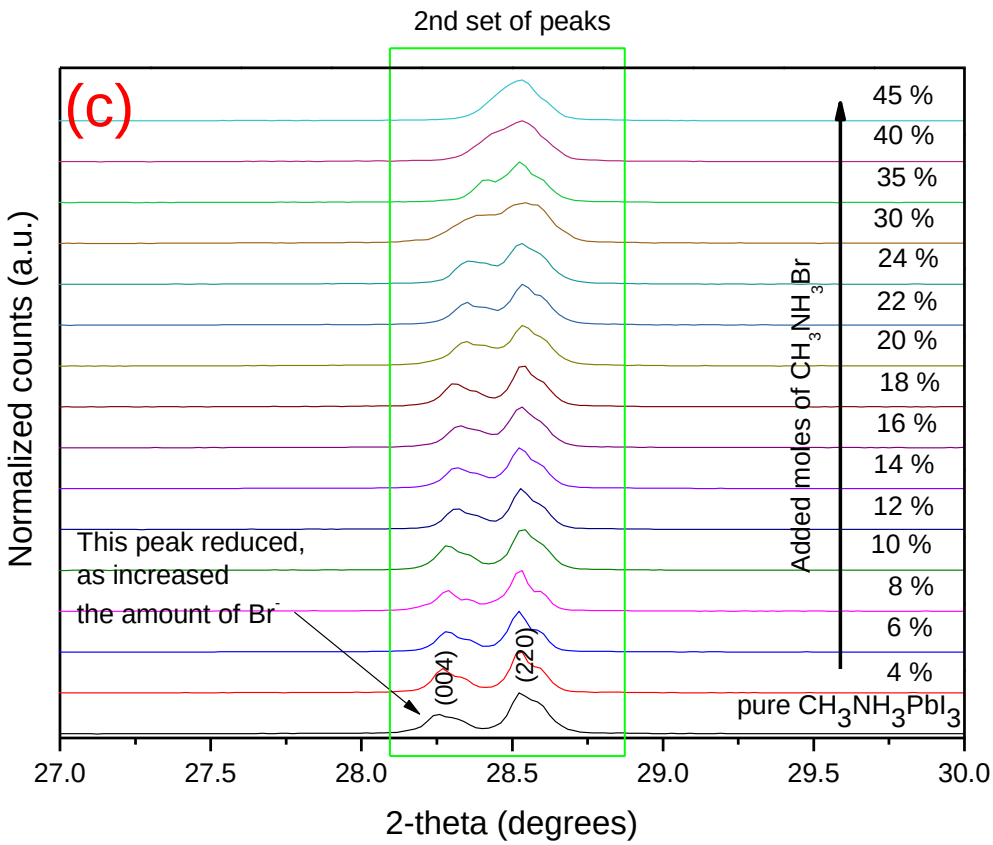
2nd set of peaks
(c)
Normalized counts (a.u.)
2-theta (degrees)
27.0
27.5
28.0
28.5
29.0
29.5
30.0
45 %
40 %
35 %
30 %
24 %
22 %
20 %
18 %
16 %
14 %
12 %
10 %
8 %
6 %
4 %
pure CH3NH3PbI3
Added moles of CH3NH3Br
This peak reduced,
as increased
the amount of Br-
(004)
(220)

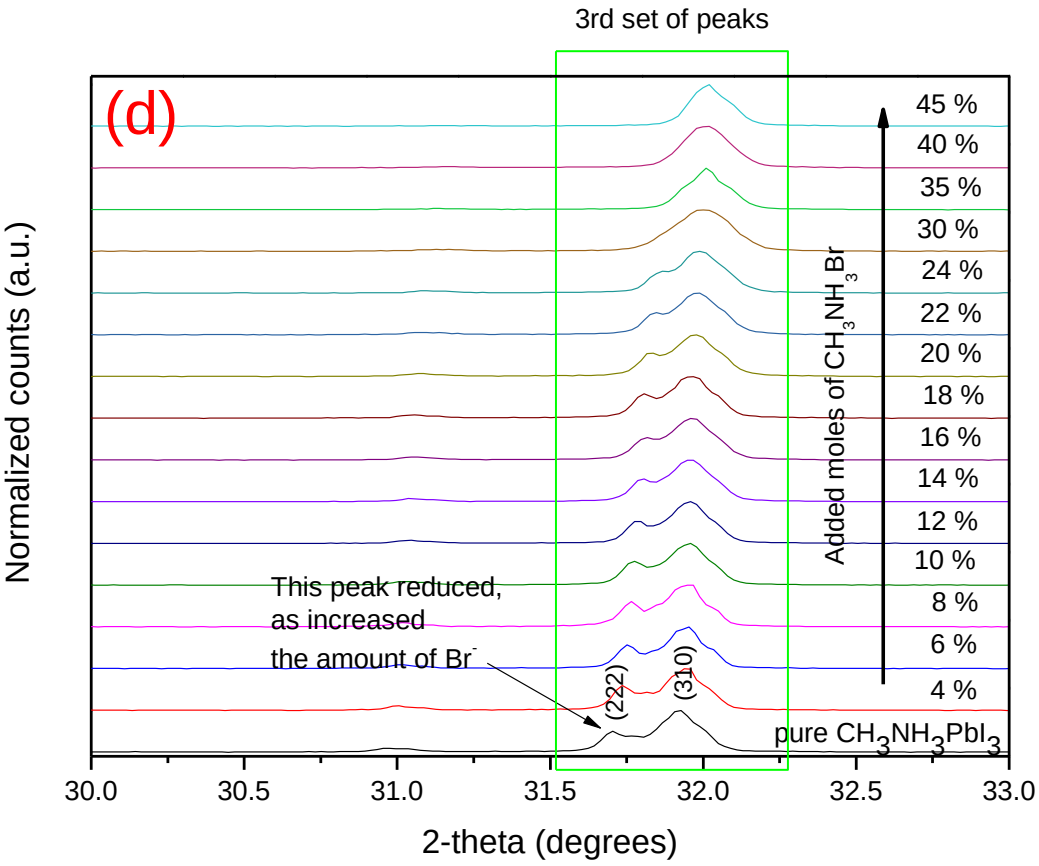

Figure 4.1: XRD patterns of $CH_3NH_3PbI_3$ micro-crystals synthesized using almost stoichiometric MC2 PbI_2 in reaction with equimolar plus an excess 10 % by weight of CH_3NH_3I and controllably added amount of CH_3NH_3Br. (a) for diffracted angle 2θ from 9 º to 55 º, (b) 1st set of peaks for diffracted angle 2θ from 11 º to 16 º, (c) 2nd set of peaks for diffracted angle 2θ from 27 º to 30 º and (d) 3rd set of peaks for diffracted angle 2θ from 30 º to 33 º. XRD peaks that correspond to crystallographic planes with Miller indices (200) and (110), referred to the perovskite with tetragonal crystal structure. Normalization in all XRD patterns, was in respect to XRD peak that corresponds to crystallographic plane with Miller indices (110).

However, this transition from tetragonal to cubic crystal structure due to the various amount of CH_3NH_3Br added, revealed only the effects of doping with respect to the X site in the general chemical formula for perovskites ABX_3.

In the second group of doped $CH_3NH_3PbI_3$ micro-crystals fabricated, a various amount of $CH(NH_2)_2I$ was used. Resulting in an optimum percentage ~ 14 % of $CH(NH_2)_2I$ moles added, again defined by the transition in the crystal structure as indicated in the high resolution XRD patterns. The transitions of the same 1st, 2nd and 3rd sets of peaks, are shown in figures 4.2 a, 4.2 b, 4.2 c and 4.2 d, as function of the $CH(NH_2)_2I$ added. [8] For the 1st set of peaks, the reduction of the diffraction peak that corresponds to the

(200) plane at angle 2θ ≈ 14.06 º, was observed and shown in figure 4.2 b. While for the 2nd and 3rd sets of peaks, a decrease in the intensity of the diffracted peaks correspond to planes with Miller indices (004) and (222) at angles 2θ ≈ 28.26 º and 2θ ≈ 31.72 º, was noted and shown in figures 4.2 c and 4.2 d, respectively. Also, when an excess amount of $CH(NH_2)_2I$ added (> 14 % moles), distortion of the crystal structure of the already doped $CH_3NH_3PbI_3$, resulted in the reappearance of peaks on the higher angle side of the main diffracted peaks that correspond to (220) and (310) planes at angles 2θ ≈ 28.52 º and 2θ ≈ 31.94 º, as shown in figure 4.2 c and 4.2 d, respectively. This is possibly related with a transition from cubic back to tetragonal crystal structure with different d spacing.

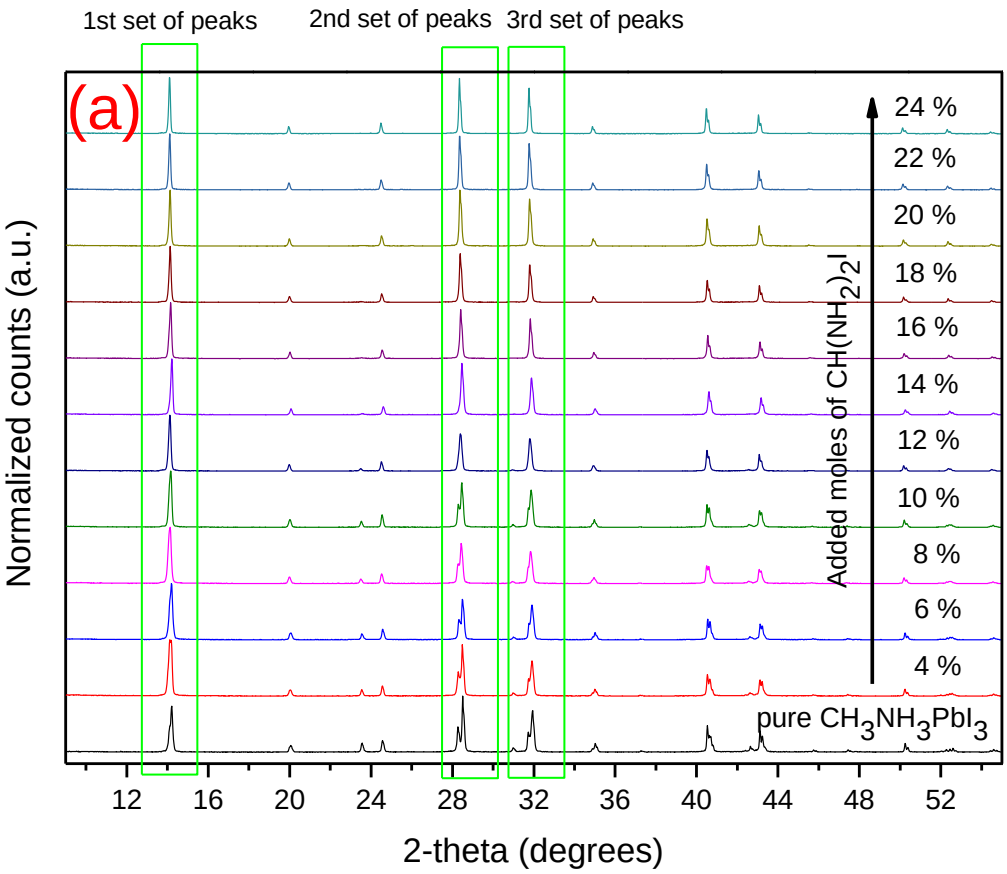

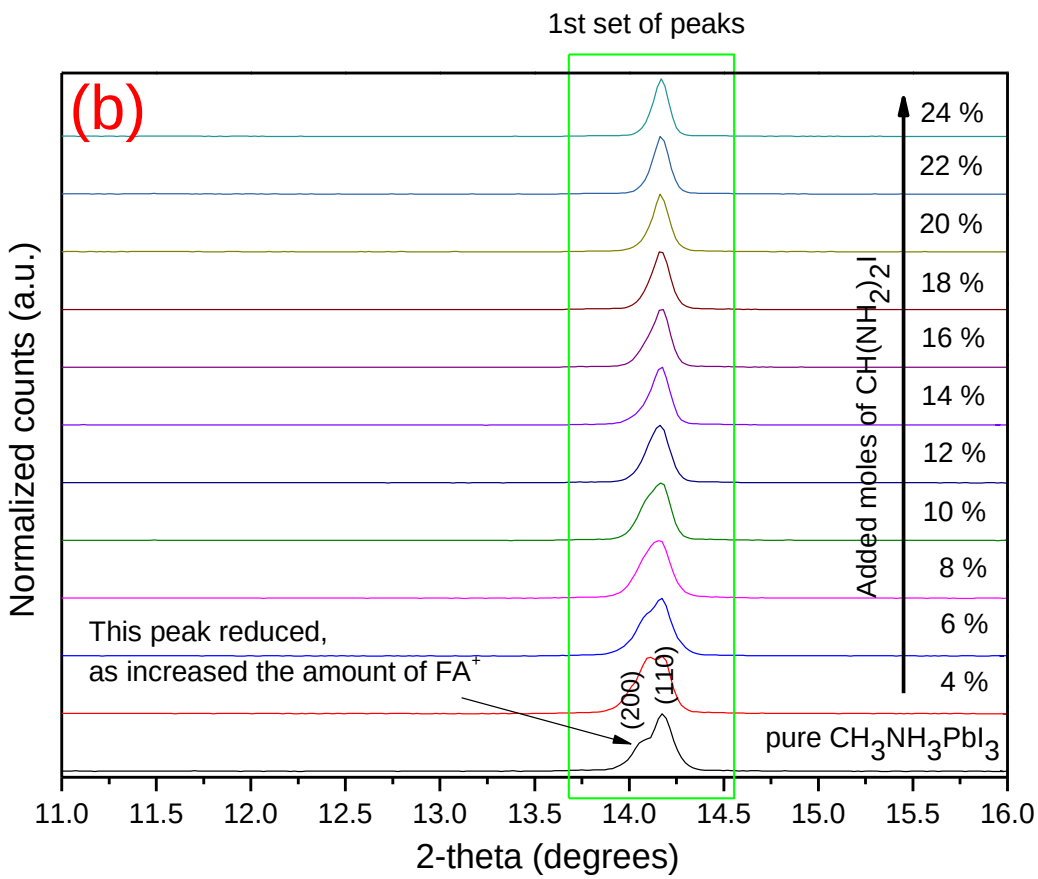
1st set of peaks
(b)
Normalized counts (a.u.)
Added moles of $CH(NH_2)_2I$
24 %
22 %
20 %
18 %
16 %
14 %
12 %
10 %
8 %
6 %
4 %
This peak reduced,
as increased the amount of FA^+
(200)
(110)
pure $CH_3NH_3PbI_3$
11.0
11.5
12.0
12.5
13.0
13.5
14.0
14.5
15.0
15.5
16.0
2-theta (degrees)

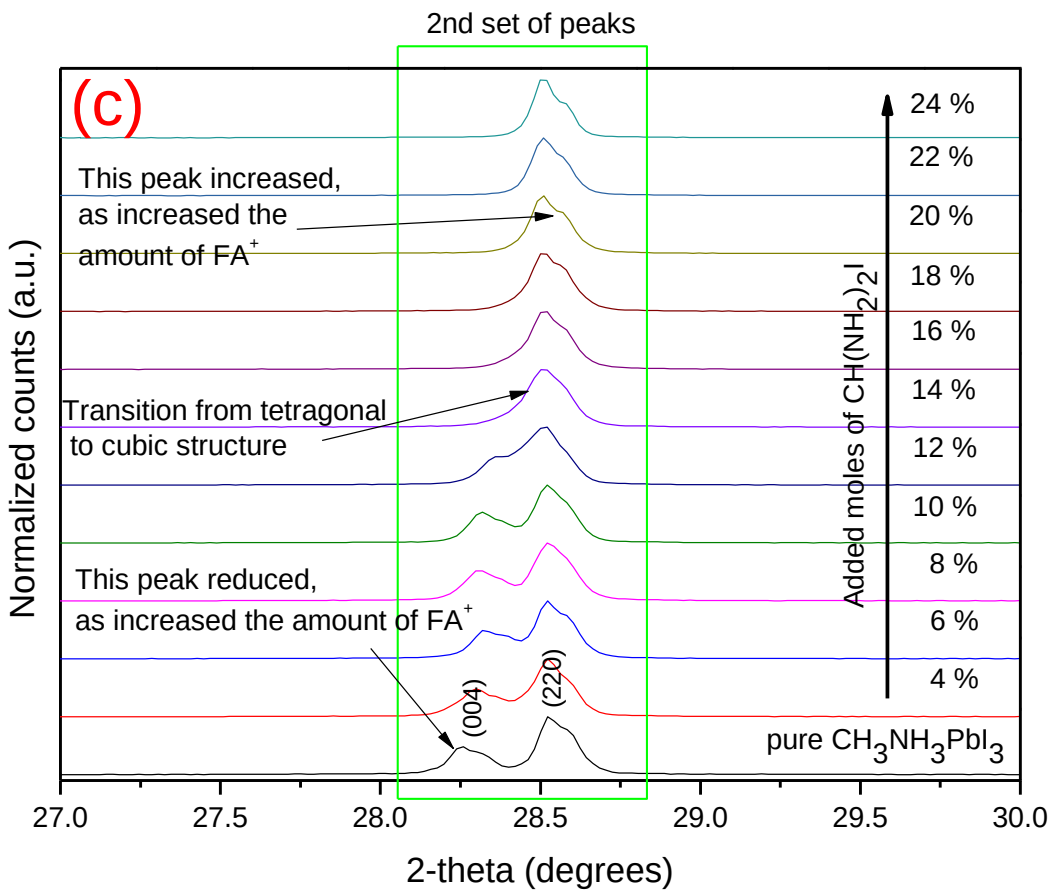
2nd set of peaks
(c)
Normalized counts (a.u.)
Added moles of $CH(NH_2)_2I$
24 %
22 %
20 %
18 %
16 %
14 %
12 %
10 %
8 %
6 %
4 %
This peak increased,
as increased the
amount of FA^+
Transition from tetragonal
to cubic structure
This peak reduced,
as increased the amount of FA^+
(004)
(220)
pure $CH_3NH_3PbI_3$
27.0
27.5
28.0
28.5
29.0
29.5
30.0
2-theta (degrees)

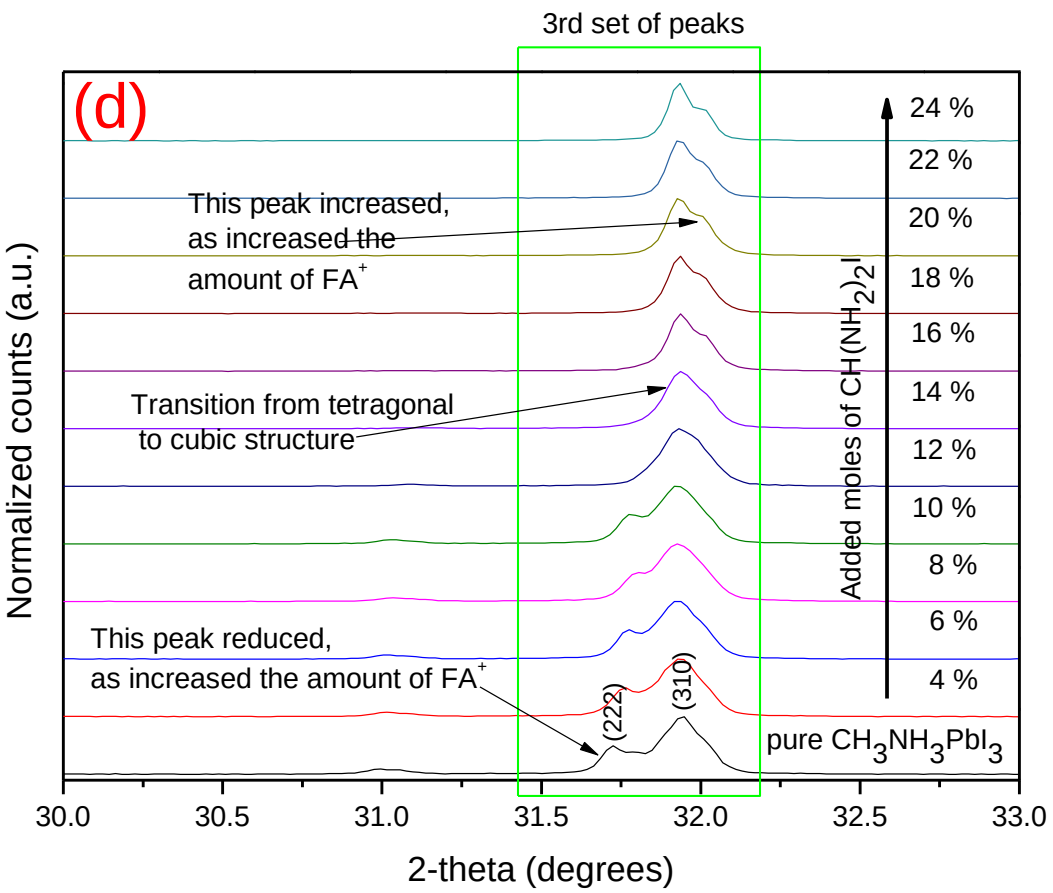

Figure 4.2: XRD patterns of $CH_3NH_3PbI_3$ micro-crystals synthesized using almost stoichiometric MC2 PbI_2 in reaction with equimolar plus an excess 10 % by weight of CH_3NH_3I and controllably added amount of $CH(NH_2)_2I$. (a) for diffracted angle 2θ from 9 º to 55 º, (b) 1st set of peaks for diffracted angle 2θ from 11 º to 16 º, (c) 2nd set of peaks for diffracted angle 2θ from 27 º to 30 º and (d) 3rd set of peaks for diffracted angle 2θ from 30 º to 33 º. XRD peaks that correspond to crystallographic planes with Miller indices (200) and (110), referred to the perovskite with tetragonal crystal structure. Normalization in all XRD patterns, was in respect to XRD peak that corresponds to crystallographic plane with Miller indices (110).

Nevertheless, the optimum amount of added $CH(NH_2)_2I$ (~ 14 % moles), caused a transition from tetragonal to cubic crystal structure, due to the doping at the A site. Consequently, the implication of a second transition at the crystal structure should be identified by a controllably introduced amount of bromide ions in X site, as previously reported by Eperon *et al*. [9]

The third group of doped $CH_3NH_3PbI_3$ micro-crystals were doped with both $CH(NH_2)_2I$ and Br_2, acting on the A and X sites in ABX_3, respectively. In this case the $CH(NH_2)_2I$ doping was fixed at ~ 14 % moles, and amount of Br_2 added was varied. The optimum amount of Br_2 used, was found to be ~ 10 % moles, as determined based on the

transitions observed in the same set of XRD peaks (1st, 2nd and 3rd sets of peaks with the highest intensity of diffraction at 2θ angle from 11 º to 16 º, 27 º to 30 º and 30 º to 33 º, respectively), as shown in figures 4.3 a, 4.3 b, 4.3 c and 4.3 d.

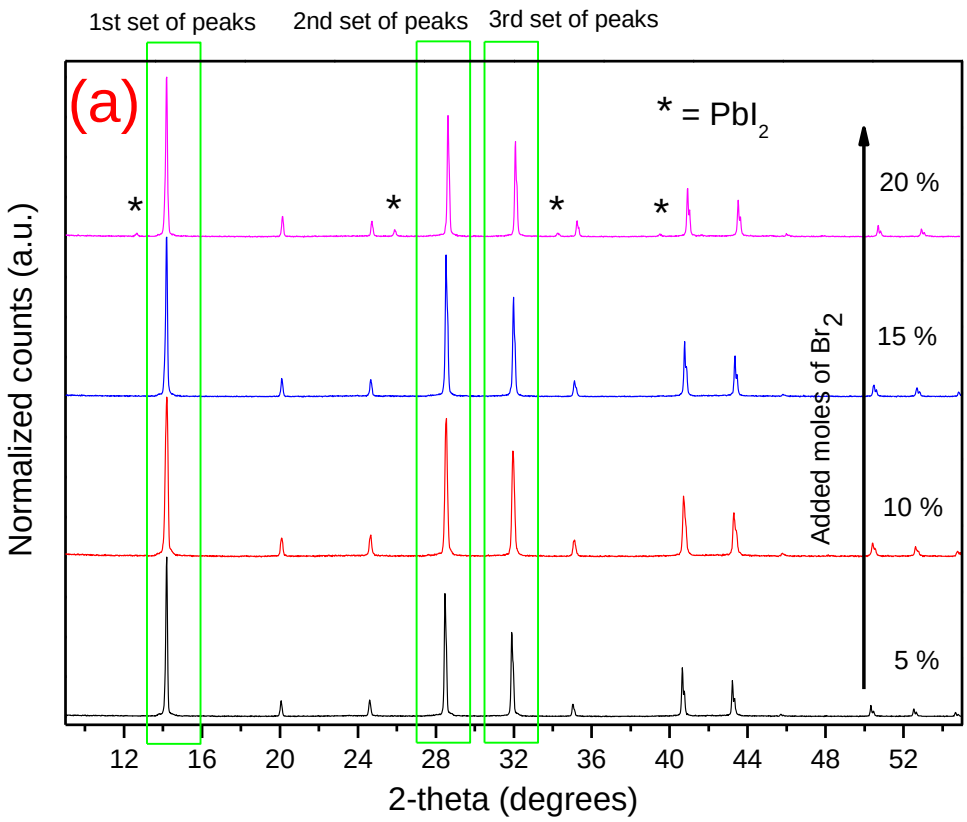

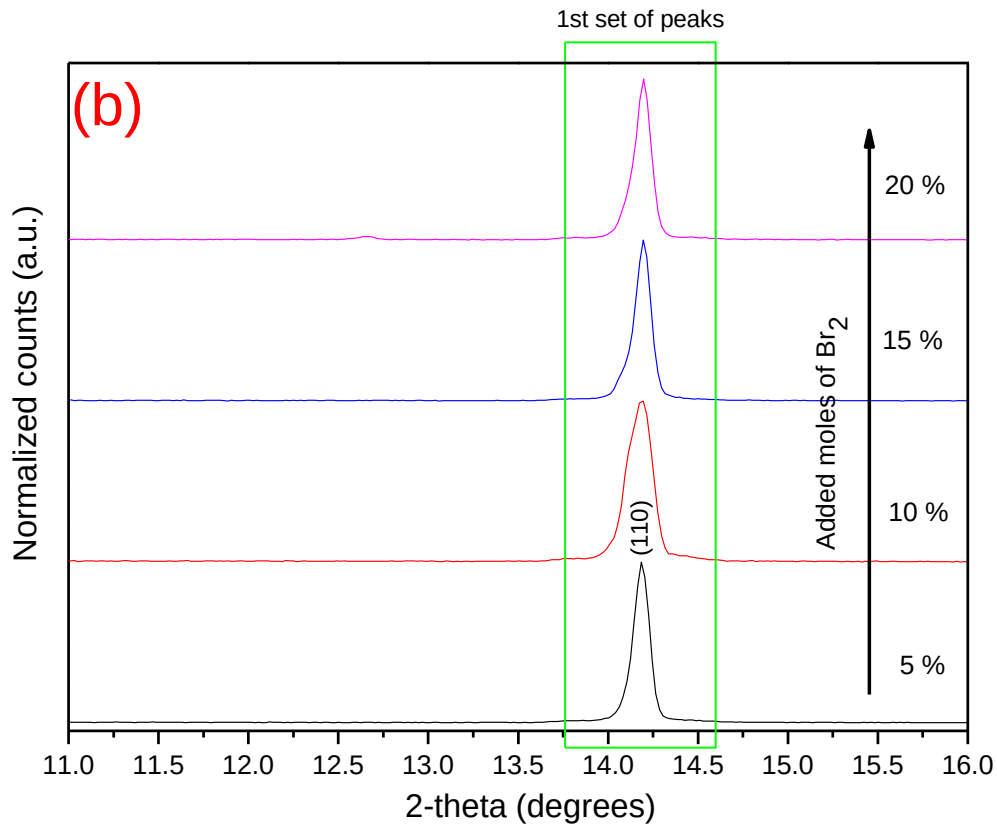
1st set of peaks
(b)
Normalized counts (a.u.)
20 %
15 %
10 %
5 %
Added moles of Br2
(110)
11.0
11.5
12.0
12.5
13.0
13.5
14.0
14.5
15.0
15.5
16.0
2-theta (degrees)

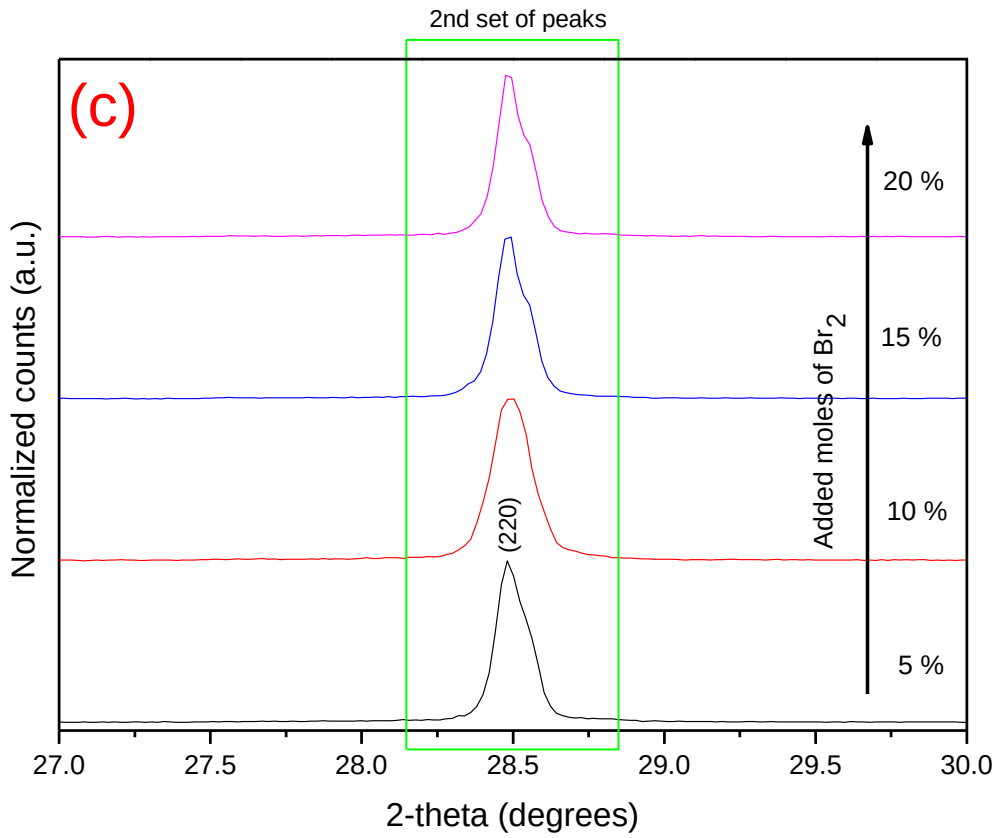
2nd set of peaks
(c)
Normalized counts (a.u.)
20 %
15 %
10 %
5 %
Added moles of Br2
(220)
27.0
27.5
28.0
28.5
29.0
29.5
30.0
2-theta (degrees)

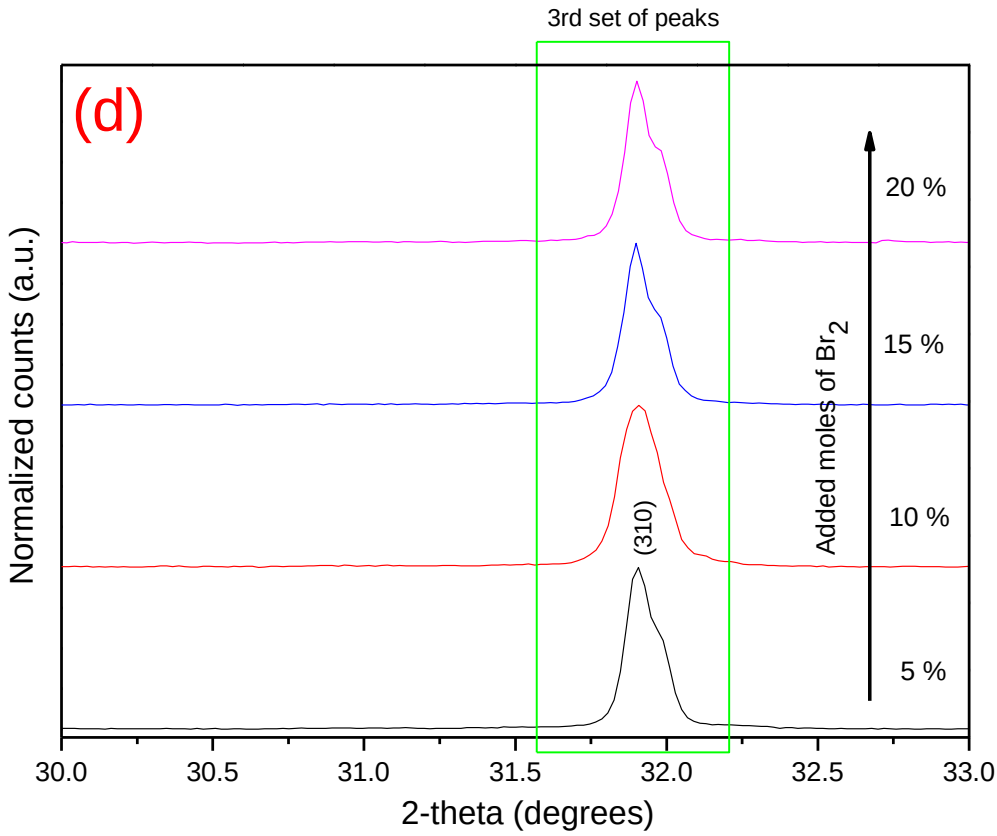

Figure 4.3: XRD patterns of $CH_3NH_3PbI_3$ micro-crystals synthesized using almost stoichiometric MC2 PbI_2 in reaction with equimolar plus an excess 10 % by weight of CH_3NH_3I, 14 % moles of $CH(NH_2)_2I$ and controllable amount of Br_2 added. (a) for diffracted angle 2θ from 9 º to 55 º, (b) 1st set of peaks for diffracted angle 2θ from 11 º to 16 º, (c) 2nd set of peaks for diffracted angle 2θ from 27 º to 30 º and (d) 3rd set of peaks for diffracted angle 2θ from 30 º to 33 º. XRD peaks that correspond to crystallographic planes with Miller indices (200) and (110), referred to the perovskite with tetragonal crystal structure. Asterisks correspond to unreacted PbI_2. Normalization in all XRD patterns, was in respect to XRD peak that corresponds to crystallographic plane with Miller indices (110).

From the 1st set of peaks, no significant change was observed at the diffracted peak that corresponds to plane with Miller indices (110) at angle 2θ ≈ 14.18 º as a function of the Br_2 added and shown in figure 4.3 b. However, for the 2nd and 3rd sets of peaks, the presence of a peak on the higher angle side of the diffracted peaks that correspond to planes with Miller indices (220) and (310) at angles 2θ ≈ 28.48 º and 2θ ≈ 31.91 º, was observed for all quantities other apart from when ~ 10 % moles of Br_2 added, as shown in figures 4.3 c and 4.3 d, respectively. Also, when ~ 20 % moles of Br_2 added, diffraction peaks that correspond to unreacted PbI_2 were noted as indicated with asterisks, in figure 4.3 a. It is assumed, when ~ 20 % moles of Br_2 are added, results in a depletion of the iodide content during the synthesis of doped $CH_3NH_3PbI_3$ micro-

crystals through formation of interhalogen compounds with general chemical formula XY_n, where n ≥ 1, Y are the bromide ions and X are the less electronegative iodide ions.[10] Consequently, the amount of dopant with respect to the size of the effective ionic radius of A and X ions substituted into the crystal structure of the PbI_2, is directly related to the specific number of moles used, resulting in a minimum of distortion of the crystal structure of the $CH_3NH_3PbI_3$. The synthesised micro-crystals were categorised as A, B, C and D type, with respect to the percentage of dopants used, providing an estimation of their chemical formula alongside with their molecular weight, as summarised in table 4.1. The calculation of the estimated molecular weight of each perovskite, was based on the summation of the atomic mass units for the estimated stoichiometry taking into account the ratio of elements present in each corresponding chemical formula.

Type of micro – crystals	Percentage of materials used (based on PbI_2 moles)	Estimated chemical formula	Estimated molecular weight ($g * mol^{-1}$)
A	PbI_2 + equimolar plus 10 % by weight of CH_3NH_3I + 40 % moles of CH_3NH_3Br	$CH_3NH_3PbI_{2.6}Br_{0.4}$	601.18
B	PbI_2 + equimolar plus 10 % by weight of CH_3NH_3I + 14 % moles of $CH(NH_2)_2I$	$(CH_3NH_3)_{0.86}(CH(NH_2)_2)_{0.14}PbI_3$	621.80
C	PbI_2 + equimolar plus 10 % by weight of CH_3NH_3I + 14 % moles of $CH(NH_2)_2I$ + 10 % moles of Br_2	$(CH_3NH_3)_{0.86}(CH(NH_2)_2)_{0.14}PbI_{2.8}Br_{0.2}$	612.40
D	PbI_2 + equimolar plus 10 % by weight of CH_3NH_3I	$CH_3NH_3PbI_3$	619.98

Table 4.1: Type of doped $CH_3NH_3PbI_3$ micro-crystals synthesised at temperature 90 ˚C for 24 hours, using the almost stoichiometric mechanochemical MC2 PbI_2 in reaction with equimolar plus an excess 10 % by weight of CH_3NH_3I and (A) 40 % moles of CH_3NH_3Br, (B) 14 % moles of $CH(NH_2)_2I$, (C) 14 % moles of $CH(NH_2)_2I$ and 10 % moles of Br_2 and (D) no other dopant. Also, estimated chemical formula and molecular weight, is provided for each type of doped $CH_3NH_3PbI_3$ micro-crystals.

4.2.2 Morphology of doped $CH_3NH_3PbI_3$ micro-crystals by SEM

Morphological characterisation of the controllably doped $CH_3NH_3PbI_3$ micro-crystals fabricated using an optimum amount of CH_3NH_3Br, $CH(NH_2)_2I$ and Br_2 as dopants, was performed by SEM. Minor differences were observed among the doped $CH_3NH_3PbI_3$ micro-crystals fabricated using an optimum amount of dopants, as shown by SEM images in figures 4.4 a, 4.4 b and 4.4 c. However, undoped $CH_3NH_3PbI_3$ micro-crystals shown less sharp edges in average, as seen in figure 4.4 d, in comparison with all the doped $CH_3NH_3PbI_3$ micro-crystals. This may be related with the transition from tetragonal to cubic crystal structure, in respect to the substitution of methylammonium with formamidinium cations and iodide with bromide anions, in A and X sites, respectively. Also, SEM images confirm the regular shape of the almost perfect cubic crystal structure adopted by the doped $CH_3NH_3PbI_3$ micro-crystals, as function of the amounts of dopants used.

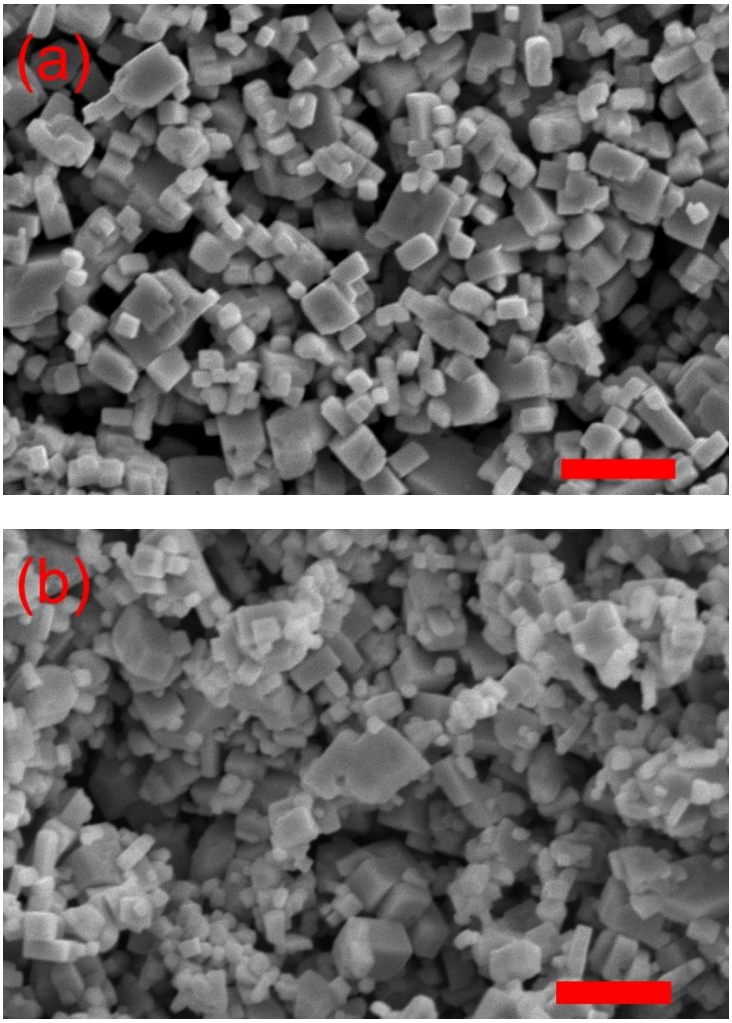

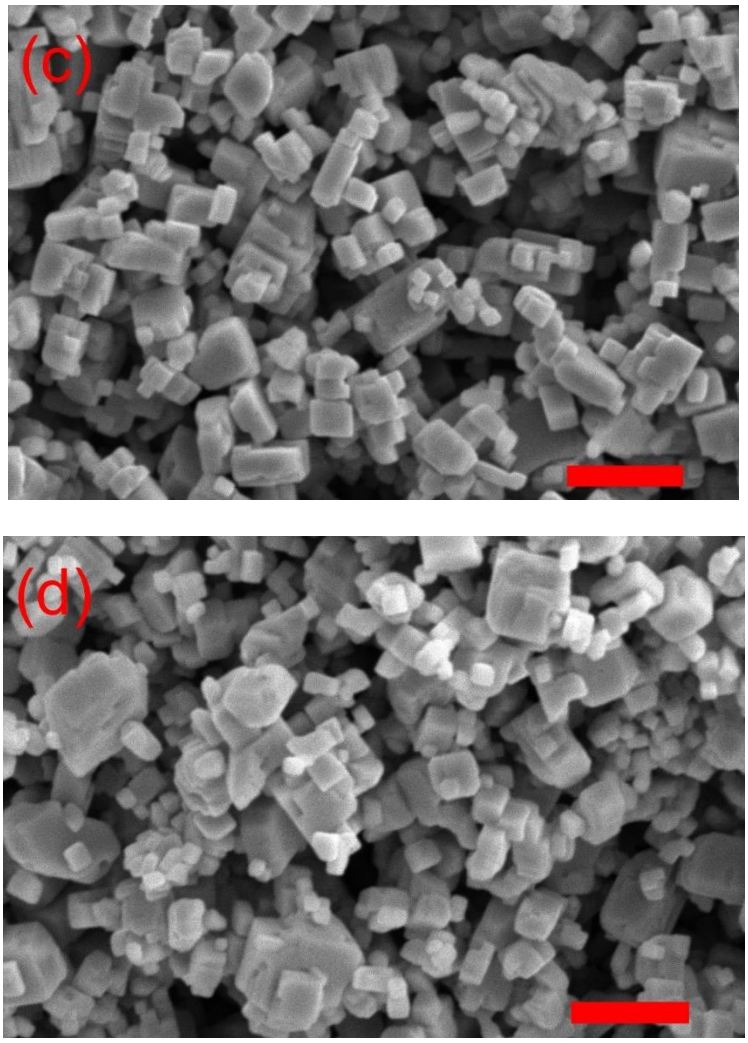

Figure 4.4: Scanning electron microscopy (SEM) images of doped $CH_3NH_3PbI_3$ micro-crystals synthesised at temperature 90˚C for 24 hours, using the almost stoichiometric mechanochemical MC2 PbI_2 in reaction with equimolar plus an excess 10 % by weight of CH_3NH_3I and (a) 40 % moles of CH_3NH_3Br, (b) 14 % moles of $CH(NH_2)_2I$, (c) 14 % moles of $CH(NH_2)_2I$ and 10 % moles of Br_2 and (d) no other dopant. Scale bars represent 5 μm.

4.2.3 Morphology of thin films made of undoped or doped $CH_3NH_3PbI_3$ micro-crystals by AFM

Morphological characterisation of the thin perovskite films formed after deposition on glass, using the controllably doped or the undoped $CH_3NH_3PbI_3$ micro-crystals, was performed by atomic force microscopy (AFM). All perovskite thin films were fabricated by re-dissolving doped or the undoped $CH_3NH_3PbI_3$ micro-crystals in Dry DMSO with

concentration 1.13M. The vacuum assisted method was used, as presented in chapter 2 (see experimental section). [11] Formation of two-dimensional randomly orientated layered structures within individual grains, were observed regardless of the level of doping in micro-crystals used. These layered structures have also been noted in literature [12–14] and confirmed by AFM, as shown in figures 4.5 a, 4.5 b, 4.5 c and 4.5 d. The measured roughness and thickness of all the thin films fabricated using doped or undoped $CH_3NH_3PbI_3$ micro-crystals, was less than 12 nm and 300 nm (± 10 nm), respectively, as measured by AFM. Also, the consistency of the values of thickness measured in all perovskite thin films (at four different points on each sample), indicates that the concentration of all perovskite solutions (1.13 M) using doped or the undoped $CH_3NH_3PbI_3$ micro-crystals, was very consistent and accurately calculated based on the corresponding estimated molecular weights.

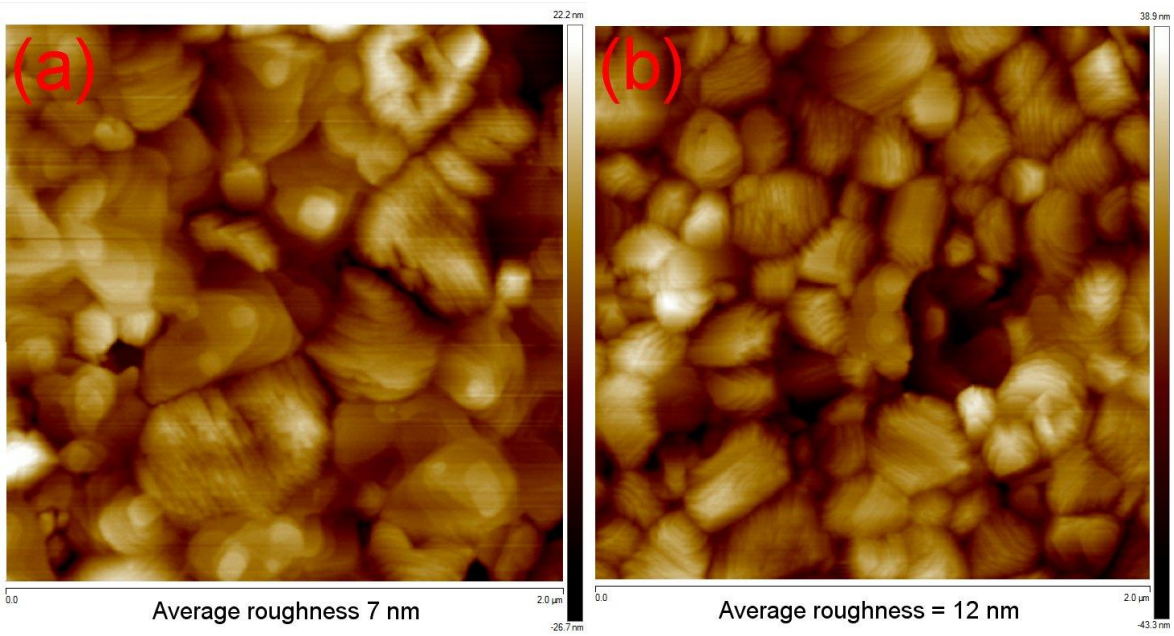

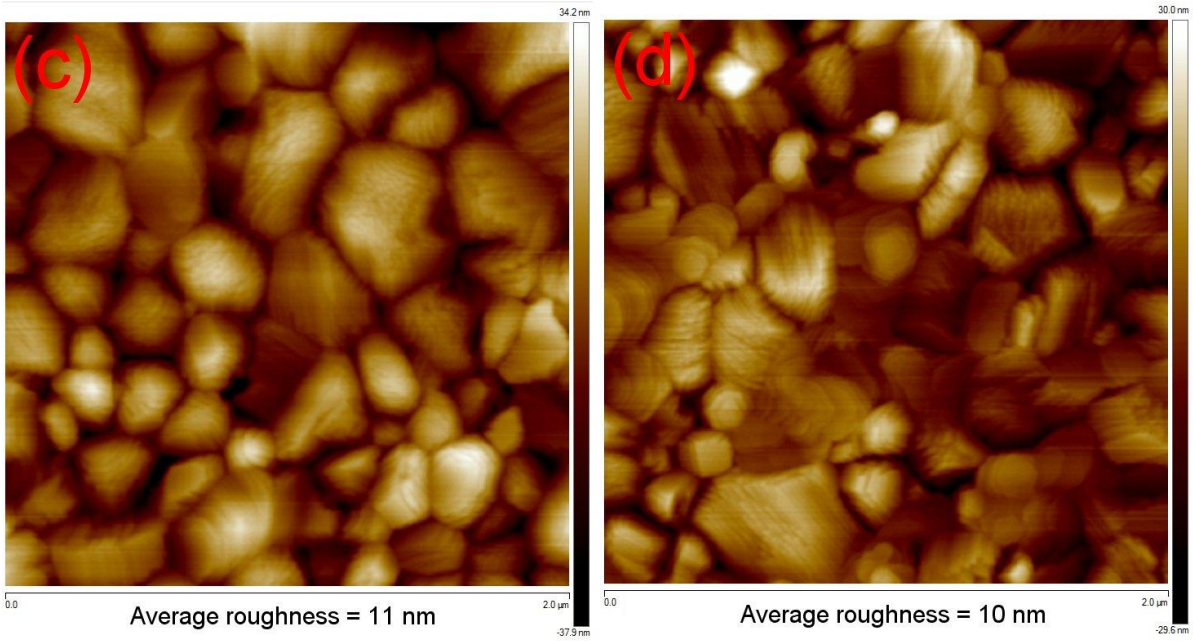

Figure 4.5: Atomic force microscopy (AFM) images of doped $CH_3NH_3PbI_3$ micro-crystals synthesised at temperature of 90 ˚C for 24 hours, using the almost stoichiometric mechanochemical MC2 PbI_2 in reaction with equimolar plus an excess 10 % by weight of CH_3NH_3I and (a) 40 % moles of CH_3NH_3Br, (b) 14 % moles of $CH(NH_2)_2I$, (c) 14 % moles of $CH(NH_2)_2I$ and 10 % moles of Br_2 and (d) no other dopant. Scale bars represent 2 µm.

4.2.4 Vis-IR spectra of perovskite thin films made of undoped or doped $CH_3NH_3PbI_3$ micro-crystals

Optical characterisation of perovskite thin films deposited on glass, using the controllably doped or the undoped $CH_3NH_3PbI_3$ micro-crystals, was performed by visible-infrared (Vis-IR) spectroscopy, as shown in figure 4.6. Also, the calculated optical band gap (E_{obg}) values of each perovskite thin film varies as function of the dopant used, as determined by the Tauc plots and shown in figure 4.7. When 14 % moles of $CH(NH_2)_2I$ incorporated into the crystal structure of $CH_3NH_3PbI_3$, the resulting E_{obg} was ~1.49 eV, additionally when 10 % moles of Br_2 were introduced, the corresponding E_{obg} was ~1.52 eV. These changes with respect to the E_{obg} of the undoped $CH_3NH_3PbI_3$, which was determined to be ~1.51 eV, indicates that the bigger effective ionic radius of $CH(NH_2)_2I$ expanded the crystal lattice leading to an E_{obg} reduction, while the addition of Br_2 with smaller effective ionic radius contracted the crystal lattice, results in an increase in E_{obg}. Also, introduction of 40 % moles of Br_2 into the $CH_3NH_3PbI_3$, causes further contraction of crystal lattice, leading to an even

higher value of the E_{obg} (~ 1.54 eV). In addition, thin films fabricated using the undoped $CH_3NH_3PbI_3$ micro-crystals, shown a weaker absorption of photons with energy ~ 1.55 eV in comparison with all thin films fabricated using the controllably doped $CH_3NH_3PbI_3$ micro-crystals, as shown in figure 4.7, which might be due to the different crystal structure adopted.

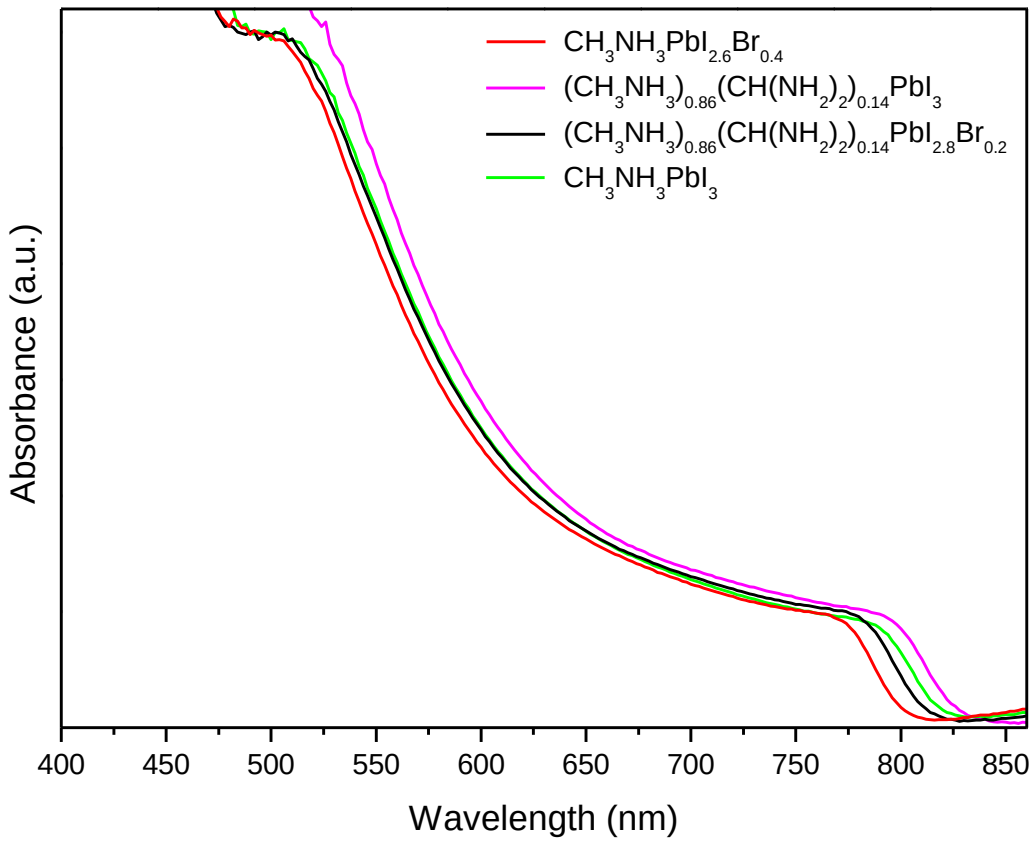

Figure 4.6: Visible-infrared (Vis-IR) absorption spectra of thin films fabricated by doped of undoped $CH_3NH_3PbI_3$ micro-crystals synthesised, using the almost stoichiometric mechanochemical MC2 PbI_2 in reaction with equimolar plus an excess 10 % by weight of CH_3NH_3I and 40 % moles of CH_3NH_3Br (red curve), 14 % moles of $CH(NH_2)_2I$ (magenta curve), 14 % moles of $CH(NH_2)_2I$ and 10 % moles of Br_2 (black curve) and no other dopant (green curve).

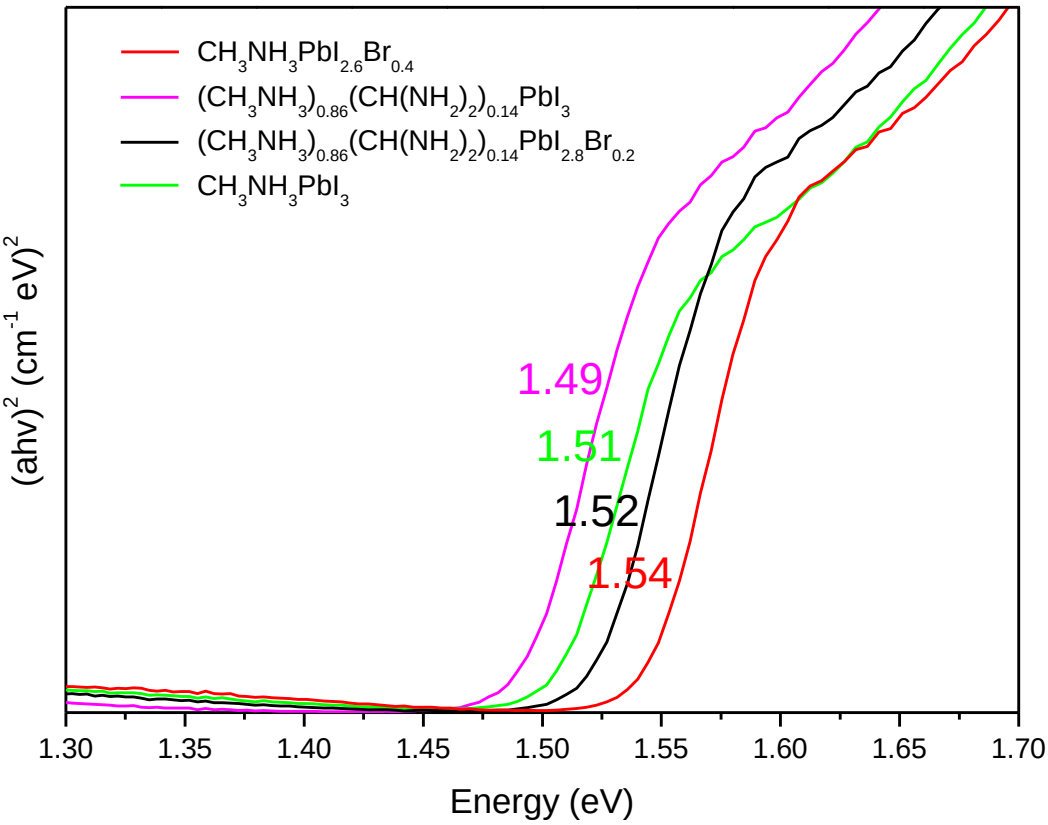

Figure 4.7: Tauc plots of thin films fabricated by doped of undoped $CH_3NH_3PbI_3$ micro-crystals synthesised, using the almost stoichiometric mechanochemical MC2 PbI_2 in reaction with equimolar plus an excess 10 % by weight of CH_3NH_3I and 40 % moles of CH_3NH_3Br (red curve), 14 % moles of $CH(NH_2)_2I$ (magenta curve), 14 % moles of $CH(NH_2)_2I$ and 10 % moles of Br_2 (black curve) and no other dopant (green curve). Optical band gap values of each perovskite thin film, are shown with corresponding colour to each Tauc plot, respectively.

4.2.5 Implications of undoped or doped $CH_3NH_3PbI_3$ micro-crystals to perovskite solar cells

Perovskite solar cells consisting of sequence of stacking layers in the order: glass / ITO / SnO_2 / $CH_3NH_3PbI_3$ / Spiro-MeOTAD / Au which corresponds to n – i – p (regular) architecture were fabricated. The devices were tested, in order to determine whether the doping improves the device performances, with respect to the optimum amount of dopant ions in the perovskite structure. Preparation of solutions and related steps followed for the fabrication of PSCs, were exactly the same as presented in chapter 3 and experimental section (chapter 2). Also, the prepared solutions of doped / undoped $CH_3NH_3PbI_3$ micro-crystals were dissolved in dry DMSO. It was noted that they remained free of premature crystallisation inside the vials after filtration using a PTFE

filter with a pore size of 0.45 μm for more than 300 hours whilst stored at room temperature, as shown in figure 4.8. In addition, the HTL layer (spiro-MeOTAD) deposited was free of FK209 cobalt dopant agent. [15] The photovoltaic parameters, Fill Factor (FF), short circuit current (J_{SC}), open circuit voltage (V_{OC}) and power conversion efficiency (PCE) of un-encapsulated PSCs devices were measured immediately after fabrication and after being kept for 120 hours and 240 hours in a plastic box covered with aluminium foil at ambient conditions. The results are illustrated graphically in figure 4.9. Measured data corresponds to the reverse scan ($V_{OC} \rightarrow 0$) with a scan step of 100 mV.

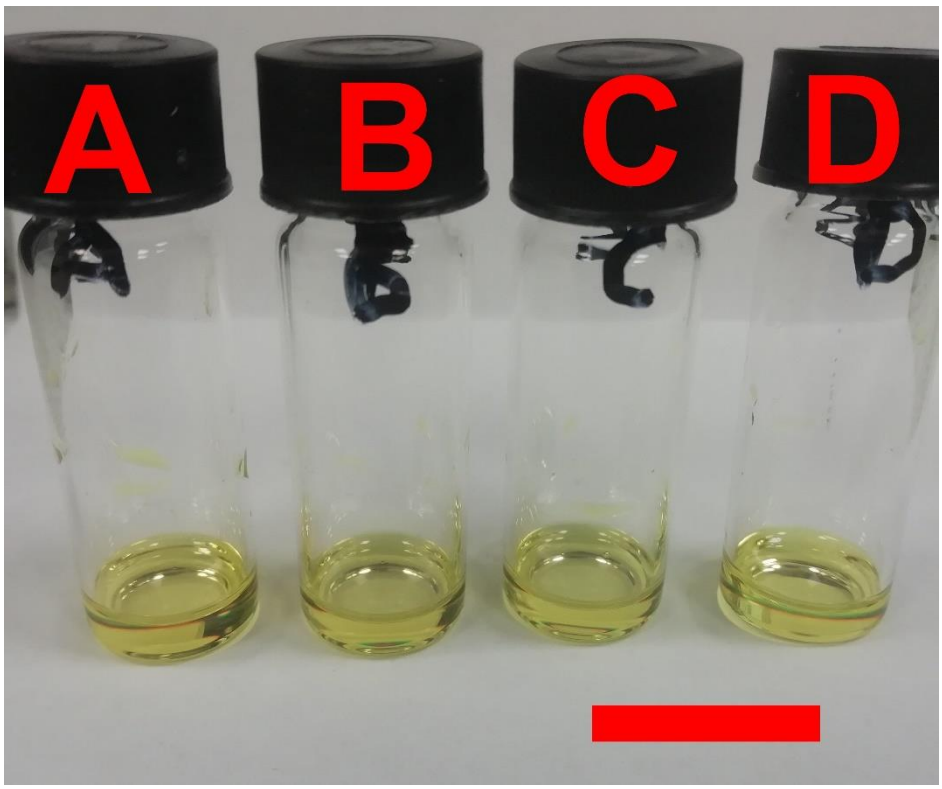

Figure 4.8: Vials with dissolved doped or undoped $CH_3NH_3PbI_3$ micro-crystals in dry DMSO with concentration 1.13 M after filtered and stored at room temperature for more than 300 hours. Doped or undoped $CH_3NH_3PbI_3$ micro-crystals fabricated using, (A) 40 % moles of CH_3NH_3Br, (B) 14 % moles of $CH(NH_2)_2I$, (C) 14 % moles of $CH(NH_2)_2I$ and 10 % moles of Br_2 and (D) no other dopant. Scale bar, represents 20 mm.

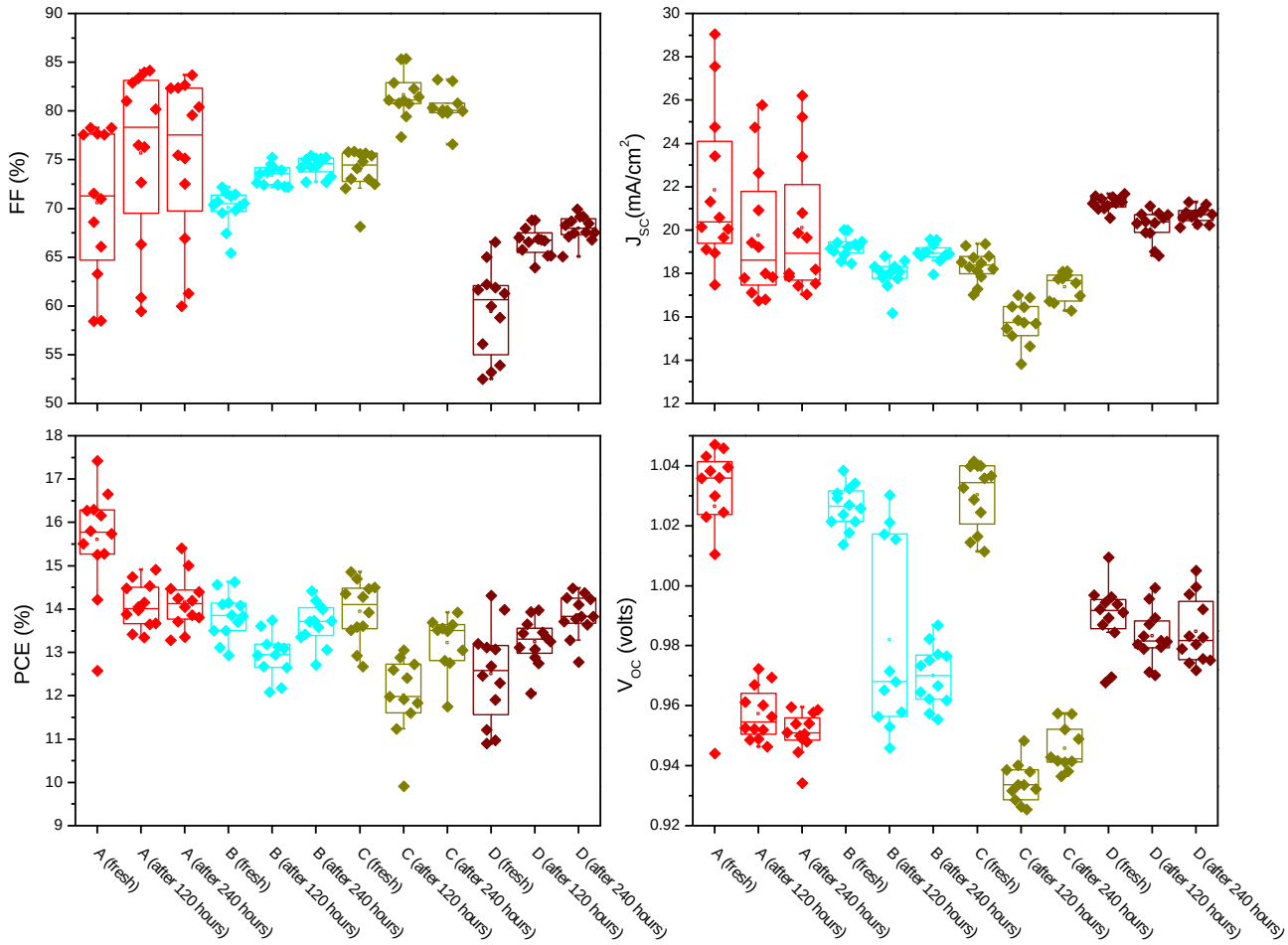

Figure 4.9: The Fill Factor (FF), short circuit current (J_{SC}), power conversion efficiency (PCE) and open circuit voltage (V_{OC}) of PSCs devices with structure glass / ITO / SnO_2 / $CH_3NH_3PbI_3$ / Spiro-MeOTAD / Au, as a function of time (fresh, after 120 hours or 240 hours) and the photoactive layer fabricated using doped or undoped $CH_3NH_3PbI_3$ micro-crystals, ((A) 40 % moles of CH_3NH_3Br, (B) 14 % moles of $CH(NH_2)_2I$, (C) 14 % moles of $CH(NH_2)_2I$ and 10 % moles of Br_2 and (D) no other dopant).

The largest deviation of the average photovoltaic parameters (FF, V_{OC}, J_{SC} and PCE), was observed when the photoactive layer was fabricated with doped $CH_3NH_3PbI_3$ micro-crystals using 40 % moles of CH_3NH_3Br, as shown in figure 4.10. It was also noted that, when Br^- ions were introduced either by using CH_3NH_3Br or Br_2, the corresponding average values of FF, were initially increased after 120 hours, following a downward trend after 240 hours. While the V_{OC} values, were the highest in fresh PSCs, which may relate to the larger values of band gap, lower concentration of defects present in the synthesised micro-crystals and transition from tetragonal to cubic crystal structure. Whereas, absence of Br^- ions into the doped $CH_3NH_3PbI_3$ micro-crystals, results in an upward trend of the FF values even after 240 hours of

fabricated PSCs. Regardless of the type of perovskite micro-crystals used, the average values of J_{SC} in all devices shown a reduction after 120 hours, followed by an increase after 240 hours of storage. The similar trend to the J_{SC}, was noted for the average values of PCE. However, PCE values of PSCs devices fabricated using undoped $CH_3NH_3PbI_3$ micro-crystals, were constantly increased in respect to the time of their storage. Also, significant reduction of the V_{OC} average values as function of time, were observed in all PSCs made using doped $CH_3NH_3PbI_3$ micro-crystals, except of those made using undoped $CH_3NH_3PbI_3$ micro-crystals.

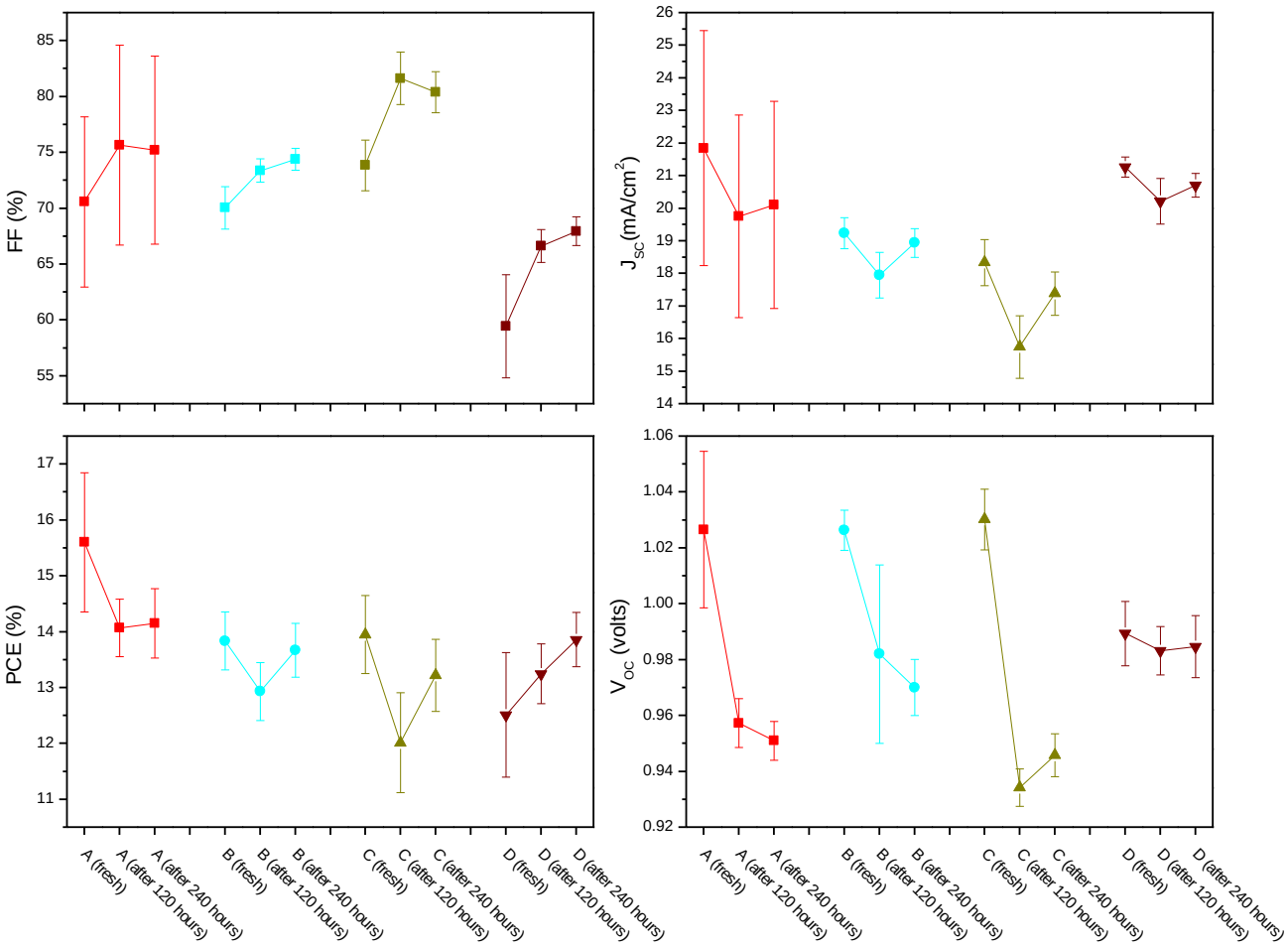

Figure 4.10: Average values (solid point) and corresponding deviations of the Fill Factor (FF), short circuit current (J_{SC}), power conversion efficiency (PCE) and open circuit voltage (V_{OC}) of PSCs devices with structure glass / ITO / SnO_2 / $CH_3NH_3PbI_3$ / Spiro - MeOTAD / Au, as a function of time (fresh, after 120 hours or 240 hours) and the photoactive layer fabricated using doped or undoped $CH_3NH_3PbI_3$ micro-crystals, ((A) 40 % moles of CH_3NH_3Br, (B) 14 % moles of $CH(NH_2)_2I$, (C) 14 % moles of $CH(NH_2)_2I$ and 10 % moles of Br_2 and (D) no other dopant).

The current density-voltage of all PSCs devices that correspond to the forward scan ($0 \rightarrow V_{OC}$) with a scan step of 100 mV, were further analysed and correlated with the time of storage and type of perovskite used. In all the following plots, black curves correspond to the average of current density-voltage curves and the coloured stripes represent the deviation between each initially recorded current density-voltage curve and the black curve. The characteristic green, red and cyan coloured stripes correspond to current density-voltage data of PSCs collected from fresh, after 120 hours and 240 hours, respectively, as shown in figure 4.11. While the characteristic orange coloured stripes correspond to current density-voltage data of fresh PSCs, collected at reverse scan ($V_{OC} \rightarrow 0$) with a scan step of 100 mV. In all sets of black curves that express the average current density-voltage, green coloured stripes that represent the measurements of fresh PSCs, are above the red and cyan coloured stripes, after storage of the PSCs by 120- or 240-hours. Also, when Br^- ions were substituted into the $CH_3NH_3PbI_3$ micro-crystals, either by using CH_3NH_3Br or Br_2, result in a more enhanced shape (better FF) of the current density-voltage indicative of a p-n junction, as shown in figures 4.11 a and 4.11 c. Consequently, the degree of hysteresis observed at the current density-voltage curves between forward and reverse scans, might directly related with the crystal lattice of perovskite during its crystallisation process, in respect to the crystal lattice or surface energy of substrate used. Specifically, the crystal lattice mismatch or surface energy at the interface between perovskite / SnO_2, may be responsible hosting only a maximum number of ions during the crystallisation of perovskite via halogen-oxygen covalent bonds formed. [16] The introduction of ultra violet (UV) ozone treatment of the SnO_2 increases the concentration of oxygen via formation of hydroxyl groups or stannate tin ($Sn(OH)_4$), leading to an enhanced number of those covalent bonds to be formed and reducing the hysteresis within the current density-voltage curves between forward and reverse scans. [17] However, we suggest that a controllably in stoichiometry deposited thin layer (< 5 nm) of perovskite metal - oxide type on TCO, might provide the necessary number of halogen-oxygen bonds, resulting in more stable PSCs. This approach is analogous with the growth of III-V doped semiconducting materials with optimum optoelectronic properties by molecular beam epitaxy (MBE), for controllable transition between the thin films with different crystal lattices.

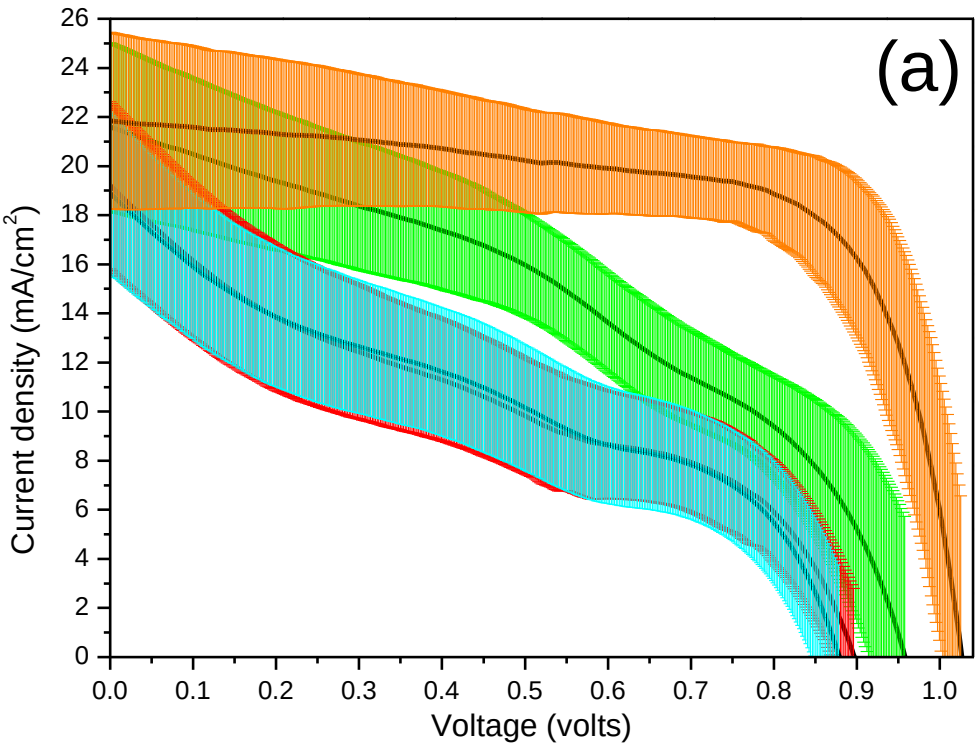
(a)
Current density (mA/cm^2)
Voltage (volts)
0
2
4
6
8
10
12
14
16
18
20
22
24
26
0.0
0.1
0.2
0.3
0.4
0.5
0.6
0.7
0.8
0.9
1.0

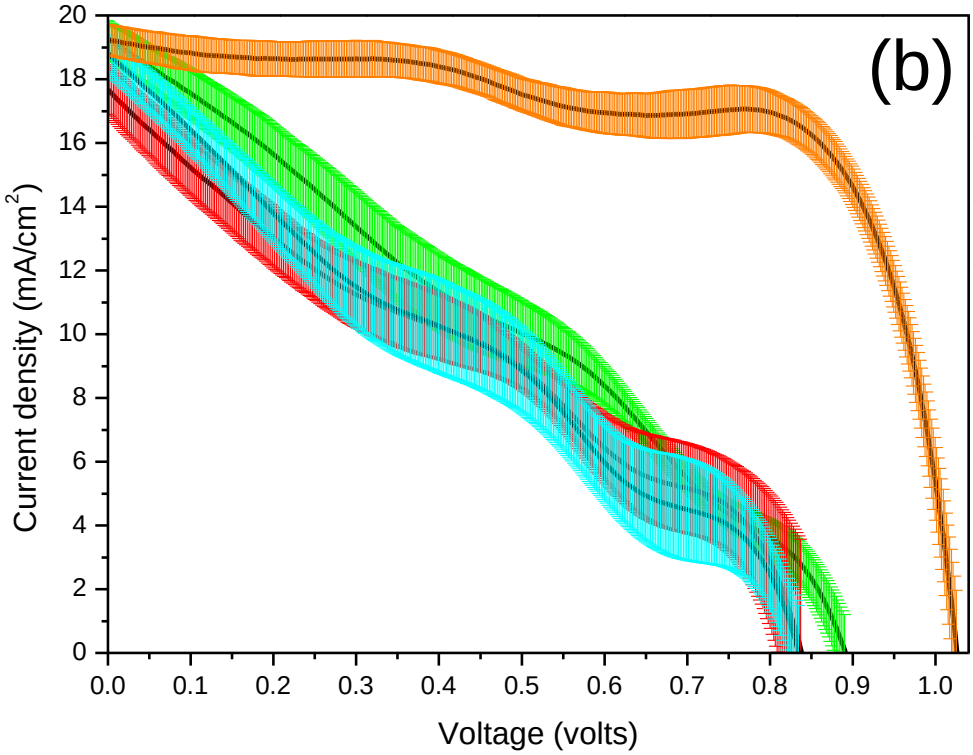
(b)
Current density (mA/cm^2)
Voltage (volts)
0
2
4
6
8
10
12
14
16
18
20
0.0
0.1
0.2
0.3
0.4
0.5
0.6
0.7
0.8
0.9
1.0

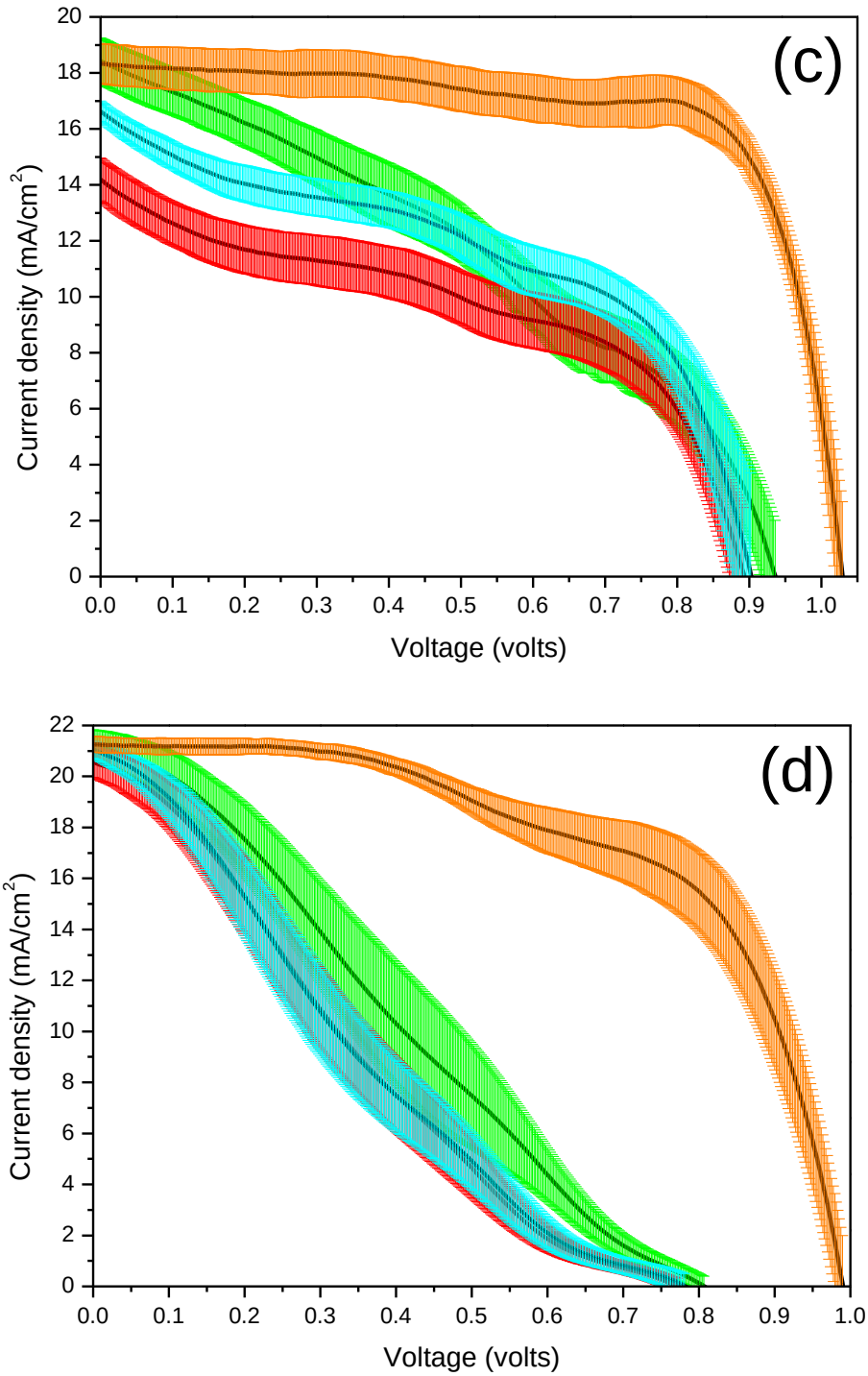

Figure 4.11: Characteristic current density-voltage curves in forward (0 → V_{OC}) and reverse (V_{OC} → 0) scans of PSC devices with structure glass / ITO / SnO_2 / $CH_3NH_3PbI_3$ / Spiro-MeOTAD / Au, as a function of time and the photoactive layer fabricated using doped or undoped $CH_3NH_3PbI_3$ micro-crystals, (a) 40 % moles of CH_3NH_3Br, (b) 14 % moles of $CH(NH_2)_2I$, (c) 14 % moles of $CH(NH_2)_2I$ and 10 % moles of Br_2 and (d) no other dopant. Black curves correspond to the average of current density-voltage curves and coloured stripes to their deviation from the average black curve. Green, red and cyan coloured stripes, indicate current density-voltage data collected from fresh, after 120 hours and 240 hours, in forward (0 → V_{OC}) scans. Whereas orange coloured stripes, indicate current density-voltage data collected from fresh, in reverse (V_{OC} → 0) scans.

4.3 Conclusion

In conclusion, synthesis of controllably doped $CH_3NH_3PbI_3$ micro-crystals with variable amount of dopants of either CH_3NH_3Br or $CH(NH_2)_2I$ or $CH(NH_2)_2I$ and Br_2, was successfully achieved without dissolving the PbI_2 used in highly toxic solvents. The optimum amount of ions selectively intercalated into the crystal structure of $CH_3NH_3PbI_3$, was defined by the transition from tetragonal to cubic crystal structure, as determined by the XRD spectra and SEM images. Also, crystal structure transition in perovskite caused by the substitution of ions with different effective ionic radius, was correlated with optical band gap values, as determined by Vis-IR spectra. However, more than one transition in the crystal structure, might exist with respect to the amount and effective ionic radius of ions used. Perovskite thin films manufactured by re-dissolving the doped or undoped $CH_3NH_3PbI_3$ micro-crystals only in DMSO solvent which is less-toxic than the widely used dimethyl formamide (DMF) solvent. In combination with a single step of fabrication, using a vacuum assisted method, free of any complicated step that promotes the crystallisation of perovskite using the method of antisolvent. Morphological characterisation of thin films, revealed the formation of two-dimensional layered structures within the perovskite grains, regardless of the ratio between the cations and anions used, as determined by AFM images. The PSC devices fabricated, showed a reduction in the average PCE from ~ 14 (±1.5) % to ~ 13.7 (±0.5) %, after storage under ambient conditions for 240 hours, regardless of the ratio between the cations and anions present into the doped or undoped $CH_3NH_3PbI_3$ micro-crystals used. Additionally, PSCs devices fabricated using photoactive layers doped with bromide anions, shown less hysteresis at the current density-voltage curves at forward scans.

4.4 References

1 C. H. Ng, H. N. Lim, S. Hayase, Z. Zainal and N. M. Huang, *Renew. Sustain. Energy Rev.*, 2018, **90**, 248–274.

2 M. Acik, T. M. Alam, F. Guo, Y. Ren, B. Lee, R. A. Rosenberg, J. F. Mitchell, I. K. Park, G. Lee and S. B. Darling, *Adv. Energy Mater.*, 2018, **8**, 1701726.

3 L. Q. Xie, L. Chen, Z. A. Nan, H. X. Lin, T. Wang, D. P. Zhan, J. W. Yan, B. W. Mao and Z. Q. Tian, *J. Am. Chem. Soc.*, 2017, **139**, 3320–3323.

4 O. Nazarenko, S. Yakunin, V. Morad, I. Cherniukh and M. V Kovalenko, *NPG Asia Mater.*, 2017, **9 (4)**, e373.

5 M. Keshavarz, M. Ottesen, S. Wiedmann, M. Wharmby, R. Küchler, H. Yuan, E. Debroye, J. A. Steele, J. Martens, N. E. Hussey, M. Bremholm, M. B. J. Roeffaers and J. Hofkens, *Adv. Mater.*, 2019, **31 (24)**, 1900521.

6 S. Kulkami, T. Baikie, P. Boix, N. Yantara, N. Mathews and S. Mhaisalkar, *J. Mater. Chem. A*, 2014, **2 (24)**, 9221–9225.

7 B. Park, B. Philippe, S. Jain, X. Zhang, T. Edvinsson, H. Rensmo, B. Zietz and G. Boschloo, *J. Mater. Chem. A*, 2015, **3 (43)**, 21760–21771.

8 Z. Yang, C. Chueh, P. Liang, M. Crump, F. Lin, Z. Zhu and A. K. Jen, *Nano Energy*, 2016, **22**, 328–337.

9 G. E. Eperon, S. D. Stranks, C. Menelaou, M. B. Johnston, L. M. Herz and H. J. Snaith, *Energy Environ. Sci.*, 2014, **7**, 982–988.

10 C. E. Housecroft and A. G. Sharpe, *INORGANIC CHEMISTRY*, Prentice Hall, ISBN: 9780273742753, 2012.

11 C. Wu, Q. Zhang, Y. Liu, W. Luo, X. Guo, Z. Huang, H. Ting, W. Sun, X. Zhong, S. Wei, S. Wang, Z. Chen and L. Xiao, *Adv. Sci.*, 2017, **1700759**, 2–9.

12 M. U. Rothmann, W. Li, Y. Zhu, U. Bach, L. Spiccia, J. Etheridge and Y.-B. Cheng, *Nat. Commun.*, 2017, **8**, 14547.

13 Y. Liu, L. Collins, R. Proksch, S. Kim, B. R. Watson, B. Doughty, T. R. Calhoun, M. Ahmadi, A. V. Levlev, S. Jesse, S. T. Retterer, A. Belianinov, K. Xiao, J. Huang, B. G. Sumpter, S. V. Kalinin, B. Hu and O. S. Ovchinnikova, *Nat. Mater.*, 2018, **17**, 1013–1019.

14 C. Lan, Z. Zhou, R. Wei and J. C. Ho, *Mater. Today Energy*, 2019, **11**, 61–82.

15 Q. Jiang, Y. Zhao, X. Zhang, X. Yang, Y. Chen, Z. Chu, Q. Ye, X. Li, Z. Yin and J. You, *Nat. Photonics*, 2019, **40 (4)**, s41566.

16 K. E. Riley and K. M. Merz, *J. Phys. Chem. A*, 2007, **111 (9)**, 1688–1694.

17 P. F. Méndez, S. K. M. Muhammed, E. M. Barea and I. Mora-seró, *Sol. RRL*, 2019, **1900191**, 1–6.

Chapter 5

Conclusions and future work

5.1 Introduction

Since the end of the previous decade, when the scientific community became aware of their remarkable and versatile optoelectronic properties, mixed organic - inorganic halide perovskite compositions with general chemical formula ABX_3, have emerged as a new class of semiconductors. Noticeable progress has been made worldwide by numerous researchers, implementing them in devices, such as photovoltaics, light emitting diodes (LEDs), photodetectors, batteries and even in the field of spintronics. [1–5] Rapid progress in the field of perovskite solar cells (PSCs) development, originates from the low cost of the materials used, variability in the optoelectronic properties as a function of the ratio between the mixed organic-inorganic halide precursors and their simplicity of fabrication. Also, astonishing values (~ 24 %) for the power conversion efficiency (PCE) in PSCs, based on a single photoactive layer of perovskite have been achieved. This performance, competes with the market dominating silicon based solar cells with PCE ~ 26.6 %. The current state of the art of devices combine together silicon and perovskite materials to result in tandem heterojunction photovoltaic devices, which reach a PCE of 28 %, as shown in the NREL (National Renewable Energy Laboratory) chart of the highest PCE values per type of photovoltaic (see figure 1.8 in chapter 1). However, long term stability and durability, remain key challenges for PSC commercialization. These parameters will be influenced by the purity and stoichiometry of the organic-inorganic halide precursors used in the fabrication of perovskites.

5.2 Conclusions

In this thesis, the importance of stoichiometry and polytypism in lead iodide (PbI_2) used in the PSCs fabrication process, was studied as presented in chapter 3. Successful synthesis of PbI_2 was achieved by employing two different methods of synthesis and their properties were compared with two commercially available materials. The two processes used were the solvothermal in which there was presence of water and a mechanochemical approach using planetary ball milling which was free of water during the synthesis of PbI_2. The solvothermal synthesis results in over-stoichiometric PbI_2, with a lead to iodide ratio be 1: ~2.05 (±0.05), as determined by X - ray photoelectron spectroscopy (XPS) and Rutherford backscattering spectroscopy (RBS). Also, a high percentage of oxygen content (~7.2 %) possibly attributed to autoionization of water molecules caused by strong Coulomb interactions between the ions (Pb^{2+} and I^-) and water molecules was detected by energy dispersive spectroscopy (EDS) predominantly in the needle shaped crystals present. That increased oxygen content was guide us to the mechanochemical approach which was free of water. Mechanochemical synthesis allowed regulation of both the stoichiometry and the number of polytypic phases present in the resulting PbI_2, as shown by X-ray diffraction (XRD). By varying the mechanochemical parameters (revolution per minute and time duration) of the synthesis, we found that at optimum conditions of 400 rpm and 1 hour, results in PbI_2 with lead to iodide ratio be from 1:2, as determined by XPS and RBS analysis, respectively. It should also be noted, that the mechanochemical method, is a low-cost, water free and energy efficient (~ 31.3 watts per hour per gram) process, producing moderate to large quantities of PbI_2 (≥ 40 grams per run and yield ~ 96 ±0.5 %). In contrast, the two commercial PbI_2 powders were found to be sub- or over-stoichiometric with a single or more than one polytypic phase materials. The ratio between the lead to iodide atoms was 1: ~ 1.8 (±0.1) for the Sigma Aldrich with purity 99.999 % and 1: ~ 2.15 (±0.15) for the Tokyo Chemical Industries with purity 99.99 %, as determined by XPS, RBS and XRD analysis, respectively. Also, the stoichiometric ratio between the lead and iodide atoms present for the mechanochemical was found to be 1: ~ 1.96 and the commercial from Sigma Aldrich to be 1: ~ 1.7 as determined and corrected by controllable synthesis of $CH_3NH_3PbI_3$ micro-crystals, as shown by XRD characterisation. [6] This discrepancy at stoichiometric ratios between the lead and

iodide atoms in PbI_2 samples as determined by different characterization techniques might be related to a formatted gradient of iodide atoms between the surface and bulk (inner volume) directly correlated with the polytypic nature of PbI_2. PSC devices fabricated with $CH_3NH_3PbI_3$ thin films as the photoactive layers, manufactured using sub-stoichiometric PbI_2, showed a reduction in the average power conversion efficiency (PCE) from ~15.5 % to ~4.6 % due to the presence of unreacted PbI_2, as further confirmed by Vis-IR spectroscopy. A comprehensive analysis was presented regarding the formation of unreacted PbI_2 in respect to the initial stoichiometry of the PbI_2 used for the formation of $CH_3NH_3PbI_3$. However, when excess iodide added to the sub-stoichiometric PbI_2 via CH_3NH_3I during the fabrication of $CH_3NH_3PbI_3$ micro-crystals, the average performance of PSCs was high (~15.5 %). Also, $CH_3NH_3PbI_3$ thin films were manufactured using only dimethyl sulfoxide (DMSO) which is a less-toxic solvent in comparison with the widely used dimethyl formamide (DMF) solvent. Deposition of perovskite thin films combined with a single step of a vacuum assisted method, promoted the formation of two-dimensional $CH_3NH_3PbI_3$ layered structures within individual grains, regardless of the stoichiometry and polytypic phases present in the PbI_2 used, as shown in AFM and SEM images. [7] We believe, that an ideal stoichiometry of materials used in the synthesis of the perovskite thin films, alongside with a simple and repeatable deposition process for the fabrication of PSC devices, might provide enhanced stability and PCE values.

The stability of PSCs fabricated with optimum stoichiometry between different ions present was assessed, as presented in chapter 4. Synthesis of controllably doped or undoped $CH_3NH_3PbI_3$ micro-crystals with various amounts of dopants of either methylammonium bromide (CH_3NH_3Br) or formamidinium iodide ($CH(NH_2)_2I$) or $CH(NH_2)_2I$ and bromide (Br_2), was achieved. [6] An optimum amount of dopants defined by the transition from tetragonal to cubic crystal structure based on the three major peaks with the strongest diffraction, as determined by XRD spectra. An optimum amount ~40 % moles of Br^- ions substituted in the crystal structure of $CH_3NH_3PbI_3$ was found. Whereas, the optimum combined amount was found to be ~ 14 % moles of $CH(NH_2)_2^-$ and ~ 20 % moles of Br^- ions substituted into the crystal structure of $CH_3NH_3PbI_3$. Also, optical band gap values of perovskite thin films fabricated using the controllably doped $CH_3NH_3PbI_3$ micro-crystals, shown fluctuation with respect to $CH_3NH_3PbI_3$. That was attributed to expansion or contraction in the crystal lattice of

perovskites, as function of the effective ionic radius of dopant ions used and confirmed by Vis-IR spectroscopy. PSC devices manufactured by re-dissolving the doped or undoped $CH_3NH_3PbI_3$ micro-crystals only in DMSO and crystalizing again as a thin film with the single step vacuum assisted method, results in the formation of two-dimensional perovskite layered structures within individual grains, regardless of the ratio between the cations and anions used, as determined by AFM / SEM images. [7] Also, un-encapsulated PSC devices with stacking sequence of glass / ITO / SnO_2 / $CH_3NH_3PbI_3$ / Spiro-MeOTAD / Au showed a small reduction in the average PCE from ~ 14 (±1.5) % to ~ 13.7 (±0.5) % after storage in dark and under ambient conditions for 240 hours. Additionally, PSC devices fabricated using photoactive layers doped with Br^- anions, shown less hysteresis in the current density-voltage curves between the forward ($0 \rightarrow V_{OC}$) and reverse ($V_{OC} \rightarrow 0$) scans. We believe, this might originated from the number of halogen-oxygen covalent bonds formed at the interface between the perovskite thin film during the crystallisation and the untreated (without the ultra violet light ozone) electron transporting layer of tin oxide (SnO_2) used.[8]

5.3 Future work

An extension to the work undertaken in chapter 3, would be the investigation of PbI_2 synthesis for identical stoichiometry by using a mixer mill MM 400 (Retsch), which is an entirely new type of mechanochemical process for powder homogenization, with typically grinding time from seconds to minutes. This process might require less time than the use of planetary ball milling, whilst maintaining a stoichiometrically accurate ratio in a range of chalcogenide compounds, such as cadmium iodide (CdI_2), lead chloride ($PbCl_2$), lead bromide ($PbBr_2$) etc., free of oxygen-halogen compounds. Also, PSCs devices manufactured by dissolving the organic-inorganic precursors or perovskite micro - crystals only in DMSO, which is a less-toxic solvent and combined with the single step vacuum assisted method, free of any antisolvent rinsing step, is likely to be an attractive deposition process for roll-to-roll or tandem (heterojunction of silicon / perovskite) development in the field of PSCs.

An extension to the work undertaken in chapter 4, would be the investigation of controllable doping of formamidinium lead triiodide $CH(NH_2)_2PbI_3$ micro-crystals with

caesium iodide (CsI) and Br_2, in order the optimum amount of Cs^+ and Br^- ions intercalated into the crystal structure to be determined by XRD spectra. Also, since the formation of two-dimensional perovskite layered structures were observed, regardless of the ratio between the cations and anions used. Progressive annealing of perovskite thin films directly after the step of vacuum assisted method, in a chamber with pressure (P): 1 bar < P < 50 bar, might accelerate the formation of the two-dimensional layered structures in a preferable orientation, resulting in perovskite thin films with larger grains and reduced number of grain boundaries. In principle, this process is similar to gas (nitrogen) quenching which, resulting in densely packed grains in perovskite thin films. [9] During the electrical characterisation of un-encapsulated PSCs fabricated with photoactive layers doped with bromide, less hysteretic effect was observed between the current density-voltage curves recorded at forward and reverse scans. Considering that ultra violet ozone treatment leads to elimination of hysteresis in PSCs by hydroxyl groups formed on the electron transporting layer (ETL) on which the crystallisation of perovskite thin film occurs. We suggest that deposition of a metal-oxide perovskite layer between the ETL and the photoactive layer of perovskite, might provide an adequate number of oxygen atoms and therefore more halogen-oxygen covalent bonds to be formed. That metal-oxide perovskite layer, could provide a crystal lattice transition between the ETL and the photoactive layer, likely leading to enhanced optoelectronic properties and stability in PSCs.

Lastly, there is an increasing number of technological devices, such as mobile phones, computers, cars, space equipment, satellites etc., electrified by batteries and thermoelectric modules. Since, batteries and thermoelectric modules can now be fabricated based on perovskites and have shown enormous values of current capacity (200 mA * h * g^{-1}) and Seebeck coefficient (~ 1700 μV * K^{-1} at temperature of 351 K). [4,10] It is highly probable that batteries and thermoelectric modules fabricated using controllable doped perovskites micro-crystals, will gain significant attention in the near future.

5.4 References

1 Z. Shi and A. H. Jayatissa, *Materials.*, 2018, **11 (5)**, 729.

2 N. Kumawat, X.-K. Liu, D. Kabra and F. Gao, *Nanoscale*, 2019, **11**, 2109–2120.

3 J. Miao and F. Zhang, *J. Mater. Chem. C*, 2019, **7**, 1741–1791.

4 N. Vicente and G. Garcia-belmonte, *J. Phys. Chem. Lett.*, 2017, **8 (7)**, 1371–1374.

5 P. Odenthal, W. Talmadge, N. Gundlach, R. Wang, C. Zhang, D. Sun, Z. Yu, Z. V. Vardeny and Y. S. Li, *Nat. Phys.*, 2017, **13**, 894–899.

6 M. Acik, T. M. Alam, F. Guo, Y. Ren, B. Lee, R. A. Rosenberg, J. F. Mitchell, I. K. Park, G. Lee and S. B. Darling, *Adv. Energy Mater.*, 2018, **8**, 1701726.

7 C. Wu, Q. Zhang, Y. Liu, W. Luo, X. Guo, Z. Huang, H. Ting, W. Sun, X. Zhong, S. Wei, S. Wang, Z. Chen and L. Xiao, *Adv. Sci.*, 2017, **1700759**, 2–9.

8 P. F. Méndez, S. K. M. Muhammed, E. M. Barea and I. Mora-seró, *Sol. RRL*, 2019, **1900191**, 1–6.

9 A. Babayigit, J. D. Haen, H. Boyen and B. Conings, *Joule*, 2018, **2 (7)**, 1205–1209.

10 T. Ye, X. Wang, X. Li, A. Yan, S. Ramakrishna and J. Xu, *J. Mater. Chem. C*, 2017, **5 (5)**, 1255–1260.